
Simulation of the KATRIN Source Plasma using Monte Carlo and Particle in Cell Methods

Zur Erlangung des akademischen Grades eines
DOKTORS DER NATURWISSENSCHAFTEN (Dr. rer. nat.)

von der KIT-Fakultät für Physik des
Karlsruher Instituts für Technologie (KIT)
genehmigte

DISSERTATION
von

M. Sc., Kellerer, Jonas

Tag der mündlichen Prüfung: 28.01.2022
1. Referent: Prof. Dr. Guido Drexlin
2. Referent: Priv. Doz. Dr. Felix Spanier



Dieses Werk ist lizenziert unter einer Creative Commons Namensnennung - Nicht-kommerziell - Weitergabe unter gleichen Bedingungen 4.0 International Lizenz (CC BY-NC-SA 4.0):
<https://creativecommons.org/licenses/by-nc-sa/4.0/deed.de>

Contents

Introduction	vii
1. The KATRIN Experiment - An Overview	1
1.1. Windowless Gaseous Tritium Source	1
1.2. Differential Pumping Section	3
1.3. Cryogenic Pumping Section	4
1.4. Pre- and Main-Spectrometer	5
1.5. Detector	6
1.6. Rear Section	7
2. Conditions of the Source Plasma	9
2.1. Neutral Gas Flow	9
2.1.1. Density Distribution	9
2.1.2. Temperature Profile	11
2.1.3. Velocity Distribution	12
2.2. Electric Background Fields	14
2.3. Magnetic Background Fields	18
2.4. Charged Particle Interactions in the KATRIN Source	18
2.4.1. Energy Dependence of the Cross Section	19
2.4.2. Electron-Interactions	19
2.4.3. Ion-Interactions	24
2.4.3.1. Interactions of H^+ Ions	24
2.4.3.2. Interactions of H_2^+ Ions	27
2.4.3.3. Interactions of H_3^+ Ions	28
2.4.3.4. Interactions of Higher Order Cluster Ions	30
3. Classification of the KATRIN Plasma	37
3.1. Introduction to Plasmas	37
3.2. Experimental Investigations	38
3.2.1. Krypton Line Measurements	38
3.2.2. Particle Current Measurements	40
3.2.3. Pro-KATRIN Measurements	41
3.3. Characteristic Length Scales	42
3.3.1. Debye Length	43
3.3.2. Landau Length	44
3.3.3. Mean Free Path	45
3.3.4. Gyroradius and Classical Diffusion	46
3.3.5. Inertial Length	48
3.3.6. Summary	48
3.4. Characteristic Frequencies	51
3.4.1. Plasma Frequency	51
3.4.2. Gyro Frequency and Synchrotron radiation	52

3.4.3.	Collision Rate	53
3.4.4.	Summary	53
3.5.	Plasma Models	54
3.5.1.	Drift-Diffusion Model	55
3.5.2.	Partly Collisional Vlasov Model	57
4.	Simulation of Particle Distributions with KARL	59
4.1.	Simulation Method	59
4.1.1.	Particle Movement	60
4.1.2.	Particle Interactions	62
4.1.2.1.	Elastic Scattering	63
4.1.2.2.	Electron Impact Ionization	65
4.1.2.3.	Electron Impact Excitation	66
4.1.2.4.	Recombination	66
4.1.2.5.	Ion Cluster Formation	66
4.1.2.6.	Ion Charge Transfer	67
4.1.3.	Density Fields	67
4.1.4.	Simulation Output and Diagnostics	68
4.2.	Validation	69
4.2.1.	Ionization	69
4.2.2.	Elastic Scattering	69
4.2.3.	Excitation	70
4.2.4.	Recombination	72
4.3.	Electromagnetic Field-Free Simulation	73
4.3.1.	Electron Spectrum	74
4.3.2.	Charged Particle Densities	76
4.3.3.	Charged Particle Currents	77
4.3.4.	Influence of External Parameters	79
4.3.4.1.	Tritium Gas Density	79
4.3.4.2.	Tritium Gas Temperature	81
4.3.4.3.	Magnetic Background Field	81
4.3.5.	Comparison to Previous Study	82
4.4.	Simulation with Electric Background Field	84
4.4.1.	Rear Wall Field	84
4.4.2.	Field from Density Data	86
4.4.2.1.	Poisson Solver	86
4.4.2.2.	Simulation with Self Generated Field	88
4.5.	Conclusion	91
5.	Particle in Cell Simulations with ACRONYM	93
5.1.	The Particle in Cell Method	93
5.1.1.	Grids for Currents and Fields	95
5.1.2.	Macro Particles	95
5.1.3.	Particle Movement	96
5.1.4.	Current Deposition	98
5.1.5.	Maxwell Solver	99
5.2.	Boundary Conditions	100
5.2.1.	Perfect Electrical Conductor	100
5.2.2.	Periodic Boundary Condition	103
5.2.3.	Perfectly Matched Layer	103
5.3.	Background Fields and Currents	104

5.4.	Particle Injection	105
5.4.1.	Initial Loading	105
5.4.1.1.	Particles Per Cell and Macro Factor	105
5.4.1.2.	Sampling of the Kinetic energy	107
5.4.1.3.	Sampling of the Velocity	109
5.4.2.	Injection During Simulation	109
5.4.2.1.	Injection through Constant Current	109
5.4.2.2.	Injection by retaining Constant Density	110
5.4.2.3.	Injection through Constant Decay Rate	111
5.5.	Electrostatic Potential derived by Poisson Equation	112
5.6.	Validation of ACRONYM Simulations	114
5.6.1.	Ion Current Approximation	114
5.6.2.	Background Electric Field	116
5.6.3.	Cavity Mode Excitation	117
5.6.4.	Boundary Layer Development	122
5.7.	Conclusion	126
6.	Particle in Cell Simulation of KATRIN Source	129
6.1.	Estimation of Computational Resources	129
6.2.	Rear Wall Section	131
6.2.1.	Electron Spectrum	132
6.2.2.	Electron Density	137
6.2.3.	Background Current Value	140
6.2.4.	Radial Dependent Background Current	142
6.2.5.	Potential at Large Time Scales	145
6.3.	Central Section	149
6.4.	Complete Source Section	155
6.5.	Conclusion	159
7.	Conclusion and Outlook	163
	Appendix	169
A.	Analytical Calculation of the Rear Wall Potential	169
B.	Conversion of Energy into Different Inertial Frames	171
	List of Abbreviations	171
	Bibliography	175
	Acknowledgement	180

Introduction

Since the postulation of neutrinos in 1930 by Pauli [64] and their direct detection in 1956 by Cowan Jr et al. [17], the neutrino has been at the center of the investigation in many particle and astroparticle physics experiments. So far, neutrinos are best described by the standard model of particles, where they are specified as charge neutral, massless fermions, which are created by weak interaction in one of the three different leptonic eigenstates ν_e , ν_μ , and ν_τ . However, the experiments of the Sudbury Neutrino Observatory [2] and Super-Kamiokande [58] showed that the leptonic neutrino flavor changes during propagation. This effect is called neutrino oscillation, which indicates that neutrinos have at least three additional mass eigenstates with non-zero mass-squared differences. Thus, the experiments proved that neutrinos have non-zero masses, contradicting the standard model. Until now, the absolute mass is still undetermined, and searched for in various experiments.

Neutrino mass experiments can be classified into two conceptually different categories: indirect and direct approaches. In the indirect search, the neutrino mass is inferred from a model, where the model itself is not fully proven. The indirect approaches include cosmological studies, supernova neutrino measurements and measurements of the neutrinoless double beta decay. In the direct search, the neutrino mass is determined directly from well tested models. The direct approaches include the spectroscopy of electron capture products and the spectroscopy of beta decay electrons. The different methods are described in short in the following. Their results are summarized in table 1.

Cosmological studies infer the sum of all neutrino masses from its influence on the large-scale structure formation in the universe. Neutrinos play a vital role in the description of small-scale structures. They can carry away mass from gravitational centers and thus reducing the amount of small-scale structures. The efficiency of this process is dependent on the mass of the neutrinos. Larger neutrino masses will reduce the formation of small-scale structures more than smaller neutrino masses. Thus, observations of the structure size can provide an insight on the neutrino mass. One of these measurements is performed by the observation of the temperature anisotropies in the cosmic microwave background. In 2018

Table 1.: Summary of experimental limits on the neutrino mass. The approach describes the method employed to determine the neutrino mass, the observable describes the variable by which the limit is determined.

Approach	Observable	Current limit (in eV/c^2)	
Cosmology	$m_{\text{cos}} = \sum_i m_i$	< 0.12	[1]
Super Nova	$m_{\bar{\nu}_e}$	< 5.7	[52]
$0\nu\beta\beta$	$m_{\beta\beta} = \sum_i U_{ei}^2 m_i $	$< 0.06 \dots 0.17$	[27]
β and EC	$m_\beta = \sqrt{\sum_i U_{ei} ^2 m_i^2}$	< 1.1	[3]

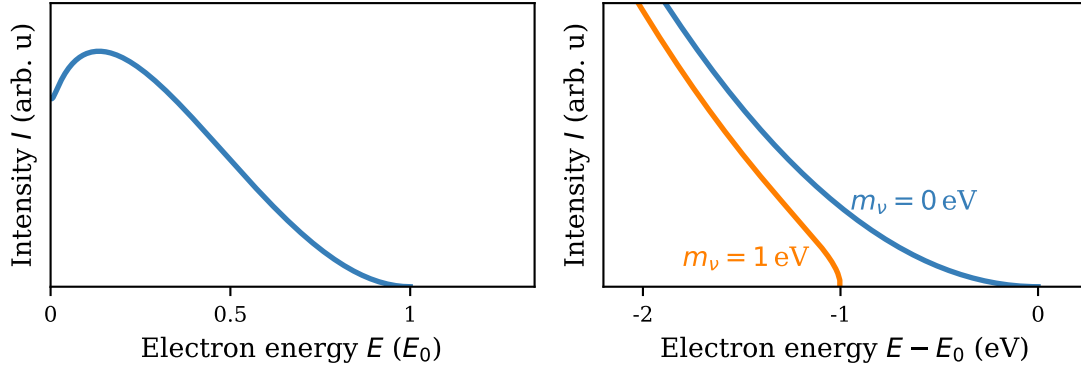


Figure 1.: Sketch of Tritium beta decay spectrum. The left side shows the full spectrum up to the endpoint energy E_0 . The right side shows a close up of the endpoint region for two different neutrino mass cases. Figure adapted from [73].

the Planck collaboration derived that the sum of all neutrino masses must be lower than 0.12 eV (95 % confidence level)[1].

In a core-collapse supernova, large numbers of neutrinos with high energies are emitted within a short period of time. The time difference of the arrival of the neutrinos at the earth is dependent on the initial energy of the neutrinos, the emission time difference and the neutrino mass. The emission time difference can be constrained by a suitable collapse model. Thus, the neutrino mass can be inferred from a measurement of the neutrino flux. In 1987, a supernova (SN 1987A) occurred in close enough proximity of earth that the neutrino flux was measurable with the detectors at that time. A reanalysis of the measurement data showed that the antineutrino mass could be constrained to values below 5.7 eV (95 % confidence level) [52].

The neutrinoless double beta studies postulate that the neutrino is a Majorana particle: a particle that can act as its own antiparticle. Therefore, some isotopes may undergo a double beta decay without emitting neutrinos. The measurement of the half-life of such an interaction would provide a limit on the sum of Majorana masses. The current best limit on the sum of the Majorana masses is provided by the KamLAND-Zen collaboration with values below 0.06 eV (90 % confidence level) [27].

Electron capture and beta decay experiments work on a similar principle. Both investigate the missing energy, which will be carried away by the neutrino, in either the electron capture process or the beta decay process. The calculations are based on energy and momentum conservation. No assumption is made on the specific nature of neutrinos. Thus, these methods can be considered as model independent. In the following, only the beta decay measurement principle will be described because both methods are so fundamentally similar. Please refer to [28] for more information on electron capture processes.

The beta decay spectrum can be described by the well tested Fermi model of beta decay [22]. In the Fermi model, the transition probability per time unit can be calculated by the use of Fermi's golden rule. From this, the differential energy can be derived as

$$\frac{d\Gamma}{dE} = \frac{G_F^2 \cdot \cos^2 \theta_C \cdot |M|^2}{2\pi^3} \cdot F(Z+1, E) \cdot p \cdot (E + m_e) \cdot \sqrt{(E_0 - E)^2 - m_{\bar{\nu}_e}^2} \cdot (E_0 - E) \cdot \Theta(E_0 - E - m_{\bar{\nu}_e}), \quad (1)$$

with Fermi's coupling constant G_F , Cabibbo angle θ_C , the nuclear matrix element M , Fermi function $F(Z+1, E)$, kinetic energy, momentum and mass of the electron E , p , m_e , endpoint of the beta decay spectrum $E_0 = Q - m_e$ and the decay energy Q [62]. An

exemplary depiction of this spectrum can be seen in figure 1. Following from equation 1, it can be deduced for small neutrino masses that the spectrum is influenced the most close to the endpoint E_0 . This manifests in a distortion of the spectrum as well as a lower endpoint of the spectrum.

The distortion as well as the endpoint shift can be detected, given a high enough event rate in the endpoint region as well as a high enough energy resolution of the experiment. Thus, the choice of beta decaying isotopes relies on a low half-life and a low endpoint energy. The low half-life guarantees that there is enough statistics in the endpoint region with a comparably small amount of source material [62]. The low endpoint energy ensures that the influence on the spectrum is comparably large.

Tritium is an ideal candidate for neutrino mass measurements. It has a short half-life of $T_{1/2} = 12.3 \text{ yr}$ [53] and has a low endpoint energy of $E_0 = 18.6 \text{ keV}$ [62]. Additionally, the beta decay of tritium is super-allowed. Hence, the matrix element M is energy independent. Because of these properties, tritium is used in many beta decay experiments [48, 11] and most recently at the KARlsruhe TRItium Neutrino (KATRIN) experiment. The KATRIN collaboration could show that the electron antineutrino mass is below 1.1 eV (90% confidence level)[4].

However, the KATRIN experiment, see chapter 1, aims to measure the electron antineutrino mass with a sensitivity down to 0.2 eV [37]. This challenging goal can only be reached through a precise examination of all systematic effects of the experiment. One of these effects is caused by a plasma in the high luminous windowless gaseous tritium source. The plasma is generated by beta decay, subsequent ionization and collisions with surrounding tritium gas, see chapter 2. The plasma produces an ab initio inhomogeneous potential throughout the source, which can change the shape of the measured electron spectrum.

The effects of the plasma on the neutrino mass measurement can be constrained experimentally by calibration measurements, see chapter 3. The most insightful data is obtained from $^{83\text{m}}\text{Kr}$ line measurements [54]. However, they can not be performed during the neutrino mass measurement runs. Hence, changes of the plasma potential can only be extrapolated between two line measurements. It would therefore be beneficial to gain knowledge on the plasma from other measurable parameters, which can be monitored permanently, for example the outgoing current of particles from the source [24]. The transfer between the measured data and the properties of the plasma requires a comprehensive plasma model. In addition, a plasma model would allow for a simple optimization of experimental conditions in respect to the plasma potential without the need of many experimental tests.

The current plasma model is based on two simulations, a Monte Carlo simulation by Nastoyashchii et al. [59], and drift diffusion simulations by Kuckert [50]. Nastoyashchii et al. derived a mean electron energy distribution for the whole source. It was found that the majority of the electrons thermalize through collisions with the surrounding tritium gas. Only a small fraction of high energy electrons were observed. Kuckert assumed that the high-energy electrons can be neglected, and that the thermalization is an indication for a collision dominated motion of electrons. Thus, a static drift diffusion ansatz was applied, deriving the plasma potential in relation to the precalculated neutral gas stream in the center of the source. However, current measurements show differences towards the prediction of the model of Kuckert, namely the radial structure of the potential, and the influence of external power supplies. Furthermore, electric current measurements show that there are particle current towards the beam tube walls, which are not predicted by Nastoyashchii et al. and Kuckert.

Hence, the main focus of this thesis lies on the development of a new plasma model, which targets three of the main assumptions of Nastoyashchii et al. and Kuckert:

- A mean electron spectrum can be used to describe the spectrum at each position of the source.
- High energy electrons can be neglected in the description, and the electrons can be described as thermally distributed.
- The motion of electrons and ions in the plasma is dominated by collisions

All three assumptions can be contested by the large longitudinal density gradient, generated by the neutral gas flow. The density varies over three orders of magnitude [49], rendering the collisionality of electrons from partly collisional in the center of the source towards non-collisional at the sides, see chapter 3.

In the context of this thesis, a two-part simulation approach is proposed. First, the electron spectrum is reevaluated, dependent on the position in the source by a new Monte-Carlo simulation tool, named KARL, see chapter 4. It will cover the interactions of electrons and ions with the neutral gas by a given neutral gas flow and static electromagnetic fields. Second, the results of KARL are then incorporated in particle-in-cell simulations with a modified version of the ACRONYM simulation tool [42], see also chapter 5. This tool will calculate electrodynamic fields from given input, assuming that there are no direct collisions between charged particles. Results of the ACRONYM simulations can then be used as an input for new KARL simulations. It is hypothesized that the iteration between both simulations tools will reach an equilibrium state.

For the two-part simulation approach, two major tasks need to be accomplished. First, the simulation tool KARL needs to be designed and tested. The necessary tasks can be summarized by the following list:

- develop a simulation strategy for the Monte Carlo approach, including interactions of electrons and ions
- determine the relevant interactions of electrons and ions in the KATRIN source
- incorporate electromagnetic fields from the ACRONYM simulation in the particle movement
- provide a suitable output of the particle currents and particle distributions
- find suitable tests to ensure the correctness of the simulation

Secondly, the algorithms of ACRONYM need to be adapted to incorporate also the specific conditions of the KATRIN source. The necessary tasks can be summarized by the following list:

- include circular boundary conditions for particle movement and electromagnetic field calculations to represent the KATRIN geometry
- include position dependent background electric fields representing surface potentials and charging of the rear wall
- include position dependent background ion currents
- include a space dependent initial arbitrary energy density distribution of electrons
- include electron generation through beta decay and ionization representing generation of electrons during the simulated time
- include particle injection at the simulation boundaries

- find suitable tests to ensure the correctness of the simulation

After design and testing, both simulation tools are applied to parameters of the KATRIN source, providing the first results of the two-part simulation approach.

Note on the System of Units in this Thesis

In theoretical and computational plasma physics, it is conventional to use the (Gaussian) CGS system of units, which reduces the number of constants in electrodynamic formulas. However, the SI system of units is predominant in experimental physics. The following thesis is targeted towards both audiences. Hence, it was decided to use a mixture of both systems for more relatable formulas and value sizes. On the one hand, the CGS unit system is used for all formulas (if not specified otherwise), rendering them easily comparable to literature. On the other hand, SI units are used to describe the values themselves, like the magnetic field strength in T), electric currents in A and potentials in V. This way, they can easily be compared to values of the KATRIN experiment. However, an exception is made on the unit of length and its derivative values (length in cm, velocity in cm/s, particle number density in cm^{-3} and electric field strength V/cm). This decision is motivated by the physical scale (radius of the beam tube 4.5 cm) at which the values are evaluated. Lastly, energies will be provided in eV, the typical unit for particle and atom physics.

Chapter 1

The KATRIN Experiment - An Overview

At the KATRIN experiment, the electron antineutrino mass is inferred from the shape of the beta decay spectrum of tritium. The contribution of the mass on the shape is most dominant in the endpoint region, see also Introduction. Thus, the KATRIN experiment is designed to provide a high-energy resolution, as well as a high event rate in this region of interest. These requirements are met by using a high luminous tritium source and a high-precision spectrometer.

The experimental setup is 70 m long and can be divided into two parts: the Source and Transport Section (STS) and the Spectrometer and Detector Section (SDS), see figure 1.1. Neutral tritium gas is injected into the center of the Windowless Gaseous Tritium Source (WGTS) and is pumped out at both sides of the source. The Differential Pumping Section (DPS) and the Cryogenic Pumping Section (CPS) are connected to the source and reduce the tritium density to a bare minimum. Thus, the amount of tritium entering the detector section is negligible. The electrons from the beta decay of tritium are guided adiabatically by a strong magnetic field to the SDS. There, both the Pre-Spectrometer (PS) and the Main Spectrometer (MS) filter the electrons according to their energy. The electrons are then counted by the detector providing an integral spectrum. The components will be discussed in the following to provide an overview of the KATRIN setup.

1.1. Windowless Gaseous Tritium Source

The windowless gaseous tritium source provides beta electrons for the measurement with an activity of up to 10^{11} Bq at highly stable conditions [6]. The source consists of a 10 m long

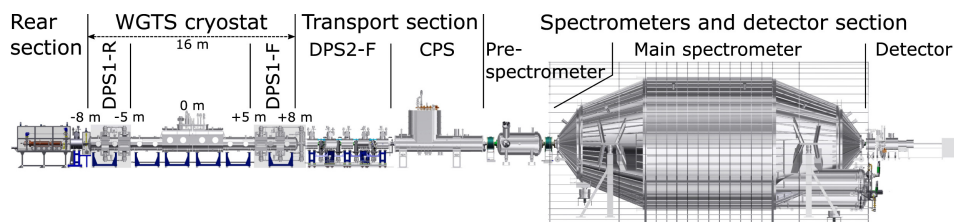


Figure 1.1.: KATRIN beam line and its components. Neutral tritium gas is injected in the WGTS and pumped out in the DPS and the CPS. Beta electrons are guided adiabatically by strong magnetic fields to the spectrometers, where they are sorted by their energy. The detector counts the incoming electrons. The rear section closes off the setup and is equipped with additional monitoring devices. Figure from [33].

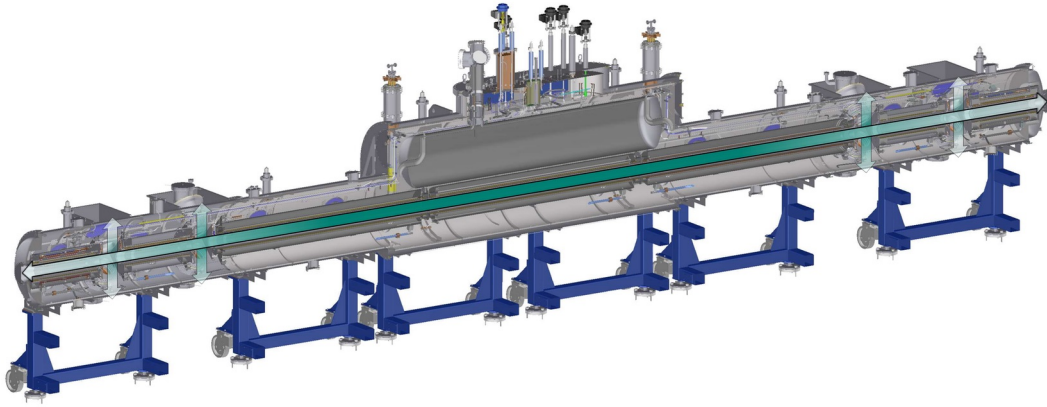


Figure 1.2.: Windowless Gaseous Tritium Source. Tritium is injected at the center and diffuses to both sides and is pumped out by turbomolecular pumps. A density gradient builds up, depicted in turquoise. The surrounding cryostat ensures stable temperatures and houses superconducting magnets. Figure adapted from [33].

stainless steel tube that is connected at both sides to turbo-molecular pumps, see figure 1.2. Tritium gas is injected into the center of the tube through a specially designed injection chamber. The gas then streams to both sides, where it is removed by the turbo-molecular pumps. It is then processed, filtered and injected again in the center of the source. In this cycle, approximately 40 g of tritium is used to maintain a constant flow of gas in the source [6]. The actual amount of tritium inside the source can be quantified by the column density. It is equal to the integral of the particle density along the source tube. At nominal source conditions, the column density is 5×10^{17} molecules/cm² [6]. For more information on the gas flow, refer to section 2.1.

The WGTS beam tube is surrounded by a two-phase cryostat, ensuring a constant temperature inside the cavity. The temperature can be adjusted at low temperatures from 28 K to 37 K and at higher temperatures from 80 K to 115 K [6]. Commissioning measurements have shown, that the temperature stays constant over a long period of time, exceeding the design value of 0.1 %/h. Also, the temperature variation along the beam tube exceeds the design value of 0.1 % [6]. For more information on the temperature profile along the complete source refer to section 2.1.2.

The cryostat also houses superconducting magnets. These magnets provide the field necessary to guide the beta electrons to the detector. The corresponding field is described further in section 2.3.

Injection Chamber

Tritium gas is injected in the center of the WGTS through a specially designed injection chamber, see figure 1.3. The gas is streaming through 415 orifices, which are designed to “guarantee a shock-wave free injection without turbulence” [33]. A pressure-controlled buffer vessel ensures a constant injection pressure. Commissioning measurement showed that the pressure is stable at a level of 0.038 %. This value exceeds the design value of 0.1 % significantly [6].

The pressure of the vessel is adjusted corresponding to the target density in the source. The inlet pressure p_{in} directly corresponds to the density right in front of the inlet n_c and is calculated through the ideal gas law

$$n_{\text{in}} = \frac{p_{\text{in}}}{k_b T}, \quad (1.1)$$

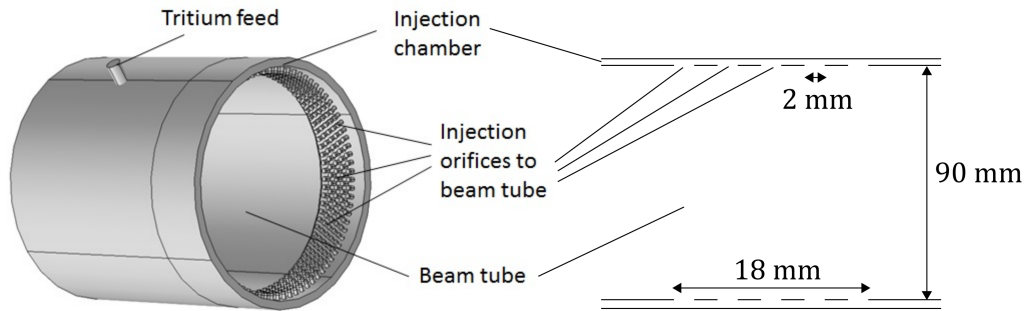


Figure 1.3.: Injection Chamber. Tritium is fed through 415 orifices, and streams to both sides of the WGTS. Figure from [33].

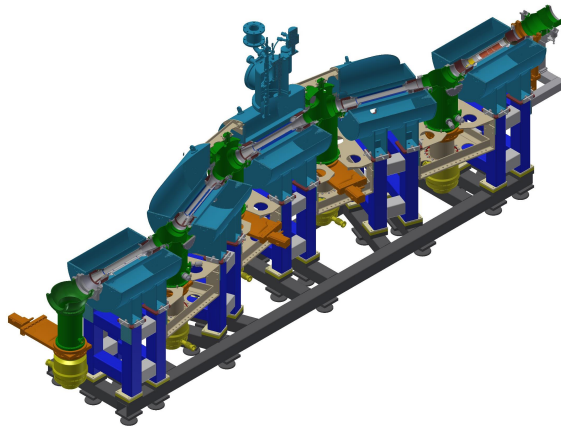


Figure 1.4.: Differential Pumping Section. Residual gas from the source is pumped out through turbomolecular pumps (yellow). The beam tube is bent in a chicane to maximize wall collisions of neutral gas. The beam tube is surrounded by superconducting magnets (light blue) to transport the beta electrons to the spectrometer section. Ions are removed by dipole electrodes. Figure adapted from [33].

where T denotes the temperature and k_b Boltzmann's constant. The inlet pressure can be adjusted to produce the needed density inside the source. The pressure for a column density of 5×10^{17} mol/cm² at 30 K is calculated to be 0.337 Pa. This value changes for lower column densities or higher temperatures. If, for example, the desired column density is 75 % of the nominal value at a temperature of 80 K, then the pressure needs to be changed to a value of 0.7 Pa. For more information on the density along the whole source tube see section 2.1.1.

1.2. Differential Pumping Section

The differential pumping section connects the WGTS to the cryogenic pumping system, see figure 1.1. It acts as an additional pumping stage to reduce the neutral particle flux in the direction of the detectors. Commissioning measurements have shown that the tritium density is reduced in the DPS by a factor of $(9.6 \pm 1.0) \times 10^7$ at nominal column density [6]. A reduction in tritium flow this large is achieved by the usage of five beam elements, attached to turbo-molecular pumps. These beam tube elements are arranged in a chicane to increase the number of wall collisions of the molecules. Thus, this special arrangement increases the pumping probability.

The beam tube elements are surrounded by superconducting magnets, which guide electrons through the chicane without collision with the tube walls. This magnetic field would in principle enable ions to traverse to the detector section as well. These ions would act as an

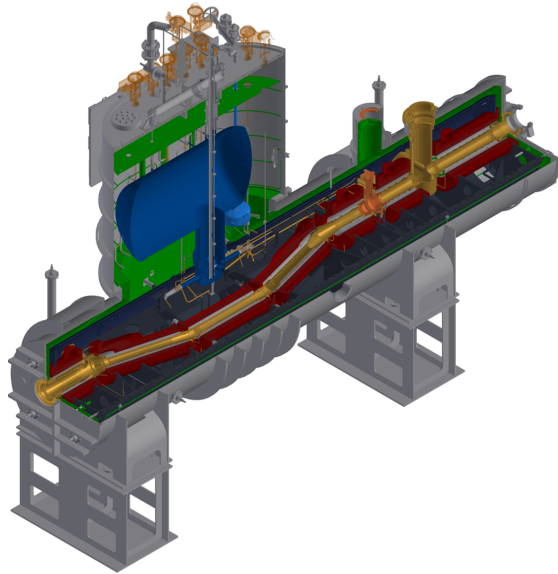


Figure 1.5.: Cryogenic Pumping Section. Residual gas from the DPS is cryosorped to the 3K cold gold plated beam tube. Additional argon frost enlarges the sticking coefficient. The beam tube is bent in a chicane to maximize wall collisions of neutral gas. The beam tube is surrounded by superconducting magnets (dark red) to transport the beta electrons to the spectrometer section. Figure from [33].

additional background to the neutrino mass measurement. Therefore, additional dipole electrodes were installed at the beam tube elements. The dipole electrodes provide an electric field which is perpendicular to the magnetic field. This configuration induces a $E \times B$ drift in the charged particle movement. The drift distance is dependent on the time spent in the cross field. Beta electrons spend only a short time in the DPS. Thus, they leave the DPS almost unhindered. The ions in turn are much slower. Hence, they drift to the beam tube walls, where they neutralize. An additional electrode at the end of the DPS is set on positive potential. Thus, any remaining ions are reflected back to the WGTS, which increases the time spent in the cross field even further. In total, ions are hindered from moving towards the detector, while electrons can pass through the DPS.

1.3. Cryogenic Pumping Section

The cryogenic pumping section concludes the source and transport section and eliminates almost all tritium gas leaving the DPS. At this stage, mechanical pumping becomes ineffective because of back-diffusion in the pumps. In the CPS the pumping is achieved by cryosorption. The tube walls are cooled down to 3K [6]. This low temperature builds a cold trap for the tritium gas. The sticking coefficient is increased by the usage of an argon frost coating on a gold-plated surface. The coating must be regenerated after 60 days to eliminate the excess tritium. Similar to the DPS the CPS beam tube elements are arranged in a chicane to increase the probability that a tritium molecule hits the tube walls. Likewise, superconducting magnets are used to guide the electrons through the setup. See figure 1.5 for a graphical representation of the CPS.

Commissioning measurements have shown that the tritium flow rate is reduced at least by a factor of 10^8 . The sensitivity of this measurement was limited by the sensitivity of the residual gas analyzer. The true reduction factor might even be lower than this value [6]. In combination with the DPS the total reduction factor of the transport section is at least 10^{14} .

The CPS houses two additional calibration systems, the forward beam monitor FBM and a condensed krypton source. Both can be inserted in the flux tube between the last two beam

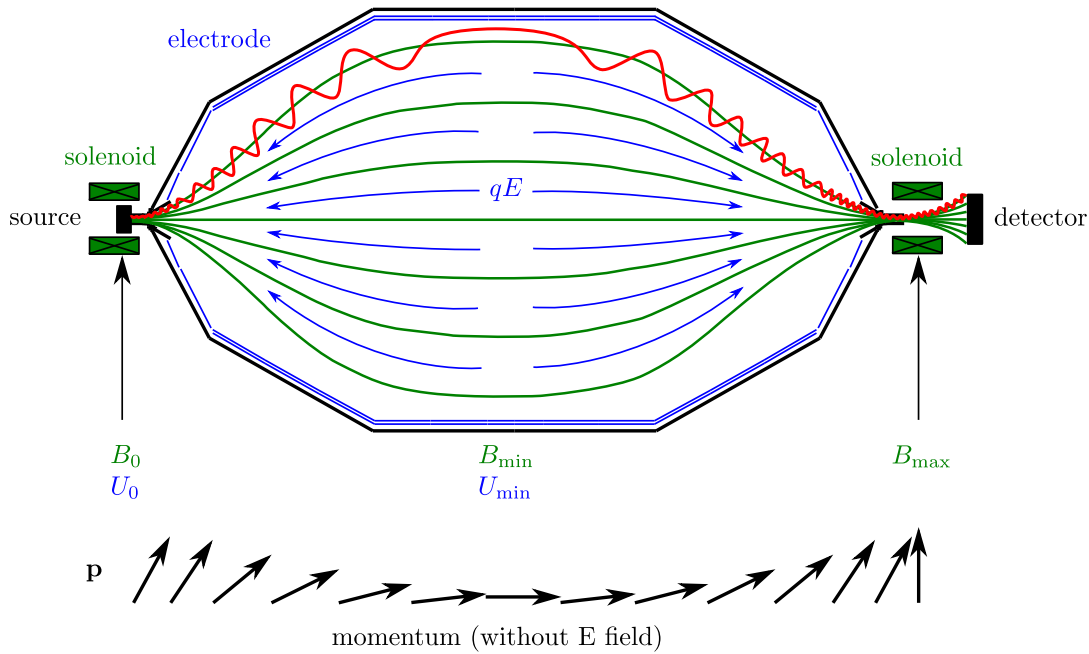


Figure 1.6.: MAC-E filter principle. Beta electrons gyrate around the magnetic field lines, shown in red. The adiabatic reduction of the magnetic field strength converts the perpendicular kinetic energy to parallel kinetic energy. Thus, the momentum vector is oriented in the direction of movement. The electrodes of the spectrometer produce an opposing electric field. Only electrons with an energy higher than qE can pass, and are collected at the detector. Figure adapted from [84].

tube elements, see figure 1.5. The FBM can measure the relative electron flux originating from the source. Two independent motion systems can move the detector throughout the cross section of the flux tube. Thus, the FBM can be used for activity monitoring of the source, as well as monitoring of the magnetic flux tube. The condensed krypton source emits conversion electrons with a small line width. These electrons are then measured by the detector. The condensed krypton source can be used to calibrate the detector section. It can provide “precise values for the magnetic fields and electric potentials in the analyzing plane, which can be used to cross-check values obtained by simulation...”[6].

1.4. Pre- and Main-Spectrometer

The pre- and main-spectrometer are used to filter the incoming electron flux corresponding to its energy. The spectrometers are used in tandem, where the pre-spectrometer filters out the main portion of low-energy electrons and the main spectrometer is used for high precision filtering. Both spectrometers work according to the same principle: magnetic adiabatic collimation with electrostatic retardation (MAC-E). A schematic representation of this principle shown in figure 1.6, and is discussed in the following.

The strong magnetic field of the KATRIN beam line guides electrons to the spectrometers. The movement of the electrons can be described by a circular motion around a guiding center, which traverses in longitudinal direction. The total kinetic energy is therefore shared by the kinetic energy of the guiding center E_{\parallel} and by the kinetic energy of the gyro motion E_{\perp} . Beta electrons are emitted isotropically in the source. Thus, the distribution of energy is divided evenly between the two kinetic energy contributions. The relation between the two kinetic energies can be changed by reducing the magnetic field adiabatically.

The magnetic moment μ is conserved in adiabatic changes of the magnetic field. The magnetic moment calculates to [3]

$$\mu = \frac{E_{\perp}}{B} = \text{const.}, \quad (1.2)$$

where B the magnetic field strength. Hence, a reduction of the magnetic field strength reduces the energy of the cyclotron motion. The energy is transferred to the kinetic energy of the guiding center due to energy conservation. So, the perpendicular kinetic energy is at its lowest at the plane of the lowest magnetic field strength. By applying an electrostatic potential U_{max} at this plane position, only electrons with a parallel kinetic energy greater than the retarding potential can pass. Hence, this plane is also called analyzing plane.

The relation between maximal and minimal magnetic field strength ($B_{\text{max}}, B_{\text{min}}$) defines the minimal energy ΔE which could not be converted into parallel direction

$$\frac{\Delta E}{E} = \frac{B_{\text{min}}}{B_{\text{max}}}. \quad (1.3)$$

The design minimum magnetic field strength of the MS is $B_{\text{min}} = 0.3 \text{ mT}$ and the design maximal magnetic field strength is $B_{\text{max}} = 6 \text{ T}$ [37]. With a maximal electron energy of the beta decay $E_{\text{max}} = 18.6 \text{ keV}$ the energy resolution of the KATRIN spectrometer calculates to $\Delta E = 0.93 \text{ eV}$ [6].

The reduction of the magnetic field strength also induces an expansion of the magnetic flux tube. To prevent electrons from hitting the walls of the experiment, the flux Φ needs to be conserved. For an area A perpendicular to the magnetic field B it calculates to

$$\Phi = A \cdot B. \quad (1.4)$$

In the source section, the design field strength has a value of $B_{\text{S}} = 3.6 \text{ T}$ [37]. The radius of the source tube is $R = 4.5 \text{ cm}$. Combining this with the minimal magnetic field at the analyzing plane B_{min} results in a flux tube diameter in the MS of approximately 10 m.

1.5. Detector

The electron beam passing the analysis plane is collimated by a strong magnet at the end of the MS. The individual electrons are then detected by a 148 pixel silicon detector. The electrons are accelerated before detection by an additional electrode, which is kept at 10 keV. This procedure reduces backscattering effects and shifts “the signal peak into a region of lower intrinsic background” [3]. Overall, the detector has a detection efficiency greater than $\epsilon_{\text{det},i} \geq 90\%$ for each individual pixel i [8].

The count rate at the detector is measured for each retarding potential of the MS. This integral spectrum of the electron flux of the source is then used to determine the neutrino mass. The count rate \dot{N}_i for each pixel i is calculated by

$$\dot{N}_i(U) = \frac{1}{2} \epsilon_{\text{det},i} \cdot \int_{eU}^{\infty} \frac{d\Gamma}{dE}(E, m_{\nu}^2, E_0) \cdot R_i(\mathbf{x}, E, U) dE, \quad (1.5)$$

where U is the potential at the analyzing plane, R_i is the response function, $\frac{d\Gamma}{dE}(E, m_{\nu}^2, E_0)$ is the Tritium beta decay spectrum, see equation 1, with the endpoint energy E_0 and the neutrino mass m_{ν} [45]. The response function evaluates all effects where electrons have gained or lost energy inside the KATRIN setup depending on their start position x and weighs them with the probability of transmission at the spectrometers. The response function also includes additional corrections of the Doppler effect or start potential differences of the electrons. The neutrino mass is then determined by an evaluation of the difference between the measured rate and the simulated rate.

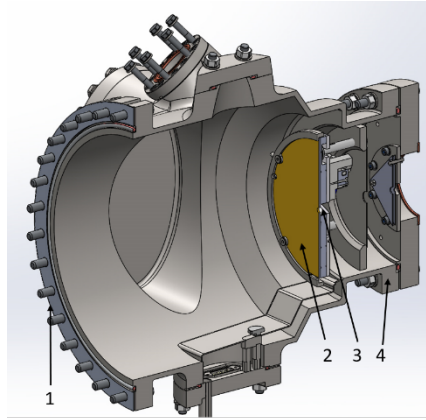


Figure 1.7.: Rear wall chamber. (1),(4) Mounting flanges, (2) rear wall, (3) central hole for egun beam transmission. Figure taken from [6].

1.6. Rear Section

The rear section RS is directly connected to the WGTS, see figure 1.1. It closes the beam line in the opposite direction of the detector. All beta electrons, which were reflected by the potential of the analyzing plane, are terminated here at the so-called rear wall. Additionally, the rear section is equipped with various diagnostic systems. These systems include a high resolution angular-selective electron gun and a beta a beta-induced X-ray spectroscopy system (BIXS).

Rear Wall

The rear wall is a gold-coated stainless-steel disk with a radius of 7.62 cm [50]. It is positioned at the end of the beam tube, see figure 1.7. It is surrounded by a superconducting magnet. This magnet ensures that the magnetic flux tube of the WGTS is mapped completely to the rear wall. So in general, all charged particles leaving the WGTS in rear direction will hit the rear wall at some point. The induced current can be measured by an ammeter.

The rear wall naturally exerts a contact potential due to workfunction differences between the rear wall and the surrounding stainless steel of the beam tube. The potential of the rear wall can be adjusted by an additional power supply. This potential is an important boundary condition for the source plasma. Thus, the adjustment of the potential can be used to investigate the plasma.

The rear wall can be illuminated by a highly luminous UV light source [25]. The UV light produces photo electrons, which move into the source. These electrons can either be used for commissioning measurements of the empty source or they can be used as an additional source of negative charges in the source plasma, see section 3.2.

Electron Gun

The Electron Gun (egun) is situated behind the rear wall. It produces high-energy electrons up to 30 keV with an intrinsic energy spread of approximately 0.2 eV [12]. These electrons are fed through a hole with a diameter of 5 mm inside the rear wall. The electron beam can be directed through magnetic and electric dipoles to cover the full beam tube cross section.

“The e-gun allows studying electromagnetic characteristics along the main beam line and has been used in the commissioning of various beam line sections. It is also suited to investigate and monitor source characteristics, such as electron scattering and the column density stability” [6].

BIXS

The BIXS system is used to measure the activity of the source during neutrino mass measurement runs. It is located at one of the access pumps of the rear wall chamber. The BIXS system consists of a silicon drift detector, which measures the bremsstrahlung of beta electrons hitting the rear wall. The count rate directly corresponds to the activity of the source. Thus, the BIXS system can also be used to monitor the column density. In commissioning measurements, it was shown that the system allows for a “stability monitoring on the 0.1 % level in measurement cycles of duration 100 s” [6].

Chapter 2

Conditions of the Source Plasma

The properties of the source plasma are directly linked to the conditions inside the source. It is beneficial to investigate these properties detached from a description of the plasma, to disentangle effects of the plasma from external constraints. Thus, the first section of this chapter focuses on the description of the neutral gas flow, which acts as a static background for the charged particle motion. In the second and third section, external electromagnetic fields in the source are discussed. Lastly, charged particle interactions with neutral, but also other charged particles, are described by an investigation of their cross sections.

2.1. Neutral Gas Flow

The tritium gas is a source of high-energy electrons, as well as an interacting partner for both electrons and ions. The interaction probability is directly related to the density, temperature and velocity distribution of the neutral tritium gas. Hence, a thorough investigation of these parameters along the length of the source is presented in the following. Nevertheless, the charged particle density is assumed to be significantly lower than the neutral gas density [50]. Thus, any influence of the charged particle motion on the neutrals is neglected.

2.1.1. Density Distribution

The neutral gas density distribution inside the source is generated by the injection of neutral gas in the center and subsequent pumping of the gas at the pump ports. Thus, the density distribution is shaped by the underlying geometry of the setup, the injection pressure and the pumping probability. The description of the gas density depends on the mean free path of neutral-neutral collisions, which is inversely proportional to the gas density. The mean free path ranges from approximately 1 mm in the center to values above 1 m at the pump ports. This means that the gas transitions from a viscous regime to a free-molecular regime. A corresponding model was developed by Kuckert et al. [49]. In this model, the source is divided into three different sections. The first section includes the central 10 m of the WGTS beam tube, where the gas can be described by a viscous flow. The second section includes the first adjacent pump port, where a transitional flow model can be used. The third section comprises the second pump port up to the beginning of the DPS, modeled as free-molecular flow. The densities of these sections were computed individually, and boundary conditions were set up to join the results of each section.

The calculation of Kuckert et al. were performed at design conditions of the source ($T = 30$ K and $p_{\text{in}} = 0.337$ Pa). Current measurements of the KATRIN experiments are performed at higher temperatures and lower injection pressure ($T = 80$ K and $p_{\text{in}} = 0.7$ Pa). In first order approximation, it is assumed that the density profile does not change significantly, and the

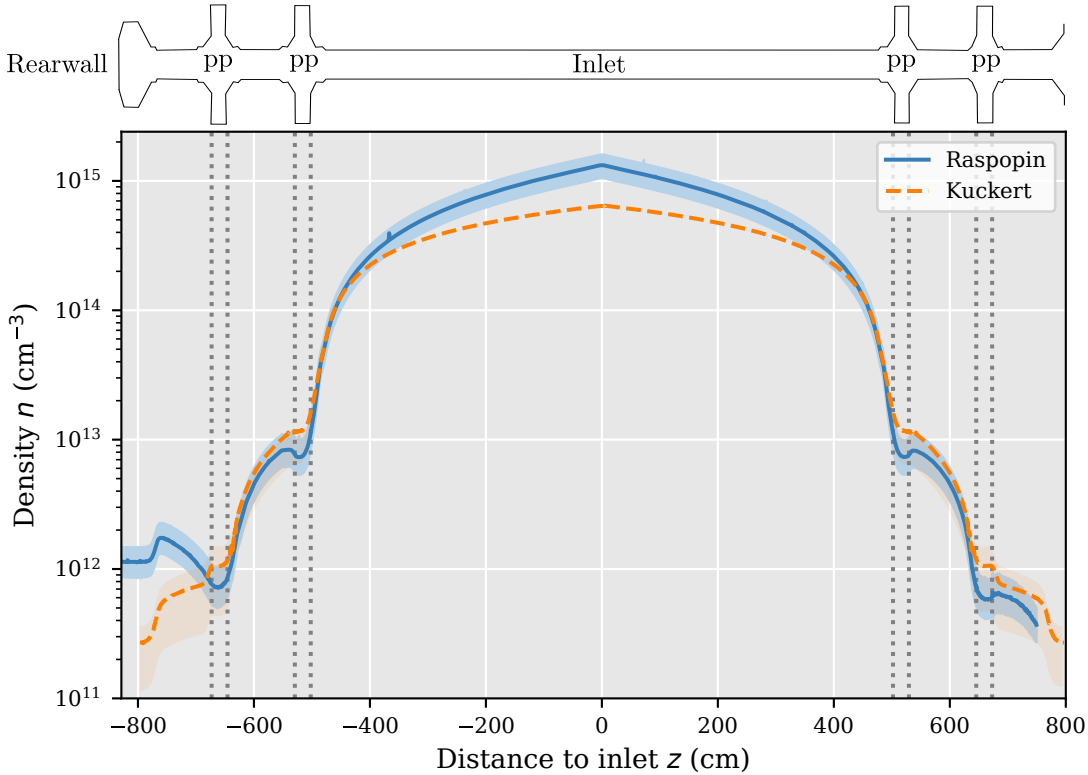


Figure 2.1.: Neutral gas density in the source. The data from Raspopin [72] was derived from free molecular simulations at $T = 80$ K. The data of Kuckert et al. [49] was scaled to higher temperature and mirrored at the inlet to negative positions. The errorband of Raspopin corresponds to different normalizations to the data of Kuckert et al. The geometry of the source is indicated at the top with vertical lines showing the position of the pump ports (pp).

density can be scaled accordingly to the inlet pressure. The resulting density distribution can be found in figure 2.1. It can be seen that the density drops significantly in the first 5 m from the injection to the first pump port. It is then further decreased when reaching the second pump port. The residual density is decreased by the pumping of the DPS.

The calculations of Kuckert et al. were only performed in the direction of the detector. In general, it can be assumed that the density is distributed similarly in the direction of the rear wall. The density is low in the region of the rear wall. It has almost no direct influence on the neutrino mass measurement. Thus, this was not investigated further in the past. The density of neutral particles plays a vital role in the context of a description of the plasma. Thus, a simulation was performed to determine the differences of the up- and downstream density in a Masters's thesis by Raspopin [72], which will be highlighted in the following.

For the simulation, it was assumed that the results of Kuckert et al. in the central region can be scaled by the ideal gas law. The adjacent section of the pump ports up to the rear wall was simulated using the software package MOLFLOW+ [40]. This package utilizes a test-particle Monte Carlo method. The absolute density of the simulation is only dependent on the initial injection of particles. Thus, the results of the simulation must be scaled accordingly. The scaling factor is chosen in such a way that the density of the Monte Carlo simulation is the same as in the simulation of the central region by Kuckert et al. The results of Kuckert et al. show an uncertainty, which is therefore also present in the simulation results of Raspopin. The resulting density profile is depicted in figure 2.1 alongside the scaled results of Kuckert et al.

A thorough description of the simulation and the scaling procedure is described in the works of Raspopin [72], but can be summarized as:

- The simulation results of Raspopin do not agree with the simulation results of Kuckert in the central region. This is expected, because the free molecular model is not valid here. Thus, Kuckert's results have to be used in this section. Nevertheless, the simulation results of Raspopin can provide a rough estimate of the density in this region.
- The simulation results of Raspopin agree well with the results of Kuckert in direction of the detector close to the pump ports. Thus, the model of Raspopin can be used here.
- There is a difference of the up- and downstream density. This difference is caused by the rear wall, which acts as a barrier for the gas. Pumps at the rear wall chamber prevent an increased accumulation of the gas.

In total, the neutral gas density in the source can be described by a combination of the simulation results of Kuckert et al. and Raspopin.

2.1.2. Temperature Profile

The temperature profile of the tritium gas is directly correlated to the temperature profile of the beam tube. The WGTS temperature is controlled by a large high-precision cryostat, see section 1.1. The cryostat is connected to the rear wall chamber, which is kept at room temperature. The resulting temperature distribution along the length of the source section for the current standard operation temperature can be found in figure 2.2.

The temperature of the beam tube and injection vessel determines the temperature of the neutral gas inside the tube. The gas is injected with the temperature of the beam tube. Each time a molecule hits the tube wall, it will adopt the temperature of the wall at the point of the collision. In the central region, the temperature of the walls is the same as the gas inside. At the rear wall chamber however, the temperature rises from 80 K to room temperature. The density in this region is so low, see section 2.1.1, that a description of the gas with a Boltzmann-like distributed velocity distribution is no longer valid. Nevertheless, this region was assigned a temperature as well for completeness.

The temperature of the gas was determined in the same Monte Carlo simulation by Raspopin [72] as mentioned in 2.1.1. Single particles were tracked in the simulation and recorded at virtual facets inside the volume. The virtual facets were aligned in direction of the gas flow and perpendicular to it. The absolute velocity of the particles was collected in a histogram. A Maxwell-Boltzmann distribution fit was applied to the data. The Maxwell-Boltzmann distribution in this case reads as

$$f(v) = \left(\frac{2}{\pi}\right)^{1/2} \left(\frac{m}{k_b T}\right)^{3/2} v^2 \exp\left[-\frac{mv^2}{2k_b T}\right], \quad (2.1)$$

where m is the mass and v the absolute velocity of the molecule, k_b the Boltzmann constant and T the temperature. An additional drifting velocity was not considered here for simplicity. For more information on the drift velocity, refer to the next section. The resulting simulated temperature distribution can be found in figure 2.2.

It can be seen that:

- The simulated temperature of the gas is similar to the temperature of the beam tube. As expected, the difference between the gas temperature and beam tube temperature is the smallest in the region with a high gas density.

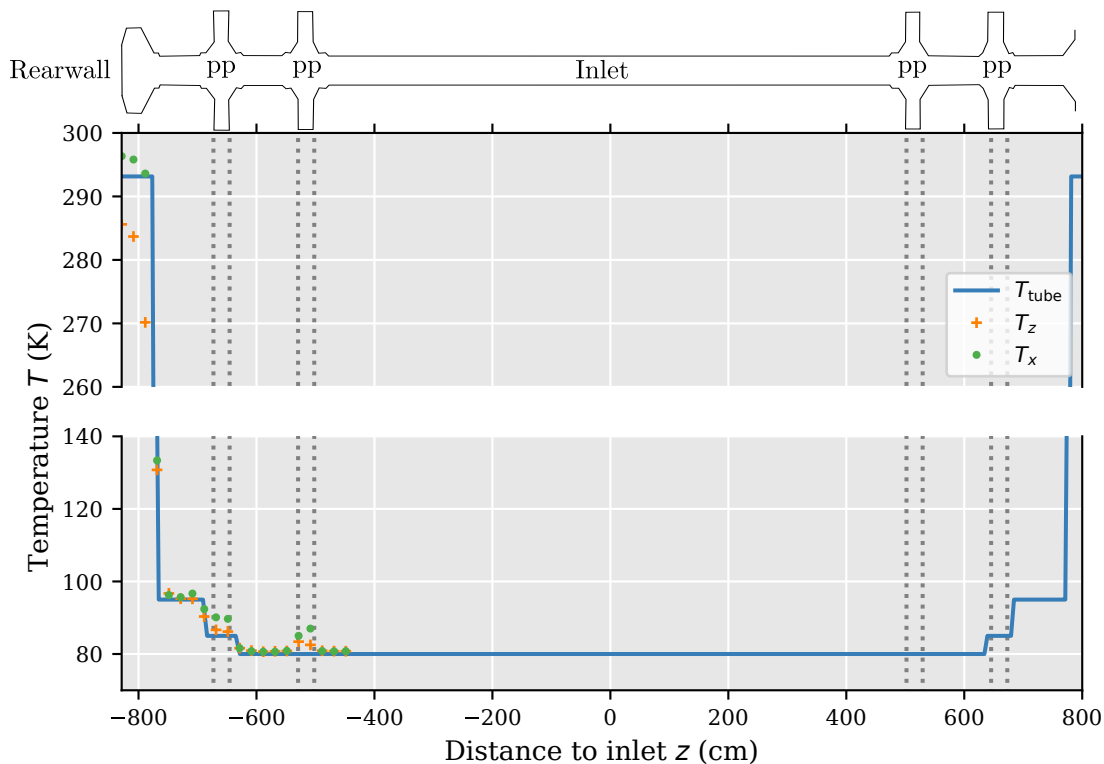


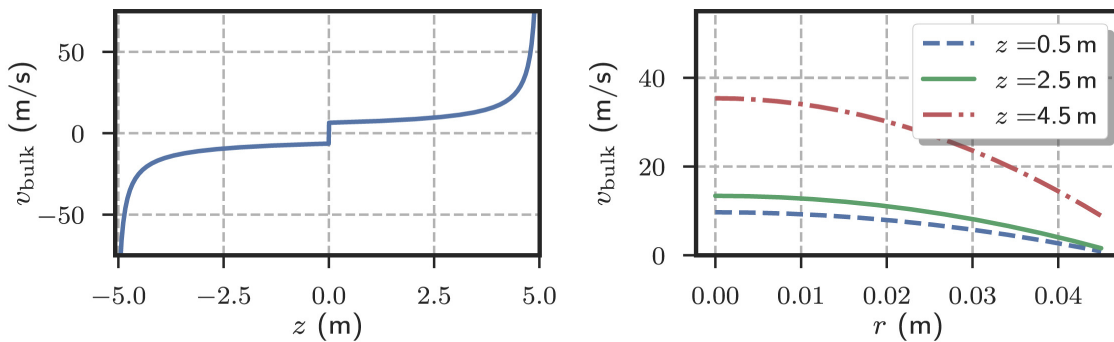
Figure 2.2.: Source temperature. Temperatures of the beam tube from the experiment T_{tube} in comparison to simulated data from Raspopin [72]. The temperature was derived from facets in z - and x -direction (T_z , T_x). The geometry of the source is indicated at the top with vertical lines showing the position of the pump ports (pp).

- The simulated temperature diverges from the beam tube temperature at the pumping port positions. This can be explained by the temperature gradient in the pumping ports themselves. Particles leaving the pump port will therefore show an increased temperature. The increase in temperature will not be distributed to the surrounding gas, due to the low scattering probability.
- The difference between the gas temperature and beam tube temperature is the highest at the rear wall chamber. The difference is dependent on the orientation of the facet. Facets directed in z -direction show lower temperatures, while the facet in x -direction show similar values to the beam tube temperature. This result hints to a beaming effect. Molecules upstream of the facet are therefore more likely to cross the z -facet as molecules from the rear chamber walls. In x -direction, there are no particles detected from the longitudinal direction. Thus, only particles which have scattered in the rear wall chamber cross the facet. These molecules have already adapted the temperature of the rear wall chamber.

In total, the neutral gas temperature in the source can be described by the temperature of the beam tube walls with an uncertainty provided by the simulation results of Raspopin.

2.1.3. Velocity Distribution

Electrons and ions can scatter off the neutral gas. These scatterings influence the movement of electrons and ions and thus the plasma. The velocity distribution of the neutral particle plays a vital role in the description of the scatterings. Thus, a thorough investigation of the velocity distribution of the neutral particles is necessary.



(a) Longitudinal velocity profile (1D)

(b) Radial velocity profile (2D)

Figure 2.3.: Bulk velocity of neutral gas. Simulated profile in the central beam tube element of the WGTS. Figure from [49].

The velocity distribution of the neutral particles is influenced by the inlet pressure and temperature, the pumping speed, and the temperature of the beam tube walls. Each contribution is weighted differently according to the density of the neutral particles. In the center, for example, there are many molecule-molecule interactions. The velocity distribution is therefore dominated by the particle flow. In the rear wall chamber, the density is reduced drastically, such that molecule-molecule interactions become negligible and collisions with the tube walls are dominant. This behavior can also be described by the different flow regimes mentioned in section 2.1.1. In the center, the gas is described by a viscous flow, while in the rear wall chamber the gas is described as free-molecular flow.

In the viscous flow regime, the velocity distribution can be described by a Maxwell-Boltzmann distribution with an additional bulk velocity in longitudinal direction [50]. The bulk velocity describes the streaming process from the inlet in the center of the WGTS to both sides. The one dimensional distribution function of the longitudinal velocity v_z then reads as

$$f(v_z) = \left(\frac{m}{2\pi k_b T} \right)^{1/2} \exp \left(-\frac{m(v_z - v_b)^2}{2k_b T} \right), \quad (2.2)$$

where v_b denotes the bulk velocity. Simulations of Kuckert [49] show that the bulk velocity is dependent on the longitudinal as well as the radial position, see figure 2.3. The bulk velocity increases from inlet to both sides. Radially, the bulk velocity is reduced at the tube walls, corresponding to wall interactions which slow down the gas movement.

At lower densities, the velocity can no longer be described through a drifting Boltzmann distribution, because interparticle collisions are reduced. The velocity of each particle needs to be tracked individually to gain an insight in the velocity distribution. The velocity distribution of the gas in this region can be determined in the same Monte Carlo simulation by Raspopin [72] as mentioned in 2.1.1. In the simulation, virtual facets are set up to collect each particle that crosses the facet. In contrast to the analysis in section 2.1.2, the velocity contribution in each space direction is collected in a histogram. The probability that a particle will cross the virtual facet is dependent on the incident angle towards the facet. Thus, the histograms is weighted accordingly. It was found by Raspopin that the velocity distribution is similar to a Gaussian distribution. In z -direction, the Gaussian distribution was shifted to lower values. Thus, the velocity distribution in z -direction was described through equation 2.2. The corresponding drift velocities can be found in figure 2.4 in comparison to the drift velocities of Kuckert.

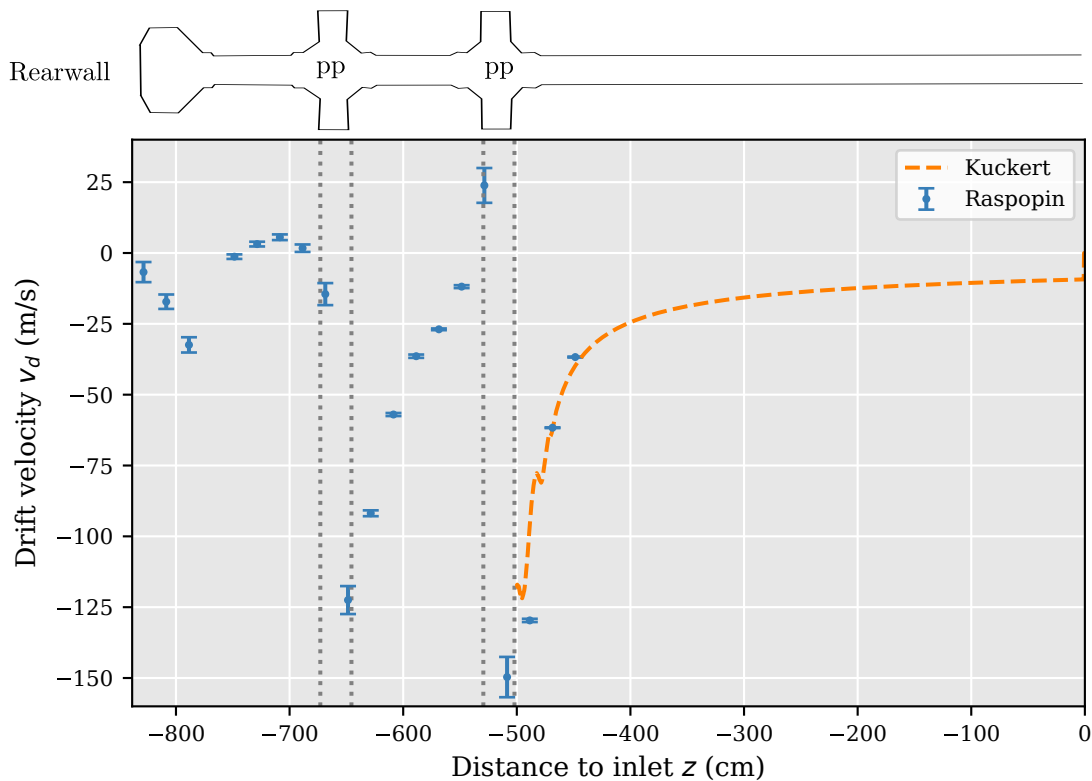


Figure 2.4.: Simulated bulk velocity in rear direction. Comparison of data from Raspopin [72] and Kuckert et al. [49] at $T = 30$ K. The errorbars represent fit uncertainties only. The geometry of the source is indicated at the top with vertical lines showing the position of the pump ports (pp).

It can be seen that:

- The bulk velocity of the simulation of Raspopin is in good agreement with the bulk velocity of Kuckert before the first pump port. It can therefore be assumed that the analysis procedure of Raspopin works correctly.
- The bulk velocity in the pump ports shows a huge spread. This can mainly be attributed to the shape difference from the Maxwell-Boltzmann distribution [72]. This means that the drifting gas model cannot be used here. In the context of this thesis, it is therefore assumed that the bulk velocity is zero at the pump ports.
- The bulk velocity is predominantly negative. Thus, the gas streams continuously in the direction of the rear wall, where additional pumps remove tritium molecules.
- The bulk velocity has positive values in the beam tube element which is connected to the rear wall chamber. The bulk velocity values are so small, that their difference from zero can be attributed to shape differences to the Maxwell-Boltzmann distribution [72].

In total, the neutral gas velocity distribution in the source can be described by a combination of the simulation results of Kuckert et al. and Raspopin with limited accuracy at the pump ports.

2.2. Electric Background Fields

The movement of charged particles is dominated by electric and magnetic fields through the Coulomb force. The fields originate from the movement of the charged particles themselves

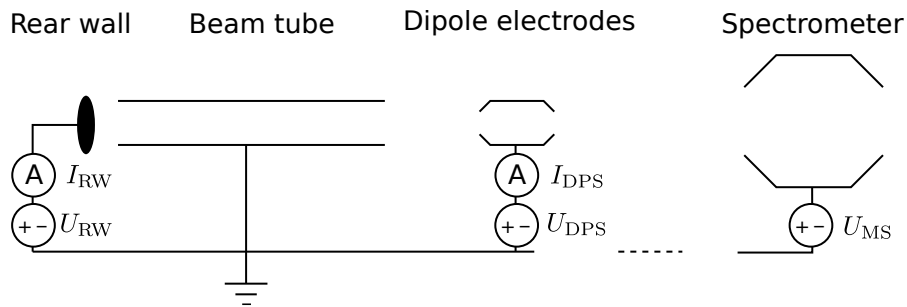


Figure 2.5.: Simplified circuit diagram of the source. All beam tube elements are electrically connected to ground. Special electrodes are fed by power supplies and the current towards the electrode is measured. Figure adapted from [72] and [24].

(plasma), and from external sources. In general, there is a self-shielding mechanism of the plasma against external fields, see section 3.3.1. Nevertheless, the external fields can penetrate the plasma up to a certain point, see 3.3.5, and thus influence the development of the plasma itself. Therefore, these fields need to be taken into account. Some electric background fields are induced directly by a connection of a power supply to an electrode, see figure 2.5. Others are generated by workfunction differences, called contact potential.

Contact potential differences can occur when two metals are brought into electrical contact with each other. The potential difference is caused by the workfunction differences of both metals. The workfunction meanwhile is inherent to each metal and to the surface conditions like granularity or contamination [82].

There exist a workfunction difference between rear wall and beam tube because they are manufactured from different metals: gold and stainless steel. Additionally, the surface contamination can be different for both beam tube elements. Furthermore, the surface contamination can be position-dependent because the exposure to tritium gas is non-homogeneous. The in situ workfunction differences are currently investigated, but no conclusive result has been published yet. In the context of this thesis, it is assumed that the position dependence of the workfunction can be neglected. Thus, the total contact potential difference can be modeled by an additional power supply connected to the rear wall.

All KATRIN beam tube elements are electrically connected, see figure 2.5. Thus, they all have the same surface potential, excluding surface potential differences. Only special electrodes like the rear wall and the dipole electrodes in the DPS are connected to a power supply. The induced potential at the electrodes U_e is measured in relation to the potential of the beam tube (in the figure U_{RW} and U_{DPS}). The total potential exerted by the electrodes U_{total} can be written as

$$U_{total} = U_e + \Delta U_{wf}, \quad (2.3)$$

where ΔU_{wf} is the workfunction difference between the electrode and the beam tube. Thus, the potential of the electrodes can be treated as an effective potential.

Measurements

Measurements of the background fields are challenging because of the intricate and closed design of the beam line. The fields are moderated by the plasma. Thus, they cannot be measured directly while there is a plasma inside the source. In general, the fields can be studied by their effect on single charged particles, either by a change in the particle trajectory or by a change in the kinetic energy of the particle. For these studies, electrons are created inside the source and their energy and position will be recorded at the KATRIN

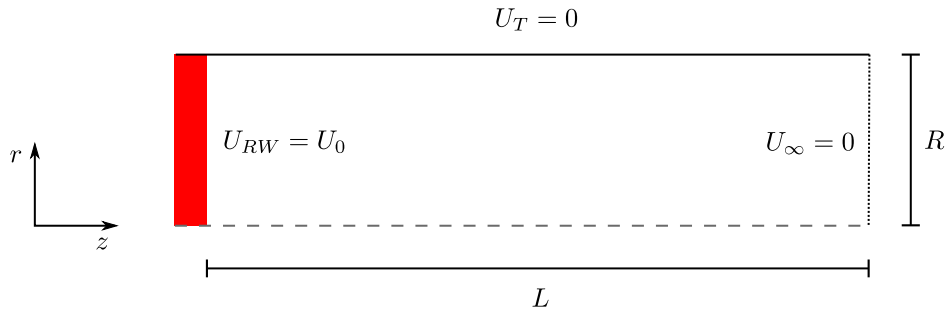


Figure 2.6.: Simplified geometry of the KATRIN source for the analytical calculation of the source potential. The potential at the rear wall U_{RW} is set to a fixed value U_0 . The beam tube potential U_T , and the potential at large distances to the rear wall U_∞ is set to zero.

main detector, at the FBM or the rear wall. A comparison with the expected electron flux and energy distribution provides an insight into the electric fields in the source. The energy at which a particle will be detected depends on the initial kinetic energy and the electric field which will be traversed during flight. The value of the traversed electric field can only be deduced if a time-dependent electric field exists.

Time-dependent electric fields accelerate the passing electrons if the time spend in the field is in the same order as the period of the oscillation. In a measurement, the field then broadens an initial monoenergetic line. The broadening is then a measure for the field strength. This technique is used by egun measurements. The egun produces electrons with a small intrinsic energy spread outside the source. The electrons then traverse the source and are collected by the detector. Results by Friedel [24] indicate the contribution of time-dependent fields are negligible in an empty source. Further results, including a time of flight measurements, will be published in the future [6].

Position-dependent electric fields are visible at the detector if the starting potential of two separate electrons are different. Thus, an initial monoenergetic energy distribution will be broadened by the field. The electrons of these measurements must originate from the source volume itself. At the KATRIN experiment, the position-dependent fields are investigated through a gaseous 83^mKr source, see section 3.2.1. Currently, there is no conclusive result available on the broadening of the conversion line width, which is directly attributed to spatial inhomogeneities of the potential in the empty source.

Numerical Simulation

The potential distribution in the source can in general be calculated by the given geometry and the potential of each surface. The field distribution in the KATRIN setup is calculated numerically using the subpackage KEMField of the software package KASSIOPEIA [26]. In KEMField the electric field is calculated using the boundary element method. The simulation yields a field map for a given geometry and surface potential input. The simulation needs to be rerun each time a parameter changes. The field maps of the simulation can then be used in the analysis for the neutrino mass measurements.

Analytical Estimation

Analytical estimations can provide faster access to the electric background field than the numerical simulations do, because the simulation time can be omitted. However, the analytical evaluation becomes more complex the more complex the geometry is. The proposed plasma simulation method of this thesis uses a simplified geometry of the KATRIN

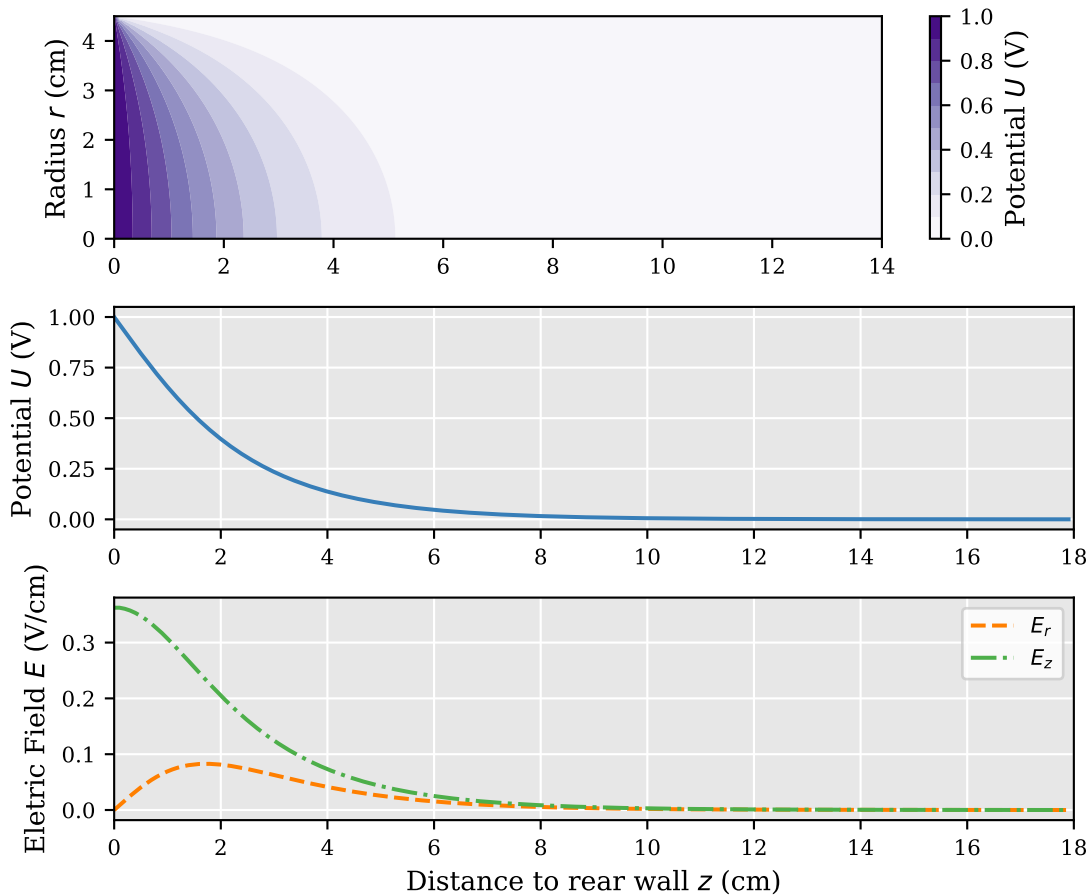


Figure 2.7.: Analytical electric background field of the rear wall chamber. Computed using a rear wall potential of 1 V.

source, see figure 2.6. Here the source tube is approximated as a cylinder with an open and a closed end. In this special case, an analytic expression can be found for the potential distribution in front of the rear wall

$$U(r, \theta, z) = 2U_0 \sum_{m=1}^{\infty} \frac{\sinh\left(k_{0m} \frac{L-z}{R}\right) J_0(k_{0m} \frac{r}{R})}{\sinh\left(k_{0m} \frac{L}{R}\right) k_{0m} J_1(k_{0m})}, \quad (2.4)$$

with the length L and the radius R of the cylinder. The derivation, presented in Appendix A, is adapted from Petrascheck and Schwabl [67]. In the end, the static electric field can be directly calculated using

$$\mathbf{E} = -\nabla U. \quad (2.5)$$

This result is analytically correct, but for a numerical calculation some adaptations need to be made

- The index m will be bound to a large number. This number is chosen in such a way that the oscillations of the Bessel function are more frequent than the radial position difference of each data point.
- If the fraction of L and R is too high, the value of \sinh is greater than the largest number on the computing system. Hence, L is bound such that the potential value at L is numerically indistinguishable from zero.

An exemplary potential and field distribution in radial and longitudinal direction can be found in figure 2.7. It can be seen that the potential drops significantly on the first

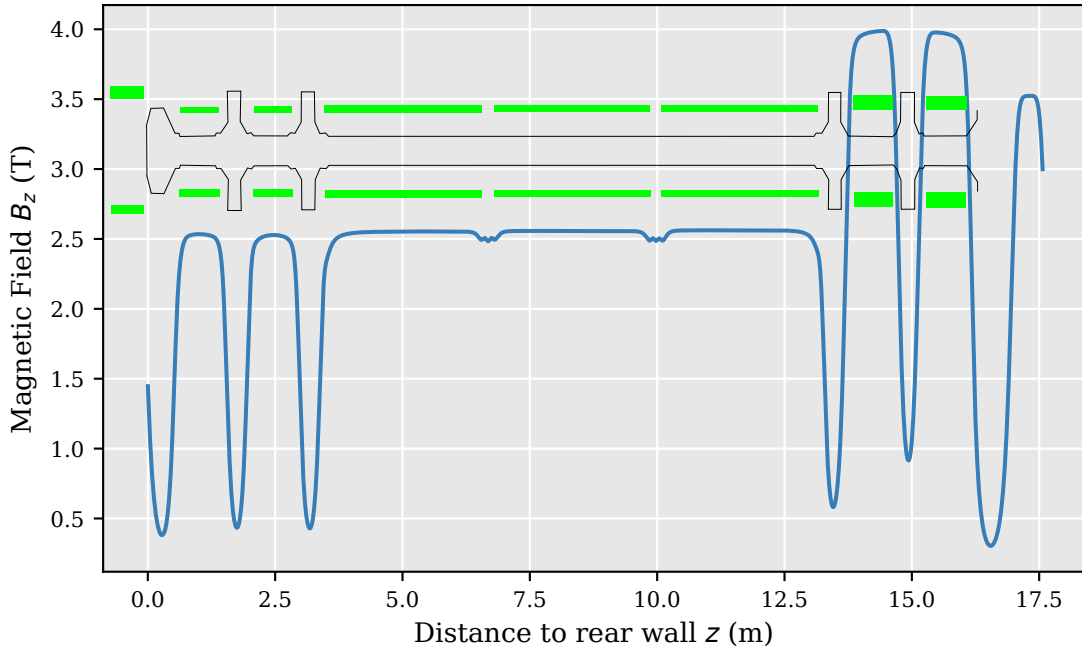


Figure 2.8.: Magnetic background field in the source. The magnetic field strength (blue) was computed using the software package KASSIOPEIA. The green bars show the position of the super conducting magnets in relation to the beam tube (black).

few centimeters and is close to zero at 15 cm away from the source. So the effect on single charged particles is only relevant in the rear wall chamber. In the center of the source, the potential is dominated by the beam tube, so close to zero. This behavior will change significantly when there is a plasma inside the source. This claim is supported by measurements, shown in section 3.2.

2.3. Magnetic Background Fields

The magnetic field inside the source is generated by a multitude of super conducting magnets, which surround each tube element of the source, see figure 2.8. They provide an up to 3.6 T strong field with a low drift (temporal change of the mean value) $< 0.03\%$ per month [9] and fluctuations below 0.2% per data acquisition run [6]. At a magnetic field this high, there exists the risk of quenching. This was investigated during commissioning measurements with the complete KATRIN beam line. It was shown that a reduction down to 70% of the design magnetic field eliminates the risk of quenching. Thus, the magnetic field strength is reduced to 2.5 T [9]. The magnetic field strength can be simulated with the software package KASSIOPEIA [26]. The magnetic field value at each position in the source can be evaluated by tracking a test particle in the source with a given set of driving currents of the magnets. An exemplary field map can be found in figure 2.8.

2.4. Charged Particle Interactions in the KATRIN Source

There exist many types of particles in the KATRIN source: neutral particles, electrons, ions and ion clusters. Each of the particle species can interact with each other. A thorough investigation of the particle interactions will be presented in the following. First, a short description of cross sections and their energy dependence will be given. Second, all interactions of electrons will be discussed, and third a summary of ion interaction will be provided.

Parts of the compilation of particles interactions inside the source are submitted for publication in a separate paper together with F. Spanier, see preprint [39]. With the kind permission of F. Spanier, a verbatim quotation was omitted in this chapter for better legibility. The interactions are displayed here for a coherent overview of the processes in the source, and extended by the investigation of cluster sizes in the source. The groundwork for the collection was comprised in the Master Thesis of Reiling [73].

2.4.1. Energy Dependence of the Cross Section

The interaction probability \mathcal{P} of a particle flying through a cloud of other particles can be written as

$$\mathcal{P} = n\sigma dx, \quad (2.6)$$

where n is the density of the particle cloud, dx is the distance that is traversed and σ is the cross section of the interaction. The cross section can be dependent on the energy of the interaction. No agreement was found in the literature if the cross section has to be given dependent on the kinetic energy or dependent on the total energy of the system. In atomic physics, most of the time the kinetic energy will be given, while in high-energy physics the total energy will be provided. In this thesis, the notation of the kinetic energy will be used. Furthermore, it is not agreed upon in which inertial frame of reference the cross section has to be provided. It can either be given in the target frame, where the cloud particles are at rest, or in the center of mass frame. A conversion of energies in different inertial frames can be found in Appendix B.

2.4.2. Electron-Interactions

Electrons of the source can interact with neutral particles, ions, ion clusters and other electrons. As mentioned before, the interaction probability is dependent on the cross section of the interaction and the target density. The density of neutral particles is much higher than the density of ions and electrons. Electron-neutral interactions are therefore much more frequent. Hence, this section will focus on electron interactions with neutral gas. Nevertheless, the recombination with ions and dissociation of ion clusters influences the density of electrons and ions. They will be discussed here as well. Electron-electron interactions will not be discussed here because of their infinite interaction range. The interaction range is reduced in a plasma. Please refer to section 3.3.3 for more information.

There is almost no data available on interactions of electrons with tritium, but there is data available on interactions with hydrogen or deuterium. In most interactions, the electron only interacts with the shell electrons of tritium. Thus, the mass of the core is not as relevant as its charge. Hence, isotopic effect should be small on the cross section [5]. In the context of this thesis, the mass difference is only taken into account at the recoil after the interaction. Nevertheless, the data will always be labeled in respect to the original hydrogen isotope to mark the origin of the data.

All cross sections in this section are given depending on the kinetic energy of the electron in the rest frame of the interaction partner of the electron. The energy range is adapted to enclose the highest energies of the beta decay electrons ($E_{\max} \approx 10^4$ eV) as well as the lowest energies of thermal electrons ($E_{\min} \approx 1$ meV).

Elastic Scattering

The cross section of elastic scattering was measured at different experiments in the energy range of 2×10^{-2} eV to 1×10^2 eV. The results of these experiments were combined by Tawara et al. [81] and parameterized by Yoon et al. [86]. Lower energies than 2×10^{-2} were not measured, but are relevant for electron interactions at the KATRIN experiment. Thus,

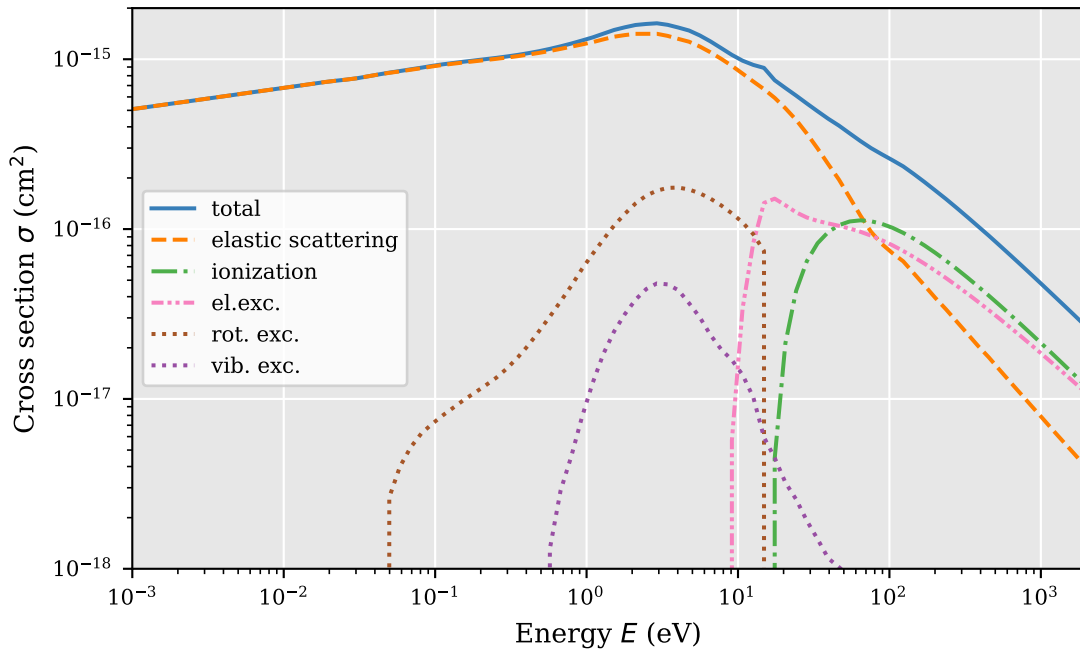


Figure 2.9.: Selection of Electron- H_2 cross sections. The energy describes the kinetic energy of the electron, when the interaction partner is at rest. Rotational, vibrational and electric excitation cross sections are given as the sum of the cross section over all excitation states. Data taken from [35, 79]. Figure adapted from [73].

cross section values below 2×10^{-2} eV were generated by an exponential extrapolation of the experimental data in the range of 2×10^{-2} eV to 1×10^{-1} eV [73]. Cross sections above 1×10^2 eV were derived from a simulation with the software package ELSEPA [74]. There, the cross section is determined using a Dirac partial-wave calculation. The resulting elastic scattering cross section is depicted in figure 2.9.

It can be seen that elastic scattering of electrons and neutral gas is the dominant interaction channel at low energies (< 100 eV). Thus, low-energy electrons will adopt the velocity distribution of the neutral gas, given they only act as independent particles and the density of the neutrals is high enough. The existence of a plasma might change this behavior. See section 3.3 for more information.

The elastic cross section drops for higher energies, and other interactions become more dominant. The total cross section drops enough that the mean free path of the interactions is comparable to the scale of the beam tube, see section 3.3.3. Thus, high-energy electrons will scatter only scarcely.

Ionization through Electron Impact

The energy of beta electrons is much greater than the minimal ionization energy of hydrogen molecules ($E_{\text{th}} = 15.42$ eV) [35]. Thus, ionization of the neutral particles can occur. There are different ionization channels. The dominant process is the non-dissociative ionization, which can be written as



Other ionization processes lead to a dissociation of the molecule producing atomic hydrogen and atomic hydrogen ions. These processes depend on the initial state of the hydrogen molecule. The energy threshold of these processes is higher ($E_{\text{th}} > 18.15$ eV) [35] due to the molecular binding energy. The total cross section of both ionization types is depicted in figure 2.9.

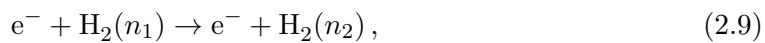
It can be seen that ionization is the dominant process at energies greater than 1×10^2 eV. Thus, beta electrons will lose their energy mainly through this channel. The lost energy E is dependent on the binding energy B and the momentum transfer W to the shell electron. After ionization, both electrons are indistinguishable from each other. Thus, the maximal lost energy E_{\max} is given by

$$E_{\max} = \frac{E_{\beta} - B}{2}. \quad (2.8)$$

The exact energy spectrum of the secondary electrons can be calculated through the works of Eugene Rudd [21] and Kim and Rudd [43]. They showed that small energy losses are more probable than high-energy losses. High-energy losses are relevant for the description of the electron energy distribution in the source. Small energy losses are relevant for the neutrino mass measurement, as they affect the shape of the beta spectrum. Thus, the energy loss of beta electrons was measured and parameterized by Aseev et al. [10].

Electronic Excitation

Free electrons of the source can excite shell electrons of the molecules



where n_1 and n_2 denote the excitation state of the molecule. The transferred energy must be equal to the difference of the energy levels. For hydrogen molecules, this difference is of the order of 10 eV [35]. The cross section of the electronic excitation is dependent on the initial electronic state of the molecule. The source of the KATRIN experiment is kept at low temperatures. Therefore, it is assumed in the context of this thesis that the molecules exist in ground state. In this case, there exist three main excitation channels: excitation to dipole allowed singlet state, excitation to dipole forbidden singlet states and excitation to triplet states [35]. The resulting state of the excitation is of no interest for the KATRIN experiment. Thus, here only the sum of the cross sections is shown, see figure 2.9.

It can be seen that electronic excitation is relevant for electrons with energies greater than 10 eV. The cross section is comparable to the cross section of ionization. Nevertheless, the energy lost per interaction is limited by the maximal excitation energy. Thus, it can be assumed that electronic excitation plays a secondary role in the cooling process of high-energy electrons with energies greater than 10^3 eV. The contribution changes for lower energies.

Rotational and Vibrational Excitation

Atoms in molecules perform a periodic movement in relation to each other. This periodic movement can be classified into a rotational and a vibrational movement for linear molecules like the hydrogen molecule. The eigenstates of the movement can be excited by the collision with free electrons. The frequency of the eigenstate is dependent on the mass of the molecule as well as the electronic configuration of the molecule. Thus, the energy levels of the oscillation are molecule specific. In this case, the assumption that there is no isotopic difference between hydrogen and tritium is not well justified. Nevertheless, due to the lack of data, they will be used in the context of this thesis as a first approximation. The cross section for the excitation of hydrogen is also depicted in figure 2.9. It can be seen, that the rotational and vibrational excitation is not a dominant process at any energy. It has a small influence on the total cross section at energies of approximately 10 eV. However, these collisions are relevant in the cooling process of electrons with energies below 20 eV because of their low threshold energy.

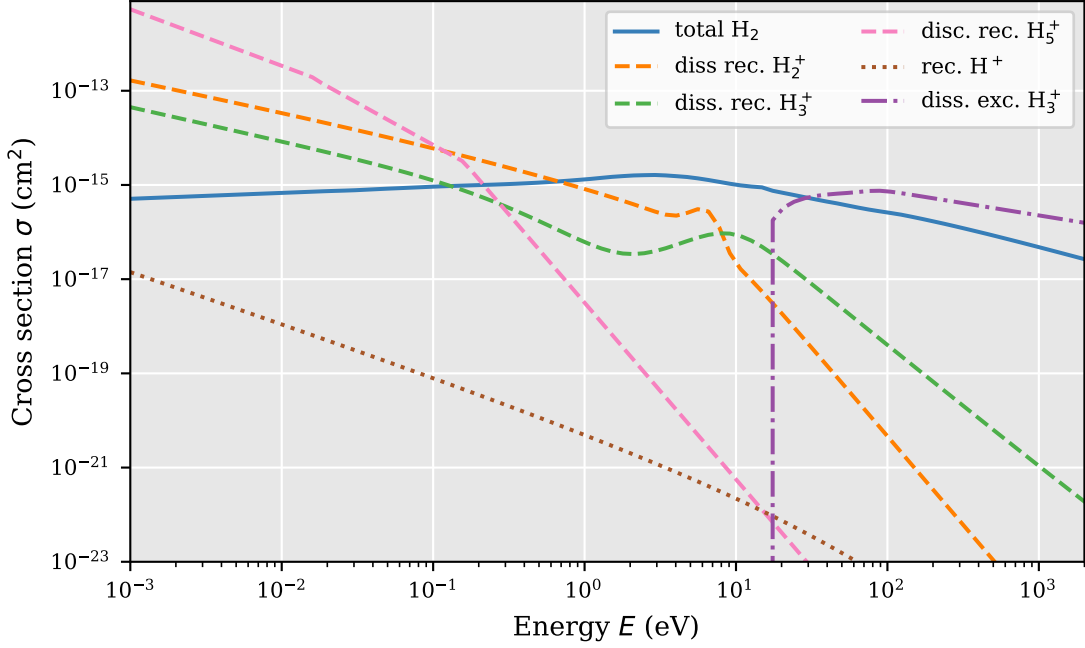


Figure 2.10.: Dissociative recombination and dissociative excitation cross sections. The energy describes the kinetic energy of the electron, when the interaction partner is at rest. Compared to the total cross section of electron- H_2 interactions from figure 2.9. Data taken from [35, 79, 47].

Recombination with H^+

Electrons can recombine directly with a proton through radiative recombination



This process was studied by Kotelnikove theoretically [47]. He found that the cross section for this reaction can be approximately calculated by

$$\sigma_r^{(0)} = \frac{2^8 \pi^2}{3} \frac{\nu^6 e^{-4\nu \arctan(\frac{1}{\nu})}}{(1 - e^{-2\pi\nu})(\nu^2 + 1)^2} \alpha^3 a_b \quad (2.11)$$

$$\sigma_r = \sigma_r^{(0)} \cdot \frac{1.202 + 0.5782 \log(\nu^2 + 1) + 0.2148 \log^2(\nu^2 + 1)}{1 + 0.3425 \log(\nu^2 + 1)}, \quad (2.12)$$

where α is the fine structure constant, a_b the Bohr radius and

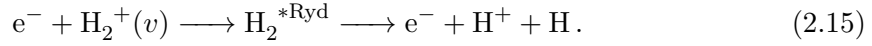
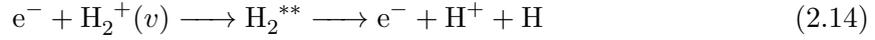
$$\nu = \sqrt{\frac{J_z}{E_{\text{kin}}}} \quad \text{with } J_z = \frac{e^4 m_e}{(2\hbar^2)}. \quad (2.13)$$

The cross section is depicted in figure 2.10 in comparison to the other recombination processes, and shown in figure 2.11 in comparison to other proton processes. It can be seen that the cross section for recombination with protons is significantly lower than for other ions. Paired with a low density of single tritium ions, it can be assumed that recombination with protons can be neglected in the description of the KATRIN plasma.

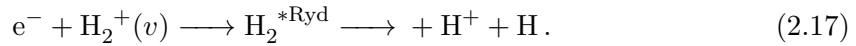
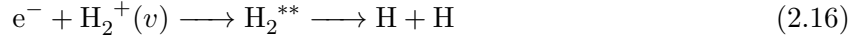
Dissociative Excitation and Recombination of H_2^+

Electrons and the hydrogen molecule H_2^+ can interact amongst others through dissociative excitation and dissociative recombination. The dissociative excitation occurs by “electron

capture into the doubly excited dissociative H_2 state [...] or into a number of auto-ionizing dissociative Rydberg states...”[35]



Dissociative recombination does occur by “...direct capture of incident electron on a double excited state of H_2 [...] or by vibrational [...] excitation of H_2^+ [...] and simultaneous capture of the electron on a dissociative auto-ionizing Rydberg state ...”[35]. The reaction equation is similar to equations 2.14 and 2.15 and reads as

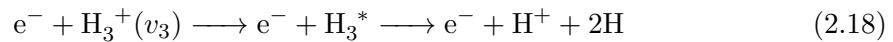


The cross section of both the dissociative excitation and recombination can be found in figure 2.12 in comparison to other H_2^+ reactions. It can be seen that dissociate recombination is the dominant process over dissociative excitation for energies below 0.5 eV. On the one hand, dissociate excitation is more dominant for energies above this threshold. On the other hand, the interaction probability is dependent on the density of the interaction partners. The ion density is higher at lower energies. Thus, dissociate recombination will have a greater influence on the electrons and ions in the source than dissociative excitation.

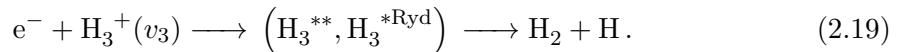
The cross section of dissociative recombination is also depicted in figure 2.10 compared to recombination processes of electrons with other ion cluster sizes and to the total cross section of electron- H_2 interactions. It can be seen that the cross section of recombination with H_2^+ is comparable to other clusters. Thus, it should have the same relevance for the description of the ions. In addition, the cross section of recombination is higher than the total cross section of electron- H_2 interactions. Nevertheless, interactions with H_2 are more frequent due to the large density difference ($n_{T_2} \approx 1 \times 10^{15} \text{ cm}^{-3}$, $n_{T_i} \approx 1 \times 10^6 \text{ cm}^{-3}$).

Dissociative Excitation and Recombination of H_3^+

The reaction formula of dissociative processes of H_3^+ clusters are similar to the dissociative processes of H_2^+ ions. The dissociative excitation occurs by the excitation to an intermediate highly excited state



and the dissociative recombination occurs by electron capture to a double excited state or an excited Rydberg state and subsequent electron capture



The corresponding cross sections are depicted in figure 2.10 in comparison to recombination processes with other ion clusters. It can be seen that dissociative excitation exhibits a threshold energy. The origin of this behavior is not examined by Janev, Reiter, and Samm but was confirmed by various measurements [35]. Dissociative excitation is the dominant process above its threshold energy (15 eV) over dissociative recombination. Nevertheless, the ion density is higher at lower energies. Thus, dissociate recombination will have a greater influence on the electrons and ions in the source than dissociative excitation.

The cross section of dissociative recombination is also depicted in figure 2.10 in comparison to recombination processes of electrons with other ion cluster sizes and to the total cross section of electron- H_2 interactions. The same conclusions can be drawn as in the description

of the dissociative recombination of H_2^+ , namely that the cross section of recombination with H_3^+ is comparable to other clusters. Thus, it should have the same relevance for the description of the ions. In addition, the cross section of recombination is higher than the total cross section of electron- H_2 interactions. Nevertheless, interactions with H_2 are more frequent due to the large density difference ($n_{T_2} \approx 1 \times 10^{15} \text{ cm}^{-3}$, $n_{T_i^+} \approx 1 \times 10^6 \text{ cm}^{-3}$).

Recombination of D_5^+

There is only limited data on the cross section of hydrogen clusters with sizes greater $i \geq 5$ available. The cross section data of the highest cluster size found is published by Pettersson et al. [68] for collisions of electrons with D_5^+ ions. They investigated the cross section by using an ion storage ring. Pettersson et al. provide a numerical expression for the recombination cross section described by the following expression

$$\sigma(E) = \begin{cases} 10^{-14.87} E^{-1.20} \text{cm}^2 & \text{for } 0.0005 \leq E \leq 0.017 \text{ eV} \\ 10^{-15.93} E^{-1.78} \text{cm}^2 & \text{for } 0.017 \leq E \leq 0.159 \text{ eV} \\ 10^{-17.50} E^{-3.75} \text{cm}^2 & \text{for } 0.159 \leq E \leq 1.0 \text{ eV} \end{cases} \quad (2.20)$$

The corresponding cross section is depicted in comparison to other recombination processes in figure 2.10. It can be seen that the cross section is significantly higher at lower energies ($< 0.1 \text{ eV}$) than for the other recombination channels. The density of T_5^+ is assumed to be only slightly lower than the density of T_3^+ . In total, T_5^+ recombination should be as relevant as T_3^+ recombination at the experiment.

2.4.3. Ion-Interactions

Interaction of ions can occur in collision with electrons, with other ions and with neutral gas. As mentioned before, the interaction probability depends on the density and the cross section of the interaction. Both the density of electrons and ions is significantly lower than the density of the neutral gas particles, whereas the cross section of the interaction is comparable. Thus, interactions with the neutral gas occur more often. Hence, this section will focus on interaction with neutral gas. Interactions of electrons and ions are described in the previous section and will not be discussed further here. Ion-ion interactions result in similar interaction products as ion-neutral interactions and have similar cross sections [35]. Taking into account that the density of ions is much smaller than the density of neutral particles, any ion-ion interactions are neglected in the following.

In the context of this thesis, only positive ions are investigated. Negative ions can be produced by radiative electron attachment to hydrogen or through electron impact dissociation of hydrogen molecules. The cross section of both reactions is small compared to other electronic interactions [35]. Thus, they are not investigated further here.

In most cases there is no data available on interactions of tritium ions with molecular tritium but for their isotopic partners hydrogen or deuterium. Thus, in the context of this thesis, it is assumed that there is no isotopic effect between the isotopes. Nevertheless, the data will always be labeled in respect to the original hydrogen isotope to mark the origin of the data.

2.4.3.1. Interactions of H^+ Ions

Hydrogen ions show multiple reaction channels with neutral hydrogen molecules. A conclusive summary is given by Tabata and Shirai [79] and Janev, Reiter, and Samm [35] combining measurement data as well as theoretical calculations. The following description is based on their results.

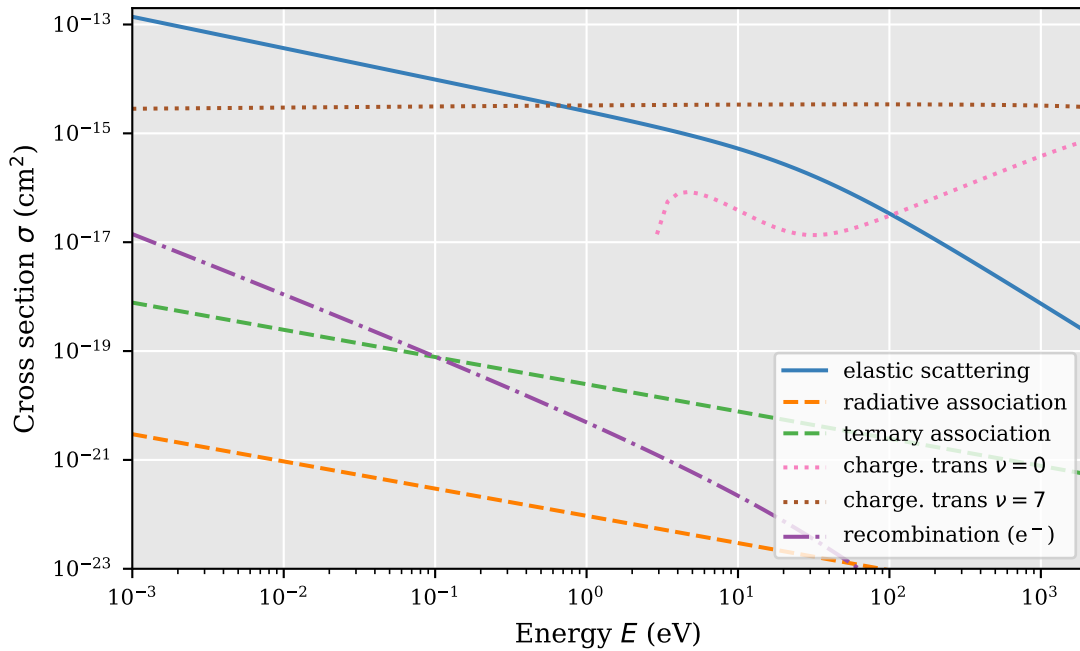


Figure 2.11.: Selection of H^+ - H_2 cross sections. The energy describes the kinetic energy of the ion, when the hydrogen molecule is at rest. Ternary association cross section calculated using a neutral gas density of $1 \times 10^{15} \text{ cm}^{-3}$ with data from [29]. Recombination cross section for comparison (in relation to the kinetic energy of the electron). Data taken from [35, 79, 47].

Elastic Scattering

Elastic scattering of ions and neutral gas is significantly different from the elastic scattering of electrons with neutral gas. First, the mass of ions is much higher. Thus, the recoil of the ions needs to be taken into account after the interaction. Second, ions have a finite extension in comparison to the point-like structure of electrons. Thus, the elastic cross section is significantly higher for ions than for electrons.

The cross section of elastic scattering is depicted in figure 2.11. It can be seen that elastic scattering is the dominant interaction for ions below 0.5 eV. At the center of the WGTS the density of neutral particles is approximately 10^{15} cm^{-3} at a temperature of 80 K. Thus, the mean free path of ions in the center is in the order of 0.1 mm, see section 3.3.3. The mean free path is therefore much smaller than the size of the system. This means that ions will fulfill many elastic scatterings with the neutral gas. Hence, it can be assumed that the ions will adapt the Maxwell-Boltzmann distribution from the neutral gas. The density is significantly reduced after the first two pump ports, see section 2.1.1. Thus, the mean free path in this region is increased by the inverse proportion. Thus, ions in this region can show a different energy distribution than the neutral gas.

Charge Transfer

In a charge transfer reaction, the proton interacts with a neutral molecule. One electron is donated by the molecule, which produces a hydrogen atom and a molecular ion



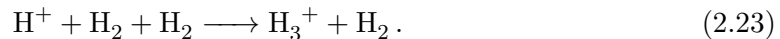
The cross section of this reaction is dependent on the initial vibrational state ν of the molecule. For $\nu = 0, 1, 2$ the reaction is endothermic. Therefore, there is an energy

threshold for the reaction [35]. At higher vibrational states this reaction becomes exothermic, and thus it loses its energy threshold.

The cross section of a charge transfer reaction with a molecule in ground state ($\nu = 0$) and an excited state ($\nu = 7$) can be seen in figure 2.11. It can be seen that charge transfer to a molecule in ground state is the dominant reaction above 100 eV. For lower energies, the only charge transfer reaction with higher order clusters are relevant. The energy difference between two vibrational states is in the order of 1 eV. Thus, it can be assumed that the molecules mostly reside in ground state because of their low temperature of 80 K. This means that charge transfer to higher states is suppressed. For a reaction with a molecule in ground state, the ion needs energies greater than the threshold energy. Thermal ions hardly ever have higher energies than the threshold energy. Thus, it can be concluded that charge transfer to the ground state is negligible. In total, it can be assumed that charge transfer plays only a secondary role in the development of the ion density distribution.

Radiative and Ternary Association

Hydrogen ions can form ion clusters with hydrogen through radiative and ternary association



Both the photon and the second molecule ensure conservation of momentum. Currently, there is no data available on the cross section of both reactions. The cross section will be derived here from rate coefficients k measured by Gerlich [29]. The corresponding conversion is presented in the following.

The number of particles which are created by a given reaction per given time interval is given by the reaction rate r . It is calculated by

$$r = k \cdot n, \quad (2.24)$$

where k is the rate coefficient and n the density of the interaction partner. From a microscopic point of view this rate can be identified with the collision rate ν

$$\nu = \frac{v}{\lambda}, \quad (2.25)$$

where v is the mean velocity of the interacting particle and λ the mean free path, see section 3.4.3. The velocity can be calculated from the kinetic energy E of the interacting particle. The mean free path can be directly derived through the cross section and the density of the reaction partner

$$\lambda = \frac{1}{n\sigma}. \quad (2.26)$$

In total, the cross section can be written as

$$\sigma = \frac{k}{\sqrt{\frac{2E}{m}}}, \quad (2.27)$$

where m is the mass of the interacting particle.

This procedure can only be taken as a rough estimate of the cross section but can provide a first order approximation, when no data on the cross section is available. The cross section of a ternary process σ_3 can be derived similarly. In that case the reaction rate is given by

$$r = k \cdot n^2. \quad (2.28)$$

Thus the cross section of the ternary process can be calculated by

$$\sigma_3 = \frac{kn}{\sqrt{\frac{2E}{m}}}. \quad (2.29)$$

Gerlich measured the rate coefficient for ternary and radiative association at different gas temperatures. As expected, they found a temperature dependence. For a gas temperature of 80 K the rate coefficient was measured to be $k_R = 1.3 \times 10^{-16} \text{ cm}^3 \text{ s}^{-1}$ for the radiative association process and $k_3 = 5.4 \times 10^{-29} \text{ cm}^6 \text{ s}^{-1}$ for the ternary association process.

The corresponding cross sections for the association processes were calculated and are depicted in figure 2.11. The ternary process cross section was calculated using the maximal neutral particle density of $6.3 \times 10^{14} \text{ cm}^{-3}$, similar to the density in the center of the WGTS. Thus, the values of ternary association only represent the maximal cross section. It can be seen that both cross sections are significantly lower than the cross section for elastic scattering. Thus, elastic scattering is the dominant process over the association processes.

The overall relevance of the association processes for the experiment can be evaluated by comparing the collision frequency of the association with the mean time a neutral particle is in the central part of the source. See section 3.4.3 for more information on the collision rate. For a central density of $6.3 \times 10^{14} \text{ cm}^{-3}$ and a ternary cross section of $4.8 \times 10^{-19} \text{ cm}^2$ the ions collide each 0.14 s. The mean time a hydrogen molecule spends in the source is in the order of 0.5 s (calculated from the mean drift velocity of the neutral gas). Thus, association processes can occur in the source, but a thorough investigation must be employed to determine the exact contribution.

2.4.3.2. Interactions of H_2^+ Ions

Hydrogen molecule ions show multiple reaction channels with neutral hydrogen molecules. A conclusive summary is given by Janev, Reiter, and Samm [35] combining measurement data as well as theoretical calculations. A short summary of the interaction channels will be provided in the following. The dominant channels are cluster formation and charge transfer. Elastic scattering is suppressed, in contrast to hydrogen ions, where elastic scattering is the dominant interaction channel. Collisions with electrons (dissociative recombination and dissociative excitation) were already discussed in section 2.4.2.

Charge Transfer

In a charge transfer reaction, the hydrogen molecule ion interacts with a hydrogen molecule. One electron is donated by the molecule to the ion and thus creating a new ion.



Ions created in this way will therefore show similar energy distribution to the neutral gas. The cross section of this reaction depends on the initial and final vibrational state of the particles. Nevertheless, Janev, Reiter, and Samm also provide a total cross section for the charge transfer, where a mean distribution of states is assumed. The corresponding cross section is depicted in figure 2.12 in comparison to other interaction channels. It is apparent that the charge transfer channel is dominant at energies greater than 2 eV. Nevertheless, it also contributes significantly at lower energies to the total cross section, only surpassed by the cluster formation. The cluster formation however will suppress the importance of the charge transfer at the experiment because the H_2^+ ions will transform very efficiently to H_3^+ .

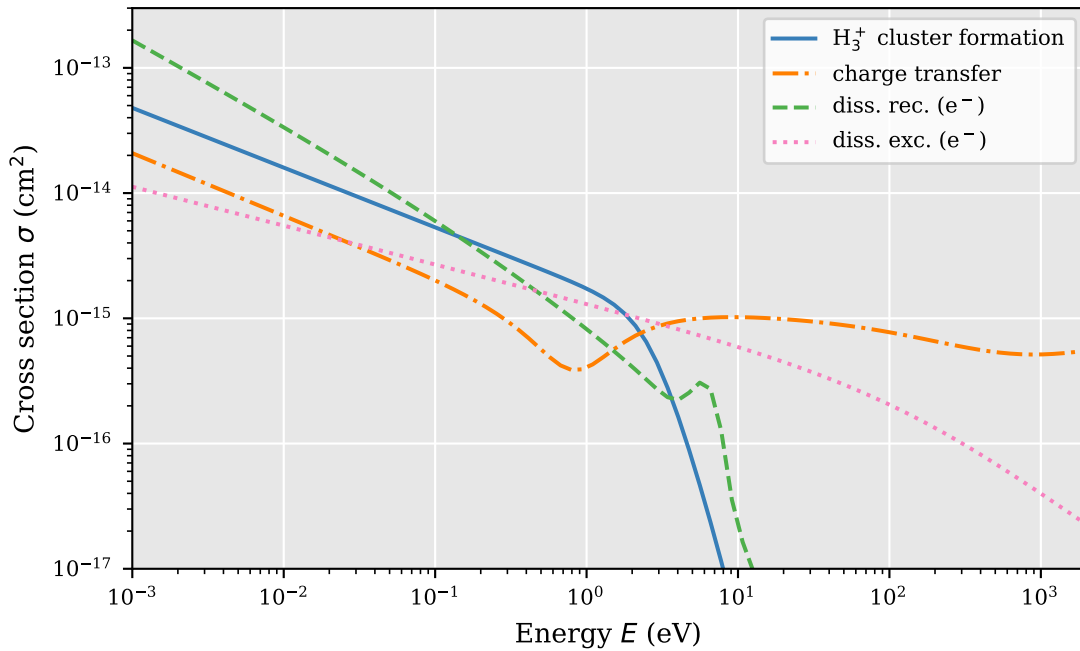


Figure 2.12.: Selection of $\text{H}_2^+ - \text{H}_2$ cross sections. The energy describes the kinetic energy of the ion, when the hydrogen molecule is at rest. Dissociative recombination and dissociative excitation cross section for comparison (in relation to the kinetic energy of the electron). Data taken from [35, 79].

Cluster Formation

Hydrogen molecule ions can form hydrogen ion clusters in collision with hydrogen molecules, either by proton transfer or by atom transfer. Most experimental studies investigated only the total cross section of both channels together. In the context of this thesis, it is not differentiated between a hydrogen ion with an attached molecule or a hydrogen molecule ion with an attached atom. Thus, the process reads as



The total cross section was measured for the vibrational ground state of both interaction partners. The cross section for higher vibrational states is determined through a linear scaling of the cross section of the ground state. The ratio of the cross sections is close to identity [35]. Thus, in the context of this thesis, only the cross section of the vibrational ground state is taken into account. The cross section of cluster formation is depicted in figure 2.12 in comparison to other interaction channels of H_2^+ . It is apparent that the cluster formation channel is the dominant channel at energies below 2 eV. It can therefore be assumed that there is only a small amount of H_2^+ in the central part of the source, where collisions are frequent. In regions with smaller amounts of neutral gas, there is the possibility that the H_2^+ ions will survive.

2.4.3.3. Interactions of H_3^+ Ions

Hydrogen cluster ions mostly interact with neutral hydrogen molecules and electrons. Experimental data or theoretical calculations of the cross section for the interaction with hydrogen molecules is scarce due to the multitude of competing channels. In the context of this thesis, the data from Tabata and Shirai [79] is used for the description of the elastic scattering and the results from Janev, Reiter, and Samm [35] for the description of the collision induced dissociation. For a description of the reactions with electrons, refer to section 2.4.2.

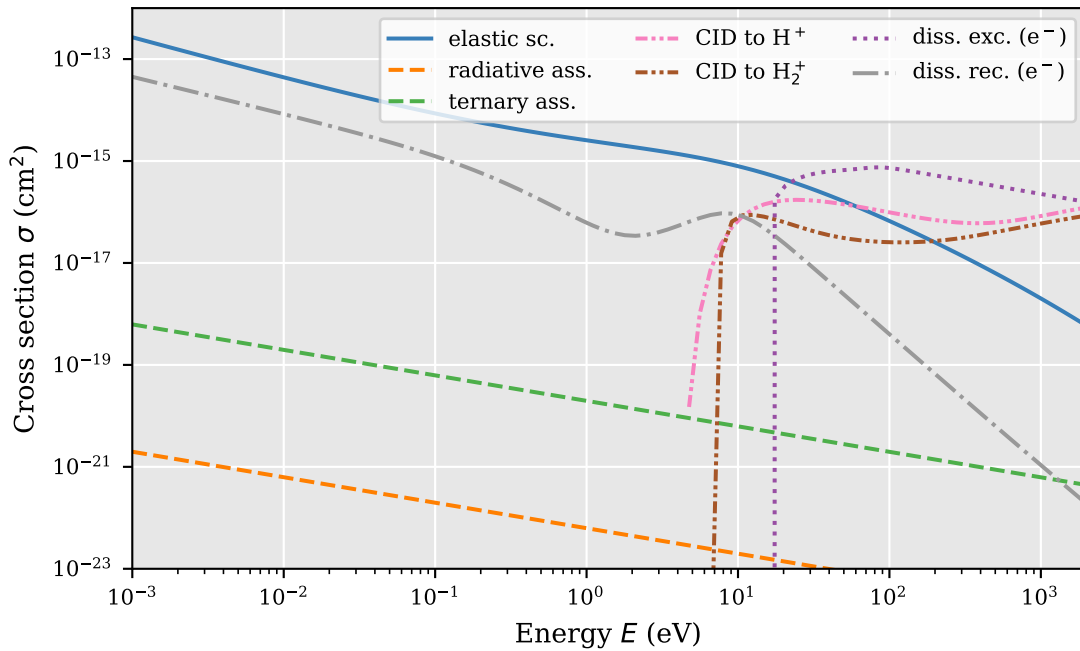


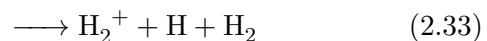
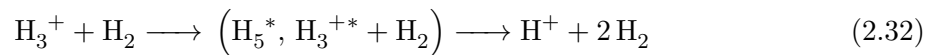
Figure 2.13.: Selection of H_3^+ - H_2 cross sections. The energy describes the kinetic energy of the ion, when the hydrogen molecule is at rest. Ternary association cross section calculated using a neutral gas density of $6.3 \times 10^{14} \text{ cm}^{-3}$ with data from [29]. Recombination cross section for comparison (in relation to the kinetic energy of the electron). Data taken from [35, 79, 47].

Elastic Scattering

The cross section for the elastic scattering were tabulated by Phelps [69] through an investigation of drift velocities of H_3^+ in a H_2 gas. The data is only available in the range of 0.1 eV to 1 eV. Tabata and Shirai found an approximate formula to describe the data of Phelps [79]. In the context of this thesis the formula of Tabata is used for all energies, even below 0.1 eV due to the lack of additional data. The cross section of the elastic scattering is depicted in 2.13 in comparison to other interaction channels. It is apparent that elastic scattering is the dominant interaction channel for energies below 20 eV. It can therefore be assumed that the ions will adopt the velocity distribution of the neutral gas in the center of the source. In regions with lower density, the ions will continue with this velocity distribution, while only being influenced by electric fields.

Collision Induced Dissociation

Hydrogen cluster ions can be dissociated by collision with hydrogen molecules to either hydrogen or hydrogen molecule ions by forming an intermediate excited state

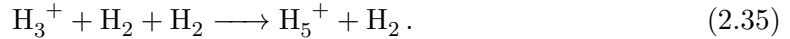


The collision energy must be greater than the binding energy of the cluster. Thus, the reaction shows a threshold energy at 4.32 eV and 6.16 eV respectively [35]. The cross section of both reactions is dependent on the vibrational state of the reaction partners. Nevertheless, Janev, Reiter, and Samm also provide a total cross section where a mean distribution of states is assumed. The corresponding cross sections are depicted in figure 2.13 in comparison to other interaction channels. It can be seen that the collision induced dissociation is the dominant process for energies above 100 eV. From the elastic scattering

cross section it can be assumed that the ions will adopt the Maxwell-Boltzmann distribution of the neutral gas. Thus, the ions will mostly have energies below 10^{-2} eV. Hence, collision induced dissociation will not significantly influence the evolution of the ions.

Radiative and Ternary Association

Higher order cluster ions can be formed by radiative and ternary association



Both the photon and the additional hydrogen molecule are necessary to fulfill the conservation of momentum. Similar to H^+ , there is no data available on the cross sections. Gerlich measured reaction rates $k_r < 0.5 \times 10^{-16}$ cm³/s and $k_3 = 2.5$ cm⁶/s at $T = 80$ K for radiative and ternary association [29]. Thus, the same procedure presented for the H^+ ions will be used here to derive an approximation for the cross section from the reaction rates, see section 2.4.3.1 and equations 2.27 and 2.29.

The corresponding cross sections for the association processes were calculated and are depicted in figure 2.13. The ternary process cross section was calculated using the maximal neutral particle density of 6.3×10^{14} cm⁻³, similar to the density in the center of the WGTS. Thus, the values of ternary association only represent the maximal cross section. It can be seen that both cross sections are significantly lower than the cross section for elastic scattering. Thus, elastic scattering is the dominant process over the association processes.

The overall relevance of the association processes for the experiment can be evaluated by comparing the collision frequency of the association with the mean time a neutral particle is in the central part of the source. See section 3.4.3 for more information on the collision rate. For a central density of 6.3×10^{14} cm⁻³ and a ternary cross section of 3.8×10^{-19} cm² the ions collide each 0.15 s. The mean time of a hydrogen molecule spends in the source is in the order of 0.5 s (calculated from the mean drift velocity of the neutral gas). Thus, association processes can occur in the source, but a thorough investigation must be employed to determine the exact contribution.

2.4.3.4. Interactions of Higher Order Cluster Ions

Higher order ion clusters H_i^+ can form through attachment of additional hydrogen molecules to existing ion clusters. There are only limited information on the interaction channels of these clusters to be found in the literature. The only tangible data is available for creation and fragmentation rate coefficients of the clusters. Thus, in the following, it is only discussed whether higher order ion clusters exist in the KATRIN source or not. First, the creation and fragmentation mechanism is described. Second, the temperature dependence of the rate coefficients is discussed. Third, the implications of fragmentation at KATRIN conditions will be described.

Creation and Fragmentation

The relative density of higher order cluster ions depends on the creation and fragmentation processes. Paul et al. investigated these processes for a hydrogen gas at 10 K with a density of 10^{14} cm⁻³ [63]. They found that there can be clusters of up to $i = 23$ in an equilibrium state. Paul et al. describe that the primary creation mechanisms for clusters are ternary and radiative association with the rate coefficients $k_{3,i}$ and $k_{r,i}$, where i denotes the size of the initial cluster. The total creation rate coefficient $k_{g,i}$ can then be written as

$$k_{g,i} = k_{r,i} + k_{3,i}[\text{H}_2], \quad (2.36)$$

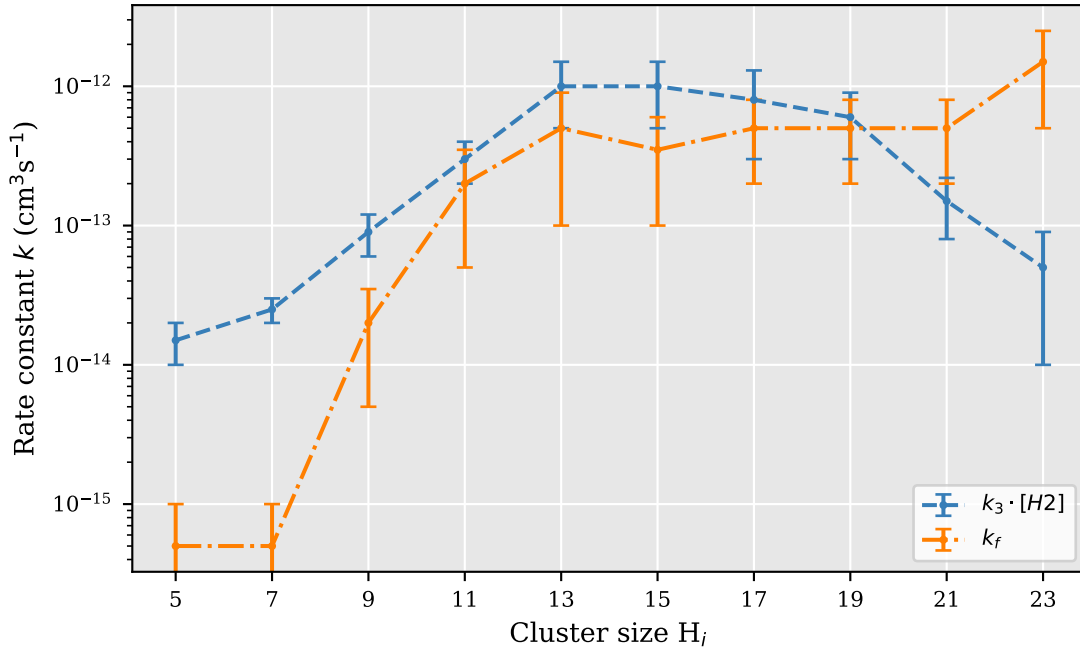
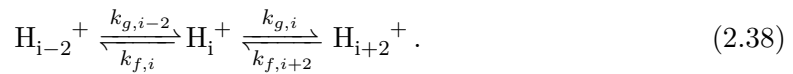


Figure 2.14.: Ion cluster creation and fragmentation at 10 K. The ternary creation rate is scaled by the density of the hydrogen gas (10^{14} cm^{-3}) for comparison of creation and fragmentation. Note the large uncertainty of the fragmentation rate at cluster sizes $i = 5, 7$. The uncertainty in these cases is as high as the measured value itself. Data taken from [63].

where $[H_2]$ denotes the density of the background hydrogen gas. Paul et al. assume that the dominant fragmentation process will occur through collision with neutral gas with the rate coefficient $k_{f,i}$. Thus, the density of an ion cluster $[H_i^+]$ can be derived from

$$\frac{1}{[H_2]} \frac{d[H_i^+]}{dt} = k_{g,i-2}[H_{i-2}^+] + k_{f,i+2}[H_{i+2}^+] - k_{f,i}[H_i^+] - k_{g,i}[H_i^+] \quad (2.37)$$

with the reaction equation



Equation 2.37 can be constructed for all possible indexes i . Thus, the density of each species can be determined by solving the coupled differential equation.

An approximate fast solution to the differential equation can be found assuming that the fragmentation rate increases with increasing order i , and that there is a maximum order l . The density of the highest order cluster $[H_l]$ then calculates to

$$[H_l] = [H_{l-2}] \frac{k_{g,l-2}}{k_{f,l}}. \quad (2.39)$$

Thus, the ratio of the rate coefficients for creation and fragmentation can provide a measure for the density of the highest order cluster relative to the density of the predecessor. The largest cluster size is found if the ratio of fragmentation and creation is smaller than one. The measured creation and fragmentation rates of Paul et al. are depicted in figure 2.14. It can be seen that the ratio of fragmentation and creation is greater than one for indexes below 21. Following the argumentation from above, this means that the highest cluster size should be 23. This estimation coincides with the measurements of Paul.

The measurements of Paul et al. cannot be directly applied to the KATRIN source. The rate coefficient is in general dependent on the temperature of the reactants. Paul et al. measured the rate coefficients at 10 K. Thus, for a description of the cluster in the KATRIN source, a corresponding scale function of the coefficients needs to be found.

Creation Rate: Temperature Dependence

Paul et al. derived a T^{-1} dependence of the ternary rate coefficient for H_5^+ clusters. In the context of this thesis, it is assumed that the ternary rate coefficients of higher order clusters scale the same as H_5^+ . This hypothesis can be tested by a comparison of the scaled rate coefficients with measurement data of Gerlich [29]. They measured the ternary creation rate at 25 K for cluster sizes of up to $i = 11$ at a slightly lower hydrogen density of $[\text{H}_2] = 3.7 \times 10^{13} \text{ cm}^{-3}$. Gerlich state that there is a large uncertainty on the creation rate of higher order cluster. The value of the uncertainty is not stated in the publication. The ternary creation rate of Gerlich as well as the scaled creation rates of Paul et al. can be found in figure 2.15. It can be seen that the scaled values of Paul et al. are similar to the values measured by Gerlich, however the values show a slight difference. This can be attributed to the measurement uncertainty of Gerlich. Hence, it can be concluded that the temperature dependence of Paul et al. can be used to determine the ternary rate at temperatures of the KATRIN source, depicted in figure 2.16.

Fragmentation Rate: Temperature Dependence

There is no conclusive data on the temperature dependence of the fragmentation constant available in the literature, however Paul et al. provide a possible scaling mechanism. This method is tested in the following by a comparison of the scaled values of Paul et al. at 10 K to approximate values of Gerlich at 25 K.

Paul et al. assume that the fragmentation cross section is proportional to $\sqrt{E - \Delta E}$, where ΔE is the binding energy of the cluster. Thus, the rate coefficient of fragmentation can be calculated at higher temperatures from the standard Arrhenius expression

$$k_f = k_c \exp -\frac{\Delta E}{k_b T}. \quad (2.40)$$

The constant k_c can be calculated from the tabulated values of k_f of Paul et al. at 10 K and from the binding energy. Paul et al. determined the binding energy of clusters $i = 11$ to a range from 23 meV to 11 meV. The binding energy of higher order clusters is claimed to reach an equilibrium value of 9 meV. For smaller clusters ($i = 5, 7, 9$) no data was provided by Paul et al., however Harrison, Massa, and Solomon [32] determined the binding energies to 260 meV, 17 meV and 108 meV respectively.

Gerlich could show that clusters up to index $i = 9$ exist at 25 K [29]. Gerlich does not provide any data on the fragmentation rate coefficient. A limit on the fragmentation rate can be derived through equation 2.39 and through the observation that the density of the clusters was lower than the initial density of H_3^+ . Thus, the fragmentation rate of these clusters was lower than the creation rate. The measured creation rates from Gerlich can therefore be used as a lower limit for the fragmentation rates.

The limits on the fragmentation rate of Gerlich can be compared to the hypothesis of Paul et al. The scaled values from Paul et al. at higher temperatures are calculated using equation 2.40 and the corresponding binding energies. The scaled fragmentation rates can be found in table 2.1. It can be seen that the fragmentation rate of small cluster sizes is extremely large. This would mean that there are no clusters at 25 K. This is contradicted by the fact that Gerlich measured clusters at this temperature. It can therefore be concluded

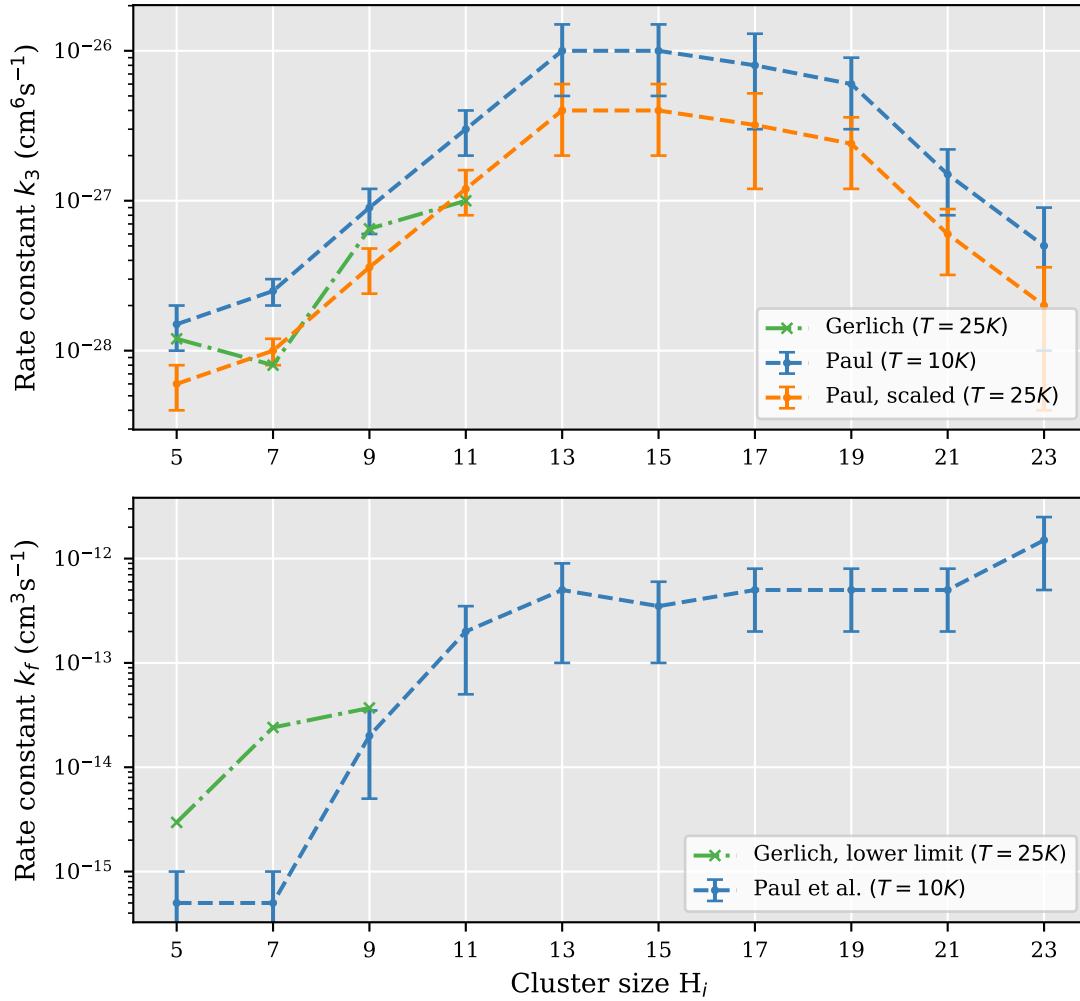


Figure 2.15.: Comparison of measurement and scaling of rate constants. Top: Comparison of the scaled creation rate of Paul et al. and the measured rates of Gerlich. No uncertainties were provided in the data of Gerlich. Bottom: Comparison of the fragmentation rate of Paul et al. and the lower limit determined through equation 2.39 from the data of Gerlich. Data taken from [63, 29].

that either the Arrhenius expression cannot be used in the way described above or that the binding energy has lower values than proposed.

Nevertheless, it can be observed that the lower limit on the fragmentation rate of Gerlich is greater than the corresponding fragmentation rate of Paul. It can therefore be assumed that the fragmentation rate is increased further at temperatures greater than 25 K. The number of particles which have energies greater than the binding energy will increase at least linear with the temperature. Thus, the fragmentation rate should scale at least linear as well.

Cluster Sizes at KATRIN

The results of Paul et al. and Gerlich can be used to provide a limit on the cluster sizes in the KATRIN source. On the one hand, the creation rate can be scaled directly to 80 K using the T^{-1} relationship of Paul et al. The corresponding values for a central neutral particle density of $6.3 \times 10^{14} \text{ cm}^{-3}$ are depicted in figure 2.16. On the other hand, the fragmentation rate cannot be quantified directly at 80 K. Three different methods can be used to define a lower boundary on the fragmentation rate:

Table 2.1.: Binding energies and fragmentation rates. Measured rates of Paul et al. were scaled using the Arrhenius expression from equation 2.40. Data taken from [32] and [63].

cluster index i	5	7	9	11	13
ΔE (meV)	260	17	108	11	11
$k_f(10\text{ K})$ ($\text{cm}^{-3}\text{s}^{-1}$)	1.5×10^{-28}	2.5×10^{-28}	9.0×10^{-28}	3.0×10^{-27}	1.0×10^{-26}
$k_f(25\text{ K})$ ($\text{cm}^{-3}\text{s}^{-1}$)	2.1×10^{63}	6.9×10^{-11}	9.1×10^{18}	4.2×10^{-10}	1.1×10^{-9}

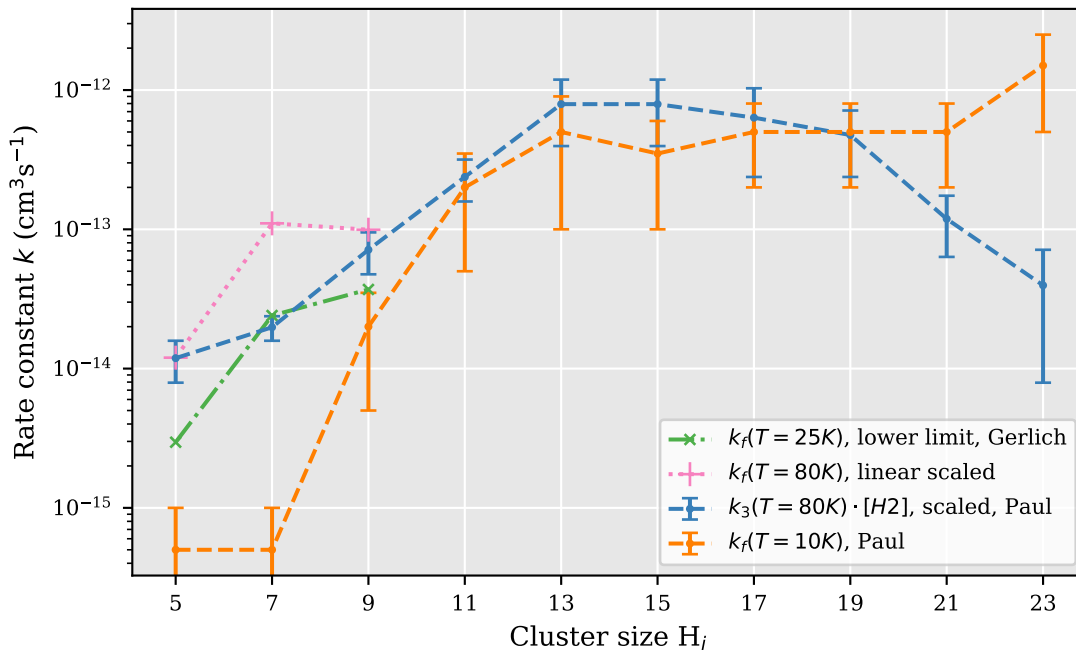


Figure 2.16.: Clustering at 80 K. Creation rate scaled from Paul et al. [63] and adjusted to a neutral density of $6.3 \times 10^{14} \text{ cm}^{-3}$. Fragmentation rate either from measurements of Paul et al. directly, derived from the data of Gerlich [29] using equation 2.39 or through linear scaling through both data of Gerlich and Paul et al.

1. The measured fragmentation rate of Paul et al. at 10 K is used directly as a lower boundary.
2. The fragmentation rate is at least as high as the measured creation rate of Gerlich.
3. The fragmentation rate can be scaled linearly. The scaling parameters can be calculated from the fragmentation rates of Paul et al. at 10 K and from the creation rates of Gerlich at 25 K.

The resulting minimal fragmentation rates of each method are depicted alongside the creation rates in figure 2.16.

In the context of this thesis, the maximal cluster size in the KATRIN source is determined following equation 2.39. Thus, the maximal cluster size is reached if the fragmentation rate is bigger than the creation rate. The maximal cluster size is dependent on the method employed to determine the fragmentation rate from above.

1. $k_f(T = 10\text{ K})$, Paul: The creation rate is well above the fragmentation rate up to index $i = 9$. Uncertainties above this index are large enough that the fragmentation rate could be higher than the creation rate. This possibility is even more pronounced considering that the fragmentation rate of 10 K can only be considered as the lower

limit of the fragmentation rate at 80 K. The maximal cluster size index is $i = 21$, when only considering the measured value without the uncertainties.

2. $k_f(T = 25 \text{ K})$, lower limit, Gerlich: A maximal cluster size cannot be determined in this case. It can only be deduced that the density of H_7^+ is lower than the density of H_5^+ . No conclusion can be derived for higher cluster sizes.
3. $k_f(T = 80 \text{ K})$, linear scaled: The fragmentation rate is well above the creation rate at index $i = 7$. Thus, the maximum cluster size in this case is $i = 5$.

In total, it can be seen that there is no conclusive result on the maximal cluster size from the data of creation and fragmentation rates. Further investigation is necessary, especially for the fragmentation rates of the molecules at 80 K.

In the discussion above, only interactions of ions with neutral gas were considered, whereas there is a non-negligible amount of electrons with energies greater than the binding energy of the cluster ions. Data on these collisions is very scarce in the literature. Following the argumentation of Miderski and Gellene [56], it can be assumed that the recombination rate coefficient for a H_5^+ cluster is increased dramatically in contrast to the recombination rate of H_3^+ . Thus, it can be assumed that the cross section for dissociative collisions is increased as well. Hence, many higher order clusters will be destroyed by electron collisions.

For the following description of the plasma, only cluster sizes of up to index $i = 5$ will be considered. In the context of this thesis, it is assumed that the density of higher order clusters is negligible.

Chapter 3

Classification of the KATRIN Plasma

Most of the know universe exists in plasma state [14]. However, the explicit description of the state depends on many parameters, like the charged particle density and the energy distribution. Therefore, this chapter focuses on the specific classification of the plasma in the KATRIN source and evaluation of suitable theoretical plasma models. A short introduction into plasmas will be given first. Secondly, measurements will be described, which constrain the plasma in the source experimentally. Then characteristic length scales and characteristic frequencies will be discussed for the conditions of the experiment. These parameters constrain the multitude of theoretical plasma models. Two specific models will be highlighted: a diffusion approach of a previous work by Kuckert [50], and a partly collisional model, the main focus of this thesis.

3.1. Introduction to Plasmas

There is no common definition, what plasma is. Hermann and Preppernau define plasma as “the entirety of relatively free moving charged particles, which interact with each other through electromagnetic forces. The total system, where the entirety of the charged particles belong to must be neutral to the outside”(translated from [34]). Cap [14] defines plasma similarly, but adds that core properties of the medium must be influenced by the presence of the entirety of the charged particles. The presence of free moving charged particles is not sufficient to describe plasma. The charged particles must show a collective behavior. Thus, a common salt solution can be described as plasma, whereas the particle cloud at high-energy accelerators might not be described this way [14].

There are many characteristics which describe a plasma, see sections 3.3 and 3.4 for an in depth description. Some of these can be used to determine if there exists a plasma at all. One easy accessible property is the quasi-neutrality.

From the definitions above, it is evident that the absolute number of charged particles is not relevant in the definitions of plasma, but the number of positive and negative charges must be approximately equal. Assume that there are negative and positive charged particles in a sphere with the number densities n_e and n_i respectively. The total charge Q in this sphere with radius R can be written as

$$Q = -\frac{4\pi R^3}{3}(n_e - n_i)e. \quad (3.1)$$

The electric field at the radius r with $r \geq R$ is then calculated by

$$E = \frac{Q}{r^2} = -\frac{4\pi}{3}(1 - a)\frac{R^3}{r^2}n_e e, \quad (3.2)$$

with the relative density factor $a = n_i/n_e$. The electric field at the rim of a sphere with radius $R = 1$ cm, a typical charge density of $n_e = 1 \times 10^{15} \text{ cm}^{-3}$ for fusion plasma, and the small relative density of $a = 0.99$ will be $E = 6.03 \times 10^6 \text{ V/cm}$ accordingly. This large electric field will attract ions and restore the quasi-neutrality. Thus, it can be assumed that there exists quasi-neutrality in all plasmas. This condition will be broken if there are boundary conditions involved, or if there exist oscillations with a sufficient high frequency [14].

Simulations by Kuckert [50] show that the electron density in the center of the WGTS is approximately $n_e \approx 10^6 \text{ cm}^{-3}$ (supported by the simulations of this thesis, see chapter 4). The radius of the source is 4.5 cm. Assuming that there are no ions ($a = 0$) would result in a field of $E = 2.7 \times 10^{-2} \text{ V/cm}$. This field is not as strong as the typical field presented above. Thus, there might be effects, which disturb the quasi neutrality. Nevertheless, the field is large enough to heavily influence thermal electrons of the source ($\mathcal{O}(E_{\text{th}}) \approx 1 \text{ meV}$).

3.2. Experimental Investigations

The KATRIN experiment is equipped with many methods to investigate the source plasma experimentally. These methods revolve either around on the measurement of electrons, which will have gained or lost energy through the plasma, or on the measurement of particle fluxes leaving the source. In the first category fall krypton line measurements, the Pro-KATRIN measurements and egun measurements. In the second category fall the measurements of the rear wall current and the measurement of the dipole ion flux. A selection of these measurement techniques will be described in the following, and a short summary of the current findings will be presented. The investigations are still ongoing. Thus, this will only provide a preliminary view of the data and will show a short insight in the current experimental exploration.

The KATRIN experiment offers many ways to influence the source plasma. While this can be used to reduce the effects of the plasma on the neutrino mass measurement, these methods can also be used to investigate the plasma itself. These methods include among others the adaptable magnetic field strength in all parts of the source, the variation of the potential at the rear wall and the dipole electrodes, the variable tritium density in the source and the introduction of additional electrons to the source through an illumination of the rear wall. These methods are employed in some analyzes described below.

3.2.1. Krypton Line Measurements

$^{83\text{m}}\text{Kr}$ is a metastable isotope which produces monoenergetic electrons in its decay. Some conversion electrons have energies close to the tritium beta endpoint energy. Others can reach energies up to 32 keV. The matching decay energy, paired with a short half-life of 1.83 h, makes $^{83\text{m}}\text{Kr}$ an ideal candidate for commissioning and calibration measurements [7].

At the KATRIN experiment, gaseous krypton can be injected into the source. The krypton decays and thus provides its monoenergetic conversion electrons. The spectrum of the conversion electrons is measured with the KATRIN detector. The data of the spectrum can be used to determine the line position and the line width of the krypton conversion. In the end, both values can be used to classify the potential inside the source. In simple words, they provide insight on the mean potential in longitudinal direction, as well as the mean deviation of the potential. The description of the deconvolution (of the line position and line broadening) towards information on the plasma potential exceed the context of this thesis. For more information, refer to the dedicated studies by Machatschek [54]. Nevertheless, two use cases will be presented here to provide an insight on the method.

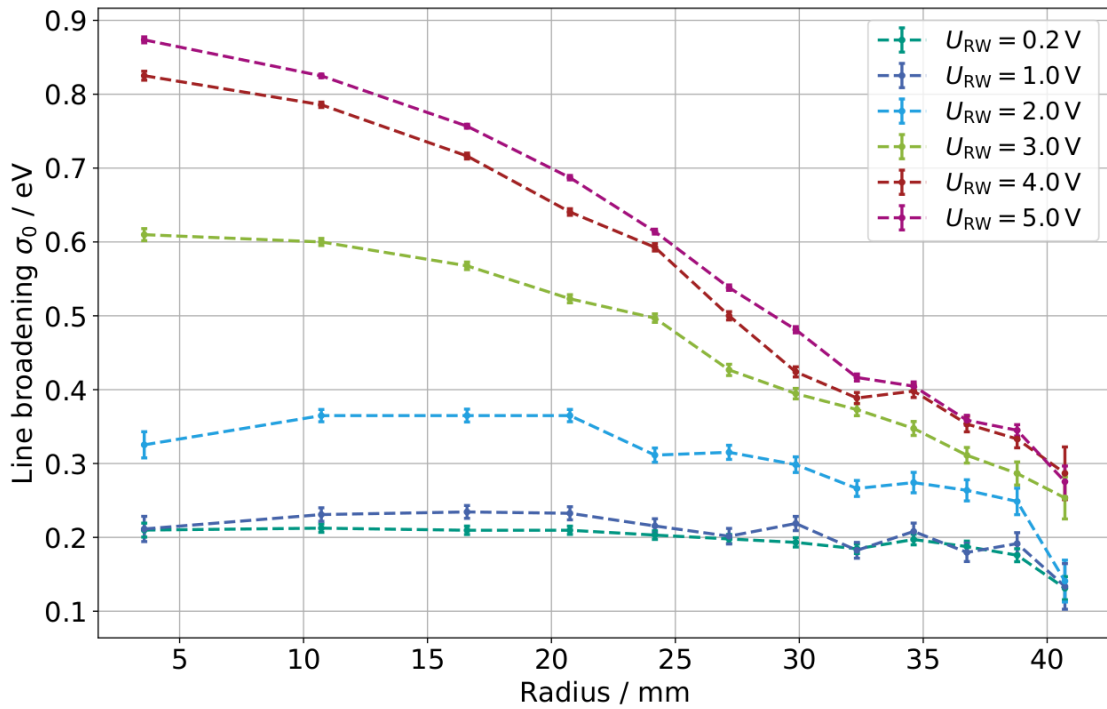


Figure 3.1.: Measured Krypton line width. Measurement of the line width for different rear wall potentials from the measurement campaign KNM2. Figure taken from [61].

The injection of krypton can be carried out with an empty source, but also with tritium inside the source. Thus, a comparison of the krypton line measurements can provide insights on the plasma properties. In 2019, a measurement of the krypton conversion lines K_{-32} , L_{3-32} and $N_{2,3-32}$ was performed in an empty source. Both, the line position and the line width of the conversion were determined with an unprecedented accuracy [7]. A similar measurement was performed later on with tritium background gas. Thus, a difference of the line position and line width can be directly attributed to the potential of the plasma inside the source. However, the explicit plasma potential distribution cannot be determined directly through these types of measurements, because of the unknown starting position of the measured electrons. Nevertheless, these measurements can provide limits on the influence of the plasma on the neutrino mass measurements.

The boundary conditions of the source can have a great influence on the plasma potential. It can be assumed that there exists a specific potential difference of the rear wall and the tube walls at which the plasma potential has the smallest effect on the neutrino mass measurement. The krypton line width can provide insights onto this specific set-value of the rear wall potential. However, this evaluation is time-consuming, and it would be beneficial to have a model of the plasma, where the potential inside the source can be determined directly from other measurement parameters. The krypton line measurements can be used for the test of such a model. For example, the line width can be determined experimentally in relation to the rear wall potential. An exemplary measurement is shown in figure 3.1. It can be seen that the line broadening is vastly influenced by the rear wall potential. This influence is different for different radii. If a model of the plasma can predict the change of the line width depending on the rear wall potential, then this would enforce the trust in such a model. In total, the krypton measurements can be used to constrain the plasma model.

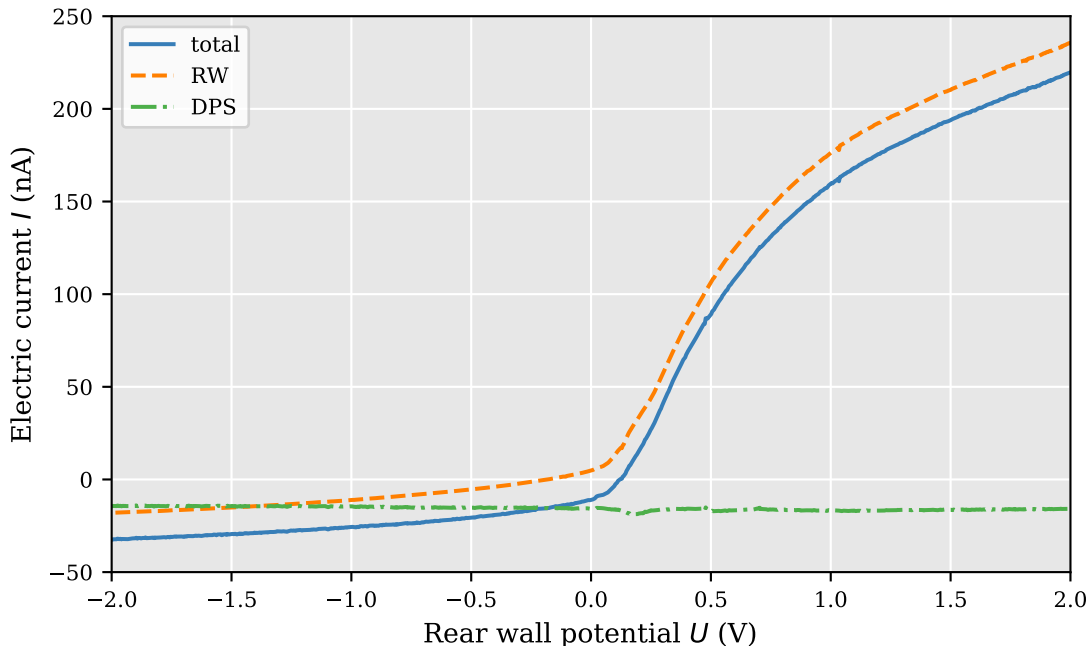


Figure 3.2.: Measured electric currents leaving the source. Data from the rear wall (RW) and from the dipole electrodes in the DPS. Total current is the sum of both measurement points. Data from [24].

3.2.2. Particle Current Measurements

The measurement of the electric current of particles leaving the source can provide a valuable insight on the plasma inside the source. It can either be used for monitoring the source or it can be used to probe the predictions of the different descriptions of the plasma.

The number of charged particles n inside the source can be described by the continuity equation

$$\frac{\partial n}{\partial t} + \nabla \mathbf{j} = k_c(n) - k_r(n), \quad (3.3)$$

where j is the particle current leaving the source, k_c the creation rate of new particles through ionization and beta decay, and k_r the recombination rate. Additionally, it can be assumed that the number of charged particles reaches a steady state after a sufficiently long time. Thus, the sum of all electrical currents I_i leaving the source is equal to zero

$$0 = \sum_i I_i. \quad (3.4)$$

The total current of particles leaving the source cannot be measured due to the intricate design of the apparatus. In general, it can be assumed that charged particles can leave the source either by collision with the tube walls, by collision with the rear wall, or by collision with the dipole electrodes of the DPS. The dominant channel is dependent on the type of particle. Ions can move in both directions of the source and can neutralize at the rear wall, as well as on the dipole electrodes, generating the currents I_{rw}^i and I_{dp}^i respectively. Whereas, electrons are reflected either by the potential of the dipole electrodes or at the potential of the spectrometers. Thus, they mostly neutralize at the rear wall (I_{rw}^e). The number of electrons leaving the apparatus at the detector can be neglected at this point, provided the small count rate at the detector. In conclusion, equation 3.4 can be written as

$$0 = I_{\text{rw}}^e + I_{\text{t}}^e + I_{\text{rw}}^i + I_{\text{dp}}^i + I_{\text{t}}^i, \quad (3.5)$$

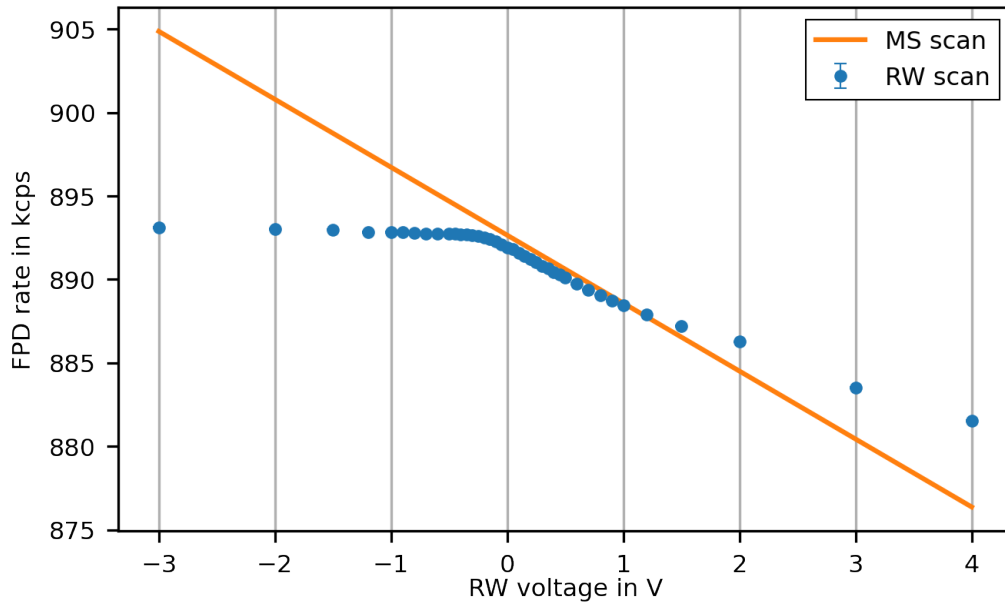


Figure 3.3.: Pro Katrin Measurement. Exemplary measurement data from the measurement campaign KNM2. The rate at the detector (FPD) is put into relation with the voltage applied to the rear wall (RW). The data from the change of the rear wall voltage (RW scan) is compared to the data from the change of the potential at the main spectrometer (MS scan). Figure from [24].

where I_t^e and I_t^i describe the electric current of electrons and ions respectively neutralizing at the tube walls. In a previous model of the plasma [50] it was assumed that the electrical current towards the tube walls can be neglected due to the large magnetic field inside the source. However, current measurements have shown that the sum of all measured currents is only zero for a specific rear wall voltage U_0 , see figure 3.2. Thus, the measurements have shown that the plasma models need to be adapted to also include an electric current towards the beam tube. Therefore, the measurement of currents provide a valuable insight to the plasma. For more information on these types of measurements refer to the work of Friedel [24]. Also, the influence of other source conditions like the dipole electric field strength, source temperature and neutral particle density are described there.

3.2.3. Pro-KATRIN Measurements

The measured electron flux at the detector depends, in first order, on the initial electron energy, the difference between the potential at the starting position in the source, and the potential at the analyzing plane in the main spectrometer. Thus, a measurement of the rate where the starting potential is increased would yield the same result as if the potential at the main spectrometer is lowered. This method allows for an investigation of the influence of external potentials on the potential inside the source, especially the rear wall potential. The method can also be used to find an optimal rear wall potential for the neutrino mass measurements. Thus, it is also called Plasma Rear wall Optimization at KATRIN, in short PRO KATRIN.

In the description of Kuckert [50], it is assumed that the potential inside the source is dominated by the potential at the rear wall. This assumption is based on a fluid description of the plasma. It is hypothesized that the strong magnetic field in the source causes a high conductivity in longitudinal direction and a low conductivity in radial direction. Thus, the potential of the rear wall would penetrate deep into the plasma. This hypothesis can be tested with the PRO KATRIN method. An exemplary measurement is shown in figure

3.3. Three different regions can be identified there. The first region is the potential range -0.2 V to 0.5 V . Here, a change in the rear wall potential results in the same shift as a change in the main spectrometer potential. The second range comprises all rear wall potential values below -0.2 V . Here, the rear wall potential has a negligible effect on the rate at the detector. The third region contains all rear wall potential values above 0.5 V . Here, a change in the rear wall potential has less effect than the change in the main spectrometer potential, but is not negligible. At the KATRIN experiment, these three ranges are also called maximally-coupled region, decoupled region and partly-coupled region. From the measurements it can be concluded that there indeed is a region, where the potential inside the source is dominated by the rear wall potential as hypothesized by Kuckert. Nevertheless, there exist also rear wall potential values, where this assumption does not hold true. Optimally, a full description of the plasma will also include these values as well. Thus, a measurement with the PRO KATRIN method allows for testing of plasma models.

The PRO KATRIN method can also be used to investigate the stability of the source. The potential values at which there is a transition between the regions depends on the specific conditions inside the source. A change in the plasma conditions will also result in a change in the transition value. For more information on the PRO KATRIN method, refer to the work of Friedel [24]. There, the method is described in detail, including additional investigation of the regions depending on the radius inside the source. These results can provide valuable insights into the plasma and its radial potential distribution in conjunction with the krypton measurements.

3.3. Characteristic Length Scales

The experimental investigations show that a suitable plasma model cannot be found by measurements only, but they provide constraints on the model itself. Thus, additional theoretical considerations must be employed. One way to distinguish between different models are characteristic length scales, described in the following. Further information can be gained by characteristic frequencies, see section 3.4.

Characteristic length scales of plasma mostly rely on the consideration of interactions between charged particles, neutral particles, and electromagnetic fields. In this section, first, the most dominant effect in plasmas, Debye shielding, will be described. The Debye length can be used to determine if there exists a collective behavior of the charged particles. Secondly, the Landau length will be discussed, which provides an insight into spontaneous recombination processes. The discussion is followed by a description of the mean free path. This parameter will provide an overview of the dominant processes apart from electromagnetic interactions. After that, the gyroradius will be brought into focus, followed by a description of the inertial length. The inertial length can be used to give a limit on boundary effects. The section will be concluded by a comparison of the parameters presented before. This comparison then allows for a first classification of the plasma at KATRIN.

Most of the presented parameters depend on the velocity and density distribution of electrons and ions in the source. For simplicity, it is assumed that the velocity distribution of the electrons follows the Maxwell-Boltzmann distribution with temperature $T = 80\text{ K}$, due to elastic collisions with the neutral gas. The electron density is not constant in the source. The precise evaluation of the electron density and its position dependence is only accessible through simulations. Initial simulations with KARL show that the electron density ranges approximately from 10^3 cm^{-3} to 10^6 cm^{-3} , see chapter 4. Thus, the parameters below are evaluated and presented for these boundary values. Additionally, they are also depicted over the whole density range in figures 3.6. The density of the ions is assumed to be the same as the electron density, following the postulation of quasineutrality.

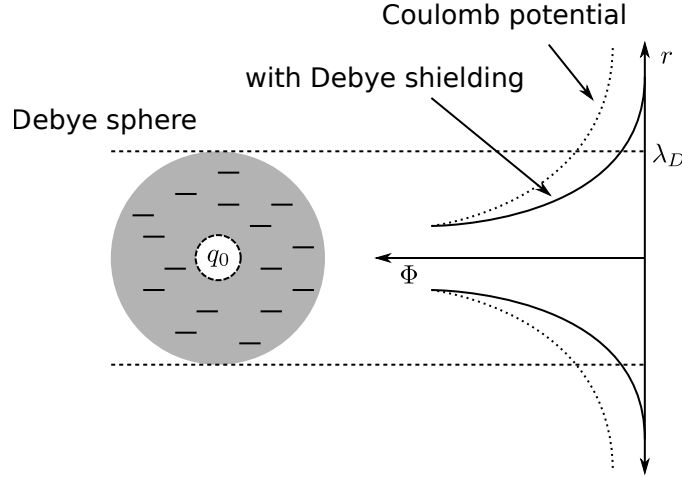


Figure 3.4.: Debye Shielding A single charge q_0 will be surrounded by other charges forming the Debye sphere. The electric potential Φ of this charge will be reduced from the infinite range of the Coulomb potential to a finite length in the order of the Debye length λ_D . Figure adapted from [78].

3.3.1. Debye Length

The Debye length λ_D describes the length of the screening effect of plasma, where the electric field of a single charged particle is attenuated by the presence of other charged particles. Consider a positive ion in free space. The electric field of the ion follows the Coulomb's r^{-2} law. Thus, the potential shows a r^{-1} dependency. The interaction strength has therefore an infinite range. Consider the same ion in a cloud of electrons and other ions. The ion will attract electrons and repel other ions, such that the electric field of the ion is reduced to a bare minimum at a certain distance. This distance is called Debye length. A graphical representation of this behavior plus the potential of a free charge can be seen in figure 3.4.

The electric potential for a Debye sphere can be calculated from Poisson's equation

$$\nabla\phi = \frac{1}{r^2} \frac{d}{dr} r^2 \frac{d\phi}{dr} = -4\pi e(n_e - Zn_i), \quad (3.6)$$

where n_e and n_i describe the density of electrons and ions respectively. Electrons and ions are assumed to follow the Boltzmann statistics. Thus, their density can be described through

$$n_i = n_{i,0} \exp\left(-\frac{Ze\phi}{k_b T}\right) \quad (3.7)$$

$$n_e = n_{e,0} \exp\left(\frac{e\phi}{k_b T}\right), \quad (3.8)$$

with the temperature T and Boltzmann's constant k_b . Assuming quasi-neutrality, and that the electric potential is much smaller than the thermal energy of the particles ($e\phi \ll k_b T$) Equation 3.6 can then be rearranged to

$$\frac{1}{r^2} \frac{d}{dr} r^2 \frac{d\phi}{dr} = 4\pi e^2 n_{e,0} \frac{1+Z}{k_b T} \phi. \quad (3.9)$$

This differential equation is solved by the ansatz

$$\phi(r) = \frac{1}{r} \exp\left(-\frac{r}{\lambda_D}\right). \quad (3.10)$$

Thus, the Debye length λ_D can be calculated by

$$\lambda_D = \sqrt{\frac{k_b T}{4\pi e^2 n_{e,0}(Z+1)}}. \quad (3.11)$$

Equation 3.10 shows that the potential drops to a fraction of e^{-1} of its initial value at the radius $r = \lambda_D$. Thus, the presence of other charged particles reduces the influence of the electric field of a single particle. The Debye length can therefore provide a limit on the length at which single particle effects play a role in a cloud of charged particles. For lengths smaller than the Debye length, direct particle interactions have to be considered, while for lengths greater than the Debye length, the collective behavior of the plasma takes over.

In section 3.1, it was stated that charged particles can be considered as plasma if there exists a collective behavior of the charged particles. Thus, the Debye length can be used in conjunction with the mean distance between charged particles a to determine if the particles have to be treated as a plasma. Collective behavior is to be assumed when

$$a < \lambda_D. \quad (3.12)$$

The same result can be obtained by requesting that there must be enough charge carriers in the near vicinity to justify a continuous description of the particles. This relation can be written as

$$\Lambda := \frac{4\pi}{3} \lambda_D^3 n_e \gg 1, \quad (3.13)$$

where Λ is called the plasma parameter. It is equivalent to equation 3.12 when identifying the mean distance between charged particles with the inverse cubic root of the particle density $n_e^{-1/3} = a$.

Debye length at the KATRIN experiment: The approximate electron density range of 10^3 cm^{-3} to 10^6 cm^{-3} and thermal temperature of $T = 80 \text{ K}$ results in a Debye length of 1.9 cm and 0.06 cm respectively. The Debye length is depicted for the whole density range in figure 3.6 in comparison with other characteristic length scales, such as the mean distance between charged particles. From the figure, it is apparent that the plasma condition of equation 3.12 is fulfilled for all possible electron densities within the KATRIN source. Thus, the charged particles in the source will show a collective behavior. The relative factor between the Debye length and the mean distance of particles is small in comparison to other plasmas [14]. Thus, the plasma at the KATRIN experiment can be described as a plasma with a low density.

3.3.2. Landau Length

The Landau length l_L describes the distance at which the electrostatic energy of two charged particles is equal to the kinetic thermal energy of these particles. The Landau length can therefore be calculated by [14]

$$l_L = \frac{e^2 Z}{k_b T}. \quad (3.14)$$

The mean distance between particles a must be greater than the Landau length ($a > l_L$) to ensure that the majority of ions and electrons have enough thermal energy not to recombine spontaneously in consequence of the Coulomb force [14]. Naturally, this does not mean that no recombinations take place, but that recombinations are not the dominant process destroying the plasma state.

Landau length at the KATRIN experiment: The Landau length is only dependent on the temperature of the electrons, which was assumed to be $T = 80 \text{ K}$. Thus, the

Table 3.1.: Mean free path. Approximate values of the mean free path for densities similar to the densities at the rear wall and the center of the source.

		Rear wall	Center
n_e	(cm^{-3})	10^3	10^6
n_{T2}	(cm^{-3})	10^{12}	10^{15}
$\lambda(e^- - T_2)$	(cm)	1600	1.6
$\lambda(T_3^+ - T_2)$	(cm)	17	0.017
$\lambda(e^- - e^-)$	(cm)	7.9×10^4	95

Landau length at the experiment is 1.8×10^{-9} cm. The Landau length is also depicted in figure 3.6. From the figure, it is apparent that the Landau length is much smaller than the mean distance between charged particles. Thus, it can be assumed that the entirety of the charged particles will not recombine spontaneously. However, recombination and dissociation processes can occur for single particles by direct interactions, see section 2.4.2. Additionally, the Landau length is much smaller than the Debye length. This implies that direct charged particle collisions play a secondary role for thermal charged particles in the source [14].

3.3.3. Mean Free Path

The mean free path λ_{mfp} describes the distance a particle will statistically move between two collisions. It can be derived from the probability that a particle interacts within a certain distance while flying through a particle cloud, see equation 2.6. In the end, the probability that a particle can be detected after a distance x reads as

$$\mathcal{P}(x) = e^{-x/\lambda_{\text{mfp}}}. \quad (3.15)$$

Thus, the mean free path describes the point at which this probability is decreased to a value of e^{-1} of its initial value. This distance can be directly calculated from the number density of the traversed particle cloud n and the total cross section of the interaction σ through

$$\lambda_{\text{mfp}} = \frac{1}{\sigma n}. \quad (3.16)$$

Limitations of the mean free path: The mean free path can only be calculated if the total cross section can be assigned a finite value. The cross section is in general dependent on the energy and the scattering angle. Thus, to obtain the total cross section of an interaction, an integral over all possible scattering angles has to be performed. This integral diverges for the Coulomb interaction between two free moving charged particles, because of the infinite range of the electromagnetic force. Therefore, it would not be possible to determine the mean free path for the collision of electrons with electrons. The electromagnetic force in a plasma is limited due to the Debye shielding. Thus, the integral can be performed for particles in a plasma. Assuming that the particle energy is equal to the Boltzmann energy $E = k_b T$ the cross section can be approximated to

$$\sigma \approx \frac{4\pi e^4 Z^2}{k_b^2 T^2} \ln \left(\frac{\lambda_D}{l_L} \right). \quad (3.17)$$

Refer to the work of Cap [14] for a full description of the derivation. This cross section has to be adapted for each interaction between different particle types, electron-electron, electron-ion, ion-ion.

Mean free path at the KATRIN experiment: The mean free path is dependent on the energy of the interacting particles through the energy dependence of the cross section. The cross section decreases in most cases with increasing energy. The mean free path of thermal energies can therefore be used as a lower limit, as the thermal energy is the lowest energy of the system.

The electron density is not constant in the source ($n_e \approx 10^3 \text{ cm}^{-3}$ to 10^6 cm^{-3}). The neutral particle density also varies over the length of the source from 10^{12} cm^{-3} at the rear wall to $1 \times 10^{15} \text{ cm}^{-3}$ in the center of the source, see section 2.1.1. Thus, the mean free path will show significantly different values depending on the position in the source. The position at the rear wall and in the center of the source will be used in the following to provide upper and lower limits on the mean free path. The corresponding values can be found in table 3.1. These values are also depicted in figure 3.6 alongside other characteristic length scales.

The calculated values of the mean free path allow for the following conclusions:

- The mean free path of ions in the center is much smaller than the diameter $D = 9 \text{ cm}$ and length $L = 1300 \text{ cm}$ of the source tube. It can therefore be assumed that ions will have many interactions before coming in contact with the tube walls. Thus, the ions in the center will show a similar velocity distribution as the neutral gas, see section 2.1.
- The mean free path of ions at the rear wall is comparable to the diameter of the source. Hence, the velocity distribution of the ions can deviate from the velocity distribution of the neutral gas.
- The mean free path of electrons in the center is smaller than the dimensions of the source tube. Hence, the electron velocity distribution will show some characteristics of the velocity distribution of the neutral particles. Nevertheless, the Debye length and mean distance between particles is smaller than the mean free path of the electrons. Hence, plasma effects will play a vital role in the description of the electron movement. The difference of the mean free path and the Debye length is comparably small. Consequently, a description of the plasma in the central region of the WGTS has to include scattering as well.
- The mean free path of electrons at the rear wall is greater than the geometric details of the source. Hence, electron interactions with neutrals can be neglected here.
- The mean free path of electron-electron Coulomb interactions is comparably high to the mean free paths of other particle interactions and to the Debye length. Hence, direct interactions between electrons and electrons play a secondary role. A fluid description of the electrons is therefore not justified, see section 3.5 for more information on the different plasma models.

3.3.4. Gyroradius and Classical Diffusion

The magnetic field of the KATRIN source is very strong ($B = 2.5 \text{ T}$). Thus, the movement of charged particles is heavily influenced by this field. Charged particles perform a radial movement around the magnetic field lines. The radius of this motion is given by the Larmor radius r_L , also named gyroradius. It is calculated by

$$r_L = \frac{mv_{\perp}c}{eB}, \quad (3.18)$$

where v_{\perp} is the velocity perpendicular to the direction of the magnetic field, m the mass of the charged particle and B the magnetic field strength. The perpendicular velocity can be

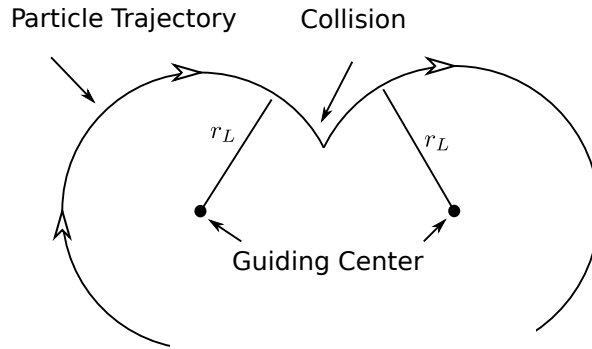


Figure 3.5.: Classical diffusion. The particle is gyrating around the guiding center until collision. The guiding center after collision can be different from the guiding center before collision. Thus, particles can diffuse across magnetic field lines. Figure adapted from [18].

expressed in terms of the temperature T in case of thermal movement of charged particles. Thus, the gyro radius can be calculated as

$$r_L \approx \frac{c}{eB} \sqrt{\frac{8k_b T m}{\pi}}. \quad (3.19)$$

Gyroradius at the KATRIN experiment: The energy of the electrons in the source ranges from the thermal energy $\mathcal{O}(1 \text{ meV})$ to the beta decay energy $\mathcal{O}(10 \text{ keV})$. Thus, also the minimum and maximum value of the electron gyroradius can deviate by a factor of approximately 3000. However, it could be shown that the majority of the electrons have thermal energies, see chapter 4. Therefore, only the gyroradius of thermal electrons is evaluated in the following, providing a minimum on the electron gyroradius. For the ions, it is assumed that they show thermal velocities because of frequent collisions with neutral gas, see section 2.4.3. Hence, the ion gyroradius is only evaluated for thermal ions.

The gyroradius of thermal particles is only dependent on the temperature of the particles and the magnetic field strength, which were assumed as $T = 80 \text{ K}$ and $B = 2.5 \text{ T}$ respectively. Therefore, the gyroradius is approximately $7.9 \times 10^{-6} \text{ cm}$ and $1.0 \times 10^{-3} \text{ cm}$ for electrons and ions respectively. The gyroradius of both species is depicted likewise in figure 3.6.

The electron gyroradius is much smaller than the ion gyroradius. This is expected due to the large mass difference. The gyroradius for both electrons and ions is smaller than any other characteristic length, except the Landau length. Hence, the magnetic field will play a vital role in the description of the plasma.

Electrons and ions which are created close to the beam tube wall can be diverted by the magnetic field, so that these particles hit the wall in one gyro motion. This effect plays only a very minor role, as both ion and electron gyroradius are much smaller than the diameter of the WGTS.

Electrons and ions can collide with neutral gas during the gyro motion. If this collision has a large scattering angle, the center of gyration will be shifted to another position, also seen in figure 3.5. Thus, the particle can traverse in radial direction. This motion can be described by the classical diffusion coefficient D . It can be approximated by [78]

$$D \approx \nu r_L^2, \quad (3.20)$$

where ν is the collision frequency. This diffusion coefficient is much smaller for electrons than for ions due to the significant difference in the gyroradius. It can therefore be assumed that diffusion due to collisions can be relevant for ions, but not for electrons. This assumption has to be tested in a thorough simulation, see also section 4.3.4.3.

3.3.5. Inertial Length

The inertial length of electrons describes the depth to which an external light wave can penetrate into plasma. For this reason, it is also called skin depth. The inertial length is calculated from the dispersion relation of a so-called Langmuir or plasma mode. This mode is generated by charge density differences in the plasma. For more information on the plasma mode refer to section 3.4.1. Light waves will traverse the plasma undisturbed if the frequency of the incoming wave is much greater than the plasma frequency. In that case, electrons cannot follow the change of electric field due to their inertia. If the frequency of the incoming wave is smaller than the plasma frequency, the electrons will cancel out the displacement current. The wave cannot penetrate the plasma in this case and becomes evanescent [78]. The penetration depth of the wave is given by the electron inertial length and is calculated by

$$l_{\text{skin}} = \frac{c}{\omega_{\text{pe}}}, \quad (3.21)$$

where ω_{pe} is the electron plasma frequency. The plasma frequency is proportional to the square root of the electron density, see equation 3.23. Thus, the skin depth is proportional to the inverse square root of the electron density.

Inertial length at the KATRIN experiment: The approximate electron density range of 10^3 cm^{-3} to 10^6 cm^{-3} results in an inertial length of $1.7 \times 10^4 \text{ cm}$ and 530 cm respectively. The inertial length is also depicted in figure 3.6. It can be seen that the skin depth is one of the largest length scale of the plasma. It is much greater than the diameter of the WGTS and only slightly smaller than the length of the source tube. Hence, it can be assumed that boundary effects will play a vital role in the description of the plasma. Nevertheless, there is a strong magnetic field in the KATRIN source, whereas the in derivation of the skin depth a non magnetized plasma was assumed. Therefore, the skin depth can only be used for a rough approximation of boundary effects, but a more precise evaluation must be obtained by simulation.

3.3.6. Summary

In the previous sections the Debye length, the Landau length, the mean free path, the gyroradius and the inertial length were discussed. Each parameter was described individually and key differences between the parameters were provided. In this section, the focus lies on the overall conclusion of all the parameters, especially for the description of the plasma at KATRIN. The parameters are depicted in figure 3.6 in dependence to the electron density due to the a priori unknown density distribution of the electrons inside the source.

Single particle vs Collective behavior: First, the focus lies on the distinction if the charged particles in the source have to be treated as single particles or if they show a collective behavior and thus have to be treated as plasma. The following conclusions can be made from the characteristic length scales:

- $\lambda_D > a; \Lambda > 1$: The particles in the source show a collective behavior.
- $L > \lambda_D; D > \lambda_D$: The collective behavior of the particles is dominant within the source. A treatment of the particles as plasma is necessary. Single particle treatment has to be employed at scales below λ_D
- $a > l_L$: Electrons and ions will not recombine through thermal motion.

Hence, it can be concluded that the particles in the source have to be treated as plasma.

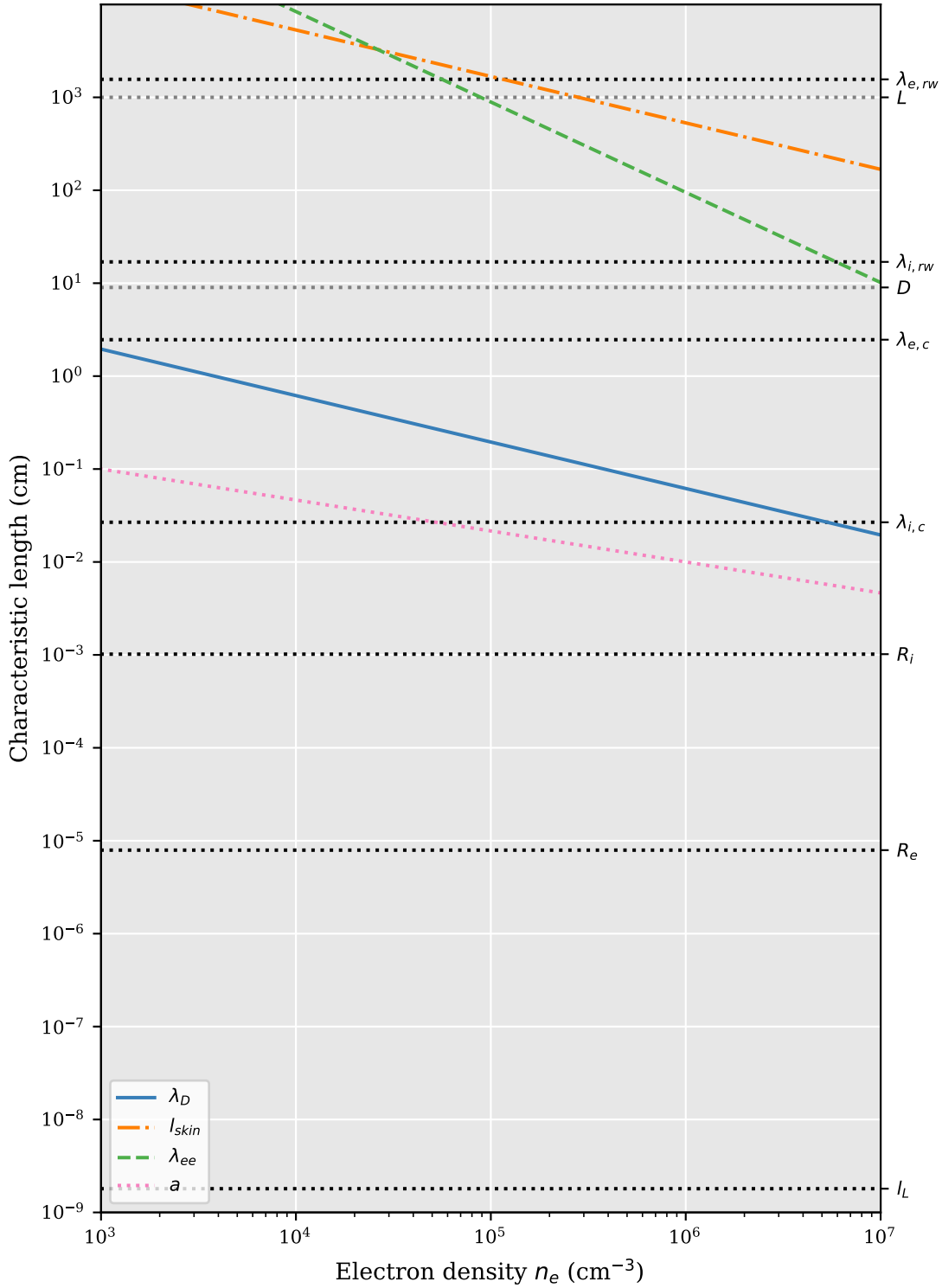


Figure 3.6.: Characteristic length scales. λ_D : Debye length, a : mean distance between electrons, L : length of the source, D : diameter of the source, l_{skin} : inetrrial length, $\lambda_{e,rw}/\lambda_{i,rw}$: mean free path of electrons/ions in front of the rear wall, $\lambda_{e,c}/\lambda_{i,c}$: mean free path of electrons/ions in the center of the source, λ_{ee} : mean free path of electrons due to Coulomb interactions. R_e/R_i : gyroradius of thermal electrons and ions. Neutral density: in front of rear wall $1 \times 10^{12} \text{ cm}^{-3}$, in center $6.3 \times 10^{14} \text{ cm}^{-3}$. Magnetic field: $B = 2.5 \text{ T}$. Temperature: $T = 80 \text{ K}$.

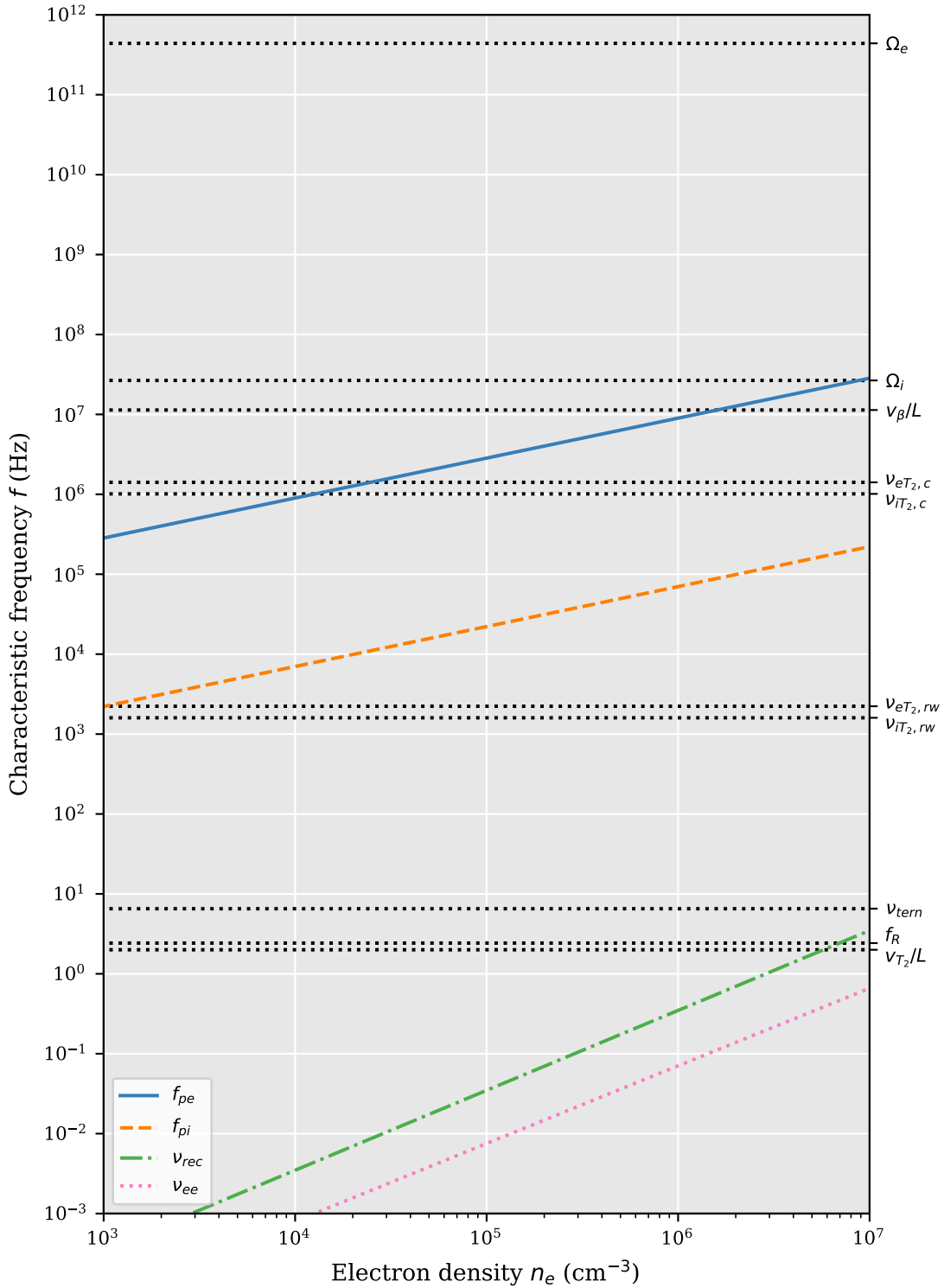


Figure 3.7.: Characteristic frequencies. f_{pe} : electron plasma frequency, f_{pi} : ion plasma frequency assuming the same ion density as electron density, ν_{rec} : collision rate of recombination, ν_{ee} : Coulomb collision rate, Ω_e : electron gyro frequency, Ω_i : ion gyro frequency, $\nu_{e,rw}/\nu_{i,rw}$: elastic collision frequency of electrons/ions in front of the rear wall, $\nu_{e,c}/\nu_{i,c}$: elastic collision frequency of electrons/ions in the center of the source, f_R : synchrotron loss frequency, ν_{tern} : ternary association rate, ν_{T_2}/L : mean inverse time of neutrals in the source, ν_β/L : mean inverse time of betas in the source. Neutral density: in front of rear wall $1 \times 10^{12} \text{ cm}^{-3}$, in center $6.3 \times 10^{14} \text{ cm}^{-3}$. Magnetic field: $B = 2.5 \text{ T}$. Temperature: $T = 80 \text{ K}$.

Plasma models: There exist many models describing plasma, see section 3.5. The choice of the model is dependent on the characteristic length scales. A suitable model can be found with the following conditions:

- $R_e \ll L, D; R_i \ll L, D; R_e \ll \lambda_D$: Electron and ion motion is dominated by the magnetic field. Thus, the plasma is strongly magnetized.
- $\lambda_{e,c} > \lambda_D$: Collisions of electrons with neutral gas play a secondary role in the center of the WGTS. Nevertheless, they have to be considered because of the small the difference of the two parameters, meaning the plasma in the center is partly collisional.
- $\lambda_{e,rw} \gg \lambda_D$: Collisions of electrons with neutral particles are negligible close to the rear wall. Thus, the plasma is collisionless in this area.
- $\lambda_{ee} \gg \lambda_D$: Electron-electron collisions are very infrequent. The electrons cannot be treated as a fluid.
- $\lambda_{i,c} < \lambda_D$: Ions interact very often with the neutral gas in the center of the WGTS. Their movement is dominated by collision.
- $\lambda_{i,rw} \gg \lambda_D$: Ions will seldom interact with neutral gas close to the rear wall. Their movement is dominated by plasma effects.

From this compilation, it can be concluded that the plasma model for KATRIN needs to treat the plasma as strongly magnetized, low density, partly collisional, bound, multi species, partially ionized with thermal and non-thermal components of low but finite temperature.

3.4. Characteristic Frequencies

The characteristic frequencies of a plasma mostly rely on the consideration of the interactions between the charged particles, neutral particles, and electromagnetic fields. The frequencies can provide an insight whether an effect has to be included in the description of the plasma, or if it can be neglected.

In this section, first the plasma frequency will be described. It provides a natural time scale at which plasma effects play a role. Secondly, the gyro frequency will be discussed, which provides an insight into synchrotron radiation processes. The discussion is followed by a description of the collision rate. This parameter will provide an overview of the dominant processes. The section will be concluded by a comparison of the parameters presented before.

3.4.1. Plasma Frequency

The plasma frequency ω_p describes the density oscillation of electrons and ions, where the quasineutrality has been perturbed. It can be derived for cold plasmas with no magnetic field, see also [14], and calculates to

$$\omega_p^2 = \omega_{pe}^2 + \omega_{pi}^2 \quad (3.22)$$

$$\omega_{pe} = \sqrt{\frac{4\pi n_e e^2}{m_e}} \quad (3.23)$$

$$\omega_{pi} = \sqrt{\frac{4\pi n_i Z^2 e^2}{m_i}}, \quad (3.24)$$

where n_e , n_i , m_e and m_i are the electron and ion density and mass respectively. ω_{pe} describes the oscillation of electrons and ω_{pi} describe the oscillation of ions. In general, it

can be assumed that the ion and electron density is equal. Thus, the plasma frequency of the electrons ω_{pe} is much higher than the plasma frequency of the ions ω_{pi} due to the large mass difference. Hence, the total plasma frequency is dominated by ω_{pe} .

The plasma frequency provides a limit on the frequency of light waves which can traverse the plasma. Waves with frequencies below the plasma frequency become evanescent, while waves with frequencies much greater than the plasma frequency can traverse the plasma undisturbed. Additionally, the plasma frequency can be used as a natural time scale of plasma effects which relate to electron motion.

Plasma Frequency at the KATRIN experiment: The approximate electron density range of 10^3 cm^{-3} to 10^6 cm^{-3} results in an electron plasma frequency of $1.9 \times 10^6 \text{ rad/s}$ and $6.0 \times 10^7 \text{ rad/s}$ respectively. Assuming the same density for the ions, the plasma frequency of ions has values of $1.5 \times 10^4 \text{ rad/s}$ and $4.7 \times 10^5 \text{ rad/s}$ respectively. The angular plasma frequency of each species is depicted in figure 3.7 in comparison with other characteristic frequencies.

It can be seen that the plasma frequency is not larger than the gyro frequency of the system. This is noteworthy because the plasma frequency, in almost all standard types of plasmas, is the highest frequency [14]. Only gas discharges show a similar behavior. However, a comparison of the KATRIN plasma and gas discharges is not gainful because the charged particle density and the temperature is much smaller at the KATRIN experiment. Thus, both plasmas will behave differently.

3.4.2. Gyro Frequency and Synchrotron radiation

While the gyroradius describes the radius at which charged particles move around the guiding center, the non-relativistic gyro frequency describes the radial frequency of this movement. It is calculated by

$$\Omega = \frac{eB}{mc}, \quad (3.25)$$

where m is the mass of the particle and B the magnetic field strength. Thus, the gyro frequency is different for electrons and ions because of their different masses.

The strong magnetic field at the KATRIN source forces the particles to gyrate with a very high frequency. It is therefore necessary to investigate the energy loss due to synchrotron radiation. The non-relativistic characteristic frequency f_R at which the kinetic energy of a particle is reduced to a factor e^{-1} of its original value is given by [80]

$$f_R = \frac{4e^2\Omega^2}{3mc^3} = \frac{4e^4B^2}{3m^3c^4}. \quad (3.26)$$

It is apparent that f_R decreases with the mass, and is accordingly much higher for electrons than for ions.

Gyro Frequency and Synchrotron Loss at the KATRIN experiment: Both the gyro frequency and the synchrotron loss frequency are independent of the charged particle density in the source, but solely depend on the magnetic field strength in the source. The magnetic field in the source is 2.5 T. Thus, the gyro frequency of electrons and ions is $4.4 \times 10^{11} \text{ rad/s}$ and $2.7 \times 10^7 \text{ rad/s}$ respectively. Both frequencies are high in comparison to all other frequencies in the system, see figure 3.7. This means that the particles will perform many gyrations before all other interactions.

The synchrotron loss frequency for electrons is 2.4 Hz. It is small in comparison to the collision frequencies in the system. Thus, many interactions will have taken place in between the radiation. Hence, these losses do not play a vital role in the description of the

plasma. Nevertheless, they will be modeled in the kinetic simulations presented in chapter 5. Radiation losses have to be taken into account for the neutrino mass measurement, where small energy losses have also to be taken into account. The synchrotron loss frequency of ions is well below any other frequency and is therefore not further mentioned here.

3.4.3. Collision Rate

The collision rate ν , also named collision frequency, describes the mean time between two collisions of a particle in a cloud of other particles. It can be directly derived from the mean velocity of a particle \bar{v} and the mean free path λ

$$\nu = \frac{\bar{v}}{\lambda} = \bar{v}\sigma n. \quad (3.27)$$

The mean velocity of a thermal particle is calculated from the standard Boltzmann statistics.

Collision Frequency at the KATRIN experiment: The collision frequency is dependent on the density and the energy of the particles. Due to the extreme amount of parameters, only the collision rate of the elastic scattering with neutral gas, recombination and Coulomb interactions of electrons will be presented here. In contrast to the mean free path, the collision rate increases directly with the velocity of the incoming particle. Here, only thermal velocities of ions and electrons are used to reduce the number of parameters.

The electron density is not constant in the source ($n_e \approx 10^3 \text{ cm}^{-3}$ to 10^6 cm^{-3}). The neutral particle density also varies over the length of the source from 10^{12} cm^{-3} at the rear wall to $1 \times 10^{15} \text{ cm}^{-3}$ in the center of the source, see section 2.1.1. Thus, the collision frequency will show significantly different values depending on the position in the source. The position at the rear wall and in the center of the source will be used in the following to provide upper and lower limits on the collision frequency. The corresponding values are depicted in figure 3.6 alongside other characteristic time scales.

The collision frequency of elastic scattering with neutral gas in the center of the source is approximately 10^6 Hz , see figure 3.7. This value is similar for electrons and ions, despite the large difference of the cross section. This is caused by the large velocity difference between the two species. It can be observed that the elastic collision frequency is below the plasma frequency. Nevertheless, it cannot be concluded from this fact that collisions do not have an influence on the development of plasma modes. The interplay of collisions, electromagnetic fields and particle motion is too extensive for this conclusion.

The collision frequency of elastic scattering with neutral gas in front of the rear wall is approximately 10^3 Hz , see figure 3.7. Again, this value is similar for electrons and ions. The elastic collision frequency does not provide any more insight, despite that it is higher than the synchrotron loss frequency. Hence, synchrotron losses do not play a role in the description of the plasma in this low neutral density section of the source.

The elastic collision rate is lower than the gyro frequency of the corresponding species. Therefore, the particles will perform multiple gyro motions until they interact through collision. The collision rate is at least three orders of magnitude greater than the collision rate of Coulomb interaction and recombination. Thus, elastic scattering is the dominant effect over the others.

3.4.4. Summary

In the previous sections the plasma frequency, the gyro frequency, the synchrotron losses, and the collision rate were discussed. Each parameter was described individually and key differences to the other parameters were provided. In this section, the focus lies on

the overall conclusion of all parameters. The parameters are depicted in figure 3.7 in dependence to the electron density due to the a priori unknown density distribution of the electrons inside the source.

In contrast to the length scales, the time scales cannot be used directly to determine if the particles have to be treated as a plasma. Nevertheless, the time scales can provide an insight into the characteristics of the plasma.

- $\nu_{eT_2} \gg \nu_{ee}$: Direct electron interactions play only a secondary role. A diffusion ansatz is not viable here.
- $\nu_{eT_2} \gg \nu_{\text{rec}}$: Recombination is only a secondary effect in the source.
- $f_R \ll \nu_{eT_2}$: Cyclotron radiation can be neglected for the description of electrons in the source. This is also true for ions.

The survey of the time scales can provide a limit on relevant effects which influence the plasma through their temporal evolution. These effects have to have frequencies which are similar to the frequency of the influenced particle. For example, if the temperature of the beam tube would change at a frequency of 1 Hz, it would not influence the plasma by its temporal evolution but through its value. In this case, the temperature can be assumed to be constant for all plasma related effects.

3.5. Plasma Models

In general, it is not possible to solve all equations of movement directly for all particles in a plasma, because of the large number of particles and the unknown starting conditions. Additionally, if the density of particles is large enough, direct particle interactions will need to be taken into account. Thus, statistical methods need to be employed [14].

In general, the evolution of a plasma system (and all its particles) can be described by the Liouville distribution function together with the Liouville equation, which follows from Liouville's theorem. In this ansatz, each single distinguishable particle is described in relation to all other particles. The interested reader is referred to [14] for an in depth description. However, solving the Liouville equation is impractical due to the vast amount of necessary parameters [38]. Thus, it is beneficial to relinquish the distinctness of the particles and to define the reduced Boltzmann distribution function $f_i(\mathbf{x}, \mathbf{v}, t)$ for the particle species i , with the position \mathbf{x} and velocity \mathbf{v} . In practical terms, it describes the probability dN to find a particle in the volume element d^3x around the position \mathbf{x} , and in the velocity interval d^3v around the velocity \mathbf{v} through [78]

$$dN_i = f_i(\mathbf{x}, \mathbf{v})d^3x d^3v. \quad (3.28)$$

The temporal evolution of f_i can be described by the Boltzmann equation, written as

$$\frac{\partial f_i}{\partial t} + \frac{\mathbf{p}_i}{m_i} \cdot \nabla f_i + \mathbf{F} \cdot \frac{\partial f_i}{\partial \mathbf{p}_i} = \left(\frac{\partial f_i}{\partial t} \right)_{\text{coll}}, \quad (3.29)$$

with the momentum \mathbf{p}_i , mass m_i and the force \mathbf{F} acting on the particles. Direct collisions between the particle species are moderated by the collision term at the right-hand side. Its form depends on the specific assumptions about collisions in the system. Assuming only two-body collisions, with short interaction range of two plasma particles with no prior correlation and forces between particles, which only depend on the distance between the particles, and external forces, which can be neglected during the collision process [14], the collision term can be written as the Boltzmann collision integral

$$\left(\frac{\partial f}{\partial t} \right)_{\text{coll}} = \sum_{j=1}^n \iint g_{ij} I_{ij}(g_{ij}, \Omega) [f'_i f'_j - f_i f_j] d\Omega d^3\mathbf{p}' \quad (3.30)$$

with distribution functions f before the collision and f' after the collision, g_{ij} the magnitude of the relative momenta for the two interacting particles, $I_{ij}(g_{ij}, \Omega)$ the differential cross section and Ω the solid angle [51].

Boltzmann equation at the KATRIN experiment: The force \mathbf{F} , in equation 3.29, comprises all forces acting on the particles. In the case of the KATRIN plasma, gravitational forces can be neglected, and the force is given by the Coulomb force $\mathbf{F}_c(E, B)$. The magnetic and electric fields are determined by the particle motion through Maxwell's equations. Thus, the field in the source can be determined by solving the Boltzmann equation in conjunction with Maxwell's equations.

As mentioned before, the solution of the Boltzmann equation depends on the specific assumption for the plasma particles, especially their behavior in collisions. The KATRIN plasma has the peculiar property that electron interactions are frequent enough that they cannot be neglected, but collisions are too infrequent that the plasma cannot be described through a diffusion ansatz, see section 3.3. Additionally, the collision properties vary over the length of the beam tube, as does the density of the neutral particles.

In a previous attempt to calculate the potential in the source by Kuckert [50], it was assumed that collisions with the neutral gas are so frequent that electrons and ions can be treated as a diffusive fluid for the central part of the source. The underlying model is shown with a short insight into the results in section 3.5.1.

The approach of Kuckert overestimated the collisions of the electrons in the center of the source, but it is not valid in the region close to the rear wall. There is no conclusive theory available, if the description of the plasma in the central region can be decoupled from the description of the plasma close to the rear wall. Thus, in the context of this thesis, a new approach is developed where the electrons are treated partly collisional and partly non-collisional over the whole length of the beam tube. The resulting model and simulation strategy is shown in section 3.5.2

3.5.1. Drift-Diffusion Model

In a previous work, Kuckert [50] assumed that electrons and ions in the source can be described as a diffusive fluid, and that the velocity distributions of electrons and ions follow the Maxwell-Boltzmann distribution. Thus, the distribution function of each species i can be described by its temperature T and its density $n_i(\mathbf{x})$. The zeroth moment of the Boltzmann equation, the species continuity equation, then reads

$$\frac{\partial n_i}{\partial t} + \nabla \Gamma_i - R_i = 0, \quad (3.31)$$

where Γ_i is the particle flux density and R_i the chemical production of the species i . The chemical production is evaluated via the Boltzmann collision integral. In the case of thermal particles, the integral can be calculated, resulting in a convolution of the cross section with the Maxwell-Boltzmann distribution. In contrast, Kuckert derived the production coefficient R not through integration but through an evaluation of rate equations of electron, ion and neutral particle interactions from literature.

The particle flux density is linked to the electric potential U through Poisson's equation and the current continuity equation. The electron flux density is modeled by Kuckert using the drift-diffusion approximation with the electron mobility μ_e and the diffusion constant D_e :

$$\Gamma_e = -D_e \nabla n_e - \mu_e n_e \left(\nabla U - \frac{k_B}{e} \nabla T_e \right) \quad (3.32)$$

This means that the flux can be solely described by the diffusion of the electron density, the thermal flux and a collective movement of electrons in an electric potential. Kuckert

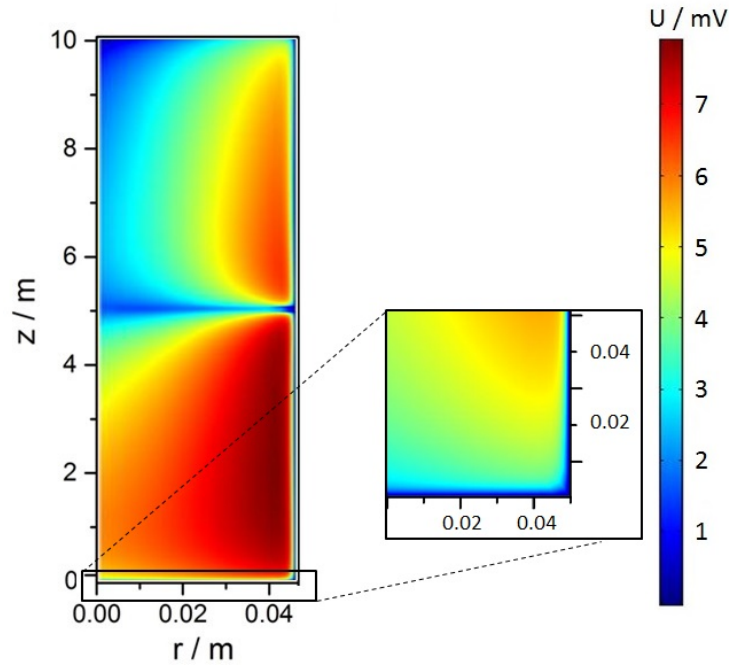


Figure 3.8.: Potential map of Drift-Diffusion Model. Simulated using the software framework COMSOL in the center of the source (only the central 10 m). Figure taken from [50].

assumed that the diffusion coefficient follows the classical diffusion, described in [18], and that the mobility can be evaluated through the Einstein relation [51].

Kuckert used the software framework COMSOL to obtain solutions for the coupled differential equations. The software uses the finite element method to solve the underlying equations. Kuckert assumed that there exists a time independent solution, such that after a long time the densities and currents of the particles reach a steady state.

The simulated geometry of Kuckert was assumed to be a cylinder with a length of 10 m and a radius of 4.5 cm. This corresponds to the central tube of the WGTS. The boundaries were chosen such that the cylinder walls and the left end cap absorb all incoming charged particles. The right end cap was assumed to reflect electrons, whereas ions are absorbed. The electric potential of the tube wall and the right cap was set to zero, while the potential of the left cap could be adjusted to represent the potential of the rear wall.

An exemplary potential map of Kuckert can be found in figure 3.8. Here the temperature of the particles was set to 30 K, the density of neutral particles was set to $8 \times 10^{20} \text{ cm}^{-3}$ and the rear wall potential was set to zero. It was found that the electron density reaches a maximum value of approximately $3 \times 10^6 \text{ cm}^{-3}$ and the potential reaches values of up to 12 mV. The density as well as the potential show a strong dependence along the length of the tube. In radial direction, the potential increases from half its maximum value to its maximum and then drops to zero at the last few millimeters.

Kuckert investigated the properties of the potential in dependence on the column density, the temperature of the electrons, the magnetic field and the rate coefficient of ion and electron recombination. It was found that the potential distribution does not change significantly through a variation of these parameters. For an elaborate description, refer to [50].

A comparison between measurements and predictions of the simulations reveals that there are significant discrepancies between both. A full comparison exceeds the context of this

thesis. Therefore, two easy comprehensive differences will be highlighted in the following. First, particle current measurements show, that there is a non-negligible current towards the beam tube walls, see section 3.2.2. This current was not described in the work of Kuckert, but is a key characteristic of the source. Second, the Pro Katrin measurements reveal, that there are rear wall potential values, where the plasma potential follows the change of the rear wall potential. However, also a region with no significant influence of the rear wall potential, and a region with reduced influence was found, see section 3.2.3. While Kuckert estimated that the plasma potential follows the rear wall potential, the reduced and non-existing dependency of both potentials were not predicted [24]. In summary, the model of Kuckert fails to predict key measurement observables, and is inconsistent in its predictions. Thus, the applicability of the model is unclear, and a new complete model is desired. The groundwork for the model of this thesis is described in the following.

3.5.2. Partly Collisional Vlasov Model

Non-Collisional Vlasov Model

Assume that there are no collisions in the plasma. This means that the collision term of the Boltzmann equation (equation 3.29) is set to zero. The resulting equation is called Vlasov equation and reads as

$$\frac{\partial f_i}{\partial t} + \frac{\mathbf{p}_i}{m_i} \cdot \nabla f_i + \mathbf{F} \cdot \frac{\partial f_i}{\partial \mathbf{p}_i} = 0. \quad (3.33)$$

It follows that the distribution of two particle species is only linked via the Coulomb force \mathbf{F} acting on the particles. The Coulomb force is calculated from the electromagnetic fields. These fields are calculated using Maxwell's equations, which in turn are affected by the charged particle current j . The current can be split into a contribution of electrons j_e and a contribution of ions j_i . Thus, the distribution of the electrons is dependent on the ion current and vice versa.

Electron and ion currents show different temporal characteristic because of the large mass difference. The electron current changes much faster than the ion current. When considering the electron movement on small time scales, the ion current can be assumed to be constant. The resulting electric field from the electron movement then influences the ion movement and thus changing the ion current on a large time scale. In the end, this influences the electron movement and the cycle starts again.

The large difference of time scales makes a simulation of both particle species at the same time unfeasible. A possible ansatz for the simulation can be an iterative approach, where the electron movement is simulated with a fixed ion current alternating with a simulation of the ion movement in a mean electric field. After a number of cycles, it is assumed that the resulting distribution functions reach a steady state. The result of such a simulation is of course dependent on the initial distributions.

Partly Collisional Model

Now consider that there are collisions. In the KATRIN source, the collisionality is different for electrons and ions, see section 3.3.3. For electrons, collisions occur on larger length scales than the Debye length, with an increasing mean free path from the center towards the ends of the source. For ions, collisions occur on a smaller length scale than the Debye length in the center of the WGTS, whereas they take place at larger length scales at the sides of the source.

Thus, both electrons and ions can be treated as collisionless close to the rear wall. It is viable to use a Vlasov model here. In contrast, electrons and ions can be considered at

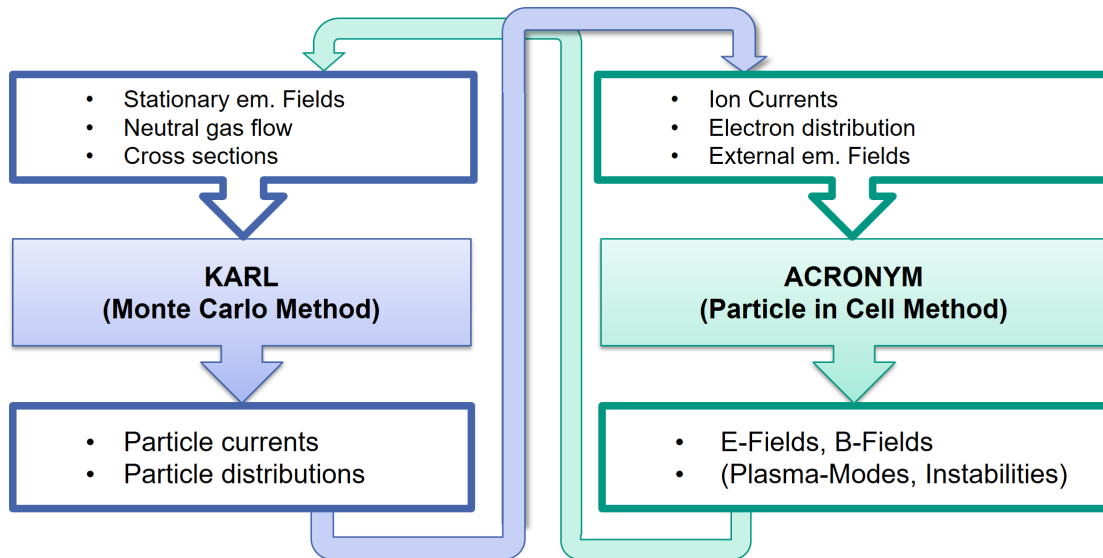


Figure 3.9.: Iterative simulation strategy of this thesis. Particle densities and particle currents are simulated in KARL, and used as an input for kinetic simulations of the electrons in ACRONYM. The resulting electromagnetic fields are used as an input for the Monte Carlo simulations.

least partly collisional in the center of the source. The movement of electrons and ions is influenced by collisions, but it is not fully dominated by them.

In the scope of this thesis, it is assumed that the electric fields are mainly moderated by electrons while ions only contribute by their constant current because of the large mass difference. Hence, the plasma physics of electrons can be simulated separately from the atom physics of ions and electrons. An iterative ansatz is proposed, also depicted in figure 3.9. First, the electron and ion distributions are evaluated in a constant electric field, while taking collisions with neutral gas into account. Second, the resulting particle currents and distributions are used to calculate the temporal evolution of the electromagnetic fields moderated by the electrons. These fields are then used as an input for the evaluation of the electron and ion distributions, and the iterative cycle starts.

The simulation of the ions and electrons in a stationary electric field with particle collisions is performed with a newly developed simulation tool, called KARL. This tool utilizes a Monte Carlo approach of particle generation, movement and collisions within self-generated particle densities. For more information on KARL refer to chapter 4.

The determination of the electron distribution functions and the electromagnetic fields is simulated using the well-tested ACRONYM code [42], see also chapter 5 for more information. In ACRONYM, the Vlasov equation is solved numerically, using the particle-in-cell method.

Chapter 4

Simulation of Particle Distributions with KARL

The density and its energy distribution of all species defines the plasma in the KATRIN source. The specific density distribution is dependent on the cross section of each interaction, the particle movement and the geometry of the source. Initially only beta electrons are created. Subsequent interactions with the surrounding gas create multiple other electrons and ions with varying energy. This scenario is best simulated using the Monte Carlo method. This method was implemented in the newly developed KATRIN WGTS electron and ion spectrum monte caRLo (KARL) computer code. This chapter focuses on the description of the algorithm and its first results. First, the simulation method will be described, where special focus will be laid on the particle movement and particle interactions. Second, the algorithm is used to provide a first insight into the density distributions of ions and electrons in the source. This first simulation will be performed without any electric background field. The electric field distribution is a priori unknown and will be determined later on. Third, simulation results will be presented, where the electric field was derived from a rear wall potential, see section 2.2, and from previous simulations with KARL.

Parts of this chapter are submitted for publication in a separate paper together with F. Spanier, see preprint [39]. With the kind permission of F. Spanier, a verbatim quotation was omitted in this chapter for better legibility. The initial idea of the algorithm was developed by F. Spanier and a first version of KARL was created in collaboration with C. Reiling in his master's thesis [73]. The computer code was extended, revised and tested in the context of this thesis. Differences in the description of the algorithm and its results between Reiling [73] and this work stem from corrections of erroneous calculations and additional extensions.

4.1. Simulation Method

The KARL code uses a special approach of the Monte Carlo method. A sketch of the simulation procedure can be found in figure 4.1. Each particle chain starts at the beta decay (particle injection), where the position of the new electron and corresponding ion is sampled from a neutral particle density distribution. The neutral density distribution is approximated from the simulated distribution from section 2.1.1. The energy is sampled from the known Fermi spectrum of the beta decay, see Introduction. The beta decay particles are then added to the particle queue, and the simulation starts its iterative cycle. In each iteration step, a particle is selected randomly from the particle queue. The mean free path is determined from the interacting partner densities at the position of the particle and the energy of the particle. The particle is then moved according to the mean free path and the electromagnetic fields, see section 4.1.1. If the particle hits the simulation

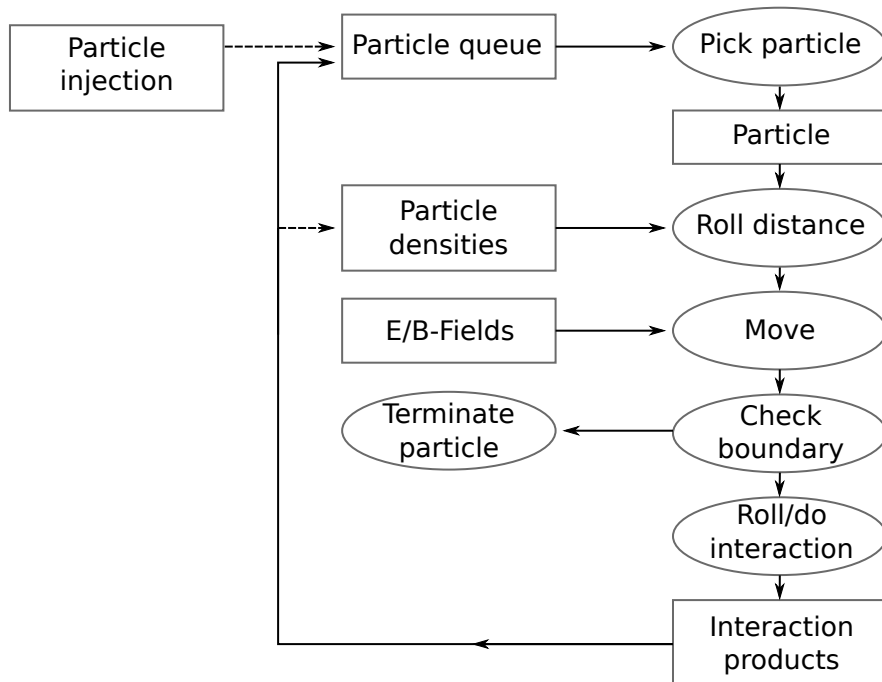


Figure 4.1.: Simulation procedure of KARL. Beta electrons are injected to the particle queue. A particle is picked from the queue and processed. The iteration step either ends in a particle interaction or through termination at the simulation boundaries. The particle queue is processed until no particle is left in the queue and a new beta particle is injected. The particle densities are determined during simulation.

boundaries, it will be deleted. Otherwise, an interaction is selected randomly from the available interactions, see section 4.1.2. The interaction products are added to the particle queue and the iteration starts from the beginning. The particle loop is repeated until there are no more particles in the particle queue. Then, new beta decay particles are created and processed until the specified target decay number is reached.

The simulation is evaluated using two methods: virtual current borders and density fields, which provide energy dependent particle currents, and particle densities in relation to the position in the source, see sections 4.1.4 and 4.1.3. The densities and currents are recorded for each particle specie during simulation. Thus, they can also be used to evaluate the interaction probability between two simulated particle species. In this way, two different particle species can interact with each other. The simulation of recombination of electrons and ions is therefore also possible.

4.1.1. Particle Movement

The particle movement is a central part of the simulation. Particles are moved from the original position to a new position depending on the mean free path and the electromagnetic fields in the source. The mean free path is calculated from the density of the target particles and the cross section of the interaction. The electromagnetic fields are provided prior to the simulation, and are considered constant over time. The movement of the particle is performed using the drift approximation algorithm, see equations 4.7, 4.8, and 4.9. In this algorithm, the motion of the particle is compound by a motion of the guiding center and the circular gyro motion around it. It is only applicable to systems where the magnetic field does not change during the particle movement. In the context of the KARL simulation, it is assumed that the magnetic field is constant over the whole source. Thus, the conditions to apply the drift approximation algorithm are met. A better approximation would be

given by the Boris push algorithm, see also section 5.1.3. Caused by higher computational costs, this needs deeper investigation and could be part of future research.

The movement of the particles is bound by the geometry of the source. For simulation, the KATRIN source tube is approximated by a cylinder with an open end. Electrons are reflected there, which corresponds to the reflection of electrons at the DPS dipole electrodes or at the main spectrometer potential. All ions are removed at the DPS side. All other boundaries of the cylinder are considered perfect electric conductors. Thus, all particles hitting the cylinder walls will be removed directly from the simulation.

Travelled Distance

Prior to the movement, it has to be determined how far a particle will travel before it will interact. The travelled distance L is subject to random fluctuations, described by equation 3.15. This randomness is reflected in the code by a pseudo random number $\eta \in (0, 1)$ and the mean free path λ . The travelled distance is calculated by

$$L = -\lambda \cdot \log \eta. \quad (4.1)$$

The mean free path is determined through equation 2.26 depending on the cross section of the interaction and density of the target particles. The mean free path of multiple competing interaction channels i is given by

$$\lambda = \frac{1}{\sum_i \sigma_i n_i}, \quad (4.2)$$

where σ_i is the cross section and n_i the density of the target particles. The cross section is dependent on the energy of the incident E_i and target particle E_t . The transformation into the target frame is dependent on the incident angle θ of the interaction and its distribution $f(\theta)$. Thus, each contribution to the mean free path can be formulated as [73]

$$\sigma_i n_i = \frac{1}{\pi} \iint dE_t d\theta f(\theta) \sigma_i(E_t, E_i, \theta) \frac{dn_t}{dE_t}(E_t). \quad (4.3)$$

In simulation it is assumed that the incident angle is isotropically distributed to reduce calculation effort. Furthermore, small and large incident angles are neglected. The transformation to the target frame can result in a vanishing energy otherwise, which in turn would result in an overestimation of the cross section toward lower energies. The energy distribution of the target density is collected in discrete bins. Therefore, the integral is not computed directly but replaced through a sum over all possible energy bins.

The actual movement of the particle is subdivided into smaller steps with length Δx . This has two different reasons. First, the drift approximation algorithm assumes that the electric field does not change radically during the movement, see also next paragraph. Second, for the calculation of the mean free path, it was assumed that the density of the interaction partners does not change during the particle movement. The former can be guaranteed through a constraint on the step length Δx . It is required, that the step size is smaller than the step size of the electric field data. The latter is more difficult to incorporate in the algorithm. It would mean that the travelled distance is dependent on the difference in density during movement, which in turn is dependent on the travelled distance itself. This effect is negligible where the mean free path is much smaller than the typical distances where the density changes. This is the case for most particles with low energies in the center of the source. The cross section as well as the density is high enough in this case. The mean free path of beta electrons and particles near the DPS or rear wall is high enough, that the change of density is relevant. This issue can be addressed by considering the random nature of the movement. Any particle with the same velocity within a homogeneous cloud

of other particles has the same chance to interact within a certain distance as the others. This probability is independent of the prior movement of the particles. So in simulation, the travelled distance will be determined anew, if the particle has moved to another section of the source, where the density is higher. A good measure for the position, where density has changed enough are the bin borders of the density fields, see section 4.1.3. Thus, if a particle crossed from one density bin to another, the travelled distance will be determined again. This procedure also provides a limit on the step size Δx . It has to be smaller than the bin width of the density fields.

Drift Approximation Algorithm

In the drift approximation algorithm, the movement of the particle can be described by the superposition of the movement of the guiding center and the gyro motion of the particle around the guiding center. The particle is moved in total by the distance L . Its motion is subdivided into small spatial steps Δx . Assuming that the magnetic field is directed in z -direction, the discretization of the spatial dimension can be translated into a discretization of the time domain to

$$\Delta t = \frac{\Delta x}{|\mathbf{v}^i|}, \quad (4.4)$$

where $|\mathbf{v}^i|$ is the absolute velocity of the particle before moving. The position z in longitudinal direction is then calculated by

$$z^{i+1} = z^i + v_{\parallel}^i \Delta t, \quad (4.5)$$

where the index i denotes the timestep at which the quantity is given and v_{\parallel}^i is the velocity of the particle perpendicular to the magnetic field. The electric field during the motion is approximated by the mean of the field value at the original position and at the new position

$$\mathbf{E} = \frac{\mathbf{E}(z^{i+1}) + \mathbf{E}(z^i)}{2}. \quad (4.6)$$

This field is used to calculate the movement perpendicular to the magnetic field and used to determine the new velocity v_{\parallel}^{i+1} . The perpendicular particle position changes to

$$x^{i+1} = x^i + v_{\perp,x} \Delta t \quad (4.7)$$

$$y^{i+1} = y^i + v_{\perp,y} \Delta t, \quad (4.8)$$

where \mathbf{v}_{\perp} is given by

$$\mathbf{v}_{\perp} = \frac{\mathbf{E} \times \mathbf{B}}{B^2}. \quad (4.9)$$

The parallel velocity changes corresponding to the Lorentz force to

$$v_{\parallel}^{i+1} = v_{\parallel}^i + \frac{qE_{\parallel}}{m} \Delta t, \quad (4.10)$$

where E_{\parallel} is the electric field strength parallel to the magnetic field, m is the mass of the particle and q its charge.

4.1.2. Particle Interactions

After the particle is moved to a new position, an interaction will occur. The interaction type depends on the type of particle. Four different particles species can be distinguished in the simulation: electrons e^{-} , tritium ions T^{+} , tritium molecule ions T_2^{+} and tritium cluster ions T_3^{+} . Higher order cluster ions can in principle be used as well, but are not used in the current version of the code because of missing cross section data. Furthermore,

it can be assumed from rate constant measurement, see section 2.4, that the density of higher order clusters is significantly lower than the density of T_3^+ . Thus, the impact of these ions on the simulation results should be small. Nevertheless, this should be further investigated outside this work's context.

Each of the particle species have multiple different interaction channels, see section 2.4. The specific interaction channel at each interaction point is determined randomly, corresponding to the probability of the interaction channel. A measure for the probability that a specific channel is chosen is given by the inverse mean free path of the channel. The higher the inverse value, the higher the probability of that interaction. In KARL, a random number η is drawn from the interval $[0, \sum_i \sigma_i n_i]$, where i denotes the different interaction channels. A specific interaction channel j is used, where

$$\eta \geq \sum_i^j \sigma_i n_i \quad (4.11)$$

is fulfilled.

After the interaction channel is determined, the chosen interaction is performed. The interaction is represented either by a change in velocity, in position, or by addition of new particles. The implementation of the interaction depends on its type. The different variants will be presented in the following.

4.1.2.1. Elastic Scattering

Elastic scattering is the dominant interaction channel for all particle species. The velocity changes its direction but not its absolute value in the interaction. It can therefore be described by a rotation of the velocity vector. The rotation is characterized in spherical coordinates by the azimuth angle θ and polar angle ϕ . The angle θ is given by the differential cross section $\frac{d\sigma}{d\theta}$, which is dependent on the particle type and the energy of the particle. Isotropic scattering is assumed for all ion interactions, and for all electron interactions below 10 eV. The azimuth angle at higher energies is sampled from the differential cross section using the ELSEPA code [74]. Large and small scattering angles are suppressed in this case. The polar angle is sampled from a uniform distribution in the interval $[0, 2\pi)$. This represents the polar symmetry of the interaction.

The new velocity vector is derived through the following procedure:

- Roll the energy of the target particle from the density field at the position of the interacting particle.
- Convert the energy of the target particle to a velocity vector (isotropic distribution with an additive drift velocity).
- Transform the velocity of the primary particle to the center of mass frame.
- Roll azimuth angle θ and roll polar angle ϕ .
- Rotate the primary velocity in the center of mass frame.
- Transform the velocity back to the laboratory frame.

The rotation of the velocity is performed using the procedure provided by Haghghat [31], which is shortly summarized in the following.

The initial velocity \mathbf{v} can be expressed by

$$\mathbf{v} = v_x \mathbf{e}_x + v_y \mathbf{e}_y + v_z \mathbf{e}_z = |\mathbf{v}|(n_x \mathbf{e}_x + n_y \mathbf{e}_y + n_z \mathbf{e}_z), \quad (4.12)$$

where n_i are the normal vector entries of the velocity. The normal vector can be transformed to a new basis, where the new z -axis is aligned with the unit vector. The new eigenvectors are

$$\mathbf{e}'_x = \mathbf{e}'_y \times \mathbf{e}'_z \quad (4.13)$$

$$\mathbf{e}'_y = \frac{\mathbf{n} \times \mathbf{e}_z}{|\mathbf{n} \times \mathbf{e}_z|} \quad (4.14)$$

$$\mathbf{e}'_z = \mathbf{n}. \quad (4.15)$$

In this new base, the rotation can be performed trivially through

$$\mathbf{n}' = \sin \theta \cos \phi \mathbf{e}'_x + \sin \theta \sin \phi \mathbf{e}'_y + \cos \theta \mathbf{e}'_z, \quad (4.16)$$

where \mathbf{n}' is the rotated unit vector. The reverse basis change then results in

$$\mathbf{n}' = n'_x \mathbf{e}_x + n'_y \mathbf{e}_y + n'_z \mathbf{e}_z \quad (4.17)$$

with

$$n'_x = - \left(\frac{n_x n_z}{\sqrt{n_x^2 + n_y^2}} \cos \phi + \frac{n_y}{\sqrt{n_x^2 + n_y^2}} \sin \phi \right) \sin \theta + n_x \cos \theta \quad (4.18)$$

$$n'_y = - \left(\frac{n_y n_z}{\sqrt{n_x^2 + n_y^2}} \cos \phi - \frac{n_x}{\sqrt{n_x^2 + n_y^2}} \sin \phi \right) \sin \theta + n_y \cos \theta \quad (4.19)$$

$$n'_z = \sqrt{n_x^2 + n_y^2} \cos \phi \sin \theta + n_z \cos \theta. \quad (4.20)$$

The new velocity vector in the original base is finally given by

$$\mathbf{v}' = \mathbf{n}' |\mathbf{v}|. \quad (4.21)$$

With this procedure, the new velocity vector can hence be determined from the scattering angles and the initial velocity vector.

The position of the primary target does not change through elastic scattering. Nevertheless, the guiding center of the movement changes its position during interaction. Thus, this change of the guiding center has to be reflected in the simulation as well. If the particles are moved by an algorithm, where the motion of the particle is resolved directly, like the Boris push algorithm, this effect is already included because the algorithm resolves each gyro motion of the particle. If the particle movement is described by the drift approximation algorithm, an additional change of the guiding center has to be added. This shift will be described in the following.

Assume that the guiding center is located at the position \mathbf{x} . The new position of the guiding center \mathbf{x}' will be shifted after the interaction by the length Δx with

$$\Delta x = 2r_L \sin \left(\frac{\theta}{2} \right), \quad (4.22)$$

where r_L is the gyro radius and θ the scattering angle, see figure 4.2. The direction of the shift is in general dependent on the polar angle ϕ of the gyration. In the context of this thesis, it is assumed that there are many gyro motions between interactions, see section 3.3.6. Thus, the polar angle is determined randomly before the interaction from a random number $\eta \in [0, 1)$. The new position is then given by

$$\mathbf{x}' = (x + \Delta x \sin 2\pi\eta) \mathbf{e}_x + (y + \Delta x \cos 2\pi\eta) \mathbf{e}_y + z \mathbf{e}_z \quad (4.23)$$

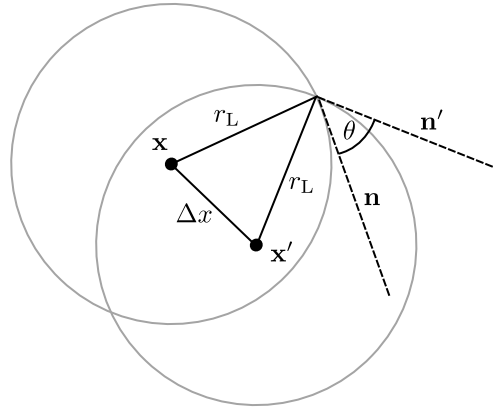


Figure 4.2.: Change of the guiding center position during elastic scattering. The initial position \mathbf{x} is moved to the new position \mathbf{x}' . The absolute distance between the points is dependent on the Larmor radius r_L , and the scattering angle θ , which is spanned between the two normal vectors of movement \mathbf{n} and \mathbf{n}' .

4.1.2.2. Electron Impact Ionization

In the ionization process, an electron hits a neutral gas particle and creates another electron and an ion molecule (T_2^+). This ion molecule can be stable, or it can dissociate spontaneously to T^+ , see also section 2.4.2. The cross section and threshold energy depends on the type of ionization process. Janev, Reiter, and Samm [35] identified three different ionization channels. These channels are incorporated in KARL. Kim and Rudd [43] developed another effective model for the ionization process. The created ion in this case is considered stable. This model was also implemented for test purposes.

In the interaction, two new particles are created alongside the original electron: an electron and an ion. The position of all three particles is considered to be the same position as the original electron. The velocity vector of the particles is however determined differently for the electrons and the ion. The velocity of the ion is sampled from the velocity distribution of the neutral gas. No recoil energy is added to the ion, due to the large mass difference of the ion and the electrons. The velocity of the electrons is determined in two steps. First, the energy of the electrons is calculated. Second, the scattering angles are established.

There is a threshold energy for the reaction, the ionization energy. The remaining collision energy T has to be divided between both electrons. The energy of the primary electron E_p is sampled from the theoretical works of Kim and Rudd [43], while the energy of the secondary electron follows directly from the energy of the primary and the collision energy ($E_s = T - E_p$). The scattering angles of the primary and the secondary electron are sampled from the semi empirical studies by Grosswendt and Waibel [30]. The polar angle ϕ_p of the primary electron is assumed to be uniformly distributed, while the polar angle of the secondary electron is given by $\phi_p - \pi$. The azimuth angle range of the primary electron is dependent on the energy. For small energies (< 100 eV) it can be assumed that the angle is uniformly distributed in the range of $[0, \pi/4)$. Similarly, the azimuth angle range of the secondary is dependent on the energy. For small energies ($E < 50$ eV), it can be assumed that the angle is uniformly distributed in the range of $[0, \pi)$. In total, the new velocity vector of both electrons is determined from the generated energy and scattering angles.

4.1.2.3. Electron Impact Excitation

Electrons can excite electrons of neutral gas particles, and both vibrational and rotational states of the gas molecules, see section 2.4. The excitation depends on the initial state of the neutral gas molecule. The different excitation states differ in their cross section and the energy loss. In KARL, it can be distinguished between the

- 15 channels of electronic excitation measured by Janev, Reiter, and Samm [35].
- experimental cross section of electronic excitation measured by Yoon et al. [86]
- first two vibrational excitations, measured by Janev, Reiter, and Samm [35].
- experimental cross section of vibrational excitation measured by Yoon et al. [86]
- first rotational excitation, measured by Janev, Reiter, and Samm [35]

The interaction process itself, is reduced to an energy loss of the electron. The direction of motion, as well as the particle position, is assumed to stay constant.

4.1.2.4. Recombination

Recombination processes between ions and electrons need to be modelled explicitly. In all processes before, the particles interacted with the neutral gas particles. The reservoir of neutral particles is considered to be infinite, such that the interactions of electrons and ions with the gas do not change the gas flow and its properties. This is no longer valid for recombination. Each time an electron recombines, not only the electron density needs to be reduced, but also the ion density. Therefore, each event in the Monte Carlo method is no longer independent of the others. Direct particle interaction is impossible to model in the context of the classical Monte Carlo method. In KARL, this discrepancy is resolved through the density fields presented in section 4.1.3: Each time an electron recombines with an ion, the electron is deleted from the particle queue and a counter in the corresponding ion bin is increased. Thus, the electron can no longer travel the source and can no longer contribute to the density. The ion density is reduced by the counter. In total, both species have reduced densities without direct interaction. The same procedure is applied, when the primary particle is the ion. In this case, the ion will be deleted and the corresponding counter of the electron is increased. In the limit of many interactions, both electrons and ions will show the same total number of recombination.

As a result of the small cross section, only T_2^+ and T_3^+ ions recombine, while T^+ ions do not take part in this process in KARL. The cross section of T_2^+ and T_3^+ ions is evaluated from the formula provided by Janev, Reiter, and Samm [35]. Due to the deletion of the particles, no new position and new velocity vector has to be evaluated.

4.1.2.5. Ion Cluster Formation

Ions can form clusters through attachment of molecules to the existing ion, see section 2.4. The cross section of the interaction depends on the initial cluster size. Three different cluster sizes are distinguished here: T^+ , T_2^+ and T_3^+ . Higher order clusters are neglected here, due to their predicted low density and missing cross section data for fragmentation processes.

The cross section of cluster formation for T^+ ions is calculated from the rate coefficient measurement of radiative and ternary association [70], see also section 2.4. The new T_3^+ ion of this reaction is initialized with the same velocity and position as the initial T^+ ion, due to missing information on the differential cross section.

T_2^+ ions show a large cross section for cluster formation, see section 2.4. In KARL, the cross section of the reaction is taken from the works of Janev, Reiter, and Samm [35].

Again, due to missing information on the differential cross section, the velocity and position of the new ion are initialized by the velocity and position of the initial T_2^+ ions.

4.1.2.6. Ion Charge Transfer

Ion molecules (T_2^+) do not scatter elastically from neutral gas but take part in the charge transfer reaction, see section 2.4. One electron of the target neutral gas molecule is transferred to the ion. Thus, a new ion is created.

In KARL, the cross section of the reaction is taken from the works of Janev, Reiter, and Samm [35]. For simplicity, the estimation of the new velocity vector is performed similar to the calculations of elastic scattering, see section 4.1.2.1. Input for these calculations are the velocity of the initial ion, the scattering angles ϕ and θ , and the velocity of the target molecule. The scattering angles are sampled from the intervals $\phi \in [0, 2\pi)$ and $\theta \in [0, \pi)$. The velocity of the target molecule is sampled from the velocity distribution of the neutral gas particles. Similarly, the calculation of the position of the new ions follows the same argumentation of elastic scattering. In principle, the position of the particle does not change in the ion charge transfer process. Due to the change of the gyro center however, the position has to be adapted. In the end, the calculation is performed analogue to the calculations of elastic scattering, see section 4.1.2.1.

4.1.3. Density Fields

Energy and position dependent particle densities have two major functions in the algorithm: they are used in the Monte Carlo method itself (for the calculation of the cross section and interactions), and are the prime output of the simulation itself. The density of each particle specie is tracked individually. An exception is the density and velocity distribution of the neutral gas. The gas density is high enough, that it can be assumed that the neutral gas flow is not influenced by charged particle interactions. Therefore, it can be specified at the beginning of the simulation. This section however focuses on the densities, which are determined during simulation.

In the simulation, the source is segmented longitudinally, radially and azimuthally. In each iteration step of the particle queue, it is recorded how long a particle stays in one segment. The density of a species α is then proportional to the total time of all particles of the species spent in the segment and the volume V of the segment. In case of recombination, an additional term has to be added corresponding to the number of recombinations of the recombination partner γ in the segment

$$n_\alpha = \frac{\sum_i t_i}{t_{\text{sim}} V} - \frac{N_\gamma}{V}, \quad (4.24)$$

where t_{sim} is the simulated time (formula adapted from [73]). The simulated time is determined by the number of decays N_β and the total activity a of the source

$$t_{\text{sim}} = \frac{N_\beta}{a}. \quad (4.25)$$

The activity of the source is calculated relatively to the activity at nominal conditions. The activity at a tritium inlet density of $n_{T_2,0} = 1 \times 10^{15}/\text{cm}^3$ is approximately $A_0 \approx 1 \times 10^{11}$ Bq [50]. So, the activity at another inlet density n_{T_2} is calculated by

$$A = \frac{n_{T_2}}{n_{T_2,0}} \cdot A_0. \quad (4.26)$$

This approximation ignores that the density profile changes, when the inlet density changes. Nevertheless, a thorough calculation would need gas simulations at each used injection density. It is therefore set aside here.

The density can also be determined depending on the energy of the particle. These densities are then binned to a predefined energy scale. Thus, the density fields can be used in equation 4.3, and also used for sampling of an interaction partner.

The sampling is performed in three different steps: sample particle energy, roll velocity direction, copy position of primary particle. First, the energy of the interaction partner is sampled from the energy distribution of the target field at the position of the primary particle. Secondly, a velocity direction is picked at random. The velocity of the new particle is then scaled according to the energy and mass of the particle. Finally, the new particle is generated with this velocity and the position of the primary particle.

4.1.4. Simulation Output and Diagnostics

The Monte Carlo approach of the simulation needs statistics with a high number of samples. The statistic is determined by the number of generated beta-decay events N_β . Each of these events produces multiple secondary particles. Recording each position and particle would result in an overwhelming amount of data. Thus, it was decided to use three different output methods: density fields, absolute particle numbers of conversion and termination and particle currents through virtual barriers.

Density Fields: The density fields of the previous section are recorded each time after a specified number of generated beta-decay events. The last output is performed after N_β decays. This output is used for the final determination of the particle densities of the simulation, which is one of the main objectives of KARL. The other outputs are only used for diagnostics of the computer code.

Interaction Counter: Special counters are implemented to track each time a particle is terminated at the simulation boundary, converted to another particle flavor or recombines. The termination counter is selective on the boundary type: rear wall, tube wall or DPS. These counters can be used for diagnostics or for tests of the computer code.

Virtual Current Borders: The second main objective of KARL is to determine the particle currents in the source. This task is performed through virtual barriers. Similar to the segmentation of the density fields, the source is segmented longitudinally, radially and azimuthally. Each particle is registered, when it crosses from one segment to another. The total current through the segment faces is then given by

$$j = \frac{N^+ - N^-}{A t_{\text{sim}}}, \quad (4.27)$$

(formula from [73]) where N^+ and N^- is the number of particles crossing the faces in positive and negative direction, A is the area of the face and t_{sim} the simulated time, see equation 4.25.

The current through the faces can be determined from the energy and type of species crossing the faces. This is performed through a selective binning to a predefined energy scale during simulation. The absolute current is then given by the sum over all energy bins.

Statistical Uncertainty

The accuracy of the simulation depends on the number of decays N_β . This number is inserted directly in the calculation of the current and the density, but it also contributes indirectly through the production of secondary particles. The specific contributions are difficult to calculate directly because of the multitude of different interactions. Hence, the accuracy of the simulation was determined through multiple simulations with the same number of decays but with different random number generator seeds. The mean

of the normalized standard deviation of each energy bin was calculated. For a counting experiment, it is expected that the standard deviation scales with $1/\sqrt{N_\beta}$, which was found to be in good agreement with the test simulation results. For a statistical uncertainty of 0.1%, it is therefore necessary to simulate at least 1×10^6 beta decays. Such a simulation (without electric background field) takes up to 24 h on 1392 CPU cores. This is a reasonable amount of calculation effort for the reached accuracy.

4.2. Validation

The algorithm of KARL was tested thoroughly, including a comparison of specific simulations with expectations. These were formulated for scenarios, where an analytical expression of the simulation output can be derived. For these simulations, each interaction was investigated detached from the others. The corresponding tests are summarized in the following.

4.2.1. Ionization

Ionization was tested through an injection of monoenergetic electrons. All interactions, except ionization, were disabled. The energy of the electrons was chosen in such a way ($E_{\text{inj}} = 30$ eV), that only one ionization could occur as a result of the energy loss. The energy distribution of the ionization products were compared to the expected energy distribution. The expected distribution is generated from the input differential cross section and an additional energy dependent factor. This factor comprises a factor for logarithmic binning

$$\frac{d\sigma}{dE} = \frac{d\sigma}{d \log E} \frac{d \log E}{dE} = \frac{d\sigma}{d \log E} \frac{1}{E}, \quad (4.28)$$

and a factor, that converts the generated spectrum to the spectrum in the source. Faster electrons, leave the source faster than slower electrons. Thus, the generating spectrum has to be divided by \sqrt{E} . In total, the generating spectrum has to be multiplied with \sqrt{E} to gain the simulated spectrum in the source. A comparison of the spectrum of a test simulation and the expected spectrum is shown in figure 4.3. It can be seen, that expectation and simulation agree well. Small differences are expected as a result of statistical uncertainty.

The ionization process can occur either through a dissociative or non-dissociative process. Thus, the number of T^+ ions in relation to the T_2^+ ions should match the relation between the cross sections of the reactions. In the tests, the number of T_2^+ was found to be ≈ 77.5 higher than the number of T^+ . At 30 eV, the relative cross sections of the two ionization processes is ≈ 77.1 , which corresponds well to the simulated ratio.

4.2.2. Elastic Scattering

Elastic scattering was tested through an injection of monoenergetic particles into a neutral gas reservoir with a Maxwell-Boltzmann velocity distribution. The temperature was set to $T = 80$ K. All interactions, except elastic scattering, were disabled. If elastic scattering is implemented correctly, then these particles will adopt the energy distribution of the neutral gas independently of the initial energy, multiplied with the conversion factor of \sqrt{E} , see section 4.2.1. In the first simulation, the cross section of elastic scattering was set to a fixed value to avoid a difference towards the Maxwell-Boltzmann distribution. The corresponding spectrum can be found in figure 4.4 alongside a least-squares fit of the Maxwell-Boltzmann distribution. It can be seen, that the data of the simulation can be described well by the Maxwell-Boltzmann distribution. This observation is underlined by the good agreement of the estimated temperature of the fit $T = (80.57 \pm 0.04)$ K with the gas temperature. Small derivations between data and fit are discernible at energies below $E < 1 \times 10^6$ eV. They can be attributed towards the statistical nature of the Monte Carlo method.

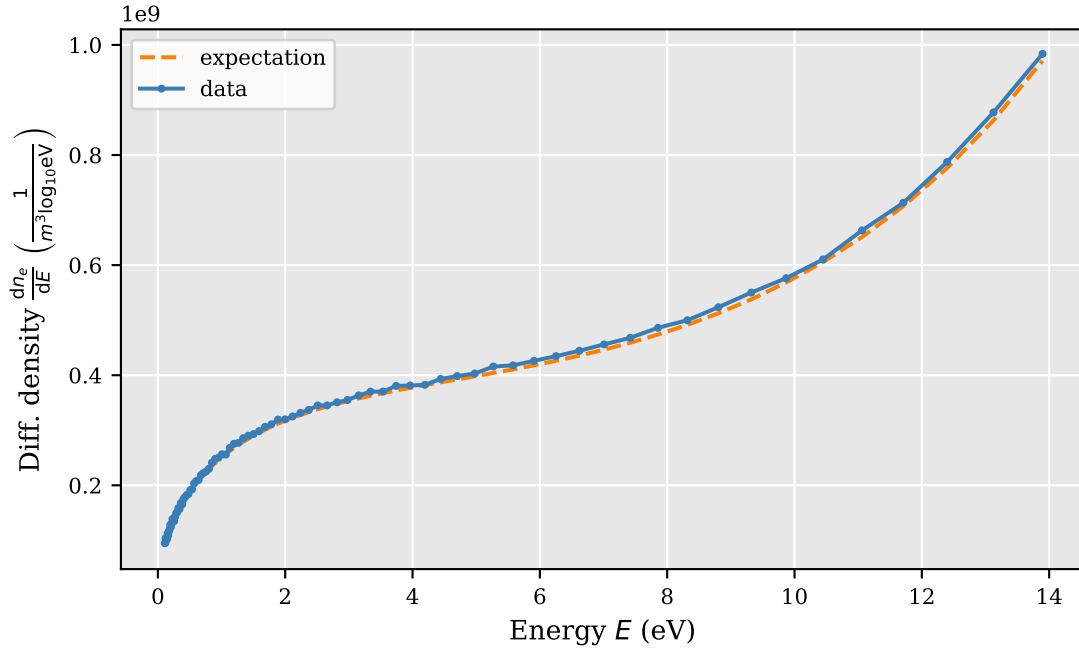


Figure 4.3.: Test simulation with ionization only. Comparison of the simulated spectrum and the generating ionization spectrum with conversion factor \sqrt{E} .

In the previous simulation, the electrons were injected with an energy of 20 meV. If elastic scattering is implemented correctly, then the spectrum will be independent of the injection energy. In the second test, three different simulations were compared, each with a different injection energy. The injection energies were chosen, such that they are below and above the most probable energy of the Maxwell-Boltzmann distribution ($E = 6.897$ meV). The temperature of the source was again set to $T = 80$ K. In order to test the final behavior of the algorithm, it was decided to use the true energy dependent cross section of elastic scattering. The corresponding spectra of the simulations can be found in figure 4.5.

It can be seen, that all three simulations show the same shape of the distribution. Only the scale of the densities is different between the simulations. After a normalization, these differences disappear (not shown). Thus, the test requirements were met, from which we can conclude that the simulation is independent on the injection energy. The test simulation also shows, that an energy dependent elastic cross section produces a spectrum, that is different from the pure Maxwell-Boltzmann distribution. The difference is most pronounced in the low-energy regime, where the cross section for elastic scattering is smaller than at higher energies. Thus, more particles will stay at their small energies than before because of the reduced scattering probability. Nevertheless, this result does not invalidate the tests from above, but shows the importance of the energy dependent cross section.

4.2.3. Excitation

Excitation (vibrational, rotational and electronic) was tested through an injection of monoenergetic electrons. In the excitation processes, electrons lose energy depending on the excitation state while keeping all other properties, see section 4.1.2.3. Thus, a comparison of the initial and final energy will result in energy loss through excitation. The simulated energy results were found to be in agreement with their expectation.

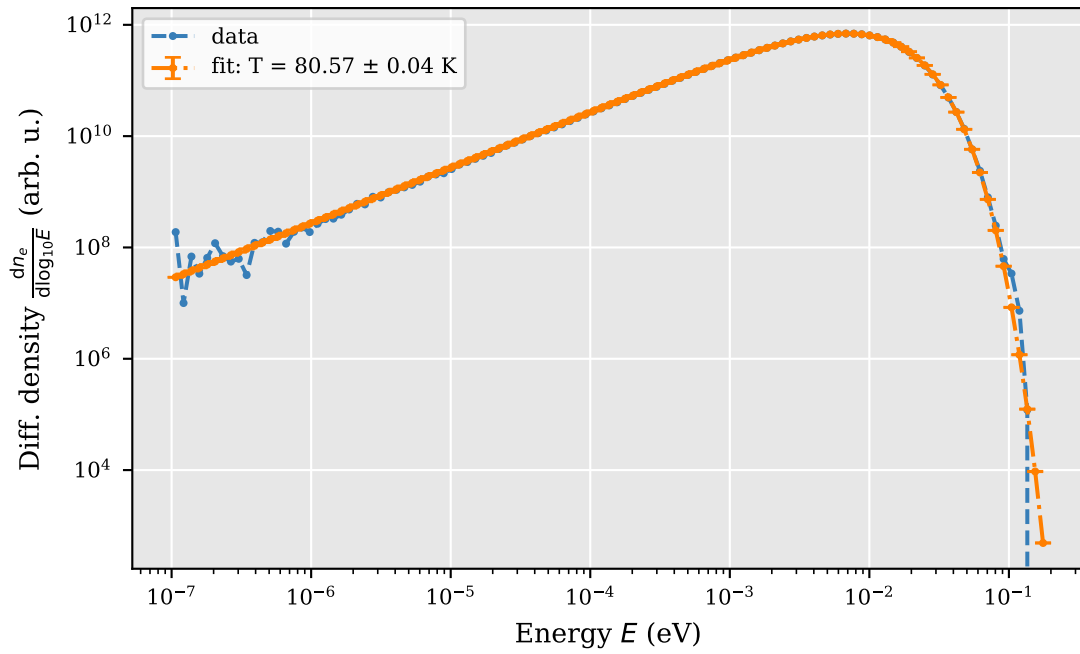


Figure 4.4.: Test simulation with elastic scattering only. Simulated spectrum with gas temperature of $T = 80$ K and fixed elastic cross section. Least-squares fit of Maxwell-Boltzmann distribution with conversion factor. Deviations at low energies arise from statistical fluctuations.

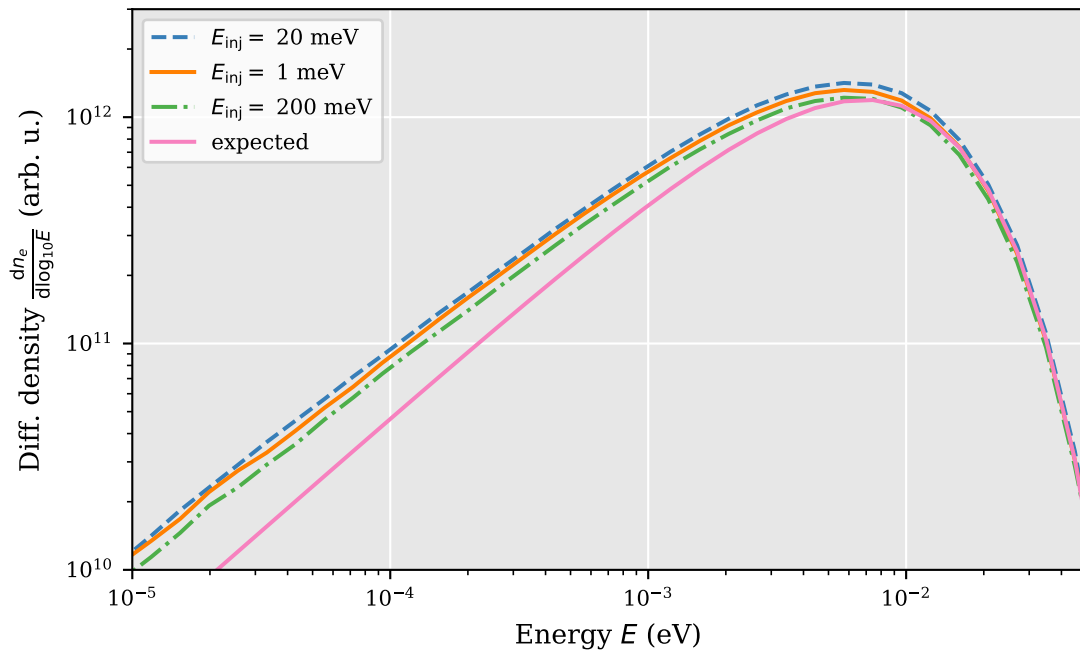


Figure 4.5.: Test simulation with elastic scattering only. Comparison of three simulations with different injection energies E_{inj} but with energy dependent cross section. Expected Maxwell-Boltzmann distribution in case of fixed cross section for comparison.

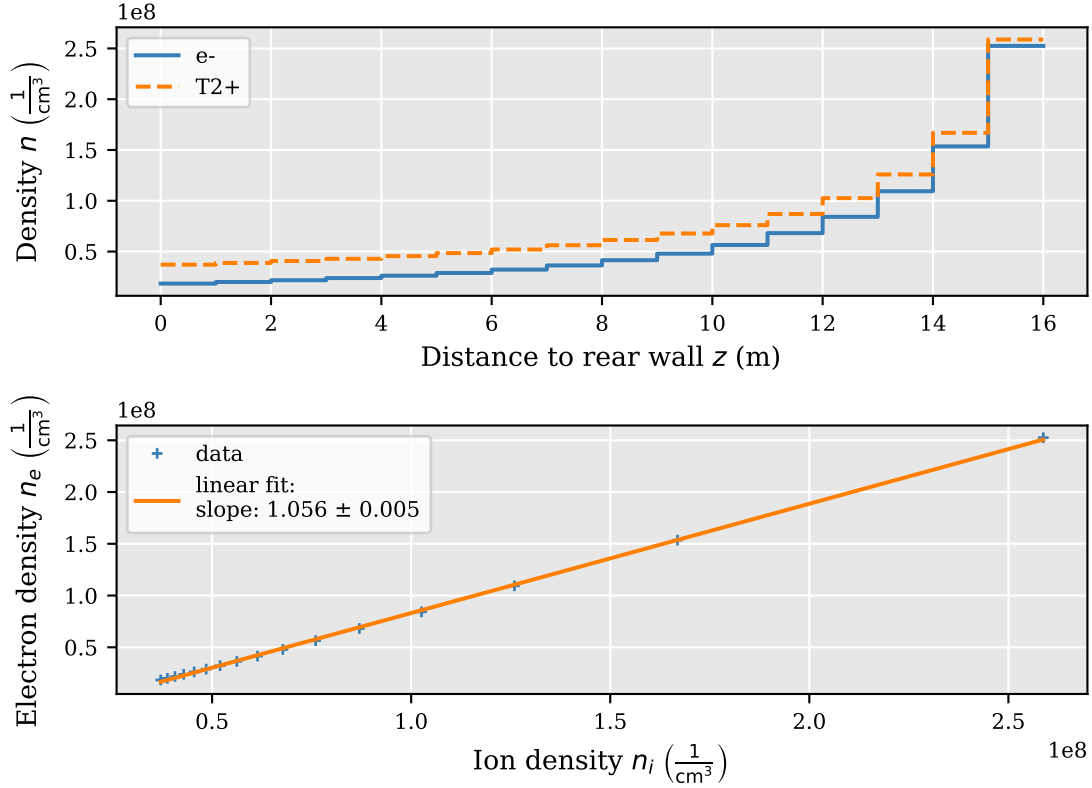


Figure 4.6.: Test simulation with recombination only. Top: The same amount of electrons and ions is injected at the right side. The particles move to the left. Some of the particles recombine, which reduces the density. Bottom: The simulated densities for each position is compared to each other. A fit was performed to investigate the expectation of equation 4.31.

4.2.4. Recombination

Recombination was tested through an injection of monoenergetic ions and electrons at one end of the simulation domain with energies E_e and E_i for electrons and ions respectively. The injection position was chosen to be located at the DPS side, while the injection velocity is directed towards the rear wall. The energies of the particles were chosen in such a way, that the density of electrons and ions show the same value as in a simulation without recombination. All other interactions were disabled and a magnetic field in z direction was applied. Thus, there exists no dependence on the x and y position. The expected density of the ions $n_i(z, t)$ and electrons $n_e(z, t)$ can be calculated from the coupled continuity equation of electrons and ions with a particle sink. The differential equations in this case then read as

$$\frac{\partial n_e}{\partial t} = v_e \frac{\partial n_e}{\partial z} + \sigma(E_e) n_e n_i v_e, \quad (4.29)$$

$$\frac{\partial n_i}{\partial t} = v_i \frac{\partial n_i}{\partial z} + \sigma(E_i) n_i n_e v_i. \quad (4.30)$$

The cross sections are given in the frame, where the target particle is at rest. So, $\sigma(E_e)$ describes the case, where the ion is at rest and $\sigma(E_i)$ describes the case, where the electron is at rest.

In the limit of large time values, it is expected that the density does not change. So this coupled differential equation can be solved by the linear equation

$$n_e(z) = \frac{\sigma(E_e)}{\sigma(E_i)} n_i(z) + c, \quad (4.31)$$

where c is an integration constant. Thus, a linear relation between electron and ion density is expected. In an ideal case, where electrons and ions both stream at the same time in the same direction, the transformation between $\sigma(E_e)$ and $\sigma(E_i)$ will result in the same value. Therefore, the ratio of the cross sections is one. The simulation is slightly off from the ideal case, since the calculation of the microscopic cross section comprises the assumption of an isotropic distributed velocity vector. The conversion to the laboratory frame therefore results in slightly different values of the cross section. Hence, small deviations from unity are expected. Additionally, the ion density spectrum is considered to follow the Maxwell-Boltzmann distribution, which provides an additional energy contribution. This contribution is minimized by choosing a small temperature of the distribution ($T = 1 \times 10^{-4}$ K), but cannot be erased completely.

The test simulation was performed with the injection of 1×10^5 electrons and ions. The resulting densities can be found in figure 4.6. It can be seen, that the density of both electrons and ions decreases from the injection position (right side) towards the rear wall (left side). This is expected, because all particles, which recombine, can no longer contribute to the density. The slope of the density is the highest at the injection position. This is caused by the increased recombination probability at this point due to the larger density. The densities of electrons and ions can be plotted versus each other, see also figure 4.6, to investigate the expectation of equation 4.31. It can be seen that there is indeed a linear relation between the densities. A linear fit to the data shows that the slope has a value of 1.056 ± 0.005 . This value is close to the expected unity. The small deviation was expected, see above.

In the case, where electrons and ions have the same velocity, they induce the same density in a simulation without recombination. Therefore, in a simulation with recombination it is expected that the number of simulated electrons, which recombine is similar to the number of the simulated ions, which recombine. It could be shown that they agree: $N_e \approx 8.9 \times 10^4$ and $N_i = 9.5 \times 10^4$. Similar to the expected value of the cross section ratio, also the number of recombined particles can be slightly different, because of the finite temperature of the ions and the isotropically distributed velocity.

4.3. Electromagnetic Field-Free Simulation

A starting point of the simulation cycle with ACRONYM and KARL is a simulation with KARL. Ab initio, there is no knowledge of the electric field, and it is therefore set to zero. The magnetic field of the superconducting magnets is not influenced significantly by the plasma due to its extremely high strength. It is therefore included in the first simulation, and set to $B = 2.5$ T throughout the whole source.

The tritium gas density was approximated according to Kuckert et al. [49]. No adjustment needed to be made in the rear wall region, due to the small difference between the density at the rear and front end of the source, see figure 2.1. Six linear functions were used to approximate the density to save computation time, see figure 4.7. The temperature of the gas was set to $T = 80$ K, and the maximal density was set to $6.3 \times 10^{14} \text{ cm}^{-3}$.

The drift velocity of the neutral gas was obtained from the results of Kuckert et al., see figure 2.4. As a starting point, the drift velocity was set to zero in the regions between the rear wall and the central source tube of the WGTS. The drift velocity was implemented through a numerical table, because of its significant radial and longitudinal structure.

The source tube was approximated by a cylinder with radius $R = 4.5$ cm and a height of $H = 16$ m. The center of the source was set at 8 m away from the rear wall for simplicity. The source was segmented into 32 z bins and 15 radial bins. No segmentation was used in the azimuth direction due to the expected azimuthal symmetry of the result. Density and currents were recorded at 100 energy bins with logarithmic subdivision.

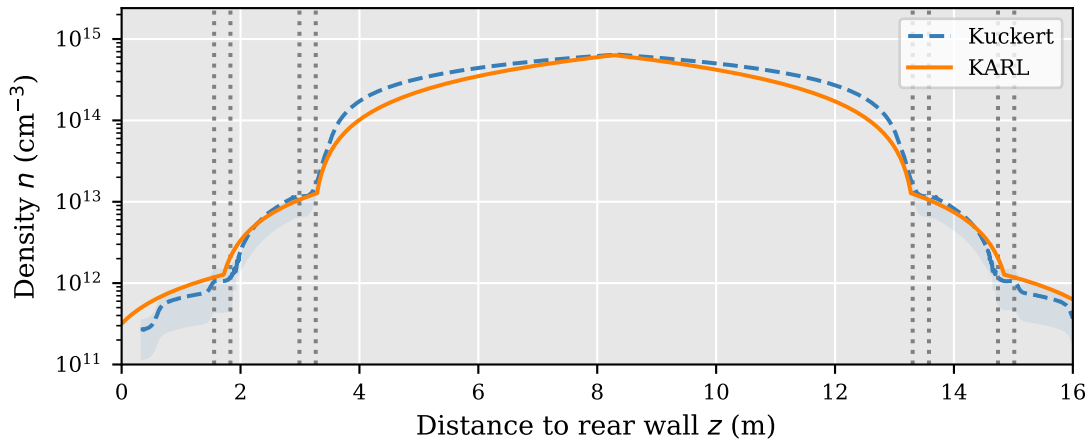


Figure 4.7.: Approximate neutral gas density. The data was taken from Kuckert et al. [49] and mirrored at the inlet position. Six linear functions were used to approximate the density in the simulation. The vertical lines show positions of the pump ports.

4.3.1. Electron Spectrum

The electron spectrum was recorded for 32 segments at different positions in the source. Three distinct segments are compared here: one, which is directly connected to the tritium inlet, a second, which is next to the rear wall and a segment, and a third, which is connected to the DPS. The corresponding spectra can be found in figure 4.8. For comparison with generating or theoretical spectra, an additional factor of \sqrt{E} needs to be taken into account, see section 4.2.1. The factor takes a conversion to logarithmic energy binning and the difference between generating and simulated density spectra into account. For simplicity, in the following this factor will be used implicitly in the description and not discussed any further. Three different energy regions can be identified: a so-called thermal region ($E < 5 \times 10^{-2}$ eV), where the electrons reached thermal equilibrium with the neutral gas, a so called beta-decay region ($E > 10^2$ eV), where the distribution is directly created by the Fermi distribution of beta-decay and a so-called secondary region in between the other two regions.

Beta Region

The energy distribution in the beta region is generated by the beta decay and subsequent streaming of the beta electrons. The scattering probability of high-energy electrons is small enough that at least half of the electrons did not scatter once in the source [54]. Hence, the spectrum at the high-energy region is similar to the beta spectrum. Deviations arise from electron-neutral scattering. The spectrum in the beta-decay region shows little deviation between the three different segments. Thus, the beta-electrons either travel the source unobstructed, or loose the main portion of their energy through ionization and subsequent scattering. Nevertheless, there is a slight difference at the lower end of the beta-region between the rear wall and the other two positions. Electrons which reach the rear wall segment can have traveled at maximum two times through the source through reflection at the spectrometer, while electrons at the DPS traversed the source only once. Therefore, more beta-electrons have scattered before reaching the rear wall segment, which reduces the density at this energy range.

Thermal Region

The energy distribution in the thermal region is generated mostly by elastic collisions with the neutral gas. Thus, the electrons adapt the energy distribution of the gas, a Maxwell-Boltzmann distribution. The spectrum shows slightly higher values at the low-energy

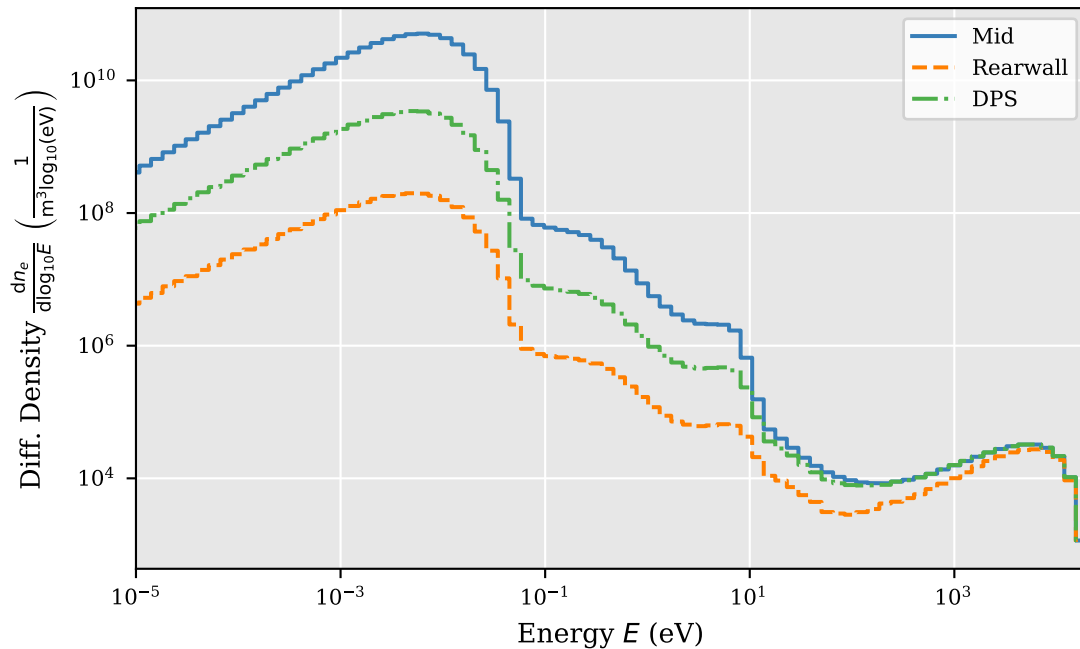


Figure 4.8.: Electron spectrum of three different segments in the source. Mid: central segment connected to the inlet, rear wall: segment in front of the rear wall, DPS: segment next to the DPS. The magnetic field was set to $B = 2.5$ T, the maximum tritium density was set to $n_{\max} = 6.3 \times 10^{14} \text{ cm}^{-3}$, and the temperature to $T = 80$ K.

tail of the spectrum, than expected from the Maxwell-Boltzmann distribution. This is caused by the energy dependent cross section of elastic scattering, see section 4.2.2. The spectral shape in the thermal region is the same for each segment. The similarity to the expected Maxwell-Boltzmann distribution with energy dependent cross section shows, that recombination is only a secondary effect. Otherwise, there would be much fewer particles at low energies, where the cross section of recombination is increased, see figure 2.10. The absolute density is the largest in the center, while it decreases towards both sides. In the center, there are many collisions, which results in increased electron density there. The density at the DPS is higher than at the rear wall. This is caused by the reflection of electrons at the DPS and neutral gas density differences.

Secondary Region

The energy distribution in the secondary region is created by the interplay between the interaction types in the source. Therefore, a full description by a theoretical distribution is not possible. Nevertheless, it is possible to compare the observed features with the cross sections of the interactions. The secondary region shows two distinct features. A power law from 5×10^{-2} eV to 1×10^1 eV and an edge at 1×10^1 eV. The energy of the edge is consistent with the threshold energy for ionization and electronic excitation. Electrons with a lower energy can no longer take part in these interactions. The power law arises as a combination between elastic scattering and rotational and vibrational excitation. The rotational excitation has a threshold energy of 5×10^{-2} eV, which is consistent with the end of the power law. The absolute values of each region are different from each other. Similar to the thermal region, there are more scatterings in the center than at the sides. So the density is higher there. The electrons are reflected at the DPS. Therefore, the density is higher in that region at the rear wall side.

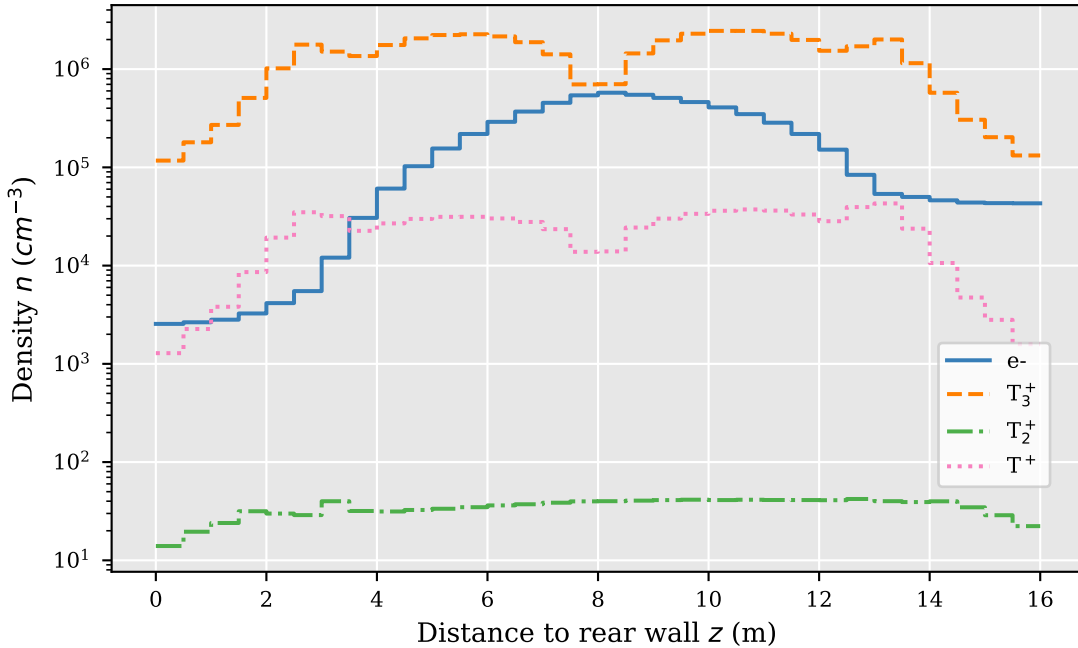


Figure 4.9.: Longitudinal particle densities. Tritium is injected at 8 m distance to the rear wall. The magnetic field was set to $B = 2.5$ T, the maximum tritium density was set to $n_{\max} = 6.3 \times 10^{14} \text{ cm}^{-3}$, and the temperature to $T = 80$ K.

4.3.2. Charged Particle Densities

The density of each particle specie can be obtained by marginalization of the density spectrum. The corresponding distribution along the source tube can be found in figure 4.9. It can be seen that the density profile of each specie is different from each other. The absolute charge density is non-zero in this simulation, despite the fact that electrons and ions are created in pairs. This is not surprising because electrons scatter less and are moving faster, and therefore leave the source tube faster than the ions. Therefore, their density value is strictly smaller than the density of the ions. In the experiment, it can be assumed in first approximation that there exists quasineutrality in the source. Thus, the density differences between electrons and ions will induce an electric field, which will ensure the quasineutrality. This field will be calculated in a separate simulation.

The electron density is dominated by the thermal part of the spectrum. Beta and secondary electrons make up only $4 \times 10^2 \text{ cm}^{-3}$ (not shown). The electron distribution has its maximum in the center of the source and falls off to both sides. The probability of scattering is the highest in the center of the source, hence the electron density is the largest here. The scattering probability is decreased to both sides as the neutral gas density decreases. The electron density is asymmetric towards the inlet, despite the symmetric shape of the density. This is caused by the reflection of electrons at the DPS, which increases the density in this region. Nevertheless, the density before the DPS is not increased drastically, which suggests that electrons can pass the high density region of the inlet.

The ion distribution is different for the three different ion species. The most abundant ions are T_3^+ ions. This is expected due to the high conversion cross section of T^+ and T_2^+ towards T_3^+ . The density of the T_3^+ ions is governed by ionization through electron impact and by elastic scattering with the neutral gas. Ionization is most probable in the center, where the neutral gas density is the highest. The resulting density of ionization is superposed by the streaming process, caused by the elastic scattering. The motion of ions

is aligned with the bulk velocity of the gas. Thus, the ions are transported to both sides of the source, increasing the density in these regions. The density drops in the region in front of the rear wall and in front of the DPS. This is caused by the reduction of the neutral gas density and the drop out of the neutral gas drift.

The density of T^+ is distributed similarly to the density of T_3^+ . The shape of the spectrum is created by the same effects as of T_3^+ , namely elastic scattering with neutral gas and particle transport. The density of T^+ is lower than the density of T_3^+ . In this simulation, T^+ can only be created through dissociative ionization. The cross section of this reaction is significantly lower than for non-dissociative ionization. Therefore, less T^+ is created in comparison to T_3^+ , which is created through the efficient conversion of T_2^+ . Additionally, T^+ can be converted to T_3^+ through ternary association, which lowers the density of T^+ in comparison to the density of T_3^+ .

The density of T_2^+ is significantly different from the other two ion species. The shape is almost constant, and the density is significantly lower. The cross section of cluster formation is higher than the cross section for charge transfer. Therefore, T_2^+ ions mostly exist only for short time between creation and their first interaction. Thus, the density of T_2^+ is significantly lower. The probability for cluster formation is dependent on the tritium density, while the creation mechanism through beta decay and ionization is also dependent on the tritium density. The T_2^+ density therefore shows no large longitudinal variation. Nevertheless, there is a slight decrease of the density in front of the rear wall and the DPS. The mean free path of the particles has increased enough that some particles can leave the source, which reduces the density.

4.3.3. Charged Particle Currents

The longitudinal particle current was determined through 33 virtual planes in longitudinal direction. The planes were aligned in such a way that the first and last longitudinal plane coincide with the rear wall and the passage to the DPS. The corresponding longitudinal current profile can be found in figure 4.10.

The shape of the electron current is as expected. Electrons are reflected at the DPS and the corresponding current is therefore zero. Electrons are most likely to be terminated at the rear wall. Thus, the electron current is the highest here. The electron current decreases continuously from the rear wall towards the DPS. Hence, the electrons can move from the upstream side towards the downstream side and are not hindered from passing by the neutral gas flow.

The ions are created in the center and stream to both sides. There is no driving force of the ions towards the other side of the inlet. Thus, the ion current at the inlet (8 m) is zero. The current heading towards the DPS and towards the rear wall is almost identical. The differences can be explained by the accessory tritium gas between the first pump and the rear wall.

The sum of the ion current leaving the source at the DPS and at the rear wall is below the electron current leaving at the rear wall. This can only be explained through an ion current, which is directed towards the beam tube. The corresponding current was detected through a radial virtual plane located at the beam tube walls. The corresponding current can be found in figure 4.11. This current is caused by the change of position of the guiding center after elastic scattering. The difference in position is dependent on the Larmor radius of the particle, which in turn scales with the square root of the mass. Additionally, the cross section of ion scattering is much higher than for electron scattering. Therefore, more collisions occur, which shift the guiding center. Thus, the radial ion current is expected to be significantly higher than the radial electron current.

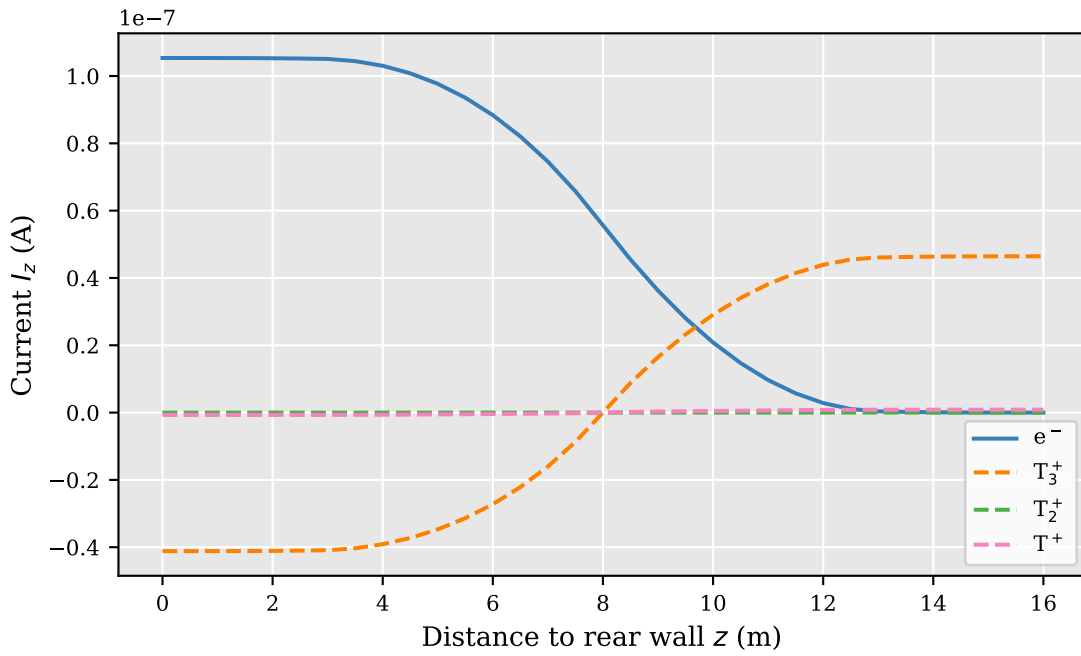


Figure 4.10.: Longitudinal particle currents. The sign of the current corresponds to the direction of the particle flow multiplied with the sign of the particle charge. Tritium is injected at 8 m distance to the rear wall.

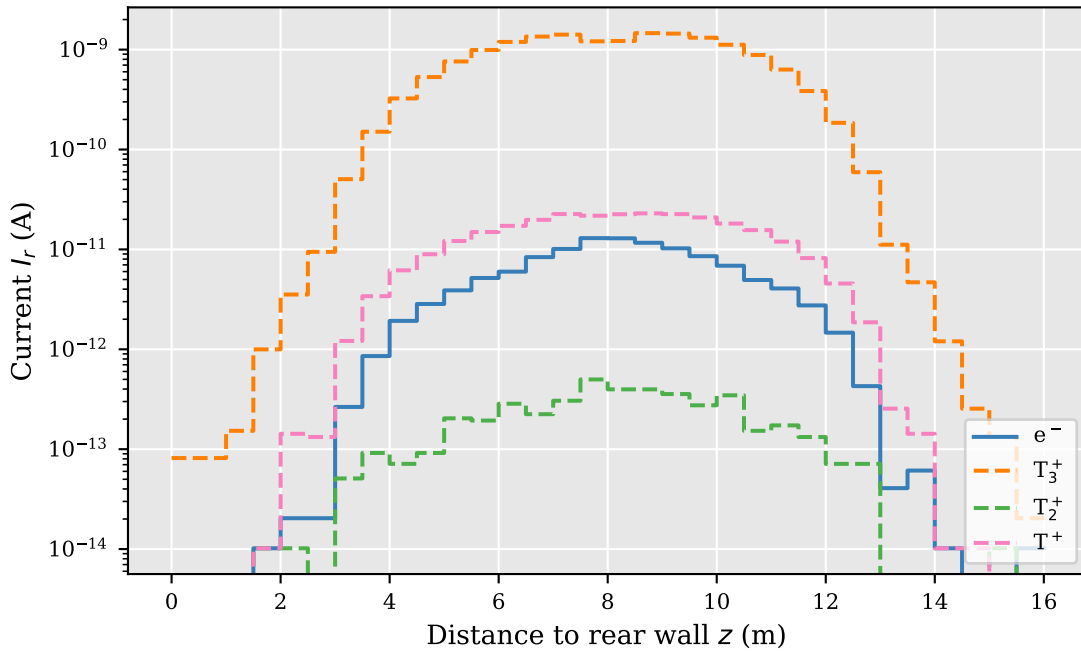


Figure 4.11.: Source tube currents. Absolute radial particle current towards the beam tube in longitudinal direction. The plateaus mark the longitudinal bin width, where the total current flows through. Tritium is injected at 8 m distance to the rear wall. The magnetic field was set to $B = 2.5$ T, the maximum tritium density was set to $n_{\max} = 6.3 \times 10^{14} \text{ cm}^{-3}$, and the temperature to $T = 80$ K.

The absolute current to the tube is also influenced by the density profile of electrons and ions. There is no analytic expression of the radial currents. It can be seen that the shape of the current towards the beam tube is similar to the shape of the neutral particle density. This is caused by the increased elastic scattering probability in the center due to the increased neutral gas density. The T^+ current is below the T_3^+ current, which is caused by the density difference and the different Larmor radius of the two ion species. The current of T^+ is in the same order of magnitude than the current of the electrons, even though the masses of both species are significantly different. This behavior is caused by the large difference in density. There is a contribution of T_2^+ to the radial current. This means that there must be a non-negligible amount of charge transfer reactions, or that enough T_2^+ is created close to the beam tube walls. The shape of the T_2^+ current does not coincide perfectly with the tritium density. Thus, it must be assumed in first order that both effects play a role.

4.3.4. Influence of External Parameters

A specific choice of parameters was made in the simulation presented above. The parameters were chosen to be as close to the current measurement settings as possible. Nevertheless, the simulation allows for a simple comparison of different parameter settings in the source. Three different parameters were investigated here: the tritium gas density, the tritium gas temperature and the magnetic background field strength.

4.3.4.1. Tritium Gas Density

The tritium density can be changed in the experiment. In KNM1, for example, the density was set to approximately 22 % of the nominal value and in KNM2 to 84 % of the nominal value [55]. This change of density can also be investigated by simulation. The tritium density is an important input parameter for the simulation. It has various effects on the charged particle behavior. It acts as an interaction partner as well as a source for high-energy electrons. Because of the intricate connection between the different interactions of the charged particles, it is beneficial to use the simulation to investigate the different behavior. Three different density settings are compared quantitatively: The nominal case, where the density is set to the current maximum of the column density, a case with half the maximum density, and another case with 10 % of the maximum density. The corresponding electron spectra can be found in figure 4.12.

It can be seen that there is no significant difference between the case of nominal density and half nominal density. The absolute density is lower, but the spectral shape is preserved. The more drastic difference can be seen in the simulation with 10 % injection density. Here, the shape of the thermal region is significantly changed to the other two simulations. No clear distinction between the thermal and the secondary region is discernible. Also, the maximum of the left-over thermal region is no longer at the thermal energy, but is shifted to the right. Hence, the electrons do not reach thermal equilibrium any longer with the neutral gas and can travel the source more freely. This is a first indication that the plasma will behave differently at 10 % than at the other two settings. Nevertheless, a thorough investigation with the electric field has to be conducted to reach a final conclusion.

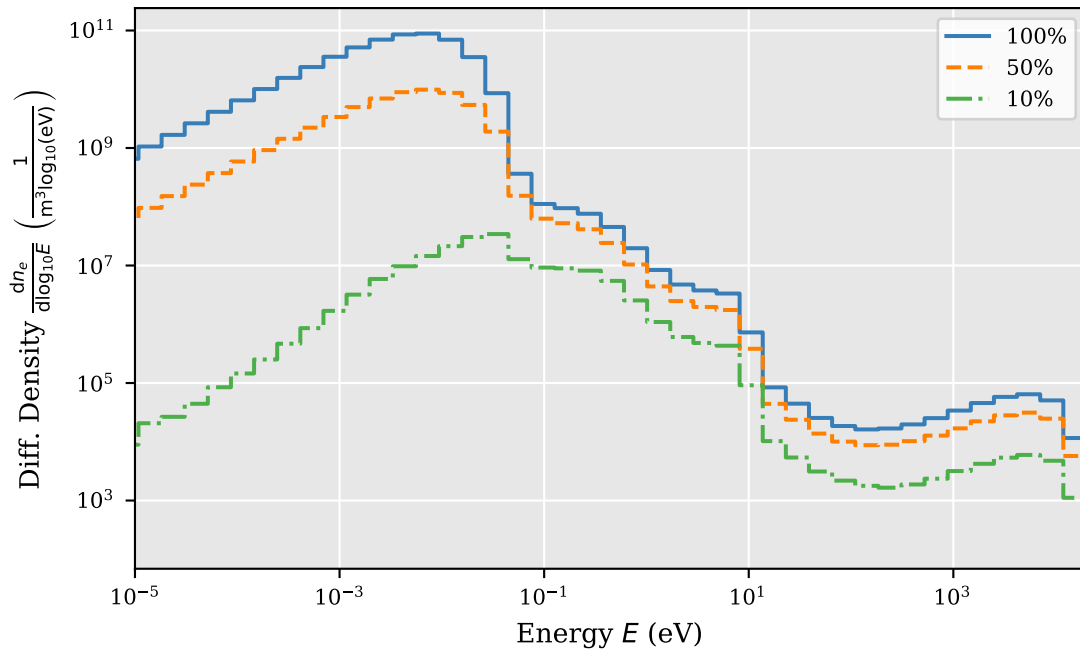


Figure 4.12.: Spectrum at different gas densities. 100 % corresponds to an inlet density of $n_{\text{in}} = 6.34 \times 10^{14} \text{ cm}^{-3}$. The source temperature was set to $T = 80 \text{ K}$, and the magnetic field strength to $B = 2.5 \text{ T}$. The spectra were recorded at 8 m distance to the rear wall.

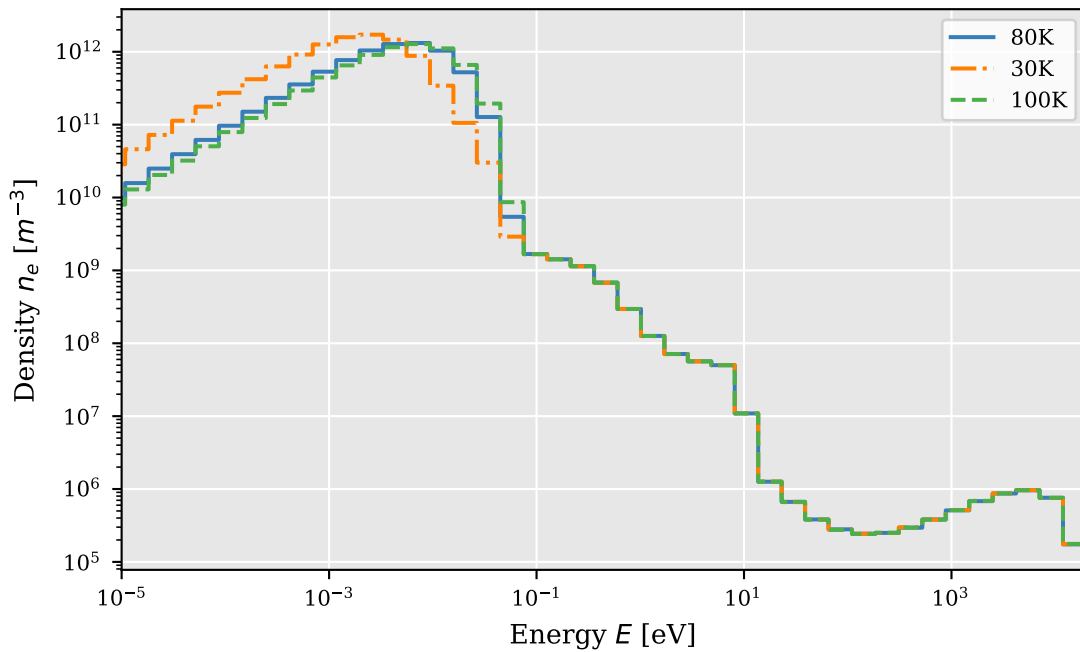


Figure 4.13.: Spectrum at different gas temperatures. The injection density was set to $n_{\text{in}} = 6.34 \times 10^{14} \text{ cm}^{-3}$, and the magnetic field strength to $B = 2.5 \text{ T}$. The spectra were recorded at 8 m distance to the rear wall.

4.3.4.2. Tritium Gas Temperature

The gas temperature can be changed in the experiment in the region of 28 K to 37 K and 80 K to 115 K [6]. The temperature can have an influence on the charged particle motion, since elastic scattering is the most probable interaction for most energies. Therefore, three different temperature settings are compared here: a setting with 30 K, with 80 K and with 100 K. The corresponding electron spectra can be found in figure 4.13. It can be seen that the general shape of the three spectra does not change significantly. Only the maximum of the thermal region shifts to the corresponding energy ($E_{\text{th}} = k_{\text{B}}T$). It is not expected that the plasma will behave significantly different from these three cases.

4.3.4.3. Magnetic Background Field

The magnetic field strength can be adjusted in the experiment. In most of the previous measurement runs, the field value is set to $B = 2.5$ T [6]. Nevertheless, the field strength can be lowered for commissioning measurements. Simulations showed that the magnetic field strength has no significant influence on the electron spectrum. Nevertheless, it can have an influence on the radial movement of charges in elastic scattering and therefore on the particle currents. The movement in radial direction is governed by the movement per collision, which is dependent on the gyro radius. The gyro radius in turn is influenced by the magnetic field. When there are sufficient scatterings with the neutral gas, then the density and current can be described by classical diffusion [14]. In the case of classical diffusion, the diffusion constant can be calculated as

$$D = \nu r_L^2, \quad (4.32)$$

where r_L is the Larmor radius and ν the collision frequency. It is therefore expected that the diffusion constant scales inversely quadratically with the magnetic field. To test the hypothesis of classical diffusion, three different simulations were performed: a simulation with the nominal magnetic field of 2.5 T and two simulations with lower magnetic field (2 T and 1 T). The resulting radial ion current and radial ion density can be found in figure 4.14. It can be seen that the magnetic field has an influence on the density, as well as on the radial particle current of ions. A quantitative analysis is shown in the following through the use of the diffusion constant.

The diffusion constant can be evaluated in the simulation through the use of Fick's first law of diffusion

$$j = D \cdot \frac{\partial n}{\partial x}. \quad (4.33)$$

In the simulation, the density is evaluated in bins and the current is recorded for planes between those bins. Therefore, the derivative of the density can be replaced with the finite difference. The diffusion constant was derived through a linear fit. The simulated diffusion constants can be found in table 4.1

It can be seen that the simulated diffusion constant scales as expected for classical diffusion. The derived value of the diffusion constant can also be compared to the expected value, see

Table 4.1.: Fit values of simulated classical diffusion constants. Density and currents were evaluated at 5 m distance to the rear wall. The diffusion constant was derived through linear fit with equation 4.33.

B_z (T)	D_{sim} (m ² /s)	$D_{\text{sim}} \cdot B^2$ (T ² m ² /s)
1	$(2.36 \pm 0.03) \times 10^{-4}$	$(2.36 \pm 0.03) \times 10^{-4}$
2	$(5.78 \pm 0.18) \times 10^{-5}$	$(2.31 \pm 0.07) \times 10^{-4}$
2.5	$(3.66 \pm 0.14) \times 10^{-5}$	$(2.29 \pm 0.09) \times 10^{-4}$

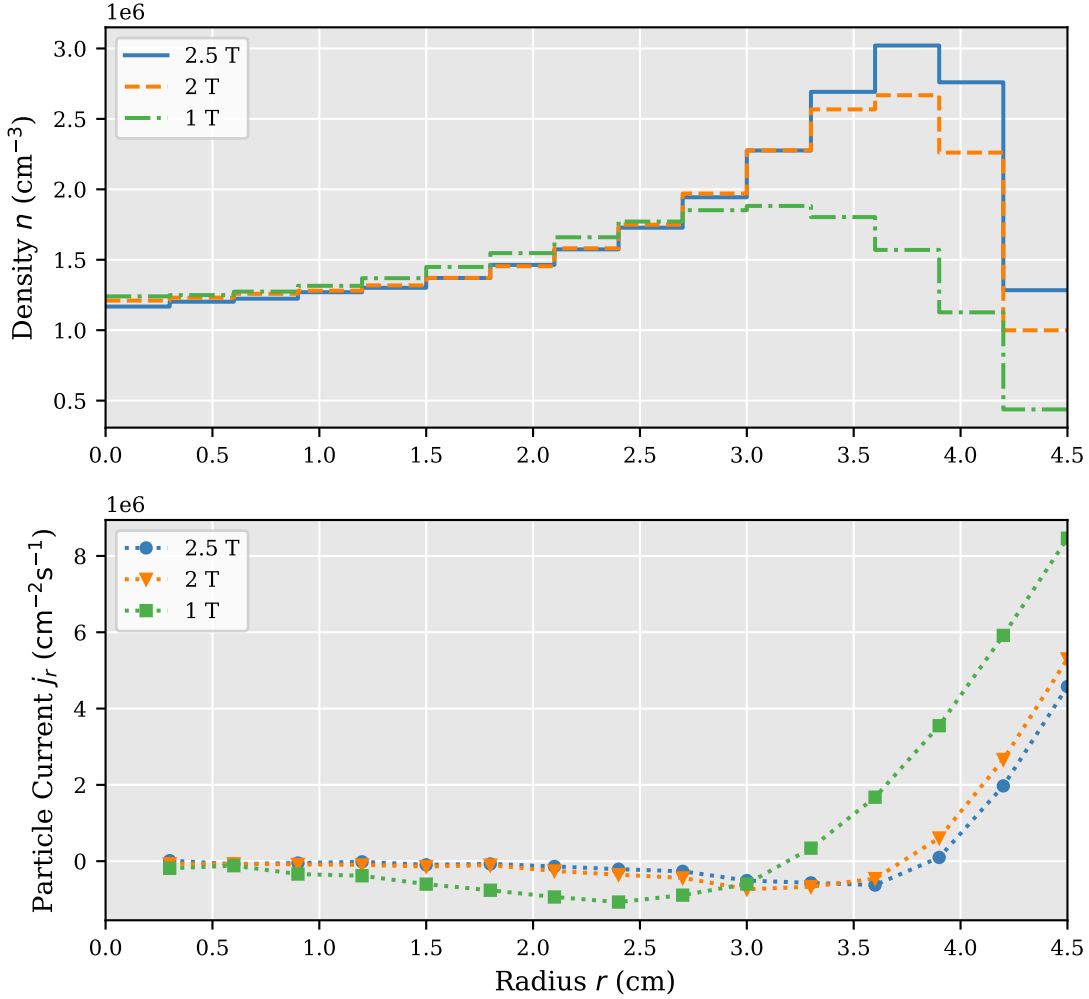


Figure 4.14.: Radial ion currents and densities. Simulated at different magnetic field strength. The values are taken at 5 m distance to the rear wall.

equation 4.32. The expected value cannot be specified directly but in a value range, because of the longitudinal bin width. Here it is assumed that the density of the longitudinal bin lies between $2.3 \times 10^{13} \text{ cm}^{-3}$ to $3.5 \times 10^{13} \text{ cm}^{-3}$ and the magnetic field is $B = 2.5 \text{ T}$. With the Larmor radius of $r_L \approx 1 \times 10^{-3} \text{ cm}$ the diffusion constant follows as $D \approx 3.6 \times 10^{-5} \text{ m}^2/\text{s} - 5.5 \times 10^{-5} \text{ m}^2/\text{s}$. It is apparent that the simulated value lies in this range. In total, it can be concluded that the radial movement of the ions in the center can be described by classical diffusion. Nevertheless, this observation might change, when considering the electric field in simulation.

4.3.5. Comparison to Previous Study

The electron spectrum was derived in a previous study in 2005 by Nastoyashchii et al. [59]. They also derived an electron spectrum of the KATRIN source through a Monte Carlo simulation. The spectrum was derived through an evaluation of the overall time spent in the simulation domain. It was therefore derived independently of the position in the source and can only be construed in first order as a mean spectrum of the electrons in the source. The implemented interactions (ionization, electronic excitation, vibrational and rotational excitation, and elastic scattering) were taken from [81] for hydrogen. Since then, new cross section data is available [35], which is included in KARL. There is no mention in the paper of Nastoyashchii et al., which cross sections were used and how the cross sections were

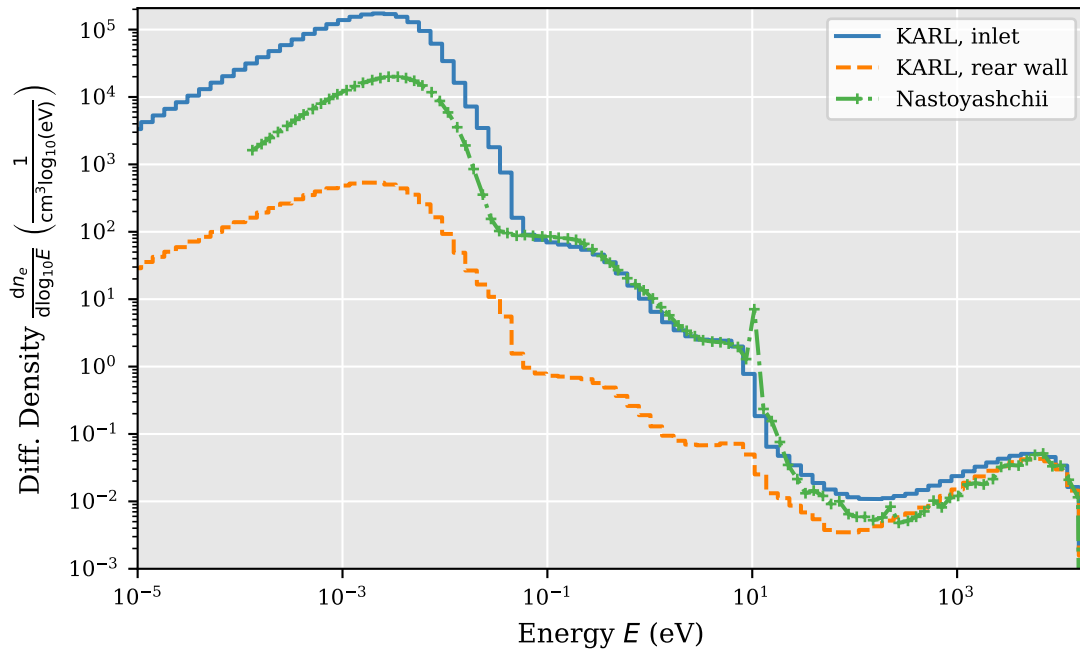


Figure 4.15.: Spectrum comparison with previous study. The data from Nastoyashchii et al. [59] is compared to the spectrum gained from KARL at two positions in the source, a segment next to the rear wall and a segment directly at the inlet. The simulation was performed at the same settings ($T = 30$ K, $B = 3.6$ T and $n_{\text{inj}} = 1 \times 10^{15} \text{ cm}^{-3}$). The results of Nastoyashchii et al. were scaled, such that the spectrum at the high-energy region coincides with the simulation results of KARL.

parametrized. Thus, there is no comparison possible between the used cross sections of KARL and the computer code of Nastoyashchii et al.

The temperature of the source was set to $T = 30$ K in the simulation of Nastoyashchii et al., the former nominal value. Also, the maximal density was set to the former nominal value of $n_{\text{inj}} = 1 \times 10^{15} \text{ cm}^{-3}$. There is no explicit mention of the used magnetic field in the paper, but at that time the nominal value was set to $B = 3.6$ T. So, in the following, the presented simulation results were also performed at that field value. The spectrum can be found in figure 4.15

It can be seen that the distribution of Nastoyashchii et al. shows similar features as the simulation with KARL: a thermal region, a beta-region and a secondary region. The general shape of these regions is similar to the simulation at hand. Nevertheless, there exist differences, which will be discussed in the following.

The results of Nastoyashchii et al. only provide a mean particle density of the source. It can be seen in the results from the KARL simulation that there exist significant differences of the spectrum at the different positions in the source. It is expected that electrons close to the rear wall scatter less than in the central part of the source. Therefore, the density of these electrons is reduced. This is not applicable to the high-energy electrons, which scatter seldom. Thus, their density is less susceptible to the position inside the source. The spatial differences of the spectrum might change the model of the plasma. Nastoyashchii et al. for example, assume implicitly in their calculation of the plasma potential that the electron density of the high-energy electrons can be neglected, whereas our simulations show, that this assumption is not true for all positions in the source. Especially close to the rear wall, the relative energy density of high-energy electrons and low-energy electrons is comparable. Thus, a different plasma description is necessary for this region, which also

includes high-energy electrons.

There exists a spike (one data point) at 10 eV in the results of Nastoyashchii et al., which is not existent in the KARL simulation results. The existence of this peak is important, because there might be plasma instabilities linked to it. The slope of the electron spectrum is positive here, which is a first indicator of an instability through the Penrose criterion [66]. Nastoyashchii et al. do not specify the origin of this peak and provide no information on the statistics of the simulation. In the KARL simulation, this peak does not occur, even at different random number seeds. A physical explanation was not found for this peak. Therefore, it is assumed that it originated from statistical uncertainty.

The thermal region of Nastoyashchii et al. shows a slightly higher maximum than the simulation results of KARL, and a slightly different shape: there are fewer electrons with lower energies in the simulation of Nastoyashchii et al. than in the KARL simulation. It is unclear, how this difference is formed. A first guess is, that the cross section of elastic scattering was set to a fixed value for low energies in the Nastoyashchii et al. simulation. Thus, the difference in the spectrum is similar to the difference in the test simulations of elastic scattering, see section 4.2.2. Nevertheless, the test simulation of elastic scattering of KARL reinforces the trust in the thermal region of the KARL simulation results. Hence, the simulation results of KARL show clear superiority to the state of the art.

4.4. Simulation with Electric Background Field

The simulation results of the previous section were performed without any electric field in the source. The density distribution of electrons and ions, see figure 4.9 suggests, that there are electric fields, which enforce quasineutrality in the source. Additionally, it is expected that there is a boundary layer electric field in the source, see section 3.3.1. This field is also not taken into account in the previous simulation. In context of this thesis, the ACRONYM simulation tool is developed to provide a precise view on the electric field given an input electron spectrum and ion currents. These simulations will be described in the following chapter. Nevertheless, at this point it is possible to investigate the influence of an electric field on the simulation results without the use of ACRONYM by either providing an external field from first principles or by deriving an electric field from the density data of KARL. Both paths will be investigated in the following. First, it will be analyzed how a given rear wall potential influences the simulation result. Secondly, the density results of KARL will be used to calculate an electric field, which is then used to investigate the behavior of the particles under this field.

4.4.1. Rear Wall Field

The contact potential differences between the rear wall and the source tube can produce an electric field, see section 2.2. A power supply, connected to the rear wall, can apply an additional potential to compensate for the contact potential differences. There is no direct in situ measurement possible at the moment to determine the electric field in front of the rear wall. Hence, it is of interest to investigate the charged particle behavior at different rear wall potentials through simulation. In the following three different cases are compared: $U_{\text{rw}} = 20 \text{ meV}$, -20 meV and 0 meV . The values are chosen to reflect the case, where the absolute rear wall potential is slightly higher than the thermal energy of the particles ($E_{\text{th}} \approx 6.9 \text{ eV}$). The potential is investigated at positive and negative values. The corresponding longitudinal densities can be found in figure 4.16.

It can be seen, that the influence of the rear wall potential is dependent on the particle type and sign of the potential. In the following, the major differences between the simulations with and without rear wall potential are discussed.

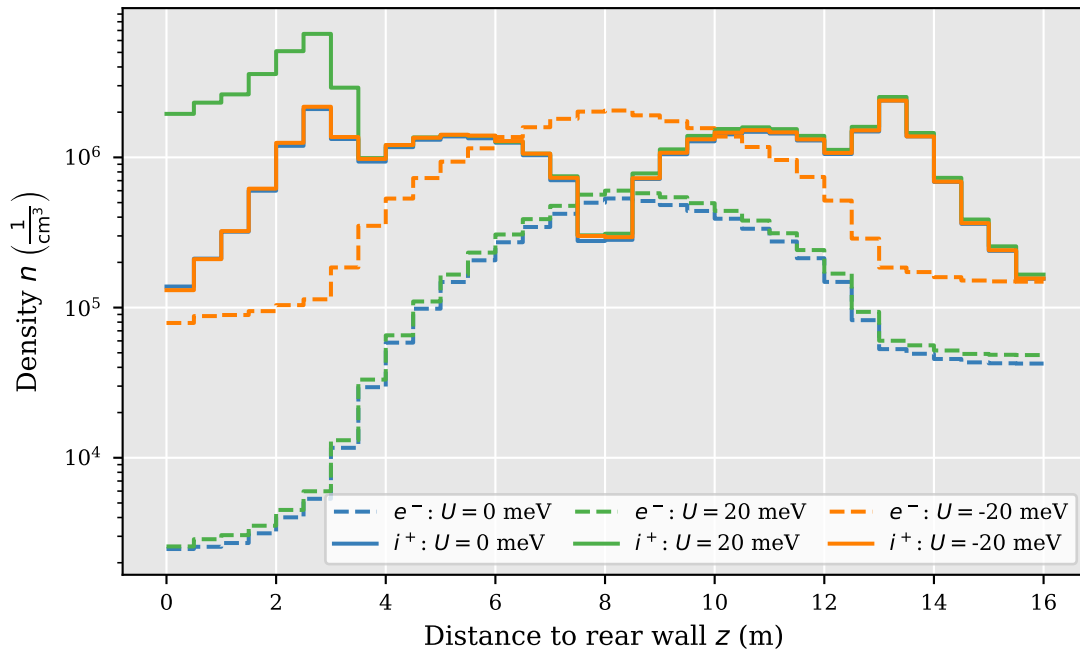


Figure 4.16.: Charged particle density with rear wall potential. The rear wall potential was set to value U . The magnetic field was set to $B = 2.5$ T, the maximum tritium density was set to $n_{\max} = 6.3 \times 10^{14} \text{ cm}^{-3}$, and the temperature to $T = 80$ K. The density of the electrons is denoted as e^- . The density of the different ion species is combined in the total density, denoted as i^+ .

In the simulation with positive rear wall potential, a fraction of the ions is reflected by the potential. The reflected ions travel towards the center of the source. The probability of ion-neutral collision increases towards the center. Until a certain point, the ions are reflected back towards the rear wall, through the stream of outgoing gas. The ions can gain energy through the scattering process. Thus, they might cross the potential wall at some point. Additionally, the guiding center of the ions can change position in each collision with the neutral gas. Hence, trapped ions can move perpendicular to the magnetic field lines and neutralize at the beam tube. In total, the density of ions is increased between the rear wall and the first pump port. The density in the rest of the source is not influenced by the potential of the rear wall, because the stream of neutral particles reduces the stream of reflected ions into the central part of the source to a bare minimum.

The electron density is not significantly influenced by the positive rear wall potential. This is expected, because they already move in the direction of the rear wall. The positive potential accelerates the electrons towards the rear wall even further. The acceleration region is only present close to the rear wall. Thus, the reduction of the density through the acceleration is therefore not resolved here.

In the simulation with a negative rear wall potential, a fraction of the electrons is reflected by the potential. In contrast to the positive rear potential case, they do not only accumulate in front of the rear wall, but throughout the source. The scattering probability for electrons is much lower than for ions. Thus, they are not reflected as much by the neutral gas flow. Therefore, the density in the whole source increases. While travelling the source, the electrons can gain energy through scattering. Hence, they can pass the potential barrier at the rear wall at some point. The shape of the ion density stays the same at negative rear wall potentials. The same argument, for the electrons in the positive rear wall potential case, applies here. The ion movement is only influenced in front of the rear wall, which is not resolved in this simulation.

In both cases, the density of the charged particles increases, because the particles stay longer in the source. In contrast, the overall longitudinal current does not change (not shown). Almost the same amount of electrons and ions is produced through ionization. Thus, these particles will move towards the rear wall eventually. Only those ions and electrons, which have scattered much, leave through the beam tube walls.

In total, it could be shown that a rear wall potential has a significant influence on the motion and density of charged particles. It is apparent, that a potential at the rear wall alone does not reinstate quasineutrality in the source. Nevertheless, it seems that a negative potential wall is likely to occur at the rear wall region as a result of the observed reduced space charge density in the simulation with negative potential.

4.4.2. Field from Density Data

The density generated by the field free simulations shows a large difference between the density of the electrons and the ions. Such a particle distribution will generate an electric field, which in turn will influence the particle distribution itself. A starting point for the simulations with an electric field can be obtained by the use of a Poisson solver. This solver will generate an electric field from the density of the field free simulation. The results can be used in future simulations with KARL. Thus, new particle distributions are produced, and an iterative cycle can be started. In the following, the Poisson solver used will be presented first. In a second step, the solver will be applied to the data of the field free simulation and a new simulation with the generated field will be performed.

4.4.2.1. Poisson Solver

The density data of the KARL simulation can be used to solve for the electrostatic potential U in the source through the Poisson equation

$$\nabla^2 U = -4\pi\rho. \quad (4.34)$$

The charge density ρ is directly calculated from the number densities

$$\rho = e \cdot (n_i - n_e). \quad (4.35)$$

It is assumed that the potential has an azimuthal symmetry. The Poisson equation in cylinder coordinates then reads as

$$\frac{1}{r} \frac{\partial U}{\partial r} + \frac{\partial^2 U}{\partial r^2} + \frac{\partial^2 U}{\partial z^2} = -4\pi\rho. \quad (4.36)$$

This equation can be used for all cases, where the radius is non-zero. In the limit of zero radius, the first summand tends to

$$\lim_{r \rightarrow 0} \frac{1}{r} \frac{\partial U}{\partial r} = \frac{\partial^2 U}{\partial r^2}, \quad (4.37)$$

through the use of L'Hôpital's rule.

The data of the KARL simulations is not available continuously, but in discrete bins. So the Poisson equation has to be transformed into discrete coordinates

$$r = i\Delta r, \quad (4.38)$$

$$z = j\Delta z, \quad (4.39)$$

with the step size Δr and Δz in radial and longitudinal direction respectively. Additionally, the bins of the simulation stretch over multiple positions. In the following, it is therefore

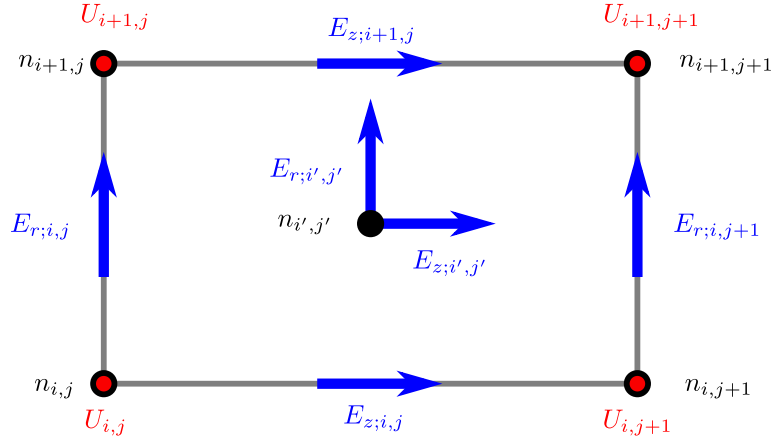


Figure 4.17.: Indexing of discrete values for the Poisson solver. The simulated density of KARL n' is assumed to be located in the center of the bin. The density is extrapolated to the bin corners (unprimed variables). The field and potential values are calculated on the unprimed grid. In a post processing step, the electric field is extrapolated back into the center of the bin.

assumed that the density of a bin is known at its center. On the other hand, the potential values of the rear wall and the tube wall are given at the corners of the bins. For simplicity of the algorithm, it was therefore decided to extrapolate the density to the bin corners, see figure 4.17. The density at the bins corners (i, j) , which are surrounded by four cells, is calculated through the mean of the surrounding cells (i', j') . The density at the corners with $i = 0$ is calculated from the mean of the two adjacent bins, while the density at the boundaries of the simulation domain is set to the mean of the two surrounding bins.

With the new indices of the potential and density, it is possible to rewrite Poisson's equation with the method of central differences. In the end, the potential at a specific position inside the source can be calculated from the neighboring potential values and the density through

$$U_{i,j} = \frac{1}{\frac{2}{\Delta r^2} + \frac{2}{\Delta z^2}} \cdot \left(4\pi\rho_{i,j} + \frac{U_{i+1,j}}{\Delta r^2} \left(1 + \frac{1}{2i} \right) + \frac{U_{i-1,j}}{\Delta r^2} \left(1 - \frac{1}{2i} \right) + \frac{1}{\Delta z^2} (U_{i,j-1} - U_{i,j+1}) \right), \quad (4.40)$$

$$U_{0,j} = \frac{1}{\frac{4}{\Delta r^2} + \frac{2}{\Delta z^2}} \cdot \left(4\pi\rho_{0,j} + \frac{4}{\Delta r^2} U_{1,j} + \frac{1}{\Delta z^2} (U_{0,j-1} + U_{0,j+1}) \right). \quad (4.41)$$

Thus, the potential at each position can be solved through an iterative approach given correct boundary conditions. This model is subject to the following conditions: the Dirichlet boundary and the Neumann boundary. The Dirichlet boundary is used, when the potential at specific points is known. In the following, these points include the beam tube surface and the rear wall surface, where the potential is set to zero, and U_{rw} respectively. The Neumann boundary is used, when the first derivative of the potential is known, namely the electric field. The electric field is in general not known for the source tube. Nevertheless, it can be assumed that the electric field at large distances from the source is zero. Thus, this boundary condition is used at the transition towards the DPS. In total, the approach can be summarized by the following steps:

1. Initialize the potential to zero.
2. Set the corresponding values of the Dirichlet boundary condition to the specified locations.

3. Loop over all possible inner potential values and determine their values through equations 4.40 and 4.41.
4. Redo step 3. for a specified number of times.
5. Determine the difference between of the calculated potential and the density through equation 4.34 for all positions.
6. If the sum of the absolute differences is below a certain threshold, return the calculated potential array, otherwise go to step 3.

The resulting potential cannot be used directly as input for the KARL simulations, because it takes only electric fields as input. Thus, the electric field must be calculated from the derived potential in a separate step.

The calculation of the electric field follows two steps. First, the electric field (E_r and E_z) between two points (i, j) is calculated from the potential difference in longitudinal and radial direction, see also figure 4.17. Second, the electric field values are extrapolated onto the position (i', j') in the center of the density bins.

4.4.2.2. Simulation with Self Generated Field

For the simulation of KARL with self generated field, first the potential and field values are calculated from the data without electric field, see also section 4.3. The potential and electric field of that calculation can be found in figure 4.18. It can be seen, that the potential values are large in comparison to the thermal energy of the particles. This is expected, because the ion density is much larger, than the electron density. Thus, there is a large positive space charge, which produces such a large field. The shape of the potential follows mostly the shape of the ion density. The corresponding electric field shows regions with positive as well as negative values. So, the charged particles will pass through multiple sections, where they are accelerated and decelerated.

The electric field values are too large, to be used directly in the simulation. Electrons and ions, would be accelerated too much, and some of them would be trapped inside the simulation domain. Nevertheless, the shape of the field can be used as a first approximation for further simulations. The measurement results with Krypton [54] show, that the scale of the potential variation is on the order of $\mathcal{O}(10 \text{ meV to } 100 \text{ meV})$. A factor c_p is used to transform the shape of the potential of the KARL simulation towards this scale. In the following simulation, the factor was set to $c_p = 1 \times 10^{-3}$. The corresponding potential, electric field and density distribution can be found in figure 4.18.

It can be seen, that the field has an influence on the particle densities, which is different for ions and electrons. For the ions, the density did not change significantly. Especially in the center of the source, the density distribution shows only a slight difference. This behavior can be explained by the collisionality of the ions. In the center, they collide very often. Hence, the low field values do not suffice to dominate the movement of the ions. At the sides, the ion density shows different values than before, caused by the reduced collision frequency and interaction with the electric field. It pushes the ions out of the source, which reduces their density.

For the electrons, larger differences between the two simulations are observable. It is noticeable in an increased density, and a change of the shape, which can also be explained by the collisionality of the electrons. The electron movement is only partly dominated by collisions with neutral gas. Thus, the field can shape the density distribution. The field is a product of the different electron and ion densities and tries to reinstate quasineutrality. This process can be observed in the alignment of the electron and ion density shape in the center of the source. Nevertheless, the density of electrons and ions is still significantly

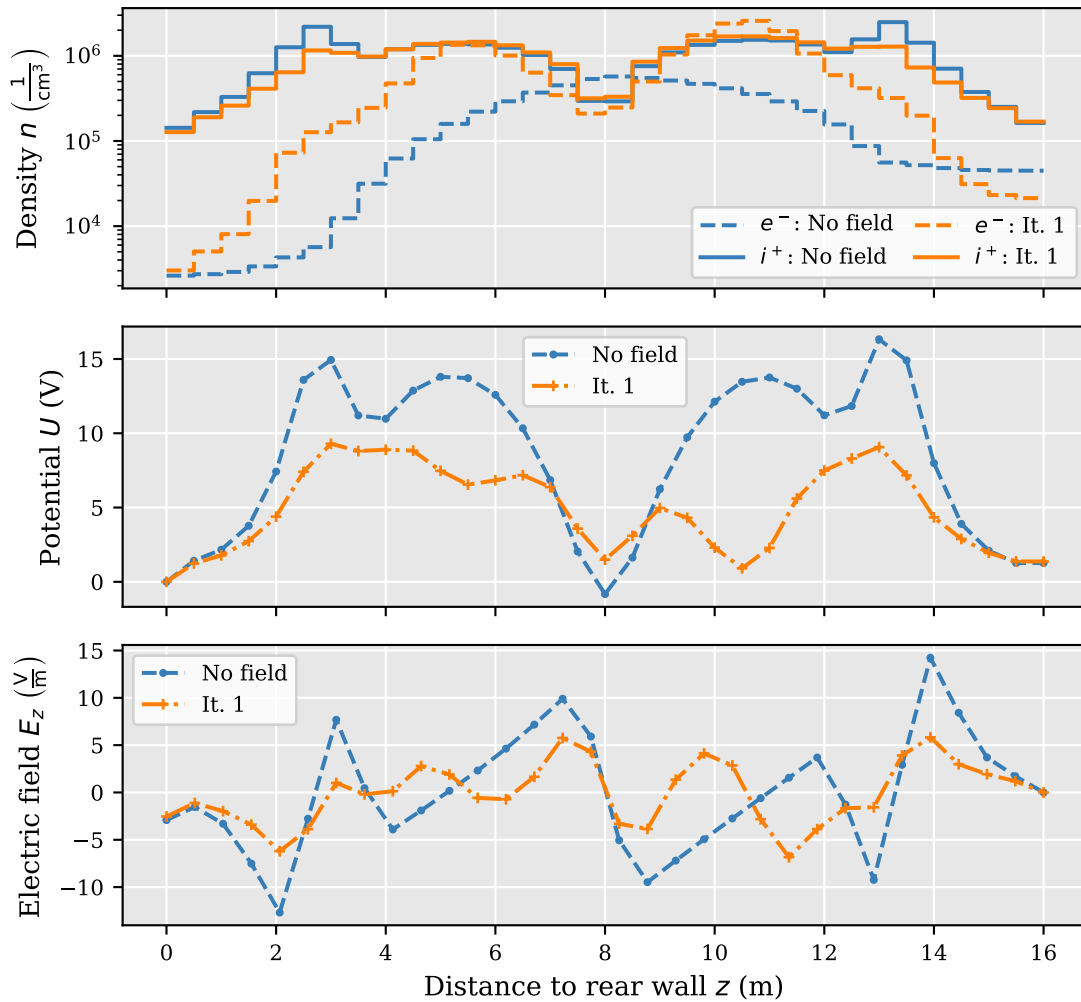


Figure 4.18.: Density, field and potential with and without electric background field. Both simulations were performed with a magnetic field of $B = 2.5$ T, a maximum tritium density of $n_{\text{max}} = 6.3 \times 10^{14} \text{ cm}^{-3}$, and a gas temperature of $T = 80$ K. The derived electric field of the simulation without background field (No field) was used as an input for the simulation with field (It. 1). The density of the electrons is denoted as e^- . The density of the different ion species is combined in the total density, denoted as i^+ .

different close to the rear wall and DPS. This difference to the quasineutrality shows that the field used in the simulation is not the true field inside the source. It has to be refined in future simulations. A starting point might be the field generated by the densities of electrons and ions in the simulation with electric field.

The resulting potential and electric field is also displayed in figure 4.18. It can be seen that the overall shape of the potential changed slightly to lower values. Nevertheless, the values are still larger than the measured field values. Thus, it must be concluded that the field did not reach an equilibrium state and further simulations are necessary.

The electric background field also influences the spectrum of the electrons. In figure 4.19, the spectrum at different positions in the source is shown for the simulation with and without electric field. It can be seen, that the influence of the electric field is dependent on the position inside the source, and the energy region. The different observations will be described in the following.

The shape of the spectrum changed significantly in the thermal region. There are fewer

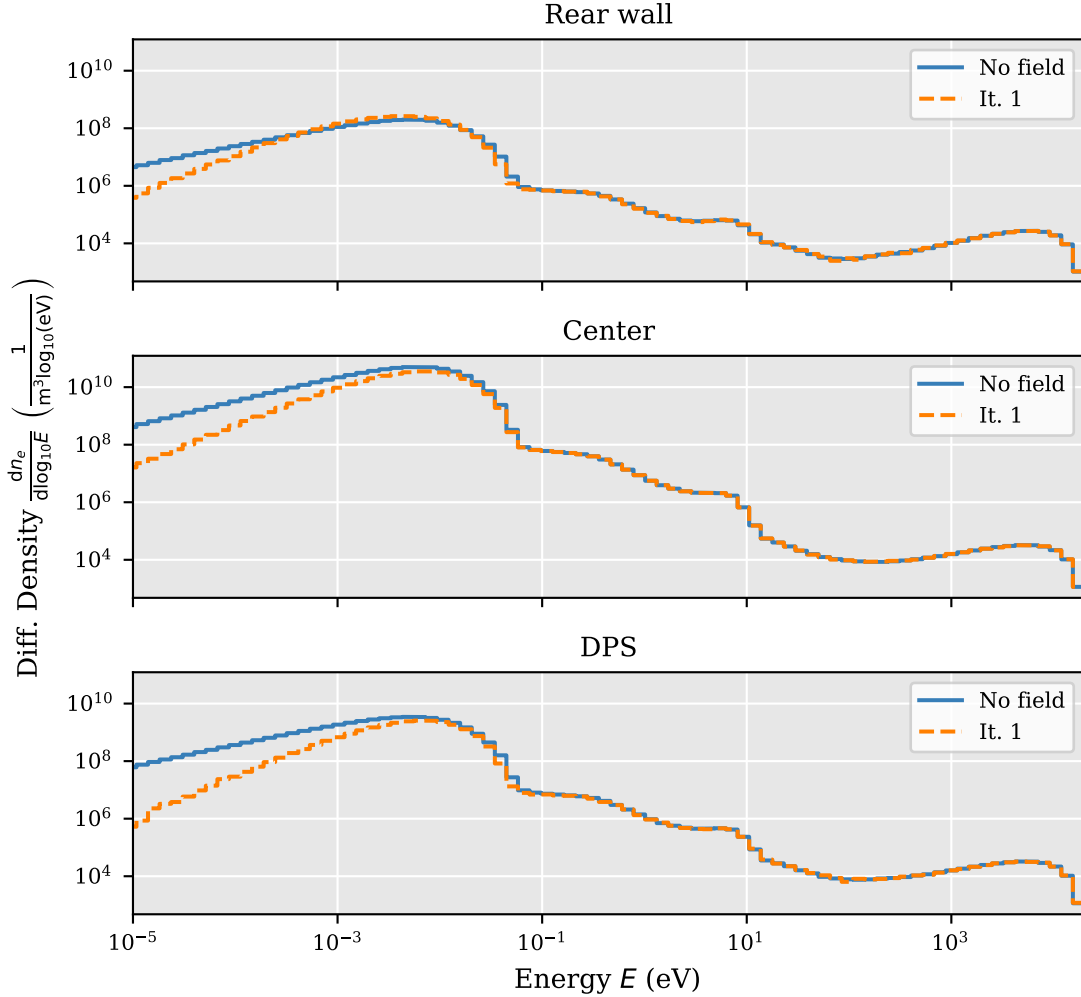


Figure 4.19.: Electron spectrum with and without electric background field. Both simulations were performed with a magnetic field of $B = 2.5$ T, a maximum tritium density of $n_{\max} = 6.3 \times 10^{14} \text{ cm}^{-3}$, and a gas temperature of $T = 80$ K. The derived electric field of the simulation without background field (No field) was used as an input for the simulation with field (It. 1). The spectrum was evaluated at three positions inside the source.

electrons with low-energy than before. This is expected, because all low-energy electrons have been accelerated by the electric field and therefore have gained additional energy. Nevertheless, the overall shape of the thermal region is maintained. This is caused by the scatterings with neutral gas, which is still the dominant interaction channel for the electrons. The difference towards the thermal spectrum is most noticeable at the rear wall. Collisions with neutral gas are infrequent here and thus, changes of the spectrum through the field are most pronounced. However, the potential difference in the simulation between the rear wall and the center are on the order of $\mathcal{O}(1 \text{ meV})$. Thus, large changes fail to appear. This might change in the future with more precise evaluations of the potential. Simulations with ACRONYM indicate that larger potential differences are to be expected, see chapter 6.

The shape of the high-energy tail of the spectrum (beta and transitional region) is not influenced by the electric field. This is expected, because the energy of these particles is much greater than the energy gained through the electric field. Again, this observation is only valid for potential differences on the order of $\mathcal{O}(1 \text{ meV})$ and might change in the

future.

Until now, the potential was derived after completion of a KARL simulation, and it was then used for following simulations. This procedure is rather slow, because subsequent iterations are blocked by the previous. It is conceivable, that an integration of the Poisson solver directly into KARL will produce faster results. In this case, the Poisson solver will be used after a given number of beta decays and the field will then be used directly in the simulation for further decays. This procedure is untested until now and up for future endeavors.

In total, the simulations with electric field have shown that even a small electric field has a significant influence on the shape of the density distributions of the particles. The results indicate that quasineutrality will be reinstated with that field, especially in the center of the source. In the regions with low tritium density, there is still a significant difference between the densities. Thus, more elaborate simulations should be performed in the future.

4.5. Conclusion

In this chapter, a new simulation tool name KARL was presented. By using the Monte Carlo method, it simulates the density and the velocity distribution of charged particles in the KATRIN source. The distributions were obtained through tracking single particles in the source until they are destroyed. The single particles can interact indirectly with each other through density fields. Therefore, this approach allows for the simulation of electron-ion interactions alongside electron-neutral and ion-neutral interactions. The algorithm was tested in multiple test simulations. It could be shown, that the implemented interactions can represent the empirical phenomena.

The KARL simulation tool was used to investigate the spectrum of the electrons in simulations without electric background field. There, the simulated electron spectra showed a trisection: a beta region, a thermal region and a transitional region. The relative density of these regions was found to be dependent on the position in the source. Additionally, the density of electrons and ions depending on the position in the source was determined. Significant differences were found between the densities of the different species. As expected, T_3^+ was the most abundant specie. T_2^+ and T^+ only played a secondary role in the total ion density. The shape of the electron density was significantly different from the ion density. So, electrons scattered less and were less influenced by the neutral gas. Additionally, the electron density in front of the rear wall was found to be lower, than the density in the center of the source. Hence, electrons can travel through the center of the source and do not accumulate in front of the DPS section. In total, the simulation showed, that electrons cannot be treated as collisional in the center of the source, while ions can be treated this way. In front of the rear wall and DPS, both electrons and ions have to be described as non-collisional.

Additionally, the particle current were determined depending on their position in the source through virtual barriers. A non-negligible ion current towards the beam tube was found. The simulated ion current provides a first explanation of the non-zero measured total current without any use of an electric field.

Furthermore, the behavior of the density and spectrum under change of external measurement parameters was investigated. It was found that the spectrum and particle densities are only influenced marginally by the temperature of the neutral gas. The neutral particle density, however, can have a significant influence on the spectrum. When, the density was reduced to 10% of the nominal value, the spectrum changed significantly. The trisection of the spectrum was no longer observed, and the low-energy part of the spectrum could no longer be described by the Maxwell-Boltzmann distribution. Also, the influence of the

magnetic field strength was investigated. It was found, that in the field free case, the ion current towards the beam tube can be described through classical diffusion.

In the end, the influence of an electric field was explored. This influence was first simulated by a contact potential difference between rear wall and tube wall. It was found that a rear wall potential has a significant influence on the charged particle motion, and on the density of the charged particles. A negative potential difference reduced the space charge density. Thus, it was hypothesized, that also the real plasma will show a negative potential towards the rear wall. Secondly, the density distribution of the field free simulation was used to determine an electric field generated by the particles themselves. The field was used as an input for a continuative simulation. Therefore, a Poisson solver was constructed. The resulting potential and electric field showed large values, due to the large total charge density. The field was therefore reduced by a scaling factor in the subsequent simulation to represent more realistic values. The simulation showed, that the field partially reinstates quasineutrality in the center of the source. However, large density differences were still observed in front of the rear wall. Thus, more elaborate simulations are necessary in the future. These simulations might include an internal Poisson solver, which calculates the electric field during the simulation.

Chapter 5

Particle in Cell Simulations with ACRONYM

The evolution of charged particles inside a non-collisional plasma can be described by the Vlasov equation, see equation 3.33, in conjunction with Maxwell's equations. The interplay between the equations make analytic calculations difficult. Numerical methods like particle-in-cell (PIC) simulations can bridge this gap. In PIC simulations, particles are simulated in a continuous space, while their density and currents are calculated on discrete mesh points [41]. These currents and densities are then used to solve Maxwell's equations for a given timestep. The resulting fields are extrapolated to the particle positions. The particles are then moved accordingly.

There exist multiple different PIC codes. They differ significantly in their treatment of the particle motion, the mesh generation and the approach to solve Maxwell's equations. The results presented in this thesis are obtained using the well tested ACRONYM code [42]. Modifications were added to incorporate the special conditions of the KATRIN source.

The first section of this chapter (section 5.1) focuses on the algorithm of the ACRONYM code to provide the groundwork for the extensions of the code. The code specific treatment of the particle motion, the mesh generation and Maxwell solver will be presented here. In the second section (section 5.2), simulation boundary conditions are introduced. An emphasis will be put on the treatment of perfect electrical conductors and their application on a cylindrical boundary, as they are the main boundary type of the KATRIN geometry. The third section (section 5.3) covers backgrounds for the simulation. They include the current background generated by ions, but also the electromagnetic background of the experiment. In the fourth section (section 5.4), the injection of particles is described. This reflects the continuous production of electrons and ions in the source. The fifth section (section 5.5) deals with the translation of the electromagnetic field output from ACRONYM towards electrostatic potentials. Lastly, the newly introduced methods of the code were tested thoroughly to ensure reliable results. The different test methods will be discussed in section 5.6.

5.1. The Particle in Cell Method

The scheme of the particle in cell method was developed to reflect the cause and effect of the particle motion in the plasma, while retaining a good numerical evaluation method. The algorithm scheme is depicted in figure 5.1. The steps of the algorithm are described shortly in this section, and each step itself more thoroughly in the following sections.

The simulation starts with the initial injection of so-called macro particles into a continuous space. The macro particles gain their initial particle properties of position, velocity, mass

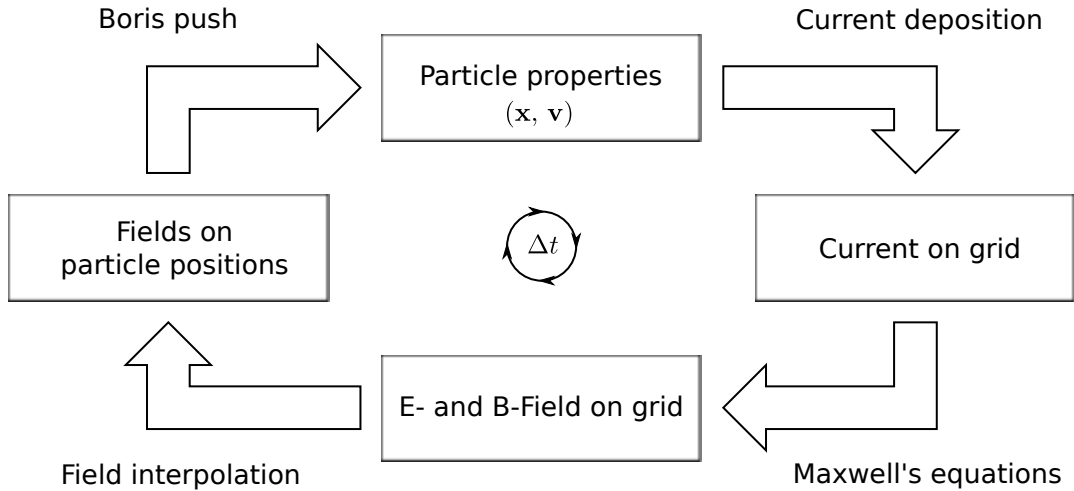


Figure 5.1.: PIC algorithm. Particles are initiated with position x and velocity v . These particles generate a current, which is mapped on a grid. The current is then used to update the electromagnetic fields on the grid for one timestep of length Δt . The fields are then interpolated on the particle positions. The particles are moved according to the electromagnetic field with the Boris push algorithm. Figure adapted from [41].

and charge (scaled by the macro factor). The movement of the macro particles generates an electric current. This current is evaluated on grid positions in the current deposition step. The information on the current is used to solve Maxwell's equations numerically for a predefined timestep. The fields on the grid positions are then interpolated towards the position of the macro particles. The position and velocity is updated in the movement step (Boris push) in dependence on the local electromagnetic fields. Thus, new particle properties are available and the cycle starts again.

The number of cycles N_t which have to be performed depend on the timestep length Δt and the desired time window. The timestep length is dependent on the used algorithms as well as on the fastest physics, which should be resolved, see section 5.1.5. The plasma frequency ω_{pe} (see section 3.4.1) acts as a natural time scale at which most of the plasma physics has taken place. The inverse of the plasma frequency is therefore also called plasma time scale. This assumes that most of the plasma physics is moderated by the motion of electrons. The number of necessary cycles of the algorithm can be written as

$$N_t \approx a \cdot \Delta t \cdot \omega_{pe}, \quad (5.1)$$

where a is a small integer number. The explicit value of a has to be determined through the simulation itself. It is expected that the simulated system will reach an equilibrium state, where the total energy of the electromagnetic fields and the total energy of the particles do not change significantly. At this point it is not beneficial to simulate more timesteps and the simulation can be terminated.

There exists a multitude of different methods for each of the simulation steps. The methods implemented in the ACRONYM code are described in the works of Kilian [41]. Nevertheless, the specific methods used in the context of this thesis are described in the following. They need to be adapted to cope with cylindrical boundary conditions of the KATRIN source.

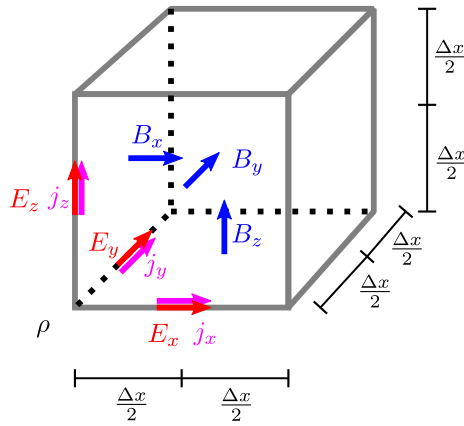


Figure 5.2.: Yee lattice. Electric and magnetic field values are stored at grid positions, which are displaced for half a cell length Δx in each direction. The staggering of the grids can also be displayed by a cubic cell, where the electric field components E_i are located at the cell edges and the magnetic field components B_i are located at the cell faces. The currents j_i are located at the same position as the electric field values. The density ρ is located at the cell corners. Figure concept from [41].

5.1.1. Grids for Currents and Fields

The motion of charged particles can be described through electric currents. They induce electromagnetic fields through Ampere's circuital law. In the simulation, both current and field values are evaluated at grid positions. The grid positions are given by the Yee-grid [85], see also figure 5.2. The Yee-grid consists of two grids, which are staggered by half the grid step size Δx in each direction. The electric field and charge current density are stored at the first grid, the magnetic field on the second grid. This layout allows for a simple numerical evaluation of the curl operator in Maxwell's equations and a simple assessment of the temporal evolution of the electric field, see section 5.1.5 for more information.

This setup can also be described through the use of equal sized cubes, which allows for a simpler enumeration of the grid positions. The electric field components E_i are stored at the center of the cube edges, while the magnetic field components B_i are stored at the center of the cube faces. The components of the charge current density j_i , in the following only named current, are located at the same position as the electric field values. Other information of the particles (particle density ρ and mass current), which are not directly used in the simulation, are also stored on the grid for analysis purposes. The particle density is stored at the cube corners, while the mass current is stored at the cube edges.

5.1.2. Macro Particles

The Vlasov equation (equation 3.33) describes the temporal evolution of the phase space density $f(\mathbf{x}, \mathbf{v}, t)$. In the particle in cell algorithm, the phase space density is discretized into small phase space elements $f_\alpha(\mathbf{x}, \mathbf{v}, t)$. The phase space density can therefore be written as

$$f(\mathbf{x}, \mathbf{v}, t) = \sum_{\alpha=1}^{N_p} f_\alpha(\mathbf{x}, \mathbf{v}, t), \quad (5.2)$$

where N_p is the number of phase space elements. The phase space elements are considered to be localized around the position x_α and the velocity v_α with the formfactors $S_x(\mathbf{x} - \mathbf{x}_\alpha)$ and $S_v(\mathbf{v} - \mathbf{v}_\alpha)$ respectively. Thus, the phase space element can be written as

$$f_\alpha(\mathbf{x}, \mathbf{v}, t) = w_\alpha \cdot S_x(\mathbf{x} - \mathbf{x}_\alpha) \cdot S_v(\mathbf{v} - \mathbf{v}_\alpha), \quad (5.3)$$

where w_α is the so-called macro factor of the phase space element. Following Kilian [41], it can be shown that

$$\frac{\partial w_\alpha}{\partial t} = 0, \quad (5.4)$$

$$w_\alpha \frac{\partial x_\alpha}{\partial t} - w_\alpha v_\alpha = 0, \quad (5.5)$$

$$\frac{\partial v_\alpha}{\partial t} - \frac{qw_\alpha}{mw_\alpha} E(x_\alpha) = 0. \quad (5.6)$$

This means that the macro factor stays constant during the evolution of the phase space element. Additionally, the position x_α of the element changes exactly like standard particles. Furthermore, the velocity v_α of the phase space element changes similarly in an electric field as the velocity of a standard charged particle. Only the mass and the charge of the particle are weighted by the factor w_α . Due to these similarities to standard particles, the phase space elements are also called macro particles. In the simulation, the macro particles are treated like particles, which makes the simulation approach very accessible.

Equation 5.6 shows how the velocity of a macro particle changes in an external field. For simplicity, this calculation did not include, how an external field is evaluated on the position of the particle or how the macro particle interacts with its surroundings. These relations are described by the so-called form factors S_x and S_v from equation 5.3. The form factor can be selected from a wide range of functions. The function must be normalized and zero in the limit of large values. The specific choice of the form factor depends on the target numerical stability of the solution and the calculation effort. In all known PIC codes, the form factor of the velocity S_v is set to a Dirac-Delta function to ensure consistency in the calculation of the Lorentz force [41].

Generally, the spatial form factor S_x can also be chosen to be a Dirac-Delta function. This would mean that each macro particle is only assigned to the next grid point of the Yee-grid. Thus, the current and particle density spikes each time a macro particle crosses from one cell to the other. This would introduce self-forces, and extremely large noise in the simulation. Additionally, the simulation would lose its isotropy because of the Euclidean geometry of the cube [41]. Therefore, the form factor S_x is chosen, throughout this thesis, to be a triangularly shaped cloud with the following structure:

$$S_x(\mathbf{x}) = S_x(x) \cdot S_x(y) \cdot S_x(z) \quad (5.7)$$

$$S_x(x/y/z) = \begin{cases} 0, & x < -\Delta x \\ 1 + x, & -\Delta x \leq x < 0 \\ 1 - x, & 0 < x \leq \Delta x \\ 0 & x > \Delta x \end{cases}. \quad (5.8)$$

This form factor ensures an easy numerical evaluation, while maintaining a good reproduction of spectra and energy conservation of the simulation [41].

5.1.3. Particle Movement

In the previous section, it could be shown, that the phase space elements can be described as macro particles. These particles have to be moved according to their position and velocity, but also according to the electromagnetic fields. Therefore, the fields of the grid have to be extrapolated to the particle positions first. In a second step, the new particle position is determined for a given timestep.

The electric field at the particle position \mathbf{x} is calculated as

$$E_\nu(\mathbf{x}) = \sum_{ijk} S_x(\mathbf{x} - \mathbf{X}_{ijk}^\nu) \cdot E_{\nu,ijk}, \quad (5.9)$$

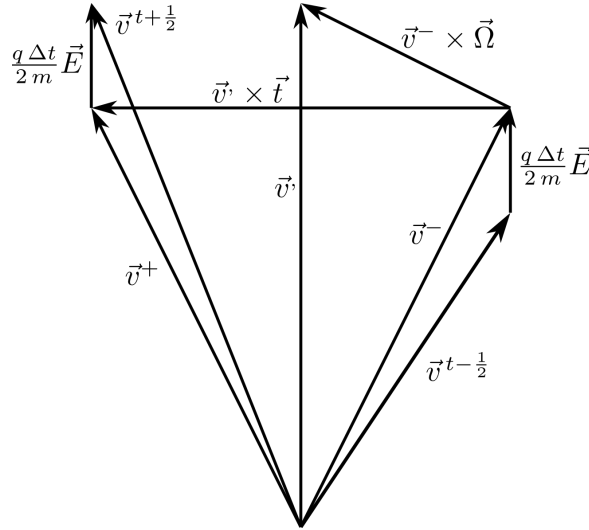


Figure 5.3.: Boris push algorithm. Grafical representation of the update of the velocity at timestep $t - \frac{1}{2}$ towards the new timestep $t + \frac{1}{2}$ (equations 5.13 to 5.18). The velocity is first boosted for half a timestep by the electric field. Second the velocity vector is rotated by the magnetic field. Third the velocity is boosted again for half a timestep by the electric field. Figure taken from [41].

where ν labels the three different Cartesian axis, \mathbf{X}_{ijk}^ν labels the positions of the field component $E_{\nu,ijk}$ in the cell (i, j, k) , and $S_x(\mathbf{x})$ labels the spatial form factor. In the code, the sum is not calculated for all possible cell positions, but only for the cell positions in the near vicinity of the macro particle. This is justified because the form factor of the triangular shaped cloud is only non-zero in proximity of the particle. The calculation of the magnetic field at the position of the particle is performed accordingly.

The electromagnetic field values can then be used to determine the force acting on the particle. In the simulation, only the Lorentz force is considered. The gravitational force is neglected here due to its comparably small value. The actual movement of the particle is performed in discrete timesteps. The equation of motion is solved numerically through the Leapfrog algorithm. In this algorithm, the velocity and the position are not calculated at the same time, but half timesteps apart. Thus, the equation of motion in one dimension calculates to

$$\frac{x_{i+1} - x_i}{\Delta t} = v_{i+1/2}, \quad (5.10)$$

$$m \frac{v_{i+1/2} - v_{i-1/2}}{\Delta t} = F(v_i), \quad (5.11)$$

where the index i denotes the timestep at which the value is available. F is the force acting on the particle, in this case the Lorentz force. The position update is straight forward and does not need any more explanation. The velocity update is more complicated, because the force on the particle is dependent on the velocity of the particle. By assuming that the velocity between two timesteps can be calculated as the mean of the values, it can be formulated that the velocity of the next timestep must read

$$\mathbf{v}_{i+1/2} = \mathbf{v}_{i-1/2} + \frac{q\Delta t}{m} \cdot \left(\mathbf{E}_i + \frac{\mathbf{v}_{i+1/2} + \mathbf{v}_{i-1/2}}{2c} \times \mathbf{B}_t \right). \quad (5.12)$$

This equation can be solved numerically for the velocity $\mathbf{v}_{i+1/2}$ through the use of the Boris push algorithm [65]. The algorithm is numerically stable with high precision and

efficiency [41]. The method can be used for low relativistic particles, up to a gamma factor of $\gamma \approx 1000$ [83]. At the KATRIN experiment, only electrons of energies up to 32 keV (Krypton conversion electrons) are created. This results in a gamma factor of $\gamma = 1.06$, which is well below the limit of the Boris push. Thus, the Boris push can be used without modification and will be described briefly in the following.

The change of the velocity vector is calculated in three steps, see also figure 5.3. First, the particle is accelerated by half a timestep through the electric field

$$\mathbf{v}^- = \mathbf{v}_{i-1/2} + \frac{q\Delta t}{2m} \mathbf{E}_{i-1/2}. \quad (5.13)$$

Secondly, the particle is accelerated by the magnetic field. This can be described through

$$\boldsymbol{\Omega} = \frac{q\Delta t}{2mc} \mathbf{B}_i, \quad (5.14)$$

$$\mathbf{t} = \frac{2\boldsymbol{\Omega}}{1 + \boldsymbol{\Omega} \cdot \boldsymbol{\Omega}}, \quad (5.15)$$

$$\mathbf{v}' = \mathbf{v}^- + \mathbf{v}^- \times \boldsymbol{\Omega} \quad (5.16)$$

$$\mathbf{v}^+ = \mathbf{v}^- + \mathbf{v}' \times \mathbf{t}. \quad (5.17)$$

Thirdly, the particle is accelerated again by half a timestep through the electric field

$$\mathbf{v}_{i+1/2} = \mathbf{v}^+ + \frac{q\Delta t}{2m} \mathbf{E}_{i-1/2}. \quad (5.18)$$

In total, the new velocity was derived from the mass and charge of the particle and the extrapolated electromagnetic field values. The information on the position and velocity can now be used in the current deposition step.

5.1.4. Current Deposition

The macro particle motion can be described by an electric current. In the simulation, this current is projected, for each time step, on the cell edges of the Yee-grid, see section 5.1.1. The specific contributions of each particle are moderated by the form factor, charge, position and velocity of the particle. The naive approach, to use the mean of the contribution before and after moving the particle, fails because the charge continuity equation is not fulfilled. A charge conserving algorithm was proposed by Esirkepov [20]. The derivation of the algorithm is extensive, so the interested reader is referred to Kilian [41] for an accessible description. Only the corner stones will be presented here.

The algorithm hinges on the calculation of the spatial derivative of the current through eight different weights W_i . These weights describe the charge distribution at the corners of a paraxial cube, where two of the corners are the start and end position of the particle. The weights are used to calculate the spatial derivative of the current \mathbf{C} . For the x -component the derivative reads as

$$C_{x,ijk}^{t+1/2}(W_i) = -\frac{\Delta t}{q_\alpha \Delta x} \left(j_{x,i+1/2jk}^{t+1/2} - j_{x,i-1/2jk}^{t+1/2} \right). \quad (5.19)$$

Hence, the current of the particle α at the cell $(i + 1/2, j, k)$ is dependent on the current of the neighboring cell $(i - 1/2, j, k)$. This recursion can be resolved directly, because the form factor of the particle has a finite extension. Thus, at a certain distance from the cell the current contribution can be considered to be zero, which provides the first element of the recursion.

The current deposition step is one of the most time-consuming step of the PIC algorithm. Each of the macro particles contributes not only to the cell it is located in but also to the surrounding cells. Thus, many calls to the computer storage have to be performed, which are time-consuming. The call time can be reduced by sorting the particles before the current deposition step [41].

5.1.5. Maxwell Solver

Maxwell's equations describe how electric and magnetic fields are generated by charges and charge currents. In vacuum, they read as

$$\nabla \times \mathbf{E} = -\frac{1}{c} \frac{\partial \mathbf{B}}{\partial t}, \quad (5.20)$$

$$\nabla \times \mathbf{B} = \frac{1}{c} \frac{\partial \mathbf{E}}{\partial t} + \frac{4\pi}{c} \mathbf{j}, \quad (5.21)$$

$$\nabla \cdot \mathbf{E} = 4\pi \rho, \quad (5.22)$$

$$\nabla \cdot \mathbf{B} = 0. \quad (5.23)$$

It can be seen, that the temporal evolution of the electric and magnetic field can be described only by the current and by the respective other field. This behavior is used in the simulation to generate new field values after a given timestep Δt .

The new field values are determined by their time derivative. The derivative can be represented numerically by their finite differences. Thus, the first two Maxwell's equations (5.20, 5.21) can be written as

$$\frac{\partial \mathbf{B}}{\partial t} \approx \frac{\mathbf{B}^{i+1/2} - \mathbf{B}^{i-1/2}}{\Delta t} = -c \nabla \times \mathbf{E}^i, \quad (5.24)$$

$$\frac{\partial \mathbf{E}}{\partial t} \approx \frac{\mathbf{E}^{i+1} - \mathbf{E}^i}{\Delta t} = c \nabla \times \mathbf{B}^{i+1/2} - 4\pi \mathbf{j}^{i+1/2}, \quad (5.25)$$

where the superscript describes the timestep, when the value is available. Thus, the magnetic and electric fields at the next timestep can be calculated directly from the field values of the previous timestep. This calculation requires the knowledge of the curl of the field values. The curl of the electric and the magnetic field can also be calculated numerically. In the simulation, the electric and magnetic field values are stored in a staggered grid, see 5.1.1. Thus, the curl operator can easily be evaluated from the neighboring field values. In the context of this thesis, the Yee-method is used for the evaluation, where the derivatives are replaced by the central differences. The x -component of the curl, for example, is calculated as

$$\begin{aligned} (\nabla \times \mathbf{E})_x &= \frac{\partial E_z}{\partial y} - \frac{\partial E_y}{\partial z} \\ &\approx \frac{E_z(i, j+1, k) - E_z(i, j, k)}{\Delta x} - \frac{E_y(i, j, k+1) - E_y(i, j, k)}{\Delta x}, \end{aligned} \quad (5.26)$$

where Δx is the step size of the Yee-grid. In the simulation, the step size is chosen in such a way, that Debye shielding effects are resolved (see Section 3.3.1). It is calculated as

$$\Delta x = \sqrt{0.5} \cdot \lambda_D, \quad (5.27)$$

where λ_D is the Debye length.

The step size is linked to the timestep length Δt through the Courant-Friedrichs-Lewy-condition (CFL) [16]. It specifies the maximal timestep for a numerical stable solution. In easy words, it describes that the electric and magnetic field cannot move more than one cell in one timestep, which would otherwise contradict the finite speed of light. For the Yee method it reads as

$$\Delta t < \sqrt{\frac{1}{3}} \frac{\Delta x}{c}, \quad (5.28)$$

where c is the speed of light.

The timestep is also restricted by other requirements of non-numerical nature. In the context of this thesis, the most important conditions are

- $\Delta t < \frac{1}{2\omega_{pe}}$: plasma oscillations have to be sufficiently resolved through the Nyquist-Shannon sampling theorem.
- $\Delta t < \frac{1}{\Omega}$: the gyro motion of the lightest particle must be resolved.

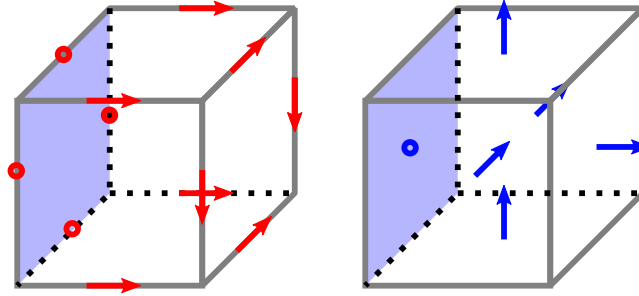


Figure 5.4.: Parallel PEC boundary. Sketch of the electric field (left, red) and magnetic field (right, blue) at a conducting surface, which is aligned parallel to the cell (light blue). Circles indicate positions, where the field value is set to zero.

5.2. Boundary Conditions

In the previous section, it was implicitly assumed that there are sufficient neighboring cells for each simulated cell. This assumption is valid for a central part of the simulated plasma. But, it is apparent that the simulation domain is not infinitely extended. A special treatment of the boundary regions is necessary. This treatment must include a description for the electric and magnetic field, as well for the current and the particle movement. In the context of this thesis, three different boundary conditions were applied: the perfect electrical conductor boundary (PEC), the periodic boundary condition and the perfectly matched layer boundary (PML). These boundary conditions are described in detail in the following.

5.2.1. Perfect Electrical Conductor

The PEC boundary is used to describe the boundary between metal and the interior of the plasma. It is used both for the transition towards the beam tube walls and the rear wall. Thus, both surfaces are assumed to be perfectly conducting and to be grounded. Any deposit of non-conducting material is neglected here. Two major cases have to be differentiated because of the Cartesian structure of the Yee-grid: a planar boundary, which is parallel to the grid, and an arbitrary shaped boundary. In the end, the arbitrary geometry will be used to simulate the cylindrical shape of the source. Nevertheless, the algorithm could also be used for more complex geometries.

Planar shape

Assume, there is a planar boundary, which is aligned with the electric field from the Yee-grid, see figure 5.4. In this case, it is easy to formulate requirements for the electromagnetic fields. The parallel electric field is always zero at the rim of a perfect conductor. Therefore, the electric field of all Yee-grid edges, which are parallel to the boundary, is set to zero. The electric field of all edges contained in the boundary is set to zero as well. The perpendicular field values of the electric field inside the simulation volume are unaltered. The magnetic field of all faces inside the PEC is set to zero. In the case of a background magnetic field, they are set to the background value. The magnetic field of the faces, which touch the boundary, is unaltered, because these fields are located $\frac{\Delta x}{2}$ away from the boundary. A graphical representation of the boundary conditions for the electric and magnetic field can be found in figure 5.4

The treatment of the current at the PEC boundary is more complicated. The macro particles show a finite extension through their form factor. Therefore, there could be a current, which is deposited behind the PEC boundary. The general treatment of this case

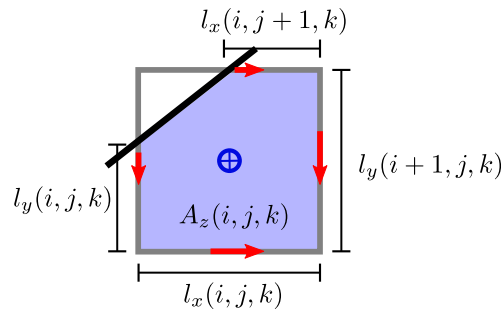


Figure 5.5.: Edge length and face area for the Dey-Mittra algorithm. Sketch of a partial cut cell face through a conducting surface (black). The magnetic field calculation is altered by the edge length l_i and the area A of the face, which is inside the boundary (light blue). Representation of the electric field vectors in red and magnetic field in blue.

would include the usage of a current, which would stem from a theoretical image charge in the conductor. This current would cancel out the parallel current of the macro particle and increase the perpendicular current. Despite the theoretical motivation, the small mirror charge current was not implemented in the context of this thesis, to ensure consistency with the arbitrary shape PEC boundary. For the arbitrary shape, no unambiguous mirror charge method could be found. In total, the current towards the boundary in cells directly in front of the boundary is underestimated in the context of this thesis. In the future, the current deposition step at PEC boundaries can be refined by better models of mirror charges.

The PEC boundary also absorbs all incoming particles. In the simulation, they are deleted directly, when they cross the boundary. Therefore, they do not contribute to the current at their last timestep. A fast beta particle would have moved at maximum a tenth of a cell ($\Delta t \approx 8 \times 10^{-13}$ s). The majority of the particles are thermal electrons, which would have only moved 6×10^{-5} parts of a cell. In the context of this thesis, it is therefore assumed that this contribution to the current can be neglected.

Arbitrary shape

The simulation of PEC boundaries with arbitrary shape needs special treatment. In general, it is only possible to simulate shapes with features bigger than the cell step size Δx . The simplest approach to simulate the arbitrary shaped boundary is the approximation through the stair step algorithm [19]. Here, the boundary is approximated by cubes of the Yee-grid. This method allows for an easy evaluation of Maxwell's equations at the cost of accuracy and robustness towards spurious solutions [19]. "Stairstepping a boundary introduces global first-order error (e.g. the frequency of a simulated cavity would have an error scaling as the cell-length). Second-order error can be attained using the Dey-Mittra algorithm." [60] In order to reach a high accuracy, the Dey-Mittra will be used in the context of this thesis.

In the Dey-Mittra algorithm, it is first calculated how the boundary cuts the cell. The corresponding edge length and face areas are calculated correspondingly, see figure 5.5. The electric field on edges which are totally contained within the conductor is set to zero. The other electric field values are left unaltered. The magnetic field calculation is adapted to

$$\Delta B_z(i, j, k) = \frac{\Delta t}{A_z(i, j, k)} \cdot (E_x(i, j, k)l_x(i, j, k) - E_x(i, j+1, k)l_x(i, j+1, k) + E_y(i+1, j, k)l_y(i+1, j, k) - E_y(i, j, k)l_y(i, j, k)), \quad (5.29)$$

where A is the face area and l_i are the length of the edges, which are inside the geometry. It can be seen that in the case of an unaltered cell, the calculation of the magnetic field is the same as the standard PIC algorithm.

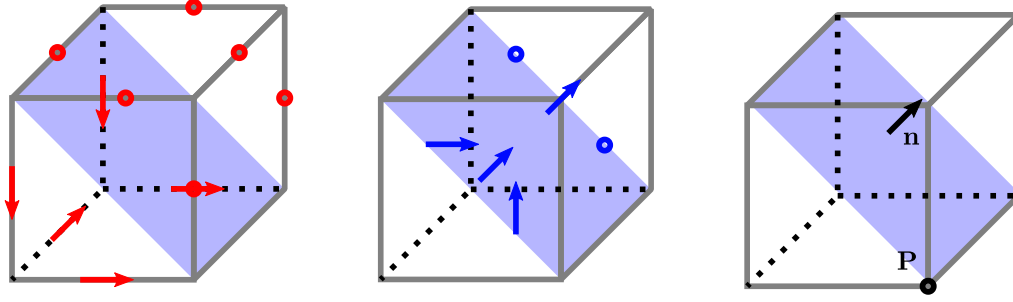


Figure 5.6.: Diagonally cut cell at a PEC boundary. Sketch of a cell, which is cut diagonally by a conducting surface (light blue). Circles indicate positions, where the field value is set to zero. The electric field (red, left) is set to zero at edges, which are contained in the conductor. The magnetic field (blue, center) is set to zero at faces, which are contained in the conductor. Particles are deleted, when they crossed the boundary. This condition is evaluated through the use of the normal vector \mathbf{n} and the point \mathbf{P} of the boundary surface.

The stability of the Dey-Mittra algorithm depends on the smallest allowed face area A_{\min} , the smallest allowed edge length l_{\min} , and the timestep length Δt . Nieter et al. [60] state that the algorithm is stable for a uniform grid when the following two conditions are met

$$\Delta t < \Delta t_{\text{CFL}} \cdot \sqrt{2a}, \quad (5.30)$$

$$\Delta t < \Delta t_{\text{CFL}} \cdot \sqrt{l}, \quad (5.31)$$

where $a = \frac{A_{\min}}{\Delta x^2}$ and $l = \frac{l_{\min}}{\Delta x}$.

The timestep length of the PIC algorithm for the conditions of the KATRIN source has to be lower than $\Delta t \approx 8 \times 10^{-13}$ s, see section 5.1.5. Thus, many timesteps are necessary to reach reasonable results through simulation. It was therefore decided to aim for the smallest timestep reduction allowed by the stability criteria of the Dey-Mittra algorithm. This means that the area factor was chosen to be $a = 0.5$ and the edge length factor to $l = 1$. This approach is equal to the request that there are only diagonally cut and non-cut cells filled with plasma.

The physical geometry of the KATRIN source has to be approximated by diagonally and non-cut cells to suit the algorithm. This procedure will be done in two steps. First, it will be determined, which edges of the grid are cut by the physical geometry. These edges are then considered outside the approximated geometry. Their edge length is set to zero. Secondly, the face areas will be determined from these new edges. This calculation is trivial, because there are only squares and triangles left. An example of the electric and magnetic field values in a cell, which is cut diagonally along one axis, is shown in figure 5.6.

The face areas and edge lengths are calculated prior to the simulation to reduce computing time. Additionally, in the simulation, it will be distinguished between cells, which are inside the geometry, outside the geometry and which are cut in any direction. This reduces the simulation time further, because the correct treatment of the field in each cell can be selected directly.

There was no conclusive result found in the literature, how the charged particle current shall be treated in the Dey-Mittra algorithm. A simple solution would be the usage of mirror charges. No unambiguous algorithm for the use of mirror charges was found in the context of this thesis. All approximations that were found were too computational extensive. It was therefore decided, that there is no special treatment of the current at the PEC boundary. This means, that the current towards the boundary in cells directly in

front of the boundary is underestimated. In the future, the current deposition step at PEC boundaries has to be refined by better models of mirror charges.

All particles that cross the PEC boundary are absorbed. They are deleted directly in the timestep, when they cross the boundary. Numerically, this condition is verified through the use of a normal vector of the cutting plane \mathbf{n} and a point on the plane surface \mathbf{P} . An example of this setup can be found in figure 5.6. A particle at position \mathbf{x} is considered inside the geometry when

$$\mathbf{n} \cdot (\mathbf{P} - \mathbf{x}) > 0, \quad (5.32)$$

is fulfilled. The normal vector and the point \mathbf{P} are calculated prior to the simulation, similar to the edges and face areas, to conserve computational effort.

5.2.2. Periodic Boundary Condition

All experimental plasmas are naturally bound, so is the simulation domain. Nevertheless, it can be profitable to assume that the plasma of the experiment is infinite, at least in one direction. This is the case if the properties of the plasma are of such a nature, that the largest possible simulation domain is significantly smaller than the experimental geometry, or if the bulk of the plasma can be studied detached from the experimental boundaries, due to Debye shielding. Both of these cases can be applied to the KATRIN source. The simulation of the whole source requires many computational resources. Thus, a subdivision of the source is beneficial. Additionally, some effects of the plasma might be observable in a section of the source.

For the periodic boundary condition, it is assumed that the simulated plasma inside the simulation domain has the same properties as the plasma outside the domain. Thus, the distribution of all particles leaving the simulation domain in one direction is the same as the distribution of all particles entering the simulation domain. Hence, in the algorithm, all particles leaving in one direction are inserted at the other side of the simulation domain. The same reasoning is applied to the electromagnetic fields. Thus, the field values are copied to the other side and used in the next field update. The use of periodic boundary condition on the electromagnetic fields limits the number of possible wave modes in the simulation to $n_x/2 - 1$, where n_x is the number of cells in one direction [41]. Thus, a sufficient simulation domain must be selected.

5.2.3. Perfectly Matched Layer

The perfectly matched layer (PML) boundary can be used to simulate the transition of a plasma into a vacuum. This means that it absorbs all outgoing electromagnetic waves and particles. For the KATRIN plasma, this condition is met in the transition region from the WGTS to the DPS.

The requirements for the particle movement are easily formulated: all particles, which leave the simulation domain through the PML boundary, are absorbed. The formulation for the electromagnetic fields is more intricate. Béranger [13] developed a method called complex coordinate stretching, where the space coordinates of a small region in perpendicular direction to the PML boundary are mapped to complex numbers. Thus, the incoming wave becomes evanescent, and the wave is gradually reduced. The specific properties of the PML boundary depend, among others, on the thickness of the layer d and the position dependent absorption coefficient α . The incorporation of the complex coordinate stretching algorithm into the field update is extensive. Therefore, it will not be discussed here. Only the key dependencies will be presented. The interested reader is referred to [13] or to [41].

Assume that the PML boundary is located in the xy -plane. In this case four additional fields (ψ_{E_x} , ψ_{E_y} , ψ_{B_x} and ψ_{B_y}) are introduced, which are added later on to the field values

of E_x , E_y , B_x and B_y respectively. The value of the fields ψ at the timestep $n + 1$ depend on the value of the fields of the timestep before n and on the local electromagnetic field values of timestep n . These dependencies can be summarized as follows

$$\psi_{E_x}^{n+1}(i, j, k) = f(\psi_{E_x}^n(i, j, k), B_y^n(i, j, k), B_y^n(i, j, k - 1), \alpha, d) \quad (5.33)$$

$$\psi_{E_y}^{n+1}(i, j, k) = f(\psi_{E_y}^n(i, j, k), B_x^n(i, j, k), B_x^n(i, j, k - 1), \alpha, d) \quad (5.34)$$

$$\psi_{B_x}^{n+1}(i, j, k) = f(\psi_{B_x}^n(i, j, k), E_y^n(i, j, k + 1), E_y^n(i, j, k), \alpha, d) \quad (5.35)$$

$$\psi_{B_y}^{n+1}(i, j, k) = f(\psi_{B_y}^n(i, j, k), E_x^n(i, j, k + 1), E_x^n(i, j, k), \alpha, d) \quad (5.36)$$

with the update function f and the cell position i, j, k . Thus, the field values ψ of a cell in the PML boundary region only depend on the field values of the electric and magnetic field in x and y -direction along the z -axis. This property simplifies the use of the PML boundary in conjunction with a PEC boundary perpendicular to the PML boundary. This configuration can be found in the transition region of the source towards the DPS at the beam tube edges. It only needs to be tested if the field values of E_x , E_y , B_x and B_y are set to zero by the PEC algorithm. In this case, the addition of ψ to the field values is omitted. Otherwise, the update will be performed through the standard PML update. The PML boundary can also be used in conjunction with the periodic boundary condition. Currently, no such combination of boundaries is needed for the simulation of the KATRIN source.

5.3. Background Fields and Currents

The application of background fields and currents plays a vital role in the simulation of the plasma in the KATRIN source. They originate, for example, from the superconducting magnets, the potential differences of the beam tube surfaces, and the motion of the ions. In the context of this thesis, only static backgrounds are considered. They can easily be added to the field values of the standard PIC algorithm.

Electromagnetic Background

The electromagnetic background can originate from various sources, see sections 2.2 and 2.3. As mentioned before, only static fields are considered here. The static fields do not contribute to the temporal evolution of the electric fields directly, see Maxwell's equation in section 5.1.5. Therefore, they do not have to be considered in the field update. They only need to be applied at the particle movement step, see section 5.1.3. The background fields are simply added to the evaluated field of equation 5.9. The background fields, which are present at the KATRIN experiment, do not change significantly over small distances. It was therefore decided to forgo an interpolation to the particle position, which reduces computational effort.

The field values of the background have to be provided, prior to the simulation. This can either be done via a position dependent function or through discrete data values in a file. The corresponding values at the cell positions are then calculated in the code. The background field needs to be evaluated at the particle position at each timestep. Thus, it is imperative that the evaluation of the field takes as little computational time as possible. It was therefore decided to store the background field values in a separate array. This array is filled at the start of the simulation through the given input. The size of the array is chosen in such a way, that it coincides with the array of the dynamic field values. This way, the cell index of a particle needs to be evaluated only once for the dynamic array and can be used also in the determination of the background field.

Current Background

The KARL code can provide position dependent particle currents. They can be used to determine a drift velocity for the injected particles (see section 5.4.1.3), or they can be directly incorporated in the current array of the simulation. The former can be used for electrons and ions. The later can only be used for ions, because the current of electrons changes significantly during the simulation. Thus, the electron current cannot be assumed to be constant. The ion movement on the other hand can be assumed to be constant during the simulation because of their large mass. Therefore, the contribution of the ions on the simulation can be represented by a static background current.

The static background current is implemented as an additive term for the current array. The current array will be calculated in each timestep from the particle movement, see section 5.1.4. Thus, the background current can be used as a starting value of the current array. In the standard PIC algorithm, this current is set to zero. The background current values have to be provided, prior to the simulation, similar to the background electromagnetic fields. Again, it was decided to store the values in a separate array, which is filled at the start of the simulation through the given input. This procedure reduces the computational overhead, in such a way that the background current have to be copied only once in each timestep.

5.4. Particle Injection

The injection of particles into the simulation domain can be classified into two separate steps. Particles can either be injected directly at the start of the simulation, called initial loading, or they can be injected during the simulation. In the initial loading step, the simulation domain is filled with particles from a given particle distribution. In the context of this thesis, the particle distribution is given by the results of the KARL simulation. The injection during the simulation can be used to describe the connection of an open simulation domain with the bulk of a plasma, or even the generation of particles through Tritium decay. Both injection steps have a significant influence on the simulation and are therefore discussed here in detail.

5.4.1. Initial Loading

The initial distribution of particles is generated by the KARL code, see chapter 4. The distribution is classified by the spectrum of the electrons, as well as the mean current of the particles. For the ACRONYM simulation, this information needs to be translated into the number of particles ppc, which are inserted in each cell, the macro factor of the macro particles w_α , the kinetic energy of these particles E_{kin} , and the direction of movement \mathbf{v} . The evaluation of each of these properties will be described in the following sections.

5.4.1.1. Particles Per Cell and Macro Factor

At the start of the simulation, each cell will be filled with a given number of macro particles. The particles will have a mass and a charge, both scaled by the macro factor. The number of particles per cell for each particle species α , short ppc_α , and the macro factor w_α are linked by the density n_α through

$$w_\alpha = \frac{n_\alpha \cdot \Delta x^3}{\text{ppc}_\alpha}. \quad (5.37)$$

The density n_α is directly provided by the KARL simulation. The cell size Δx is calculated from the maximum absolute density, see equation 5.27.

The density of the particles is dependent on the position inside the source. Thus, two different scenarios are possible to incorporate this effect into the simulation: either the macro factor is position dependent and the number of particles per cell is fixed, or the other way around that the number of particles per cell is position dependent and the macro factor has a fixed value. The KARL simulations show, that the electron density varies by approximately two orders of magnitude, whereas the ion density varies by approximately one order of magnitude. In a plasma, quasi-neutrality can be assumed, see section 3.1. Thus, the electron and ion density will equalize at some point in the simulation cycle between ACRONYM and KARL. Hence, it can be assumed that the density differences will be lower in the plasma at KATRIN than in the first simulation of KARL. This also means, that large fluctuations of the number of particles is no longer the governing issue for the simulation. Therefore, it was decided to use a position dependent number of particles per cell. An additional benefit of this decision is the reduced effort in the analysis of the output data, because the number of particle species is kept low.

The choice of a position dependent number of particles per cell introduces a new challenge: the number of particles is an integer value, while the density has continuous values. This issue is resolved by the following consideration. The integer number of particles, which are injected in a cell $\text{ppc}(i, j, k)$ is calculated from the continuous value $\text{ppc}(\mathbf{x})$

$$\text{ppc}(i, j, k) = \begin{cases} \text{ppc}_f & \text{ppc}(\mathbf{x}) - \text{ppc}_f < \eta \\ \text{ppc}_c & \text{else} \end{cases} \quad (5.38)$$

where $\eta \in [0, 1)$ is a random number, ppc_f is the next lower integer value of $\text{ppc}(\mathbf{x})$, and ppc_c is the next higher integer value of $\text{ppc}(\mathbf{x})$. The continuous value $\text{ppc}(\mathbf{x})$ is calculated from the position dependent value of the density $n(\mathbf{x})$ through

$$\text{ppc}(\mathbf{x}) = \frac{n(\mathbf{x})}{n_{\max}} \cdot \text{ppc}_{\max} \quad (5.39)$$

where ppc_{\max} is a predefined number. For a large enough number of cells, this method will reproduce the shape of the density. As described before, the accuracy of this method hinges on the expected density variation, but also on the maximal number of particles per cell ppc_{\max} . The larger ppc_{\max} is, the better is the accuracy.

The procedure of a variable number of particles per cell requires a position resolved density with a position resolution of the cell size. In general, the size of density bins of the KARL simulation is larger than the cell size of the ACRONYM simulation. Therefore, the output of the KARL simulation needs to be interpolated to the cell positions \mathbf{x} . The density at position \mathbf{x} is evaluated through a bilinear interpolation of the radial and longitudinal bin centers [44]. The azimuthal discretization is neglected because of the azimuthal symmetry of the simulation.

The maximum number of particles in each cell ppc_{\max} from equation 5.39 needs to be specified before the simulation. In general, it is preferable to have many particles per cell to reduce the noise of the simulation. Nevertheless, the particle update is very time-consuming. Thus, the maximum number of particles in each cell is bound by the computational resources available. The necessary computational resources for a simulation can be described by the time the simulation takes and how many processors are involved in the calculation. The use of many particles per cell increases the time a simulation takes. This time can be reduced by facilitating parallel computation, by increasing the number of processors. The particle update and the field update can each be done in parallel, because the outcome is only dependent on the prior status. ACRONYM is designed to be used with many processors. The simulation domain is subdivided into cubes, each containing several cells of the Yee-grid. Each processor is responsible for the particle and field update in its region.

Corresponding boundary conditions and communication between the processors were set up. Kilian [41] evaluated the number of particle updates per wall-clock second in dependence on the number of processors. Thus, it can be evaluated how long a simulation will take, given the number of simulated particles and number of processors. This evaluation needs to be in line with the available computational resources.

The evaluation of the number of particles can be applied to the data of the KARL simulation to find the best values of ppc_{max} . Three distinct regions can be found in the electron spectrum: a thermal region, a beta region and the transitional region, see section 4.3. The densities of these regions are significantly different from each other. Most of the electrons reside in the thermal region, whereas the other two regions make up only a small fraction of the total electron density. If all electrons are represented through a single particle species with one macro factor and assuming $\text{ppc} = 20$, this will result in a macro factor of $w \approx 5.5$ for a total density of $n \approx 5.7 \times 10^5 \text{ cm}^{-3}$. Thus, almost every real particle can be represented in the simulation as a macro particle. If the particle energy is sampled from the entire spectrum, the simulation can suffer from a large statistical uncertainty, because of the large density difference between the high-energy region and the thermal region. It was therefore decided to subdivide the spectrum into the three distinct regions in the simulation. Each region will be represented by its own particles, with their own number of particles per cell and therefore own macro factor.

This procedure introduces a new issue: the macro factor of the transitional and beta region is well below one ($w_{\text{tr}} \approx 0.08$ and $w_{\text{beta}} \approx 6.5 \times 10^{-5}$ at $\text{ppc} = 1$). This way, each macro particle represents only a fraction of an electron. From a numerical standpoint, this is no problem. Nevertheless, this procedure also introduces an artificially homogeneous plasma. Dedicated simulation will have to be performed to study this behavior.

5.4.1.2. Sampling of the Kinetic energy

Each particle is initialized with a given kinetic energy. This energy needs to be sampled from a given distribution. This distribution can either be provided by theoretical considerations, approximated functions, or directly through data of a histogram. The sampling method depends on the type of input data. The different methods used in the context of this thesis are described in the following.

Theoretical Consideration

Some parts of the source spectrum can be classified through an investigation of the origin of the features. Two major contributions can be identified directly from the spectrum of the KARL simulation, see section 4.3: a thermal region and a beta region. The sampling of an energy value from each of these distributions will be described in the following.

In the source, there are many elastic collisions with the neutral gas. It can therefore be assumed that the particles adopt the energy distribution of the neutral gas. It is assumed in first order that the gas follows the Maxwell-Boltzmann distribution. Thus, the electrons follow the Maxwell-Boltzmann distribution as well. The temperature of the gas is then equal to the temperature of the particles. The energy of the injected particles is sampled in the code directly through the gamma distribution with the parameter $\alpha = \frac{3}{2}$ and $\beta = E_{\text{th}}$, where E_{th} is the thermal energy of the particles. The gamma distribution is a built-in distribution function in the C++ standard library [36] and can be used directly without modification.

The particles of the beta decay initially follow the Fermi distribution. It is therefore beneficial to sample the high-energy part of the spectrum through the Fermi distribution (equation 1). The kinetic energy is sampled in the code through the rejection method [31].

In the rejection method, a probability distribution function $f(x)$ is sampled through two random numbers $\eta_1 \in [f_{\min}, f_{\max}]$ and $\eta_2 \in [x_{\min}, x_{\max}]$. The sampled value η_2 is used as the result of the method if the following condition is met

$$\eta_1 \leq f(\eta_2). \quad (5.40)$$

Otherwise, the two numbers are rolled again. The rejection method models the underlying function correctly, but needs the generation of many random numbers to produce one value x . The efficiency of the method is given by [31]

$$\text{efficiency} = \frac{\int_{x_{\min}}^{x_{\max}} f(x) dx}{f_{\max} \cdot (x_{\max} - x_{\min})}. \quad (5.41)$$

In simple terms, the efficiency is low for a function, which covers many orders of magnitude. The Fermi function is one of these functions. Nevertheless, this does not pose an issue for the ACRONYM simulations, because the energy only needs to be sampled once at the creation of a particle.

Approximate Function

Some parts of the spectrum can be described by an arbitrary function $f(x)$. It is not necessary to know the connection of this function to the underlying physics to sample an energy from the function. This method is used in the transitional region of the KARL results, see section 4.3. Here, the spectrum can be approximated by two power law functions.

In general, the sampling can be done again through the rejection method, which was presented above. If the function is reversible ($f(f^{-1}(x)) = x$) the sampled value x can then be determined directly by the random number $\eta \in [f_{\min}, f_{\max}]$ through

$$x = f^{-1}(\eta). \quad (5.42)$$

The inverse method has an efficiency of one. Each roll of a random number generates one random number x . Hence, the inverse method is preferable over the rejection method, if the inverse function is available. This is not the case for the Maxwell-Boltzmann distribution and the Fermi distribution.

Histogram Data

The spectral data from the KARL simulation is available as a histogram. In this case, the random number x can be sampled directly from this data $f(i)$. The bin index i is found through the random number $\eta \in [0, \sum f(i)]$ for the first bin, which fulfills [31]

$$\sum_0^i f(i) > \eta. \quad (5.43)$$

The random number x must be in the interval $[x_i, x_{i+1}]$, where x_i is the left bin border of the bin i . The exact value of x is therefore not determined directly. In first order, it can be assumed that the value x is given by the position of the bin center. A more precise resolution is reached through a linear interpolation towards the neighboring bins and a subsequent sampling.

The efficiency of this algorithm is dependent on the efficiency of the search algorithm. The time complexity of most search algorithms scale with $\mathcal{O}(\log N)$. Thus, the efficiency of the algorithm scales with $\frac{1}{\log N}$, where N is the number of bins. The energy resolution of the KARL simulation is on the order of 100 bins, which is comparably low. The histogram method can therefore be used for a wide range of the spectral data.

5.4.1.3. Sampling of the Velocity

The velocity of the new particles is initiated with entries in all three spatial directions. The norm of the velocity v_0 is given by the kinetic energy, which is sampled from a given spectrum, see the previous section. The distribution of the velocity to the three spatial directions is non-trivial.

In first order, it can be assumed that the velocity is distributed isotropically. Thus, the velocity vector \mathbf{v} is sampled through two random numbers $\eta_1 \in [0, 2\pi)$ and $\eta_2 \in [0, \pi)$ and ultimately given by

$$\mathbf{v} = v_0 \begin{pmatrix} \cos \eta_1 \sin \eta_2 \\ \sin \eta_1 \sin \eta_2 \\ \cos \eta_2 \end{pmatrix}. \quad (5.44)$$

The benefit of this initiation lies in the simplicity of the algorithm.

The KARL simulations show that there is a current of the electrons. This current is not represented in the first order approximation. This shortcoming is approached by another approximation, namely that the current can be represented by an additive contribution to the first order approximation of the velocity. Thus, the total kinetic energy of the particle will be greater than the originally sampled energy. On the one hand, this procedure overestimates the kinetic energy of the particles. On the other hand, the current will be represented correctly. A more precise description of the velocity would need to resolve the three velocity directions in the KARL simulation directly and import them into the ACRONYM simulation.

In the second order approximation, the current is divided into a current in longitudinal direction j_z and a current in radial direction j_r . These currents can be translated into a drift velocity through

$$v_z(\mathbf{x}) = \frac{j_z(\mathbf{x})}{n(\mathbf{x})}, \quad (5.45)$$

$$v_r(\mathbf{x}) = \frac{j_r(\mathbf{x})}{n(\mathbf{x})}, \quad (5.46)$$

with the density $n(\mathbf{x})$. The velocity gained through equation 5.44 is then boosted by these two velocity contributions. The calculated radial velocity v_r is in general much smaller than the smallest thermal velocity due to the large magnetic field. Thus, it will be neglected in the following. Future extensions might include this contribution. It may also be included through a background current, see section 5.3.

5.4.2. Injection During Simulation

After the initial loading of particles, there can still be the need of injecting particles during the PIC cycle. This can be the case, where the simulation domain is smaller than the plasma or when there occurs particle decay in the simulated time range. The former is simulated through the use of the PML boundary condition in conjunction with the injection of particles at that boundary. The injection can be done in two ways, through the knowledge of the incoming current, or through the assumption of a virtual plane, at which the density is kept constant. Both methods will be shown in the following, followed by the description of the injection of particles through a constant decay rate.

5.4.2.1. Injection through Constant Current

In the injection method through a constant current, it is assumed that the current $j(\mathbf{x})$ flowing towards the simulated plasma is given prior to the simulation, for example by the

KARL simulation. This current can be translated into the number N_j of physical particles, which have to be inserted into a cell per timestep

$$N_j(i, j, k) = j(i, j, k) \cdot \Delta t \cdot (\Delta x)^2, \quad (5.47)$$

where i, j, k are cell indices. This number needs then to be scaled with the macro factor to produce the right amount of macro particles, which need to be injected.

This procedure reproduces the external current at the boundary correctly, but the injection is also independent of the local field at the injection site. The injected current produces an opposing electric field through Ampere's circuital law. In a real plasma, this field will reduce the current flowing towards the plasma and an equilibrium will be found. Contrary to the real case, the current in this method will be kept constant. Thus, the equilibrium is only found if the incoming current matches the outgoing current. In total, this method of injection overestimates the electric field in the plasma and is therefore not favored in the context of this thesis. This assessment might change if a relation between the incoming current and the electric field at the boundary can be found.

5.4.2.2. Injection by retaining Constant Density

The injection method through a constant current can show non-physical results, because the electric field at the injection site is not taken into account in the injection process. This problem can be bypassed by the use of the injection method, which retains a constant density at the boundary, also described by Kilian [41]. Here, a virtual layer of cells is created at the injection plane. The virtual cells have to coincide with cells of the simulation domain. Therefore, they have access to the electric field at the boundary. The virtual layer will be filled each timestep with particles. The particle loading is analogous to the initial loading step, see section 5.4.1. The particles will then be moved by one timestep, corresponding to the local electric field at the virtual layer. Only those virtual particles which leave the virtual layer of cells into the simulation domain are copied to the list of macro particles. The other virtual particles will be deleted. This procedure ensures that the incoming current is closely linked to the electric field at the boundary.

Up to this point, the position of the virtual layer inside the simulation domain is not specified. An obvious choice is the last row of cells of the simulation domain. Nevertheless, in combination with the PML boundary, two effects have to be taken into account. First, the electric field inside the PML boundary is reduced through the PML algorithm itself. Thus, there is a reduced dependence of the incoming current with the field of the simulation. Therefore, an injection position closer to the undisturbed simulation domain is preferable. Second, the field in front of the injection site is altered by the injection. In order to keep the size of the boundary layer to a minimum, an injection position, close to the simulation domain boundaries is preferable. In total, a tradeoff between both effects has to be found. No investigation of the injection position was found in the literature. Thus, test simulations were performed with varied injection position.

The test simulation was designed for the case of a plasma inside a conducting cylinder, which is bound at one side by a conducting plate and at the other side by the PML boundary condition. The height of the cylinder was chosen to be much greater than the PML layer thickness. The PML layer was chosen to be 10 cells thick, which has shown good results in the past [41]. The virtual layer of injection was set up at three different positions inside the PML layer. The spectrum of the injected electrons was chosen to a combination of a low-energy thermal part ($T = 80$ K) and a high-energy tritium beta decay part with densities of $n_{\text{th}} = 1 \times 10^5 \text{ cm}^{-3}$ and $n_{\beta} = 7.9 \times 10^{-1} \text{ cm}^{-3}$, which corresponds to the conditions found at the rear wall region. The results of the simulations can be found in figure 5.7.

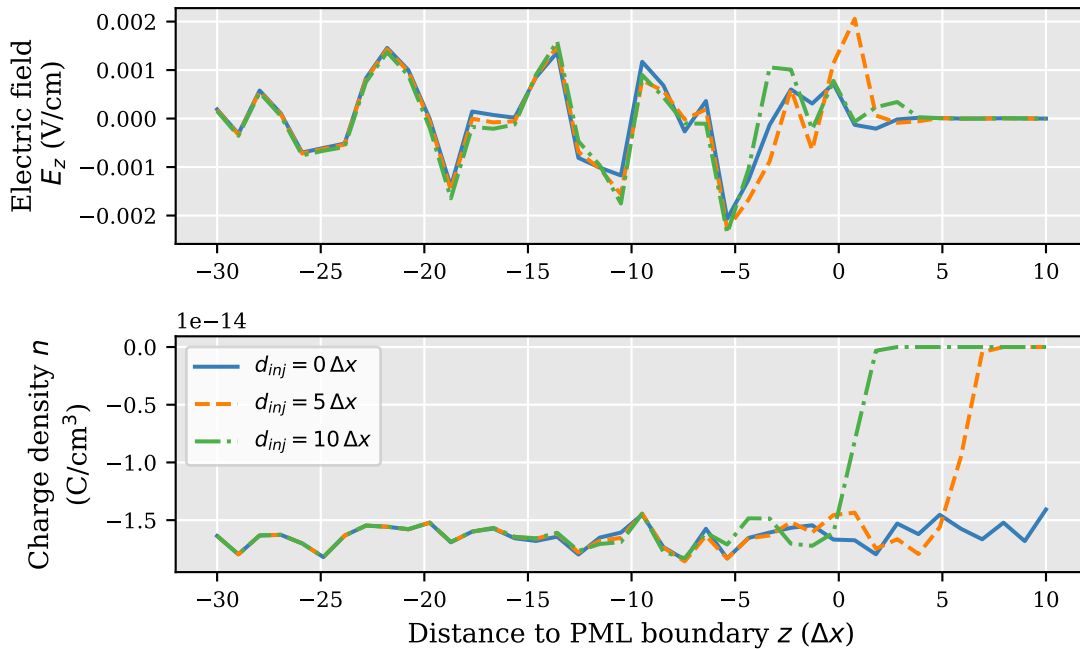


Figure 5.7.: Test of injection position at PML boundary. Electric field and charge particle density are collected in the center of the simulated tube after four plasma time scales for three different positions of the injection position. The distance d_{inj} provides the number of cells towards the simulation domain boundary. The simulation was performed in a cylinder with a radius of 32 cells and a height of 1434 cells. The magnetic field $B_z = 2.5$ T was set in longitudinal direction. Only electrons were simulated. The electron distribution was chosen to include a thermal part ($n_{th} = 1 \times 10^5 \text{ cm}^{-3}$ and $T = 80$ K) and a tritium beta decay part ($n_\beta = 7.9 \times 10^{-1} \text{ cm}^{-3}$).

It can be seen that there is an influence of the injection position on the electric field and density close to the PML layer. Further away (more than 25 cells), this influence is negligible. Thus, the total boundary layer of the PML boundary with injection of particles is only extended by approximately 25 cells in any of the tested configurations. For simplicity, it was therefore decided to use the injection position at the start of the PML layer. More elaborate investigations of the injection position, in respect to the particle density and particle spectrum, might provide a more optimized setup.

5.4.2.3. Injection through Constant Decay Rate

In the source, electrons are created continuously through beta decay of tritium and subsequent ionization. To take this into account, a new injection method was developed, where new particles are injected in each timestep of the simulation. The injection process itself is straightforward. First, the number of injected particles is calculated. Then, this number is converted to the integer number of macro particles to be injected, similar to the initial loading step. After that, the macro particles are sampled from a predefined energy distribution and put into the corresponding cell. In total, only the number of injected particles is the relevant quantity. For this number, a distinction between the primary beta electrons and electrons created by ionization was made, due to their different creation mechanism.

The number of particles created by beta decay of tritium depends only on the density of the neutral gas n_{T_2} and the decay constant λ_{T_2} . Therefore, the number of macro particles,

which have to be injected in each cell per timestep, can be calculated by

$$N_{\beta}(i, j, k) = \frac{n_{T_2}(i, j, k) \cdot (\Delta x)^3 \cdot \Delta t \cdot \lambda_{T_2}}{w_{\beta}}, \quad (5.48)$$

where w_{β} is the macro factor of the beta particles. The simultaneous creation of tritium ions is neglected here, but could be implemented with the same number of injected particles.

Each beta electron can create several other electrons through ionization, named here secondary electrons. The interplay between the movement of the beta particles, the ionization process and subsequent scatterings of the secondary particles is complex. Thus, it is difficult to estimate the correct position and with which energy the secondary particles have to be injected. A first order approximation can be gained through two assumptions. First, each beta electron creates a fixed number of secondary electrons a_{sec} . Second, the density of the secondary electrons scales with the initial density of the beta particles. The number of injected secondary particles N_{sec} is then calculated as

$$N_{\text{sec}}(i, j, k) = \frac{1}{w_{\text{sec}}} N_{\beta}(i, j, k) \cdot a_{\text{sec}} \cdot \frac{n_{\text{sec}}(i, j, k)}{\max(n_{\text{sec}}(\mathbf{x}))}, \quad (5.49)$$

where $n_{\text{sec}}(i, j, k)$ is the predefined density distribution and w_{sec} the macro factor of the secondary electrons.

It is apparent, that the injection through a constant decay rate neglects the particle flow of secondary and primary electrons, as well as interactions with the neutral gas. Nevertheless, assuming that the collisionality between electrons and gas is low, it can act as a first approximation. Future connected atom- and plasma-physics simulations might resolve this issue.

5.5. Electrostatic Potential derived by Poisson Equation

One result of the ACRONYM simulations is the electric field on the Yee-grid at different timesteps. A more accessible parameter can be the electrostatic potential. A method for the evaluation of the electrostatic potential from an input electric field will be presented in the following.

In general, the electric field can be represented by the superposition of a curl-free and a divergence-free field, following the Helmholtz-theorem. These fields are also called longitudinal (\mathbf{E}_l) and transversal (\mathbf{E}_t) fields. A curl-free field can be resolved to a scalar potential ϕ , whereas a divergence-free field can be resolved to a vector potential \mathbf{A} through

$$\mathbf{E} = \mathbf{E}_l + \mathbf{E}_t, \quad (5.50)$$

$$\mathbf{E}_l = -\nabla\phi, \quad (5.51)$$

$$\mathbf{E}_t = \nabla \times \mathbf{A}. \quad (5.52)$$

The scalar potential can be derived directly from the electric field by using $\nabla(\nabla \times \mathbf{A}) = 0$ through

$$\mathbf{E} = -\nabla\phi + \nabla \times \mathbf{A}, \quad (5.53)$$

$$\nabla \cdot \mathbf{E} = -\nabla^2\phi. \quad (5.54)$$

The last equation can be identified with the Poisson equation through the use of Gauss's law. So, the electrostatic potential can be derived from a generic electric field in two steps. First, the electric field is converted into a charge density through Gauss's law, see also equation 5.22. Second, the density is then used to solve for the electrostatic potential. The

solution of the Poisson equation in cylinder coordinates with an azimuthal symmetry is already shown in section 4.4.2.1. Thus, only the conversion of the electric field will be discussed here.

The approach can be described in three steps. First, Gauss's law is described in cylinder coordinates. Second, the derivatives in Gauss's law are converted into finite differences. Third, boundary conditions are set up. Special treatment is needed in the case of zero radius.

Gauss's law in cylinder coordinates can be written as

$$\begin{aligned} 4\pi\rho &= \nabla \cdot \mathbf{E} \\ &= \frac{\partial E_r}{\partial r} + \frac{E_r}{r} + \frac{\partial E_z}{\partial z}, \end{aligned} \quad (5.55)$$

assuming an azimuthal symmetry. This equation can be solved numerically through the use of finite differences. The central difference scheme is used here for the derivatives, because density and fields are given at different positions, see section 5.1.1. For the second term, it is assumed that the field at the position of the density can be calculated as the mean value of the neighboring field values. So in total, the density at the cell corners with radial and longitudinal coordinates (i, j) calculates as

$$4\pi\rho_{i,j} = \frac{E_{r;i,j} - E_{r;i-1,j}}{\Delta r} + \frac{E_{r;i,j} + E_{r;i-1,j}}{2i \cdot \Delta r} + \frac{E_{z;i,j} - E_{z;i,j-1}}{\Delta z}, \quad (5.56)$$

where Δr and Δz are the cell sizes in radial and longitudinal direction.

It can be seen, that equation 5.56 diverges for zero radius ($i = 0$). L'Hôpital's rule can be used to resolve this issue, because the radial electric field vanishes in the limit of zero radius. The second term in Gauss's law can therefore be written as

$$\lim_{r \rightarrow 0} \frac{E_r}{r} = \frac{\partial E_r}{\partial r}. \quad (5.57)$$

The derivative of the electric field at zero radius can be evaluated through the method of finite differences, because the electric field at position $i = -1$ is equal to the negative value at $i = 0$ (radial symmetry). The density at zero radius can therefore be calculated as

$$4\pi\rho_{0,j} = 4 \frac{E_{r;0,j}}{\Delta r} + \frac{E_{z;0,j} - E_{z;0,j-1}}{\Delta z}. \quad (5.58)$$

Lastly, the calculation of the density is completed by setting up boundary conditions. Three different boundary conditions are described here: Dirichlet boundaries, Neumann boundaries and periodic boundaries. Dirichlet boundaries are used for the transition towards the beam tube walls (PEC boundary). For the ACRONYM simulations, it is assumed that the potential is only generated by the particles inside the cavity. Any external field, like the rear wall field, is added only in the particle movement step, see section 5.3. Therefore, only the dynamic field data is exported from the simulation each timestep, and the background only once. For the total electric field, both values have to be added. This also means, that in the estimation of the potential from the dynamic field values with Dirichlet boundaries, the boundary can be treated as grounded and with zero density. The background potential is then added later on. The Neumann boundary is used at the transition of the plasma towards vacuum (PML boundary). Here, the longitudinal electric field is set to zero. Thus, the calculation of the density is carried out with $E_{z;i,J+1} = 0$, where J is the maximum index of the electric field in longitudinal direction. At the periodic boundary, the density is calculated with $E_{z,i,-1} = E_{z,i,J}$.

5.6. Validation of ACRONYM Simulations

In the context of this thesis, the generic ACRONYM code was extended to incorporate circular boundary conditions, background electromagnetic fields and background currents. These additions need to be tested to ensure their functionality. Each single module in the code underwent a standard unit test, in order to verify that the module produces the intended result. These tests however cannot show, if a module produces physical results. Thus, additional tests were set up. They are described in the following.

5.6.1. Ion Current Approximation

In the simulation, it is assumed that the movement of the ions can be described by a constant contribution to the total current, see also section 5.3. Hence, no simulation of the ion movement is necessary. This hypothesis was validated through a comparison between a simulation with ion macro particles and a simulation with background current, later on called simulation with particles and simulation with background. If the hypothesis is true, then both simulations should show the same behavior in the development of the total current and of the electric field. Small variations are expected due to the statistical nature of the particle initiation.

Both simulations were carried out with an electron density of $n_e = 1 \times 10^5 \text{ cm}^{-3}$ and 20 electrons per cell. The electrons were initiated with a thermal velocity distribution ($T_e = 30 \text{ K}$). The simulation domain was chosen to be a cube with periodic boundary conditions in all three dimensions of space. No magnetic background field was used. Both simulations were performed for two plasma time scales.

In the simulation with particles, the ion density and number of particles per cell were chosen equal to the settings of the electrons. The ions were initiated with a thermal velocity distribution ($T_i = 30 \text{ K}$) and with an additional drift velocity in z -direction $v_d = 1 \times 10^6 \text{ cm/s}$. The value of the background current j_c for the other simulation then calculates as

$$j_c = e \cdot n_i \cdot v_d \approx 16 \text{ nA/cm}^2 \quad (5.59)$$

where n_i is the ion density. The charge current, mass current and electric field of the test simulations on the central axis in z -direction can be found in figure 5.8.

At first, it was inspected, how the ions have moved during the simulation and if they retained their movement during the simulation. The behavior of the ions was investigated through the mass current. The mass current is dominated by the mass of the ions, and therefore it only shows the movement of the ions. The simulated mass current showed the expected value of

$$j_m = m_i \cdot n_i \cdot v_d \approx 1.6 \times 10^{-16} \text{ kg}/(\text{cm}^2 \text{ s}), \quad (5.60)$$

compare center of figure 5.8. Small variations in the simulated mass current were expected due to the statistical nature of the particle initiation. The mass current did not show any indication, that it has changed after initialization. It can therefore be assumed that the ion current was directed at the positive z -direction at all timesteps and that it had the same value during the simulation.

In a second step, it was compared if both simulations show the same result for the electric field and the electric current. It can be seen in figure 5.8, that both simulations produced similar values. Only slight differences are observable, which is expected. Thus, the electrons behaved similar in both simulations, even though the origin of the ion current was different.

The absolute value of the charge current and electric field is of no special interest for the validation. Nevertheless, two interesting observations can be made: the electric field E_z is

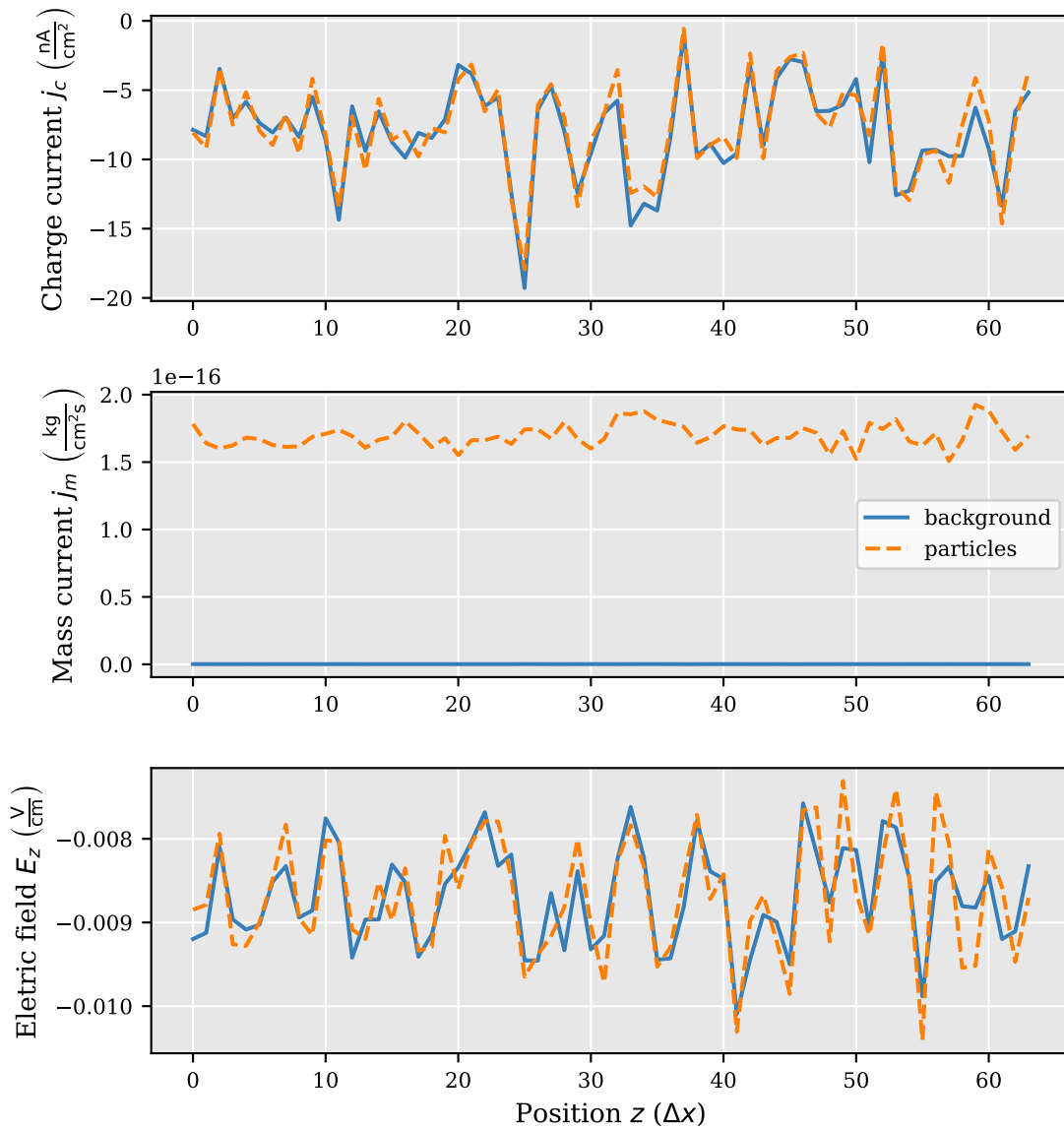


Figure 5.8.: Validation of background current. Comparison of two simulation with ion macro particles (particles) and with background current (background). The z -component of the charge current and mass current are measured along a line in z -direction in the center of the simulation domain.

negative at all positions, and the charge current is negative as well. Thus, the ion movement induces an electric field, which is opposing the movement of the ions. This electric field accelerates the initial static electrons to the positive z -direction. Therefore, the initial positive charge current is reduced, in this case even to negative values. This simplistic explanation can only provide a rough estimation of the processes in the plasma and is no full analytic calculation. Nevertheless, the general idea, that an ion current will be opposed by the electron movement, can be grasped.

In total, it can be concluded that the background current can be used to simulate the movement of ions in the plasma. This approximation is only valid for short time scales, where the ion movement is not changed significantly by the electric field.

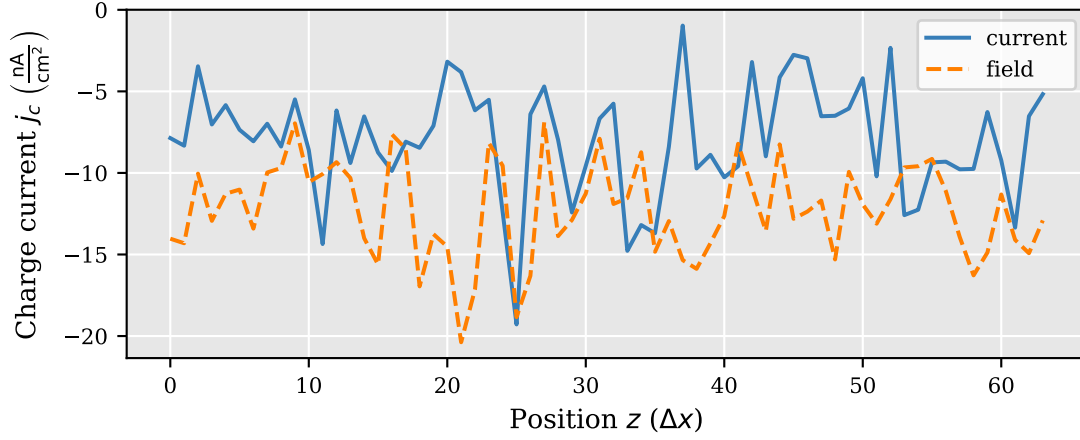


Figure 5.9.: Validation of background electric field. Comparison of two simulations with background current (current) and with background electric field (field). The z -component of the charge current is measured in z -direction along a line in the center of the simulation domain.

5.6.2. Background Electric Field

Simulations with background current showed, that the background current incites an electric field. The field accelerates electrons, to match the movement of the ions. This observation is now reversed to test the use of a background electric field. In the tests, a simulation with background current was compared to a simulation with background electric field. It was expected, that the electric field with the same strength as in the background current simulation incites a similar current in the particles.

Both simulations were carried out with an electron density of $n_e = 1 \times 10^5 \text{ cm}^{-3}$ and 20 electrons per cell. The electrons were initiated with a Maxwellian velocity ($T_e = 30 \text{ K}$). The background current was set to $j_{\text{bg}} \approx 16 \text{ nA/cm}^2$. The background electric field was set to $E_{z,\text{bg}} = -8.7 \times 10^{-3} \text{ V/cm}$, which corresponds to the mean electric field of the simulation with background current. Both simulations were performed for two plasma time scales. The comparison of the resulting currents can be found in figure 5.9.

It was observed, that the electric background field generates a current in the simulation. This current is pointed in the same direction and has a comparable value as in the simulation with the background current only, see figure 5.9. This shows qualitatively that the basic expectation of the test could be confirmed: the background field incites a movement of the electrons. A quantitative analysis can be performed through a look on the mean value of the current. The mean values over the whole simulation domain calculate to

$$j_z(j_{\text{bg}}) = (-8.3 \pm 3.3) \text{ nA/cm}^2 \quad (5.61)$$

$$j_z(E_{\text{bg}}) = (-11.7 \pm 2.7) \text{ nA/cm}^2 \quad (5.62)$$

The uncertainty of the mean value is calculated as the mean deviation. It is apparent, that the simulation with the background field shows a higher mean value. Nevertheless, both mean values show overlapping uncertainties. Therefore, both simulations could in principle show the same result, only moderated by statistical fluctuations. However, both simulations also show a basic difference. In the simulation with background current, the current excites an electric field, which in turn accelerates charges. In the simulation with background field, the field directly accelerates the charges. Thus, there is no intermediate step in the simulation with background field. It is therefore likely, that the time scales of both simulations do not match and one simulation is ahead of the other. A determination

of this effect is of no further interest for the validation step, and is therefore not pursued here. Notwithstanding, it can be concluded that the background electric field works as expected, because the simulated current shows the expected behavior from the simulation with background current.

5.6.3. Cavity Mode Excitation

A hollow conducting cylinder can act as a waveguide for electromagnetic waves. Only waves with a specific frequency and shape are allowed by Maxwell's equations. These specific waves are called cavity modes. Cavity modes can be used to test and classify electromagnetic solvers, which also deal with conducting boundaries. The method described in this section mainly follows the approach of Nieter et al. [60]. First, the frequency of all possible modes will be determined analytically. Second, cavity modes in an empty cylinder will be excited in the simulation through a driving current. Third, the simulated frequency of the modes will be compared to the analytically calculated frequency, which provides an estimate on the error of the simulation.

The frequency of possible modes will be derived through the use of the wave equation in a cylindrical geometry. If the waveguide is aligned in z -direction, then the wave will travel in that direction as well. The electric field in this case can be written as

$$\mathbf{E}(\mathbf{r}, t) = \mathbf{E}(r, \phi) \cdot \exp(i(\omega t - k_z z)), \quad (5.63)$$

where ω is the frequency of the mode, k_z the wave mode number in z -direction, \mathbf{r} a space vector, r the radius, and ϕ the polar angle. The same ansatz can be pursued for the magnetic field. The full derivation of the fields can be found in [71]. Here it will be focused on the solution only.

The solution for the electromagnetic fields is obtained by using the boundary conditions of the cavity. Two general boundary conditions have to be fulfilled for the electric and magnetic field at conducting boundaries: a vanishing tangential component of the electric field and a vanishing normal component of the magnetic field. The resulting solutions for the wave equation can be classified into two categories: the TM modes, where the magnetic field is zero in the direction of propagation, and the TE modes, where the electric field is zero in the direction of propagation. The corresponding electric fields will be presented in the following.

The spatial distribution of the electric field of a TE mode is calculated by

$$E_r(\mathbf{r}) = E_{r,0} \cdot \frac{-n\omega}{k_{n,m}^2} \cdot \frac{J_n(k'_{n,m} \cdot r)}{r} \cdot (A \cos(n\phi) - B \sin(n\phi)) \cdot \sin(k_z z), \quad (5.64)$$

$$E_\phi(\mathbf{r}) = E_{\phi,0} \cdot \frac{\omega}{k'_{n,m}} \cdot J'_n(k'_{n,m} \cdot r) \cdot (A \sin(n\phi) - B \cos(n\phi)) \cdot \sin(k_z z), \quad (5.65)$$

$$E_z(\mathbf{r}) = 0 \quad (5.66)$$

with the Bessel function J_n and its derivative J'_n , the factors A and B , which will be chosen to $1/\sqrt{2}$, and the so-called cutoff wavenumber $k'_c := k'_{n,m}$. The cutoff wavenumber must fulfill

$$J'_n(k'_{n,m} \cdot R) = 0, \quad (5.67)$$

with the radius R of the cylinder and the number m of the root of the derivative of the Bessel function. If the cylinder is also terminated by a conducting plate, then the wavenumber k_z must fulfill

$$k_z = \frac{l\pi}{L}, \quad (5.68)$$

where L is the length of the cylinder and l is an integer value. In the end, the frequency of the TE wave is calculated by

$$\omega^2 = (k_c'^2 + k_z^2) c^2. \quad (5.69)$$

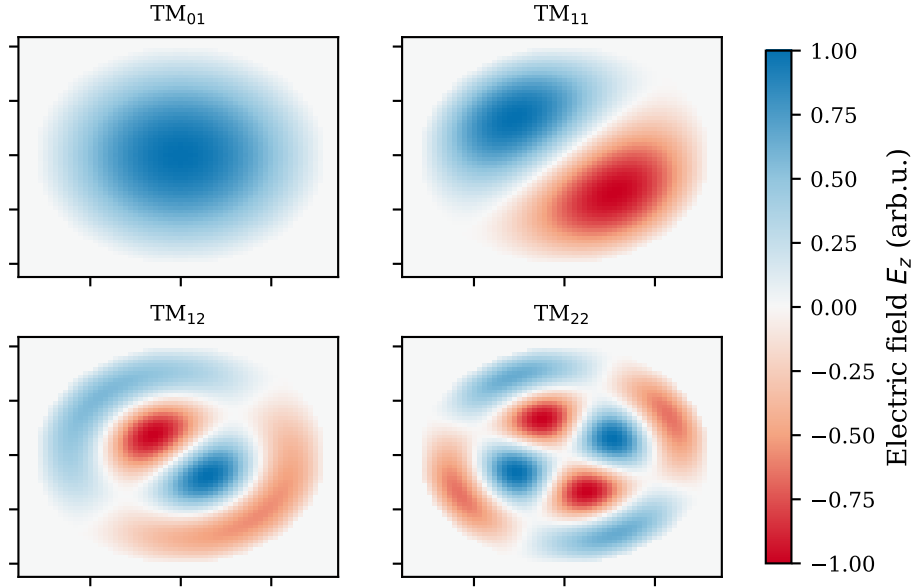


Figure 5.10.: Electric field distribution of TM modes. The values are generated by simulation through mode excitation with $n \in [0, 1]$ and $m \in [1, 2]$. The fields show structure of the Bessel function in radial direction and sine structure in azimuthal direction.

The derivation of the field for the TM mode follows analogously to the derivation for the TE mode. The spatial distribution of electric field of a TM mode is calculated by

$$E_r(\mathbf{r}) = E_{r,0} \cdot \frac{k_z}{k_{n,m}} \cdot J'_n(k_{n,m} \cdot r) \cdot (A \cos(n\phi) - B \sin(n\phi)) \cdot \sin(k_z z), \quad (5.70)$$

$$E_\phi(\mathbf{r}) = E_{\phi,0} \cdot \frac{nk_z}{k_{n,m}^2} \cdot \frac{J_n(k_{n,m} \cdot r)}{r} \cdot (A \sin(n\phi) - B \cos(n\phi)) \cdot \sin(k_z z), \quad (5.71)$$

$$E_z(\mathbf{r}) = E_{z,0} \cdot k_{n,m} \cdot J_n(k_{n,m} \cdot r) \cdot (A \cos(n\phi) - B \sin(n\phi)) \cdot \sin(k_z z), \quad (5.72)$$

with the cutoff wavenumber $k_c := k_{n,m}$. The cutoff wavenumber must fulfill

$$J_n(k_{n,m} \cdot R) = 0. \quad (5.73)$$

All in all, the frequency of the TM mode is calculated by

$$\omega^2 = (k_c^2 + k_z^2) c^2. \quad (5.74)$$

An example of the spatial distribution of the electric field of a TM mode in z -direction can be found in figure 5.10 for variable values of n and m .

In total, the frequency of the TE and TM modes can be calculated directly from the radius and height of the cylinder and the mode numbers n , m and l through equations 5.69 and 5.74.

In the second step, the frequency and spatial distribution of the modes can be used to excite cavity modes in a simulated cylinder geometry. The excitation is performed with a driving current, "whose spatial profile approximates the profile of the known mode (...). The current source will have a Gaussian envelope in time and with a center frequency that matches the known mode frequency." [60] An example of the driving current can be found in figure 5.11.

In the third step, the electric field is recorded over time after the driving current is reduced to zero, see also figure 5.11. The frequency of the mode is then determined from the temporal evolution of the field. Nieter et al. [60] use a fit with multiple sine functions to

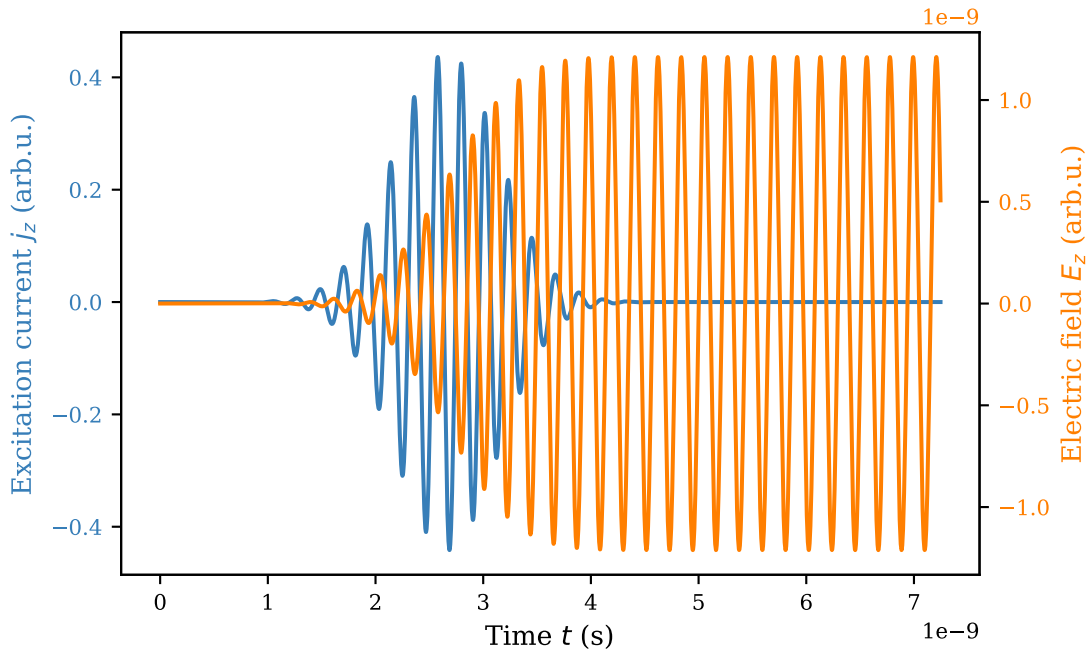


Figure 5.11.: Driving current and field response for cavity mode excitation. An excitation current with spatial shape of a cavity mode is applied, with the corresponding frequency of the mode and and gaussian envelope. The field in the cavity is excited and the frequency of the mode is determined after the excitation current is switched off.

the data, and use only the frequency of the mode with the largest amplitude as a result. This procedure will not be used here, because it was found to be unstable. In the context of this thesis, the frequency was determined through the use of the fast Fourier transformation of the electric field signal and through the subsequent fit of a Lorentzian to the peak with the highest intensity, see figure 5.12. This frequency f_{sim} is then compared to the initial excitation frequency f_{ex} . The relative error ϵ is then calculated by

$$\epsilon = 1 - \frac{f_{\text{sim}}}{f_{\text{ex}}} \quad (5.75)$$

The uncertainty on the frequency and on the relative error is calculated through the maximum between the uncertainty of the fit and the sampling rate. The sampling rate is given by the inverse of the timestep length.

Validation

At first, it was investigated qualitatively, if cavity modes can be excited at all in the cavity. Therefore, four different simulations were performed, each with different mode numbers for n and m . The excited electric field can be seen in figure 5.10. The structure of the field corresponds to the expected structure of equation 5.72. It can be seen, that the mode number n increases the azimuthal subdivision of the electric field, while the mode number m increases the radial subdivision. Therefore, it can be concluded that cavity modes can be excited.

In a second step, the algorithm was used for a quantitative analysis of the excited cavity modes. This way, it allowed for a classification of the Maxwell solver of ACRONYM with cylindrical boundaries. For this analysis, it was decided to use the excitation of a TM mode with indices $n = 0$, $m = 1$ and $l = 2$ only. This choice of mode numbers is motivated by the simple structure of the electric field. There are no additional features in radial

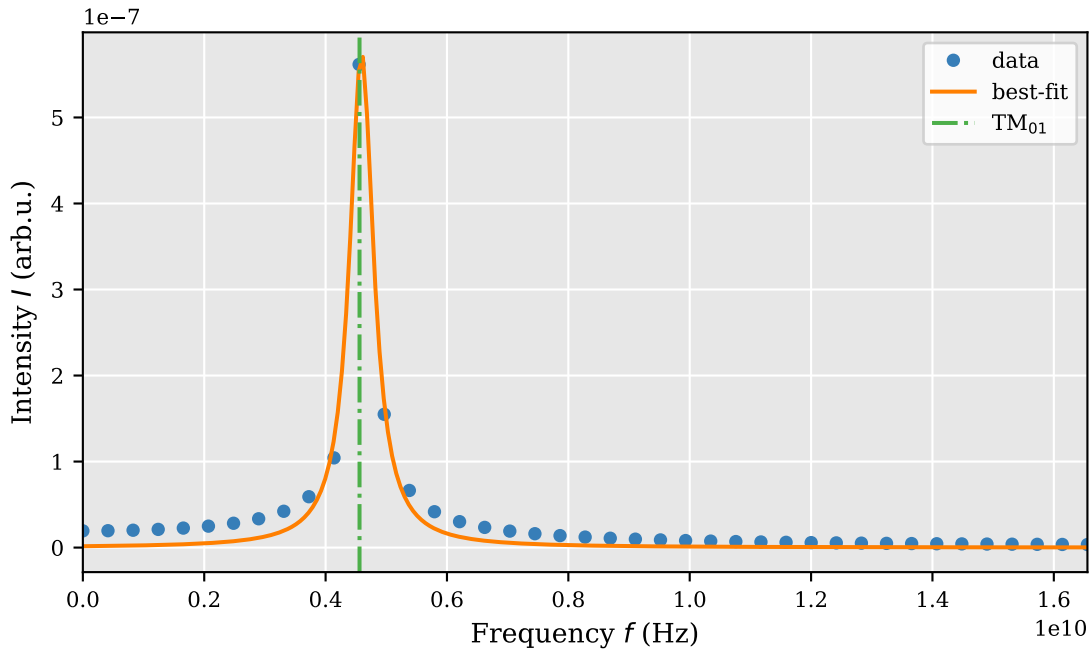


Figure 5.12.: Determination of the simulated cavity mode frequency. The field values are collected at a given position over many timesteps. The signal is then Fourier transformed and the frequency of the highest peak is determined through a fit of a Lorentzian to the data. The estimated frequency is compared to the expected theoretical frequency.

direction, which allows for its use in a simulation with small number of cells in radial direction. Additionally, the frequency of this mode is significantly different from other cavity modes, which reduces the possible confusion of the measured frequency with other modes.

The implemented Maxwell solver in ACRONYM was classified in a scenario, where the radius R of the cylinder is set to a fixed value, and the number of cells in radial direction are varied. The cell length Δx was determined from the number of cells in radial direction N_r and the radius R of the cylinder

$$\Delta x = \frac{R}{N_r}. \quad (5.76)$$

In the ACRONYM code, the cell length is not chosen directly, but rather the electron density, see equation 5.27. As a consequence also the timestep length is affected by changes of the cell length and electron density, see section 5.1.5. In principle, the timestep length can be adjusted through an additional predefined factor in the code. This adjustment was not done here, to provide an accuracy of the simulation under standard operation conditions. In total, 8 different numbers of cells in radial direction were compared, ranging from 30 to 100 cells. The specific numbers were chosen to reflect the number of cells used later on in the simulations of the KATRIN source, see also chapter 6.

The results of the different simulations can be found in figure 5.13. In general, it can be observed that the cavity is excited by a mode, whose frequency is close to the theoretical frequency. In all cases, the simulated frequency agrees with the theoretical frequency in the limit of the uncertainty of the value. Nevertheless, three additional features are discernible. First, the uncertainty increases with the number of cells. Second, there seems to be a substructure in the simulated frequency. Third, most of the simulated frequency values lie above the theoretical value.

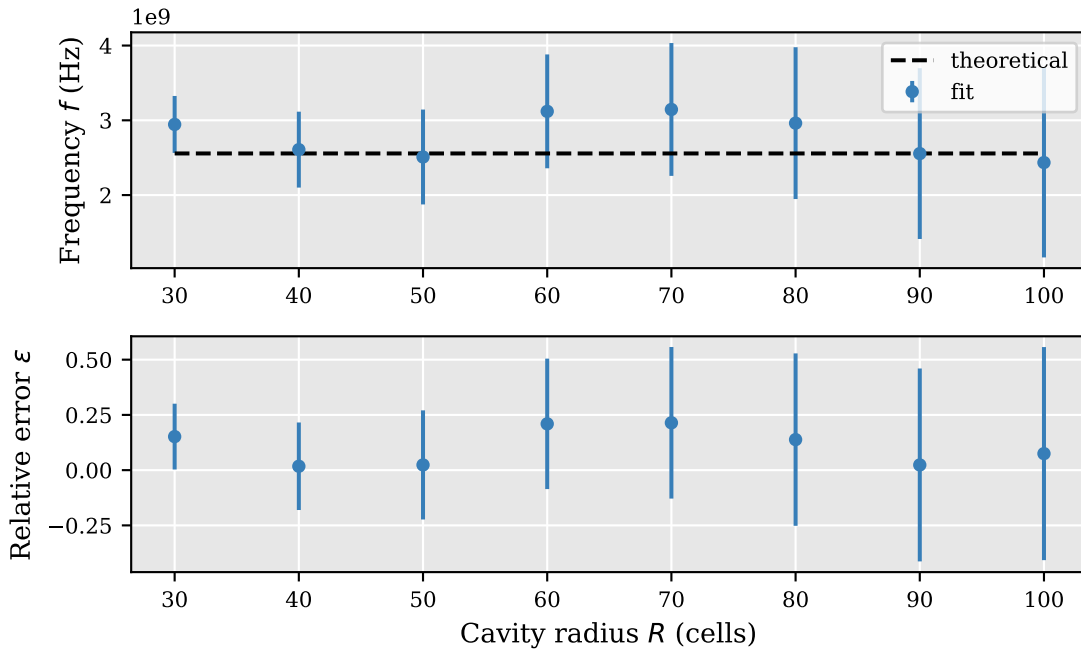


Figure 5.13.: Simulated and theoretical cavity mode frequency for various divisions of the radius. Theoretical cavity mode frequency and fit of the excited frequency by simulation at different segmentations of a fixed radius. The uncertainty describes the maximum between the uncertainty of the fit and the resolution of the simulation.

The first feature can be explained by a look at the evaluation of the uncertainty. It is calculated as the minimum between the fitted uncertainty and the sampling rate. The fitted uncertainty is much lower than the sampling rate. Thus, only the sampling rate determines the uncertainty. The sampling rate is dependent on the timestep length, which in turn depends on the number of cells in radial direction. Thus, the uncertainty increases with N_r .

The second feature, the substructure in the simulated frequency, can be explained by a combination of two effects: a reduction of the relative error through the increased number of cells, and again the sampling rate. On the one hand, it is expected that the more cells are used for the simulations, the better the geometry can be approximated by the algorithm. Thus, the frequency shows more precise values the higher the number of cells. On the other hand, the simulated frequency is bound by the sampling rate. This means, that if the true frequency is between two frequency data points, then the fit result might abruptly jump from one value to another. This explains the jump of the frequency between 50 and 60 cells. This hypothesis is supported through the fact that the theoretical frequency is always within the uncertainty bounds of the simulated frequencies, which are dominated by the sampling rate. An additional simulation was performed to test the hypothesis with a reduced timestep length by a factor of five. Here, the relative error was reduced to $\epsilon \approx 0.03 \pm 0.06$, not shown in the figure. This value is significantly lower than before, which is expected for a better frequency resolution.

The substructure of the simulated frequencies remembers of a sinodial wave pattern. Nevertheless, the uncertainties are too large to deny or verify this hypothesis from the presented data, and more elaborate simulations would be necessary. However, such an investigation is not gainful in respect to the validation of the implemented algorithm, but rather useful for an improvement of the algorithm itself. The explanations from above are sufficient for a validation of the implementation. It was therefore refrained from an

investigation of the substructure pattern in the context of this thesis.

The third feature, the overestimation of the simulated frequency, can be explained by a look on the algorithm, which generates the simulated geometry, see section 5.2. This algorithm determines the actual division of the simulation domain into cells and identifies, which cells are half cut, outside or inside the geometry. The algorithm is set up in such a way, that the mean radius of the simulated geometry is in almost all cases lower than the actual radius. Thus, the radius in the simulation is always underestimated, which in turn overestimates the resulting frequency.

In summary, it was found, that cavity modes can be excited in the cavity. The distribution of the field corresponds to the distribution of the excitation current. The simulated frequency corresponds to the expected theoretical frequency in the limit of the uncertainty. Deviations arise from the sampling rate and the approximation of the cylindrical shape with half cut cubes. In total, it can be concluded, that the Maxwell solver works as expected and produces reliable results of the electromagnetic fields in a cylindrical cavity.

5.6.4. Boundary Layer Development

When a plasma comes in contact with a metallic or dielectric boundary, it will interact with that boundary. This interaction will create a boundary layer, which will shield the plasma from the influence of the boundary, see section 3.3.1. A cohesive theory of all possible plasma states and boundary geometries does not exist. There exist solutions for specific sets of conditions. These solutions mostly assume that the plasma is infinitely extended in one or the other direction, that the velocity distribution of the electrons and ions follows the Maxwell distribution, and that the boundary surface is flat. In these cases, the electric potential drops towards the boundary. The potential difference between the bulk of the plasma and the boundary will adopt values of several k_bT . The thickness of the boundary layer will be in the order of the Debye length [57].

The development of a boundary layer was used to test the new PEC boundary in conjunction with the PIC algorithm. The test was subdivided into two steps. First, it was tested if a boundary layer developed towards the PEC boundary, especially in radial direction. Second, the observed boundary layer thickness and potential drop were used to investigate the behavior of the ACRONYM algorithm under similar plasma conditions but different simulation parameters.

The first test was performed for a plasma inside a closed cylinder with radius $R = 4.5$ cm and height $H = 19.17$ cm. The radius was chosen to represent the radius of the KATRIN beam tube. The height was chosen to be significantly larger than the radius, while keeping simulation effort to a minimum. Thus, the height was set to the discretionary value of approximately four times the beam tube radius. The plasma was initialized with an electron density of $n_e = 1 \times 10^5 \text{ cm}^{-3}$ at $\text{ppc} = 20$. The velocity of the electrons was initiated from a Maxwell Boltzmann distribution with a temperature of $T = 30$ K, which corresponds to a thermal energy of $E_{\text{th}} = 2.59$ meV. The simulation was performed for four plasma time scales. No background fields were used. The electric field was recorded at the last timestep. In a post-processing step, the field components in the Cartesian directions were transformed to the radial field E_r through

$$E_r(i, j, k) = E_x(i, j, k) \cdot \cos \theta + E_y(i, j, k) \cdot \sin \theta, \quad (5.77)$$

$$\theta = \arctan \left(\frac{j - j_0}{i - i_0} \right), \quad (5.78)$$

where (i, j, k) are cell indices and i_0 and j_0 are the cell indices of the cylinder origin. This procedure provided simple access to the radial electric field, but is not accurate in the

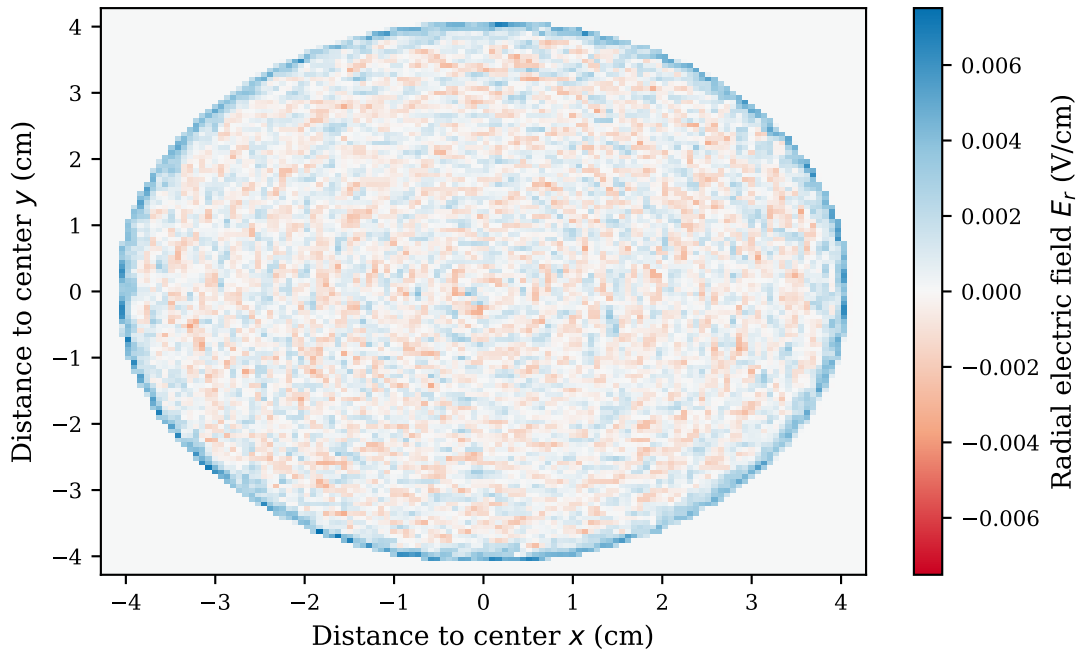


Figure 5.14.: Boundary layer in radial direction. Simulated boundary layer in a conducting cylinder filled with a plasma with an electron density of $n_e = 1 \times 10^5 \text{ cm}^{-3}$ with a thermal velocity distribution ($T = 30 \text{ K}$) after four plasma time scales. The radial electric field is generated in a post processing step.

sense, that the field components are positioned at different locations, see section 5.1.1. Nevertheless, this inaccuracy was neglected for simplicity.

The simulated radial electric field of a two-dimensional slice in the center of the cylinder is depicted in figure 5.14. It can be seen that the radial electric field fluctuates around zero in the center of the plasma. The fluctuations are expected for a thermal plasma far away from a boundary. The behavior changes closer to the boundary. There, the field shows a predominant direction and increases towards the boundary. The boundary layer is several cells thick, which corresponds to several Debye lengths. Again, this is expected for a thermal plasma. The thickness of the boundary does not show an azimuthal behavior, which corresponds to the azimuthal symmetry of the simulation. In total, the results of the simulation indicate that the cylindrical boundaries are implemented correctly in the ACRONYM code. A more precise analysis was performed in the second test step.

In the second step, the cylindrical boundaries were tested under similar plasma conditions but different simulation parameters: in a simulation with half the number of cells in radial direction and in a simulation with half the cell size. In the later case, the number of particles in the cells was adapted to ensure that the electrons have the same macro factor as before. In both cases it was expected that there is also a region in the plasma, which is not influenced by the boundary and a boundary region, which shows the same potential drop as the simulation with the original radius.

The resulting radial electric field and potential can be found in figure 5.15. The radius was normalized to the cylinder radius of the simulated cavity for a better comparability. The potential was derived from a two-dimensional slice in rz -direction, through the use of the Poisson solver from section 5.5. The potential of the beam tube and cylinder ends was set to $U = 0 \text{ V}$. It can be seen, that all three simulations showed similar results for the electric field and the potential. The specific properties will be described in the following, and differences will be pointed out.

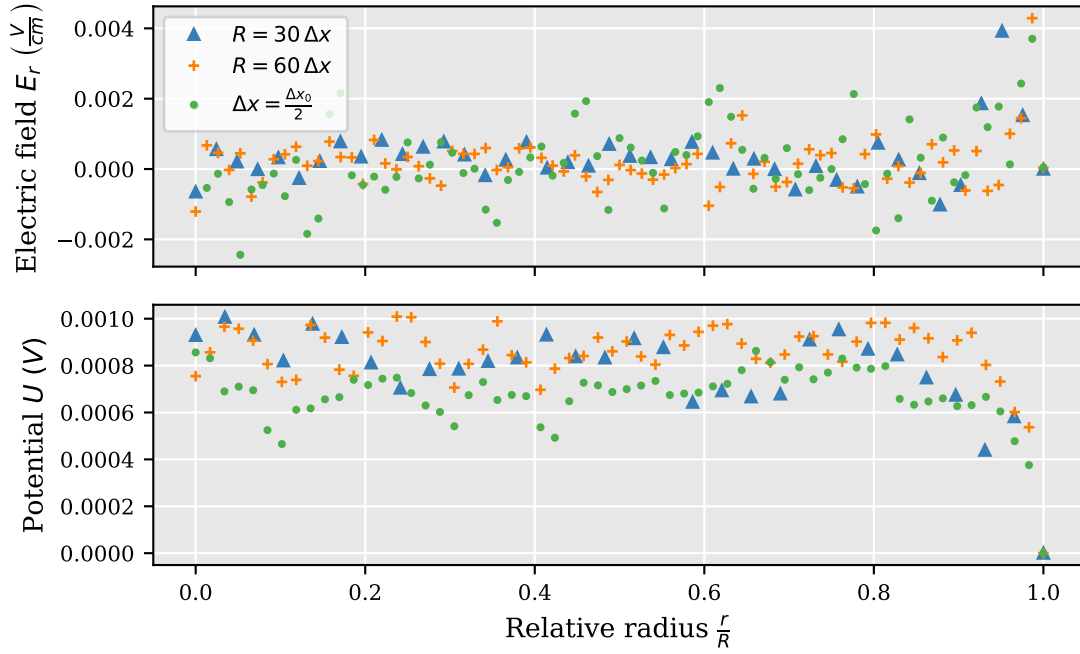


Figure 5.15.: Radial boundary layer in a cylindrical cavity. The cavity was filled with an electron density of $n_e = 1 \times 10^5 \text{ cm}^{-3}$ following a thermal velocity distribution ($T = 30 \text{ K}$). The simulation was performed in a cavity with a radius of 30 cells ($R = 30\Delta x$), with double the radius ($R = 60\Delta x$), and with the same physical radius but each cell was divided in half ($\Delta x = \frac{\Delta x_0}{2}$). The radius of the data points was normalized to the radius R of the cylinder. The data was taken after four plasma time scales.

There is a region ($r < 0.8R$) in the center of the cylinder, where no influence of the boundary is discernible. Due to the random nature of the variation, it is assumed that the fluctuations of the potential arise from thermal fluctuations. There is another region ($r > 0.8R$) with an increased electric field and a potential drop towards the PEC boundary. The boundary layer is several cells thick, as expected for a Debye sheath. The data indicates that the boundary layer is smaller for the simulation with double the original radius. This behavior can be attributed to the normalization of the radius and has no physical foundation.

The potential drops in all three simulations towards the boundary by approximately 0.8 mV. This value corresponds to only a third of the thermal energy, and is lower than expected for a classical Debye sheath. Two explanation attempts can be made. First, the algorithm of the PEC algorithm used in the context of this thesis, see section 5.2, underestimates the current towards the beam tubes. Thus, the field generated by that current is lower than expected. The second explanation could be that the potential drop in a cylindrical cavity with a low electron density is lower in reality than in the case of an one-dimensional planar surface. No analytic calculation was found in the literature to prove or disprove this hypothesis. More simulations are necessary in the future to disentangle the effect of the potential at cylindrical boundaries.

The same three simulations can also be used to investigate the electric field and potential in longitudinal direction. The height of the cylinder of all three simulations was set to the same value. It is expected that there is a boundary layer before both end caps of the cylinder, and that there is a region, where the potential only fluctuates through thermal variation. The corresponding potential and electric field can be found in figure 5.16. It can be seen that both expectations were met by the simulations. Nevertheless, additional features are discernible, which will be described in the following.

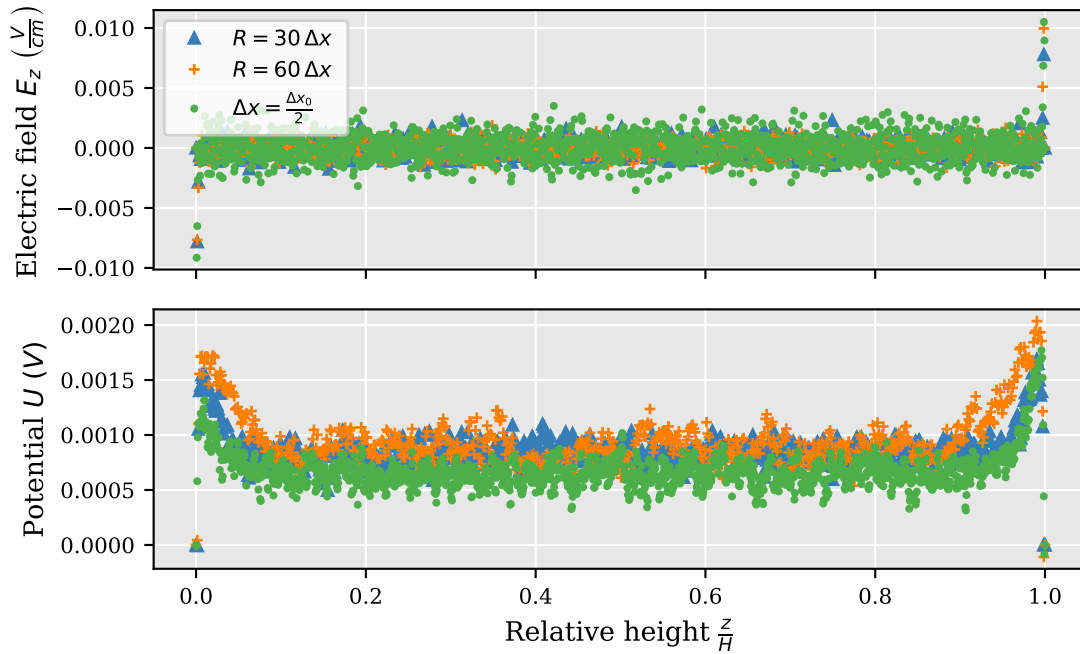


Figure 5.16.: Longitudinal boundary layer in a cylindrical cavity. The cavity was filled with an electron density of $n_e = 1 \times 10^5 \text{ cm}^{-3}$ following a thermal velocity distribution ($T = 30 \text{ K}$). The data was taken after four plasma time scales. The simulation was performed in a cavity with a radius of 30 cells ($R = 30\Delta x$), with double the radius ($R = 60\Delta x$), and with the same physical radius but each cell was divided in half ($\Delta x = \frac{\Delta x_0}{2}$). The height of the cylinder was kept the same for all three simulations. The position of the data points was normalized to the height H of the cylinder.

The boundary layer is thicker in longitudinal direction than in radial direction. The layer can be subdivided into two sections. In the first section, there is an initial increase of the potential over a few Debye lengths. In the second section, the potential then decreases over many Debye lengths towards a potential plateau. It seems that the bisection of the potential shape is a result of the intrinsic interaction of the longitudinal and radial boundary condition. In longitudinal direction, the potential builds up for a few Debye lengths, independent of the radial boundary. The interaction with the radial boundary flattens then the potential to lower values in the second section. This hypothesis is supported by another feature observed in the data: The potential difference in longitudinal direction is higher for the simulation with the increased physical radius than for the other two simulations. Thus, the influence of the radial boundary is less strong in the simulation with increased radius. In other words, it seems that the interaction between the tube boundary and end cap boundary impacts only a small region at the end caps. The central part is only dominated by the tube walls.

The absolute value of the potential drop at the longitudinal boundary is larger than in radial direction. It reaches values up to approximately 2 mV (depending on the radius of the cavity). Again, this value is below the expected height of a few $k_b T$. Similar to the description of the radial potential drop, it is unclear if the difference to the expected value originates from the missing current of the mirror charges or is a physical reality. The latter hypothesis is underlined by the fact that the potential reaches higher values in the simulation with an increased radius. Thus, the radial boundary seems to have less influence on the longitudinal boundary layer. Nevertheless, more simulations are necessary for a validation of both hypothesis.

In total, it can be concluded that the implemented PEC boundary conditions work well

with cylindrical boundaries. Simulations show, that a thermal plasma inside a cylindrical cavity produces a boundary layer towards the cavity walls. The absolute potential values were found to be lower than expected. Nevertheless, it could not be differentiated if the observed potential values are of physical nature or a relic of the used boundary conditions.

5.7. Conclusion

This chapter focused on the description of the ACRONYM PIC code, which will be used for the dynamic simulation of the KATRIN plasma. First, the generic code was described in detail. Then the newly added features of the code were presented.

The most prominent feature is the adaptation of cylindrical PEC boundaries to the simulation. The used algorithm follows the method of Dey-Mittra [19], where the Maxwell solver calculates the new field values corresponding to the edge length of the cells inside the geometry. A reduction of the timestep length was not necessary, because it was decided to use only half cut cells.

The ACRONYM code is newly equipped with a particle loading algorithm, which allows for position dependent particle densities and velocity distributions. The velocity distributions can be sampled from arbitrary functions through the rejection method, the inverse method and from histogram data. This tool will be used to insert the simulated energy distribution from the KARL simulation. A position dependent drift velocity can be added to the particles, which will be calculated from the current and density distribution of the KARL simulations. Aside from the initial loading, new particles can be added to the simulation domain during the simulation. The injection can be achieved through a virtual layer of cells, which emits particles. This injection method can also be used in conjunction with the PML boundary condition, which allows for a simulation of the rear wall section with a connection to the bulk of the source plasma. Additionally, there is the possibility to inject beta particles in dependence on the tritium density during the simulation. This injection method can be extended with the injection of secondary particles from ionization in dependence of the mean number of particles created through a beta particle.

Another new feature of the ACRONYM code is the possibility to use position dependent background fields and currents. They can be used to represent the potential difference between beam tube and rear wall, the background magnetic field of the WGTS and the ion movement. The background can be modeled from data or from a given position dependent function.

The evaluation methods of the ACRONYM code were extended with a Poisson solver. This solver can calculate the electrostatic potential from an arbitrary electric field in a cylindrical cavity.

All additions to the code were validated through specific targeted tests. It could be shown that the addition of the background ion current is the same as simulating the ion movement directly for a small time scale. Thus, this method can conserve simulation time, while keeping the ion motion incorporated in the simulation. In a similar test, it could be shown that the background electric field can be used to simulate external electric fields, like the contact potential between rear wall and beam tube wall.

The addition of the new cylindrical PEC boundaries was tested in two steps. In a first step, the algorithm was tested in an empty cylinder. Cavity modes were excited in that cylinder, and the simulated cavity mode frequencies were compared to theoretical frequencies. A good agreement was found between simulation and theory. However, the simulated frequencies showed a large uncertainty, caused by the limited resolution of the timestep length. A reduction of the timestep length reduced the uncertainty and the relative error, enforcing the trust in the algorithm.

In the second step, the test cylinder was filled with particles. It was proven that an expected Debye boundary layer is formed between the cylinder walls and the plasma. The extent of the layer was found to be similar to the expected Debye length, both in radial and longitudinal direction of the cylinder. However, the absolute potential was lower than expected from a one dimensional Debye sheath ($\approx k_b T$). More simulations are necessary to disentangle effects from the used PEC algorithm, the inherent phase space resolution, and possible physical influences on the layer formation like the low electron density and cylindrical shape of the cavity. The latter hypothesis is supported by simulations with increased radius, which showed an increased potential.

Chapter 6

Particle in Cell Simulation of KATRIN Source

In this chapter, ACRONYM will be applied to the simulation of the plasma inside the KATRIN source. The size of the source is large compared to the Debye length. It is therefore imperative to evaluate the needed computational resource before the simulation, which will be described in section 6.1. The evaluation showed that it is beneficial to segment the source into smaller parts and simulate the plasma in those parts first. One of these parts is a section in front of the rear wall. The interaction of the boundary with the plasma is assumed to be the strongest here due to the movement of the charged particles towards the boundary and subsequent absorption. Currently, there is no conclusive information available, which parameters of the plasma (spectrum, particle currents, etc.) significantly influence the plasma in the rear wall region. Therefore, the second section of this chapter (section 6.2) focuses on the simulation of the plasma with varying parameters in this region. Another distinct section of the source is a segment in the center of the WGTS. This section is the furthest away from the longitudinal boundaries. Therefore, it is used for the investigation of the plasma independent of the longitudinal boundary condition. The investigations are described in the third section of this chapter (section 6.3). Lastly, the experiences from the smaller sections are applied to a simulation of the whole KATRIN source, see section 6.4.

6.1. Estimation of Computational Resources

The estimation of the computation resources for the simulation of the plasma inside the source hinges on four different parameters: the size of the simulated geometry, the cell size Δx , the timestep length Δt and the plasma time scale. These parameters can be used to evaluate the necessary number of cells, the number of timesteps, and the number of macro particles. In the end, the necessarily needed computational resources result from the available number of CPUs and from the performance of the code. The evaluation of each of the different parameters will be described in the following for the conditions inside the KATRIN source to provide an estimate of the necessary computational resources and suggestions for how to proceed with the simulations.

The size of the simulated geometry is given by the extends of the KATRIN source. In first approximation, the source is a cylinder with a radius of $R = 4.5$ cm and a height of $H = 16$ m. The geometry of the pump ports and the rear wall chamber is neglected here.

The cell size is calculated from the Debye length through equation 5.27. The Debye length in turn is dependent on the electron density and the temperature of the electrons. The KARL simulations revealed that there is a difference between the electron density and the ion density. Assuming quasineutrality in the source, the larger value of both densities is

used as a first approximation on the maximum electron density. The KARL simulations showed that the ion density is higher than the electron density. It reaches values of up to $n_i \approx 3 \times 10^6 \text{ cm}^{-3}$. The temperature is assumed to be $T = 80 \text{ K}$, which is also the temperature of the surrounding tritium gas. Thus, the Debye length is $\lambda_D \approx 3.56 \times 10^{-2} \text{ cm}$, and the cell size is $\Delta x \approx 2.52 \times 10^{-2} \text{ cm}$.

Both the cell size and the size of the geometry can be used to calculate the number of cells in each direction of the Cartesian simulation domain. The cylinder is assumed to be aligned with the z -axis. Thus, the minimal number of cells in z -direction calculates to

$$n_z = \frac{H}{\Delta x} \approx 63506. \quad (6.1)$$

In the other two directions, the simulation domain must be large enough to cover the diameter of the source. Thus, the number of cells in x - and y -direction must be at least

$$n_x = n_y = \frac{2R}{\Delta x} \approx 362. \quad (6.2)$$

In total, approximately 8.3×10^9 cells must be simulated. Each cell will be filled with macro particles. The number of macro particles in each cell should be large enough to avoid statistical fluctuations. A rule of thumb are 20 particles per cell. This means that if all cells are filled homogeneously, there are $N_p \approx 1.66 \times 10^{11}$ particles in the simulation.

The number of timesteps N_t is calculated from the plasma frequency and the timestep length Δt , see equation 5.1. The timestep length Δt is limited by many factors (gyro frequency, plasma frequency, etc.), see section 5.1.5. In the case of the WGTS, the timestep length is bound by the CFL limit, which provides $\Delta t < 4.4 \times 10^{-13} \text{ s}$. With the approximate density of the electrons, the plasma frequency calculates to $\omega_{pe} \approx 98 \text{ MHz}$ and the plasma time scale to $t_{pe} \approx 10 \text{ ns}$. Therefore, to cover one plasma time scale, the number of timesteps must be at least $N_t \approx 23204$.

The ACRONYM code is highly paralizable on many CPU cores, see also [41]. The performance of the code can be classified as the number of particle updates, which can be performed simultaneously per second on a given number of CPUs. A rough estimate of the performance of the current version of the code is $P = 2.5 \times 10^5$ particle updates per second and CPU (with no particle output). This number can be used to calculate the time t_{sim} a simulation will take with a given number of CPUs N_{cpu} through

$$t_{\text{sim}} = \frac{N_p \cdot N_t}{N_{\text{cpu}} \cdot P}. \quad (6.3)$$

Thus, the simulation time scales inversely with the number of CPUs. A small simulation time is preferable, partly because the computational resources are only available for a certain time and partly because the results shall be available at a reasonable time. The simulation time can be reduced by increasing the number of CPUs, by increasing the number of particle updates per second, or by reducing the number of simulated particles or the number of simulated timesteps. The latter two are inherent to the plasma which should be simulated, and can therefore not be reduced. The number of particle updates per second depends mostly on the current deposition step of the PIC algorithm. Nothing fundamental was changed in the current deposition step from the optimized basic ACRONYM code. Therefore, there is not much room for improvement. This means, only the number of CPUs can be increased to reduce the simulation time.

The number of CPUs cannot be increased to arbitrarily high values because of the cylinder geometry of the source and the partitioning of the simulation domain. The simulation domain is partitioned into cuboid sections, where each CPU simulates the plasma in its

section [41]. Corresponding communication between the CPUs was set up. The total number of CPUs N_{cpu} is calculated from the number of CPUs s_i in each spatial direction through

$$N_{\text{cpu}} = s_x \cdot s_y \cdot s_z. \quad (6.4)$$

The values of s_i can be specified before the simulation. In general, it is preferable that each CPU has the same load. This is the case for the cylindrical geometry of the source if $s_x = s_y = 2$ (division in quarter circles), or if $s_x = s_y = 1$ (no division). This would also mean, that the number of CPUs can only be increased by increasing the partition in z -direction. Therefore, this procedure is limited by the minimal number of cells in z -direction. Additionally, there is a large magnetic field in z -direction. Thus, particles will most likely move in this direction. So, there will be more communication necessary between the CPUs in z -direction than in the other two directions. So in total, for each simulation it has to be evaluated if it is preferable to have an uneven load on the CPUs or if more communication steps have to be performed.

The simulation time at large-scale computation facilities is granted, in most cases, for the cumulated computation time t_{cum} of each single CPU. The typical unit is CPUh, which denotes that one CPU has been used for one hour. If all CPUs are used in parallel then the cumulated computation time is calculated through

$$t_{\text{cum}} = t_{\text{sim}} \cdot N_{\text{cpu}}. \quad (6.5)$$

The simulation time scales inversely with the number of CPUs, compare equation 6.3. Thus, the cumulated computation time does not scale with the number of CPUs. It can therefore be considered as a hard limit on the necessary computational resources for a specific problem.

Following the calculation from above for the total number of particles, the number of timesteps and the performance of the code, the cumulated computation time for one simulation of the KATRIN source is calculated to $t_{\text{cum}} = 3.25 \times 10^6$ CPUh. In the context of this thesis, it was possible to obtain a grant for $t_{\text{cum}} = 36 \times 10^6$ CPUh at the Leibniz Supercomputing Centre. One simulation of the whole source section would take up at least a tenth of this quota. This shows that parameter studies and tests of the new code are not feasible for the simulation of the whole KATRIN source.

Hence, it was decided to break down the simulation domain into smaller segments, namely a region in front of the rear wall, see section 6.2, and a region in the central part of the tube, see section 6.3. This way, the length of the cylinder is reduced, which reduces the number of simulated particles. Additionally, the electron density in front of the rear wall is lower than in the center of the source. Thus, the cell size and timestep length is increased, which reduces the required computational resources further. So, parameter studies can be performed in the rear wall region without any concern of the computation time.

6.2. Rear Wall Section

The plasma of the KATRIN source is surrounded by a strong magnetic field, which mostly confines the movement of the charged particles in longitudinal direction. Therefore, interactions of the plasma with a boundary in longitudinal direction are of special interest. The results from Kuckert [50] suggest, that the potential of the rear wall has a significant influence on the fields inside the source. The simulations of Kuckert assumed a collisional plasma throughout the source. This assumption was shown to be invalid in the context of this thesis, especially in the rear wall region, see section 4.3. Therefore, ACRONYM is used for the investigation of a collisionless plasma in front of the rear wall. Because there are no previous dynamic simulations available, it is unclear which plasma parameters have

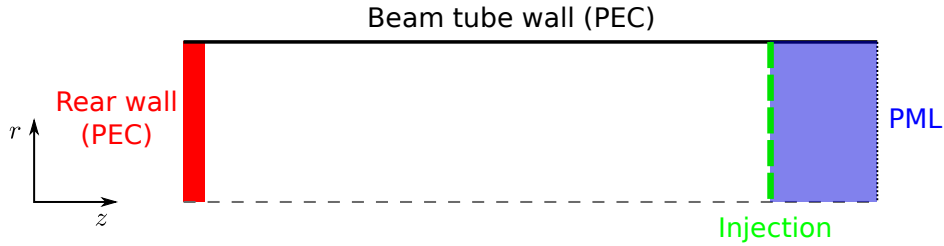


Figure 6.1.: Simulation setup for the rear wall section. The geometry is approximated as a cylinder with a closed end (rear wall) and with an open end (PML). Particles will be injected initially in the volume, and during the simulation at the injection plane.

a significant influence and are indispensable for a complete model of the plasma. Hence, this section will focus on the investigation of the plasma under the variation of different parameters. The examined parameters will include the electron spectrum, the electron density and the background current. Their extent is obtainable by KARL simulation. They provide a good starting point for the investigations.

The same simulation setup was used in each of the parameters studies in order to obtain results that are as comparable as possible. The setup will be described shortly in the following. The rear wall chamber and the attached beam tube is approximated by a cylinder with radius of $R = 4.5$ cm and a height of $H = 1.5$ m. The height corresponds approximately to the distance between the rear wall and the first pump port. The cylinder is closed at one side by the rear wall and is open on the other side, see figure 6.1. The rear wall is considered as a perfectly conducting surface. Hence, it is simulated through a PEC boundary condition. The open end of the cylinder will be represented by a PML boundary. Particles from the bulk of the plasma enter the simulation domain through an injection plane in front of the PML boundary. The number of injected particles will be determined by retaining a constant density at the boundary, see section 5.4.2.2.

The tritium density in front of the rear wall is significantly lower than in the center of the source, see section 2.1.1. It can therefore be assumed that no significant amount of beta decays or ionization processes occur here. Thus, there will be no injection of additional particles in the volume after the initial loading.

6.2.1. Electron Spectrum

Simulations with KARL, see section 4.3.1, show that the electron spectrum can be subdivided into three regions: a thermal region, where the energy follows the Maxwell Boltzmann distribution, a beta region, where the energy follows the Fermi distribution of beta decay and a transitional section between the other region. In this section, it will be investigated how these distributions influence the potential of the rear wall section. Additionally, it will be assessed if the parts of the spectrum are relevant for the solution or if they can be neglected in future simulations. Three different cases were compared: a spectrum with only the thermal region of the spectrum, a spectrum with the thermal region and the beta region, and a spectrum with all three regions.

Simulation Setup

Four parameters need to be set prior to the simulation: the background fields, the particle densities, the particle velocity distributions, and the background ion current. Each of these parameters will be described shortly in the following.

The background magnetic field was set to $B = 2.5$ T homogeneously distributed over the whole rear wall section. For simplicity, the variation of the field strength in the rear wall

Table 6.1.: Simulation parameters for spectrum analysis. Parameter were determined from a KARL simulation without background electric field, see section 4.3.

	n_e (1/cm ³)	j_e (1/(cm ² s))	v_D (cm/s)	ppc	macro factor
thermal	1×10^5	9.2×10^9	-9.2×10^4	20	13.2
transitional	2.27×10^2	2.37×10^8	-1.04×10^6	1	0.60
beta	2.50×10^{-1}	7.04×10^8	-2.81×10^9	1	6.6×10^{-4}

chamber and pump ports, see section 2.3, was neglected. No electric background field was used. Thus, the contact potential difference between the rear wall and the beam tube wall was assumed to be zero.

The total electron density was set to $n_e = 1 \times 10^5 \text{ cm}^{-3}$, due to the assumption of quasineutrality. Therefore, the density corresponds to the simulated ion density in front of the rear wall and not the simulated electron density. An investigation of the influence of the total electron density on the result can be found in section 6.2.2.

The individual electron densities for the different parts of the spectrum were set to a homogeneous value throughout the simulation domain. No longitudinal or radial variation was considered, due to the small variation of the density in the rear wall region, see section 4.3.2. The specific values of the densities were determined using two approximations. First, it was assumed that the density of the beta particles is constant in the source, and the simulated value of KARL can be used directly. This assumption is supported by the results of the KARL simulation, see section 4.3.1. Second, it was assumed that the density of the transitional region can be expressed relatively to the density of the thermal segment. Thus, the density of the transitional region can be calculated directly from the density of the thermal region. This is of course only a first approximation, because the simulations with KARL showed that the density of both regions scales differently with the position in the source. The proportionality constant a was determined from the KARL data at the position directly in front of the rear wall to $a \approx 2 \times 10^{-3}$. The resulting density values used for the simulation can be found in table 6.1.

The electron energy was sampled using the methods of section 5.4.1.2. The energy of the thermal electrons was determined from a Maxwell Boltzmann distribution with a temperature of $T = 80 \text{ K}$. The energy of the beta electrons was rolled from the histogram data of the spectrum of the KARL simulation directly in front of the rear wall. The minimum energy was set to $E_{\min} = 100 \text{ eV}$. The energy of the electrons in the transitional region was sampled directly through the histogram data of the spectrum within the energy range of $E_{\min} = 5 \times 10^{-2} \text{ eV}$ and $E_{\max} = 100 \text{ eV}$.

In the end, the velocity distribution was determined from the sampled energy with an additive drift velocity. The drift velocity was calculated from the simulated particle current, see section 4.3.3, through equation 5.45. The corresponding values of the estimated currents and drift velocities can also be found in table 6.1. The drift in radial direction was neglected, due to the comparably small value of the radial electron current.

The longitudinal current of the ions was represented in the simulation as a background current. It was set to a homogeneous value of $j_i = 0.73 \text{ nA/cm}^2$ throughout the simulation domain. A radial variation was neglected. An investigation of a radial dependent ion current can be found in section 6.2.4.

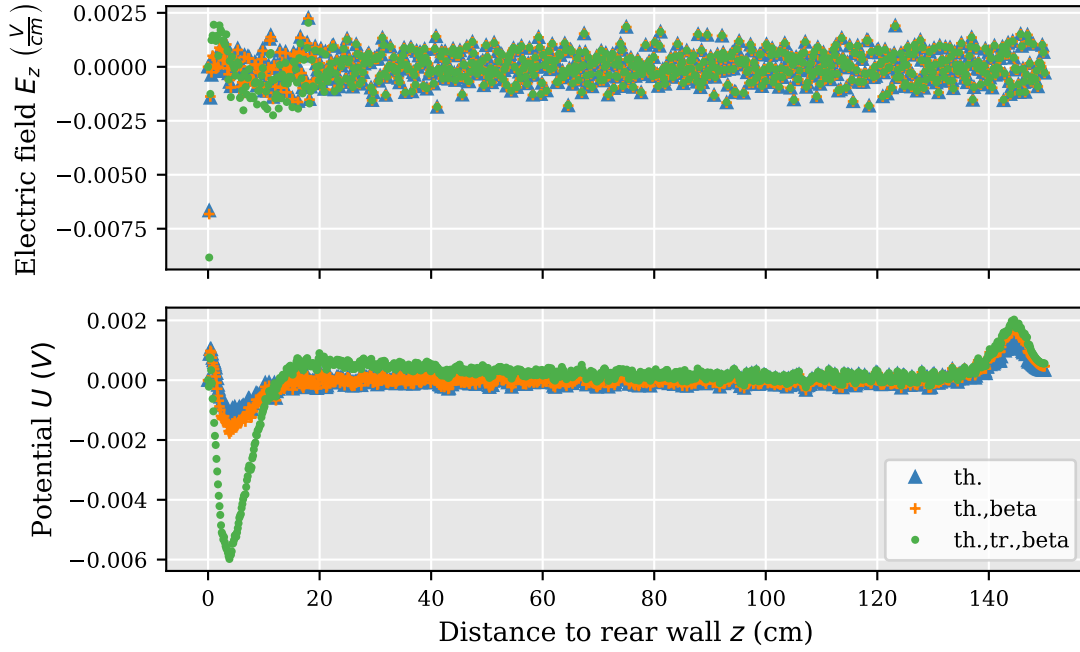


Figure 6.2.: Potential and electric field for varied electron distributions. Potential and electric field are evaluated along the longitudinal axis of the cylinder in a simulation with a background magnetic field of $B = 2.5$ T and a background ion current of $j_i = 4 \times 10^9$ s/cm². Three different spectra are compared. (th.): only a thermal region, (th.,beta): thermal spectrum and beta region, (th.,tr.,beta): full spectrum. The density values of the different spectrum regions can be found in table 6.1.

Results

The three simulations were performed for five plasma time scales and the electromagnetic fields, currents and particle distributions were recorded. Because of the strong longitudinal magnetic background field, it is expected that the largest difference between the simulations can be found in the electric field along the central axis of the cylinder. The radial dependency of the plasma will be investigated in more detail in section 6.2.4 together with a radial dependent background current.

The recorded electric field values were transformed into an electrostatic potential through the newly developed Poisson solver, see section 5.5. The electric field E_z and electrostatic potential in the center of the tube of the three simulations can be found in figure 6.2. It can be seen that all three simulations show a similar behavior of the potential and electric field. Three distinct regions can be identified: a region directly in front of the rear wall ($z < 20$ cm), a region in front of the injection plane ($z > 130$ cm), and a region between the other two regions. The following discussion will therefore focus on each of the regions separately.

In all three simulations, the potential in front of the injection plane, also called injection region, shows a similar behavior. The potential increases initially when moving away from the injection plane. Then the potential decreases towards zero. This feature was, in the context of this thesis, also observed in other simulations which used the PML boundary in conjunction with the injection of particles. It can be explained by the numerical injection process itself. The electric field in this region guarantees that only the correct number of particles are inserted into the simulation domain. The height of the potential wall in this region is determined by the current of ions and the current of electrons. In these specific simulations, the current of electrons is higher than the current of ions. Thus, some electrons

are reflected by the negative electric field, which reduces the incoming electron current. The height of the potential wall is higher for the simulation with all three electron species activated. This is expected, because each species increases the total electron current. Thus, a stronger electric field is necessary to reflect the electrons. All in all, the injection region is only located at the simulation boundary, and has no significant influence on the rest of the simulation domain. It is therefore not considered further.

The region directly in front of the rear wall shows three distinct features: a small positive potential wall in the first centimeter in front of the rear wall, a big negative potential wall of approximately 20 cm thickness, and a potential relaxation towards zero. This relaxation can extend over the central region of the simulation domain towards the injection region. The explanation of the origin of these three features will be illustrated in the following. The discussion will be guided by heuristic arguments. These arguments provide a good way to reason about the simulation results. Nevertheless, the behavior of the plasma is more intricate to be fully described by these arguments.

The negative potential wall can be explained by the large mass difference between electrons and ions, which lets electrons move faster than ions. Therefore, electrons can reach the rear wall faster, which produces a positive space charge of ions in front of the rear wall. Thus, a negative potential barrier is created, which balances the difference of electrons and ions leaving the source. This reasoning is supported by the simulations of section 5.6.4, where an electric field has developed to reduce the outgoing thermal electron flux.

The height of the negative potential wall depends on the spectrum of the electrons. High-energy electrons of the transitional region and of the beta region can pass the barrier. Thus, a larger electric field is necessary to maintain the balance between ion and electron current. It is noteworthy that the potential barrier increased more, when including electrons of the transitional region than in the case of beta electrons only. This is especially interesting because the mean current was higher in the beta region than in the transitional region, see table 6.1. This behavior could be explained by the difference of the density of the two electron species. There are much more electrons in the transitional region than in the beta region, which surpass the potential barrier. The energy difference between the two species does, most likely, not play a role because the beta electrons can leave the source at any potential value. This is not the case for the electrons of the transitional region, and a direct interaction of the potential with the electrons of the transitional region is possible.

There is a small positive potential wall in the first few centimeters in front of the rear wall. This wall can be directly linked to the positive electric field at this region, compare figure 6.2. It is possible, that this feature is a relic of the fixed ion background current. The true ion movement is influenced on large time scales by the potential generated by the electrons, whereas in the simulation, the ion current is set to a fixed value. This discrepancy is most notable directly in front of the rear wall, where the boundary effects are assumed to be the strongest. The positive electric field suggests, that the ion current is set too high in this region. This hypothesis is discussed in section 6.2.3 and will not be investigated further here.

The negative potential wall turns into a region ($z > 20$ cm) where a positive potential tends towards zero over a large distance. The positive potential value and the extent of the decrease depends on the used electron species. This behavior could not be observed in the electric field data. Thus, there seems to be an intricate interaction between the radial boundary and the longitudinal potential. No heuristic argument could be found for the origin of the expanded transition towards zero potential. This, however, does not diminish the meaningfulness of the simulation, but rather enhances it. It can be seen, that the used electron species do not only influence the height of the negative potential wall, but also

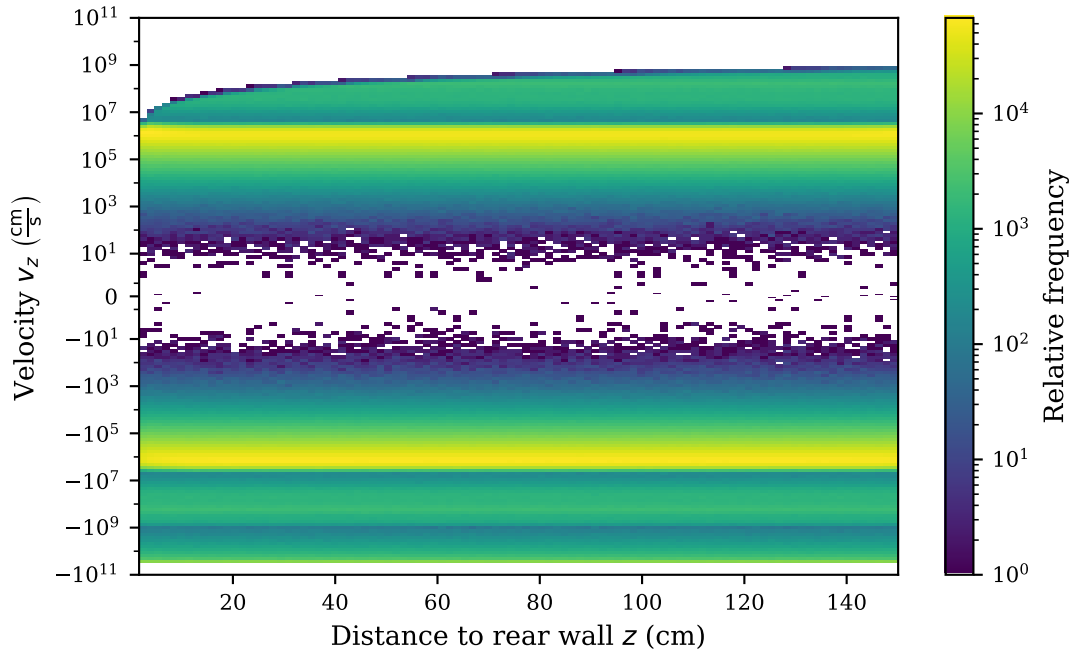


Figure 6.3.: Electron phase space of rear wall region. Data used from the simulation with full electron spectrum. Each position z represents a longitudinal slice of the rear wall region of 1.5 cm length. The velocity was segmented into 100 logarithmic bins. White regions indicate regions with no data entry.

introduce long range effects of the potential. These effects reach well into the bulk of the plasma, and are therefore of specific interest for the KATRIN experiment.

There are fluctuations of the electric field throughout the simulation domain. These fluctuations are similar in all three simulations. They also manifest in the fluctuations of the potential. It is assumed that the fluctuations of the electric field originate from thermal fluctuations of the plasma. This hypothesis is underlined by the fact, that they occur in all three simulations. Nevertheless, more investigations are necessary here.

In total, it can be concluded from figure 6.2, that the specific choice of the electron spectrum has a significant influence on the potential. It can also be seen, that it does not suffice to take only the beta and thermal region into account. The transitional region has a non-negligible effect on the result. In previous simulations of the KATRIN plasma [50], it was assumed that the electron spectrum can solely be described by thermal electrons. The results presented here show that the electron spectrum plays an important role, and the full electron spectrum needs to be considered in the plasma simulations. This claim is further supported by an investigation of the phase space of the electrons, which will be discussed in the following.

The position and velocity of all the simulated electrons can be recorded at a given timestep. This information can be used in a post-processing step to evaluate the phase space of the electrons. The phase space of the simulation with the complete electron spectrum can be found in figure 6.3. Here, only the velocity component along the cylinder axis is considered.

It can be seen, that there are electrons with negative, as well as positive velocity. This means, that electrons stream both towards the rear wall and away from it. This behavior is expected for thermal electrons inside a plasma at a conducting boundary. Nevertheless, it can also be seen that there are electrons of the transitional region, which do not solely flow towards the rear wall and are absorbed there, like the beta electrons, but they are also reflected at some point. Therefore, they are not only source of a background current, but

they also directly take part in the development of the plasma through their movement. This observation has extensive implications. First, it is apparent, that not all electrons, which reach the rear wall chamber are directly absorbed. There is the possibility, that they are reflected back into the center of the source by the plasma potential. Thus, more interactions of electrons with neutral gas could occur. Only, beta electrons seem to be unaffected by the potential and are absorbed fully at the rear wall. However, this consideration did not include the reflection and multiplication of electrons through scattering at the rear wall material [23]. Thus, even more electrons and also beta electrons could be reflected in the real experiment. Secondly, it can no longer be assumed that all particles travel towards the rear wall, which leaves the room open for additional plasma instabilities, foremost the two-stream instability [15].

In summary, the description of the plasma needs to take the full spectrum into account. A simplification to a thermal spectrum does not only underestimate possible plasma instabilities, but does also show significant differences in the plasma potential. Therefore, only the full spectrum is used in the following simulations.

6.2.2. Electron Density

In the previous section, the total electron density was set to $n_e = 1 \times 10^5 \text{ cm}^{-3}$ due to the assumption of quasineutrality. This density is significantly higher than the electron density, which is obtained by the KARL simulations, see section 4.3. In this section, it will be investigated how the total density influences the plasma in front of the rear wall. Three different cases are compared: a simulation, where the electron density is determined by the electron density from the KARL simulation, a simulation, where the total electron density is determined by the ion density of the KARL simulation and a simulation, where the electron density is set to the approximate maximum electron density of the KARL simulation, see table 6.2.

Simulation Setup

Similar to the previous section, four parameters needed to be set prior to the simulation: the background fields, the particle densities, the particle velocity distributions, and the background ion current. The background fields and background ion current were set to the same value as before for a good comparability. This means, that the magnetic background field was set to $B = 2.5 \text{ T}$ and the ion background current was set to $j = 0.73 \text{ nA/cm}^2$. No electric background field was used.

The results from the previous section show that the whole spectrum needs to be taken into account for the simulation of the plasma. Thus, all three simulations were performed with the full spectrum. The same segmentation of the spectrum was used. Only the density and the drift velocity of the segments were changed.

The density of the thermal electrons was set to three different values, see table 6.2. The density of the transitional region was determined in dependence on the density of the thermal region through a constant proportionality constant $a \approx 2 \times 10^{-3}$ for all three simulations. This way the shape of the spectrum is kept the same for the two regions and the density is the only distinctive feature. It is not expected that the density of the beta segment is influenced by small fields, which reinstate the quasineutrality in the plasma. Therefore, the density of the beta segment was set to a constant value.

The drift velocity was determined from the simulated current of the KARL simulations and the density of the corresponding segment. The current was not adjusted even though the density changed in the simulations. This is motivated by the assumption that the number of particles which are created in the source does not significantly increase, when assuming

Table 6.2.: Density of spectral regions for the density comparison simulations.

The density of the the thermal region n_e^{th} was changed and the density of the transitional region n_e^{tr} was scaled through a constant factor. The density of beta electrons n_e^β was kept constant.

	n_e^{th} (1/cm ³)	n_e^{tr} (1/cm ³)	n_e^β (1/cm ³)
reduced	2.54×10^3	5.78	2.50×10^{-1}
standard	1×10^5	2.27×10^2	2.50×10^{-1}
increased	1×10^6	2.27×10^3	2.50×10^{-1}

Table 6.3.: Drift velocity for the density comparison simulations. The drift velocities of the regions was calculated through equation 5.45 from fixed currents, see table 6.1, and the corresponding densities, see table 6.2.

	v_D^{th} (cm/s)	v_D^{tr} (cm/s)	v_D^β (cm/s)
reduced	3.6×10^6	4.1×10^7	2.8×10^9
standard	9.2×10^4	1.0×10^6	2.8×10^9
increased	9.2×10^3	1.0×10^5	2.8×10^9

fields which retain quasineutrality, and that the particles are still mostly absorbed by the rear wall. The specific values of the drift velocity can be found in table 6.3. It is apparent, that the drift velocity scales inversely with the density. Only the drift velocity of the beta region is kept constant because the density was also kept constant.

Results

The three simulations with different electron densities were performed for five plasma time scales and the electromagnetic fields, currents and particle distributions were recorded. Similar to the simulations of the different electron spectra, it is expected that the largest difference between the simulations can be found in the electric field along the central axis of the cylinder.

The recorded electric field values were transformed into an electrostatic potential. A section of the electric field E_z and electrostatic potential in the center of the tube of the three different simulations can be found in figure 6.4. It can be seen, that the general shape of the potential coincides with the simulations with variable spectrum. For a detailed description of the shape please refer to the previous section 6.2.1. From this point forward, only the differences between the three simulations of variable density are analyzed. First, the differences towards the increased density will be discussed. Secondly, the difference of the reduced density will be investigated.

The potential of the simulation with increased density shows larger values than the "standard" simulation. This is evident in an increase of the height of the negative potential wall, the positive potential wall, and also in the height of the potential in the relaxation region. The features of the potential are located at the same position. The origin of this behavior is unknown. Nevertheless, conclusions can be drawn about the plasma, which will be described in the following.

In a classical Debye sheath, it would be expected that the depth of the potential barrier is given only by the temperature of the electrons, and that it is independent of the density of the electrons. The simulations show a different behavior. Here the density has an influence on the depth. This is not concerning because, the presented simulation setup differs significantly from the classical Debye sheath, due to the magnetic field and the additional

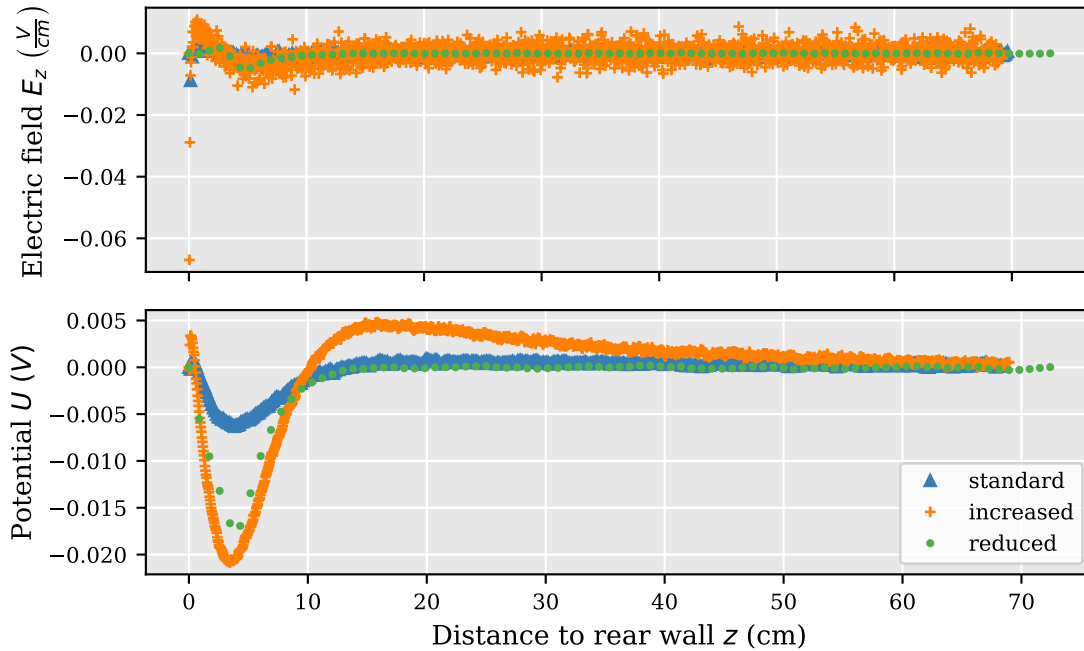


Figure 6.4.: Potential and electric field for varied electron densities. Potential and electric field are evaluated along the longitudinal axis of the cylinder in a simulation with a background magnetic field of $B = 2.5$ T and a background ion current of $j_i = 0.73$ nA/cm². Three different densities scenarios are compared. (standard): values assumed from quasineutrality, (reduced): electron density directly from KARL results, (increased): electron density similar to the density in the center of the source.

non-thermal part of the spectrum. This also means that additional processes than classical Debye shielding are at work. This assumption is underlined by the observation that the position of the features did not change between the simulations, even though the Debye length changed.

The electron density of the beta region is kept constant in all three simulations. In the case of the increased density, it would be expected that the influence of the high-energy electrons is reduced, because their relative density is reduced. Thus, the beta electrons cannot be responsible for the increased potential. This assumption is underlined by the simulations of section 6.2.1. It was observed there too, that the beta region has only a minor influence on the development of the potential.

The value of current of the three spectral regions is kept constant between the simulations. If the current would dominate the height of the potential wall, it would be expected that the height will stay the same between the simulations. This is not observed in the simulations. In contrast to that assumption, the potential shows even larger values. Thus, other processes must determine the potential height than the current alone.

The height of the potential barrier exceeds the thermal energy of 6.9 meV and reaches values up to $U \approx 20$ meV in the simulation with increased density. This is remarkable in two ways. First, the test simulations with a thermal electron distribution in a non-magnetized plasma, see section 5.6.4, showed a lower potential difference than the thermal energy. The additional ion current of this simulation should further reduce the potential wall, as it was observed in the simulation with the thermal part of the spectrum only, see figure 6.2. However, an increase over the thermal energy of the potential difference is observed. This indicates that there is a correlation between the potential difference at the boundary and the electron density. Hence, it is of importance to set limits on the electron density as accurately

as possible, as well as on the electron spectrum. Second, the observed potential drop is higher than the simulated potential drop of Kuckert [50] ($\Delta U \approx 12$ meV). This shows that there is a not unlikely configuration of plasma parameters, where the potential variation is larger than predicted by the previous plasma model. Especially, when considering the uncertainty on the electron density by the KARL simulation.

The simulation with reduced density shows an increase of the height of the negative potential wall. The height of the other features, the small positive potential wall and the relaxation region, are reduced. It seems, that this result contradicts the results of the increased density. However, the results can be interpreted through an evaluation of the additional kinetic energy, which is added through the additive drift velocity in the simulation with reduced density. For the thermal electrons, the drift velocity corresponds to $E_D \approx 3.7$ meV and for the transitional electrons of $E_D \approx 410$ meV. Thus, the additional energy is comparable to the initial energy of the particles and the spectrum is shifted significantly to higher energies. Therefore, a higher potential barrier is necessary to compensate for the electrons leaving the source. It stands to reason, that this mechanism is responsible for the increased potential and not the density itself. It is however difficult to evaluate this effect detached from others, and further simulations would be necessary. Nevertheless, the results show, that a precise knowledge of the density and velocity distribution of the electrons is necessary.

In total, it can be concluded that a knowledge of the full relative spectrum does not suffice for a description of the plasma. The absolute density values of the spectral regions, as well as the correct drift velocities, play an important role in the development of the potential in front of the rear wall. Again, it was observed that the influence of the rear wall boundary is not only visible a few Debye lengths in front of the rear wall, but reaches well into the bulk of the plasma. The potential shows values comparable to the thermal energy of the particles, but can also show higher values.

6.2.3. Background Current Value

The simulated ion and electron current of the KARL simulation provide a first insight in the current, which hits the rear wall. In the simulation, the total ion current is approximately $I_z \approx 50$ nA. Measurements show that the total current at the rear wall ranges from $I_z \approx -30$ nA to 250 nA at different rear wall potentials [24]. Thus, it is apparent to investigate the influence of the current on the plasma. Three different scenarios are tested

- a scenario, where the ion current is given by the KARL simulation
- a scenario, where the ion current is increased by a factor of 10
- a scenario, where the ion current is set to zero

The setup of the simulation is analogue to the simulations with the full spectrum of section 6.2.1. Only the background current value was adapted.

Results

The three simulations with different background current values were performed for five plasma time scales and the electromagnetic fields, currents and particle distributions were recorded. Again, it is expected that the largest difference between the simulations can be found in the electric field along the central axis of the cylinder.

The recorded electric field values were transformed into an electrostatic potential. A section of the electric field E_z and electrostatic potential in the center of the tube of the three different simulations can be found in figure 6.5. It can be seen, that the background current can have a significant influence on the absolute scale of the potential, as well as on the

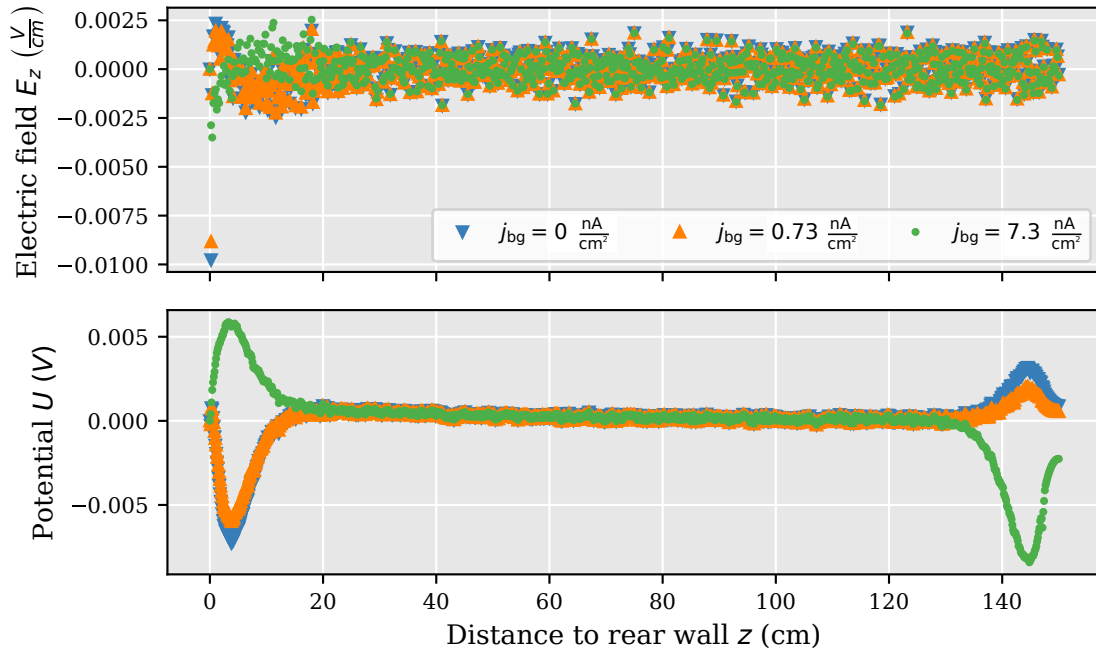


Figure 6.5.: Potential and electric field for varied current amplitudes. Potential and electric field are evaluated along the longitudinal axis of the cylinder in a simulation with a background magnetic field of $B = 2.5$ T. Electron densities and drift velocities are taken from table 6.1. The background ion current was set to the specified homogeneous value j_{bg} throughout the simulation domain.

overall shape of the potential. The specific influence will be discussed in the following. Similar, to section 6.2.1 heuristic arguments will be presented to provide an explanation of the features. However, it is self-evident that the processes in the plasma are more intricate. The discussion is divided into two parts. At first, it will be investigated how the reduction of the background current influences the plasma. Secondly, it will be explained how an increased ion current shapes the potential.

It can be observed that the negative potential wall in front of the rear wall increases, when the ion current is reduced to zero. Similarly, the potential increases at the inlet of the rear wall region. This behavior is best described through the space charge of electrons and ions. Similar to before, the argumentation hinges on the different speeds of electrons and ions. Electrons reach the rear wall faster. Therefore, a positive space charge builds up in front of the rear wall. A negative potential barrier is generated, to prevent an increasing positive charge buildup. The height of the barrier depends on the number of ions, which reach the rear wall. Thus, if the ion current is lowered, then the height of the potential increases, to reduce the electron current in the same manner. This behavior is also observed in the simulated potential data. Similarly, at the injection site, the incoming electron flux is reduced to match the incoming ion current.

The shape of the potential flips, when increasing the background ion current. This behavior can also be explained through space charges. In this case, the ion current is set to larger values than the electron current. Thus, a negative space charge region builds up in front of the rear wall, which reduces the outgoing ion current and increases the electron current. Therefore, there is a positive potential wall observed in the data. Similarly, the potential wall in front of the inlet flips to the negative values. Again, the large ion current drags electrons towards the simulation domain to counter the higher ion current.

It is remarkable, that there is no small negative barrier directly in front of the rear wall in

the simulation with increased ion current compared to the small positive barrier in other two simulations. In the two previous sections, the existence of this barrier was attributed to the fixed ion current, which cannot react to the change of the potential. In the case of a higher ion current, the potential is already at positive values, which does not need to be compensated. Thus, the simulation results with increased ion current further encourage the explanation attempts of the previous sections. Nevertheless, further investigations will be necessary, to investigate the double structure of the potential. One of these investigations can be found in section 6.2.5, where the movement of the ions is directly simulated.

In total, it can be concluded that the value of the background current can have an influence on the development of the potential in front of the rear wall, depending on the scale of the value. On the one hand, if the value of the current is below the value from the KARL simulation, then the influence is less pronounced. On the other hand, if the value is above the simulated value, then huge differences are to be expected.

6.2.4. Radial Dependent Background Current

The ACRONYM code produces three-dimensional data of the electric field and the potential. In the previous sections, the analysis was focused on the one dimensional data along the central longitudinal axis of the cylinder. This procedure was employed because of the strong longitudinal bias produced by the strong magnetic background field. This way, the observed parameter space was reduced, and simple comparisons of the settings were possible. In this section however, the focus lies on the radial structure of the potential and its implications. Additionally, in the previous simulations, it was assumed that the background ion current is homogeneously distributed throughout the source. Simulations with KARL show that the ion current has a radial structure, see section 4.3.4.3. Therefore, in this section the influence of radial ion current will be also investigated.

Two different simulations are compared here: a simulation with the standard settings of section 6.2.1 and the full electron spectrum of table 6.1, and a simulation with the same settings, except that the background ion current has a radial structure. The radial structure was chosen to be a linear function, which decreases from the maximum value in the center towards the beam tube walls. This specific structure was chosen over the direct use of the data from the KARL simulations, because the simulated radial structure of the current is almost negligible at the rear wall.

Results

The two simulations with different background current shape were performed for five plasma time scales and the electromagnetic fields, currents and particle distributions were recorded. The recorded electric field values were transformed into an electrostatic potential. The discussion of the results will be separated into two parts. First, the general two-dimensional structure of the potential will be discussed at the example of the simulation without radial current structure. Second, both simulations are compared in detail.

The two-dimensional structure of the potential for the simulation with the standard settings can be found in figure 6.6. It can be seen that there is a radial structure of the potential. This radial structure is the most prominent close to the rear wall and at the inlet region. It manifests as a reduction of the potential towards the beam tube wall. In the center of the simulation domain, there is no radial structure discernible (in this form of representation). The specific origin of the radial shape is ambitious to estimate and is therefore not tried here. It can be assumed that there is a unique interaction between the strongly bound movement of the electrons with the electric field and grounded boundaries.

The shape of the potential in front of the rear wall reminds of the shape of the potential in an empty source with a rear wall with negative potential, see figure 2.7. There, the potential

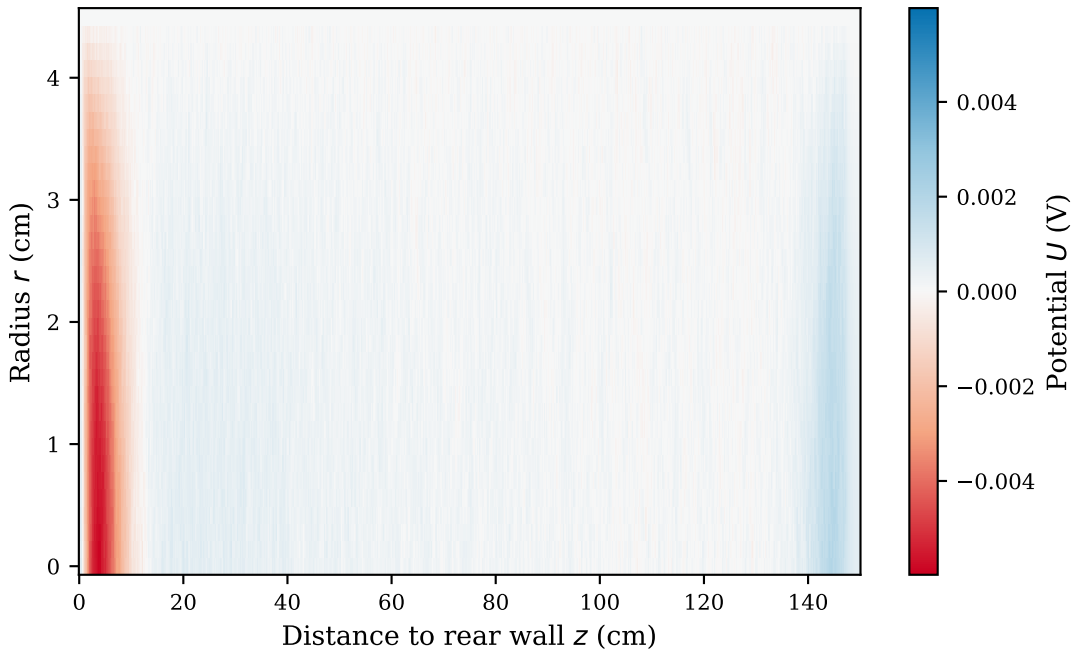


Figure 6.6.: Two dimensional potential distribution. The potential was evaluated after five plasma time scales. The background magnetic field was set to $B = 2.5$ T. Electron densities and drift velocities are taken from table 6.1 (full spectrum). The background ion current was set to a fixed value of $j_{bg} \approx 0.73$ nA/cm² throughout the simulation domain.

of the beam tube dominates the potential in the source, except in the rear wall region. Nevertheless, a closer look at the potential reveals that there are unique features of the potential, not least the reduction of the potential towards zero at the last few centimeters in front of the rear wall, and the small positive potential wall, which were not present in the empty source.

In total, the two-dimensional plot shows, that there is a strong radial structure of the potential, even though the density and current of electrons and ions is distributed homogeneously. This radial structure is significantly different from the plasma simulations without magnetic field, see section 5.6.4, because of the strong confinement of the movement by the magnetic field. In the future, this radial distribution of the potential can be used, to provide more precise estimations on the charged particle currents and densities by the KARL simulations.

Up to this point, the ion current was set to a fixed value throughout the simulation domain. The results of section 6.2.3 suggest that there is a dependency of the potential in respect to the absolute value of the current. In the following, it will therefore be investigated how a radially dependent current influences the solution. The differences between the two simulations (with and without radial dependent ion current) are difficult to grasp in two-dimensional plots of the potential. Therefore, a comparison of the potentials along the longitudinal axis of the cylinder, and along three lines in radial direction can be found in figure 6.7.

It can be seen that the overall shape of the potential does not change significantly between the simulations. Especially, the longitudinal values of the potential agree well with each other. The similarity of the longitudinal potential suggests, that the background current only influences the potential in the near vicinity and does not exert long-range effects.

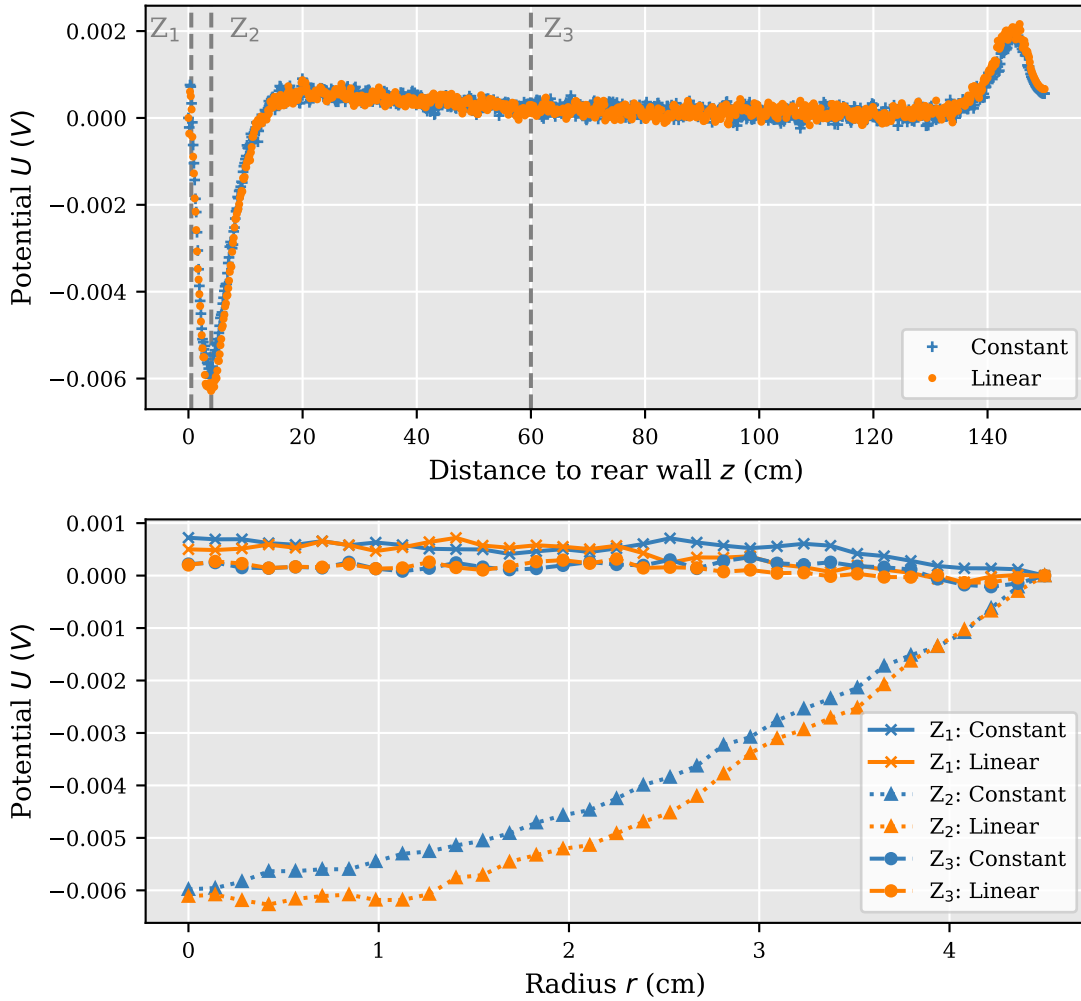


Figure 6.7.: Potential comparison for radially linear decreasing and constant background current. The potential was evaluated after five plasma time scales. It is displayed for a longitudinal axis along the center of the cylinder, and in radial direction at three different longitudinal positions in the source. The longitudinal positions are marked in the longitudinal plot through vertical lines Z_i . The background magnetic field was set to $B = 2.5$ T. Electron densities and drift velocities are taken from table 6.1 (full spectrum). Constant: simulation with fixed background ion current throughout the source ($j_{bg} \approx 0.73$ nA/cm²). Linear: simulation with radially linearly decreasing background current from a maximum value of $j_{bg} \approx 0.73$ nA/cm² towards zero.

In radial direction there are minor differences visible. These differences are most prominent at the negative potential wall. Here, the potential of the simulation with the radially dependent background current shows slightly lower values than the simulation with fixed current. Heuristically, this behavior can be explained by the velocity differences between electrons and ions. Following the argumentation of section 6.2.1 the potential is a consequence of initially different electron and ion currents towards the rear wall. Thus, in the simulation with radial dependent current, a larger potential is necessary to maintain an equilibrium between electron and ion current. The differences of the potential between both simulations decreases towards larger radii. This is caused by the adherence of the potential at the grounded beam tube walls, where both simulations must show the same zero potential value.

There are also differences in the potential discernible at the last centimeters in front of the rear wall. Here, the height of the positive potential wall is lower in the simulation with radially dependent background current than for the simulation with fixed background. The difference of the potentials is more pronounced the larger the radius. In the previous two sections, the existence of the positive potential wall was attributed towards the artificially high value of the ion background current. This hypothesis is supported by the current observations. In the simulation with radially dependent background current, the potential wall is less pronounced at larger radii, where also the background current value has lower values. In the simulation with fixed background current, the background current is higher at larger radii. Thus, also the positive potential wall is higher.

In total, it can be concluded that the potential is significantly radially dependent. This dependency manifests mostly at the negative potential wall, but it is also present at the small positive potential wall. The comparison of the simulation with radially dependent background current with the simulation with fixed background current showed that the radial dependency of the current has only a minor influence on the potential. However, this conclusion is only valid for a maximum background current value of 0.73 nA/cm^2 . The simulations of section 6.2.3 showed that the absolute value of the current has a significant influence on the solution. It is therefore likely that a radially dependent current which covers a large range of values also shows a significant influence in radial direction.

6.2.5. Potential at Large Time Scales

So far, the potential was analyzed on time scales of the electron movement. The results from the previous sections indicate that the ion movement is significantly influenced by the potential generated by the electrons. This is especially the case close to the rear wall, where the boundary effects are the strongest. Until now, the motion of the ions inside the plasma was reduced to their contribution towards the current. It is apparent that this approximation is only valid for short time scales. At higher time scales, it is necessary to simulate the movement of the ions directly. In this section, it will be therefore investigated how the movement of ions influences the solution. The investigation was subdivided into two parts. At first, two simulations were compared at small time scales, one simulation with background current and one simulation with ion macro particles. In the second part, the simulation with ion macro particles was extended to larger time scales.

Ions move much slower than electrons of equal temperature. Thus, the dynamics of the plasma is governed on small time scales by the movement of electrons. In the ACRONYM simulations it is not feasible to resolve the true motion of ions due to the necessary computational resources, see section 6.1. The hindering factor is the large discrepancy between the mass of the electrons and the mass of the ions. In some plasma simulations [75], this issue is resolved by artificially reducing the ion mass towards a more manageable level. In the following, the mass of the ion is given relative to the mass of the electron through the mass factor f_m . In order to maintain the dynamics of the plasma, it is important that the ion mass is still much larger than the electron mass. A good starting point of the simulations is a mass factor of

$$f_m \approx \sqrt{m_i/m_e}, \quad (6.6)$$

where m_i is the mass of the ion. In the case of a single tritium ion, the factor is approximately 74. Nevertheless, also smaller factors were tested in the context of this thesis, down to values of $f_m \approx 21$. No significant differences in the solutions were found. The results presented below were calculated with a factor of $f_m \approx 74$.

In the first part of the analysis, two simulations were compared, one simulation with background current and one simulation with ion macro particles. The setup of the simulation with background current was equal to the setup of section 6.2.1 with the full electron

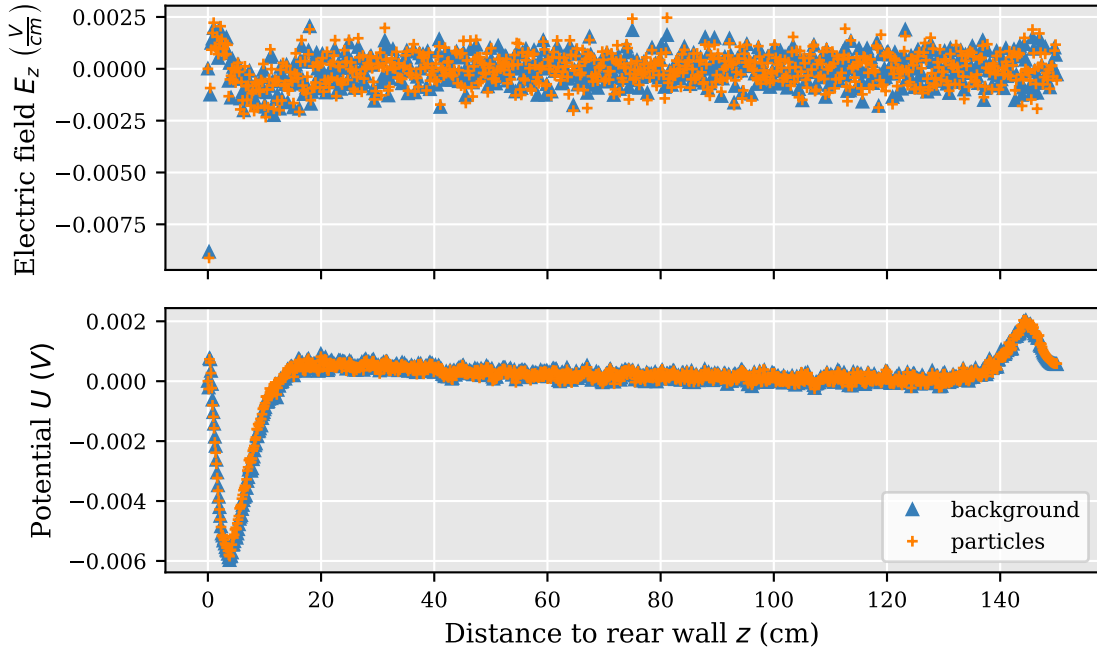


Figure 6.8.: Potential and electric field for two implementation of the ion current. Potential and electric field are evaluated along the longitudinal axis of the cylinder in a simulation with a background magnetic field of $B = 2.5$ T and a ion particle current of $j_i \approx 0.73$ nA/cm² after five plasma time scales. Two different implementations were tested. Background: the ion current is implemented as a fixed background, which is added to the total current. Particles: ions are simulated directly with an additive velocity, which corresponds to the given background current.

spectrum. The corresponding settings can be found in table 6.1. In the simulation with ion macro particles, the background current was set to zero, and the current was directly represented by ion macro particles. They were initialized with the same density and number of particles per cell as the thermal electrons ($n_i = 1 \times 10^5$ cm⁻³, ppc = 20). The velocity distribution of the ion particles were chosen to be a Maxwell-Boltzmann distribution with an additive drift velocity. The drift velocity was calculated from the value of the fixed background current through equation 5.45.

The corresponding electric field and potential of both simulations after 5 plasma time scales along the central axis of the cylinder can be found in figure 6.8. It can be seen, that both simulations produce similar results. The difference of the fluctuations can be attributed to the additional noise generated by the ion particles.

The similarity of both simulations is not surprising, because the setup of the simulations is similar to the validation simulations of section 5.6.1. In the test simulations too, both simulations with and without simulated ions agreed well with each other. Nevertheless, the simulations at hand showed, that the background current approximation is valid for short time scales even with additional boundaries. Additionally, they provide a common starting point of the following investigations of the potential at higher time scales.

In a second step, it was tested, how the evolution of the potential changes at larger time scales. This test was performed with the same settings as the simulation before, where ion macro particles were used. In this simulation, the generated potential of the electrons can now influence the motion of the ions, which changes the current generated by the ions. For the ion mass factor of $f_m \approx 74$, the ion plasma frequency calculates to $\omega_{pi} \approx 8.6 \omega_{pe}$. Simulations with a time scale larger than the ion time scale should show some effects

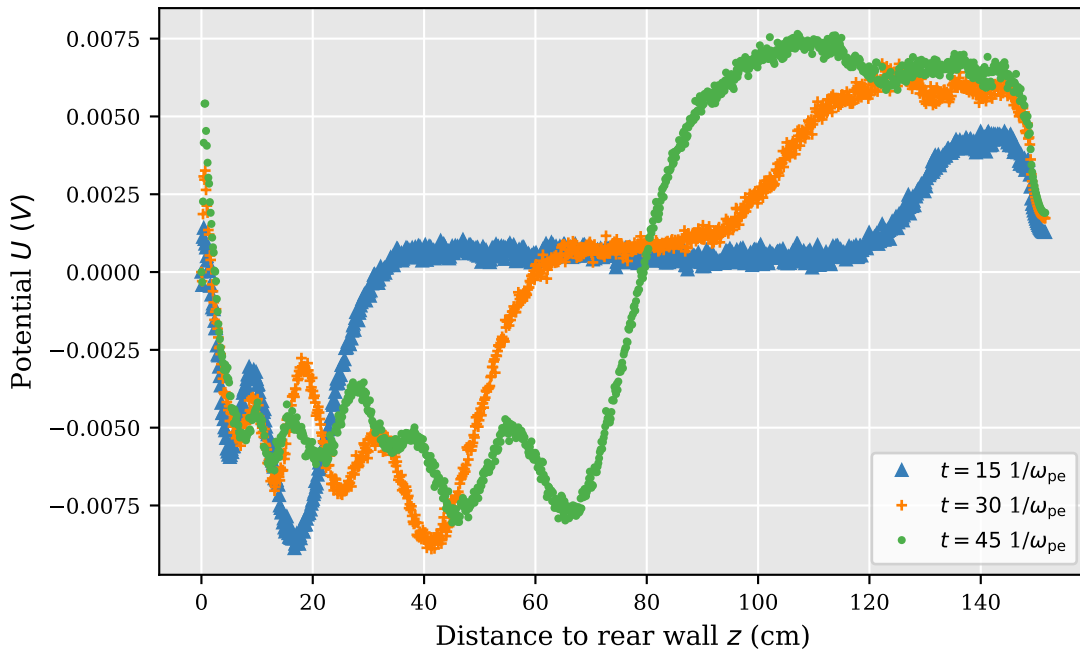


Figure 6.9.: Temporal evolution of the potential. Potential and electric field are evaluated along the longitudinal axis of the cylinder in a simulation with an background magnetic field of $B = 2.5$ T and a ion current of $j_i \approx 0.73$ nA/cm² produced by simulated ions. The potential is evaluated at three different times.

generated by the ions. The corresponding potential distribution for three different time scales is depicted in figure 6.9.

It can be seen, that the potential changes significantly over time, and is evidently different from the potential at small time scales, see figure 6.8. The change of the potential can be noticed as an extension of the negative potential wall in direction of the center, as a development of an additional substructure of the potential wall, and as an extension of the positive potential wall at the inlet of the simulation. The origin of these features is not fully understood yet.

The simulations show that the potential is not static on large time scales for this specific set of initial conditions. This behavior can be explained by three different hypotheses. Firstly, the simulation did only reach a quasi-equilibrium state, and the system progresses to the equilibrium state over long term effects. This indicates that the initial parameters of the simulation are significantly different from the real values. The potential mutation is therefore a product of a compensation of these faulty initial conditions. Thus, better initial conditions would have to be found. Secondly, the simulation domain is too small to resolve the true behavior of the plasma. At large enough time scales, the negative potential will stretch over the whole source with an additional substructure, and the positive potential wall is only a relic of the injection of electrons. Thirdly, there is no static potential to be found at the rear wall, and the potential fluctuates on the time scale of the ion plasma frequency. There might be plasma instabilities linked to this behavior. All three hypotheses are viable explanations, and only more elaborate simulations can provide an answer to their applicability. Nevertheless, it is possible to derive other conclusions from the simulation result.

- It is noticeable, that the simulated potential of the rear wall extends well into the source. Thus, it can be assumed that the potential of the rear wall also extends well into the source in the experiment. It is up to future simulations to investigate this

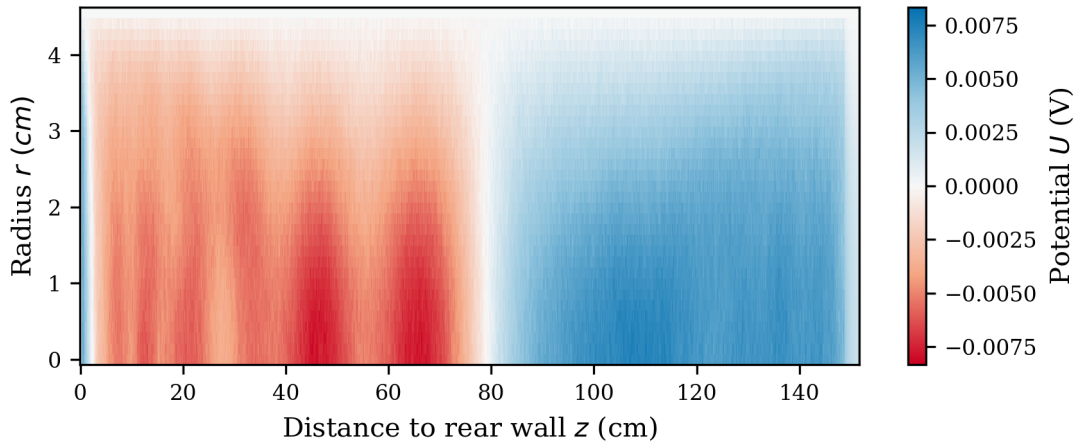


Figure 6.10.: Radial distribution of potential at large time scales. The potential was evaluated at 45 plasma time scales for a simulation with a background magnetic field of $B = 2.5$ T and a ion current of $j_i \approx 0.73$ nA/cm² produced by simulated ions.

behavior for different rear wall potentials. These results can then be compared to the results of Kuckert [50], who predicts a dominant role of the rear wall potential on the overall source potential. However, a complete comparison will be difficult, due to the different assumption of the plasma state. Nevertheless, comparisons with measurement data might be possible, where also a dominant role of the rear wall potential was observed, see section 3.2.3.

- The overall potential is on the order of the thermal energy $E_{\text{th}} \approx 6.8$ eV. However, this result might change, when using different values of the electron density, compare section 6.2.2. Additionally, it was observed in the test simulations, see section 5.6.4, that the simulation underestimates the potential towards the boundary. Thus, larger values are expected in reality.
- The variation of the potential inside the negative potential wall is smaller than the thermal energy of the particles. The origin of these features is still unknown.
- The positive potential wall directly in front of the rear wall is increasing over time. The origin of the potential wall was attributed so far to the ion background current. If this assumption is valid, then it is most likely that the simulation is not in an equilibrium state. Thus, even longer simulations would be necessary.
- There is still a large radial dependency of the potential to be found, see figure 6.10. The absolute value of the potential decreases towards the beam tube wall. This is the case for the positive as well as for the negative potential values. Thus, the evaluation of the mean longitudinal potential and potential variation is very complex and needs special treatment.

In total, it can be concluded that the simulations with an ion background can be used to describe the plasma at small time scales. At larger time scales, the motion of the ions is changed and produces additional features to the potential. However, this observation paired with the long measurement time at the KATRIN experiment does not necessarily result in the conclusion, that only simulations with ions should be performed. It depends on the specific circumstances. On the one hand, ions collide frequently in the center of the source. Thus, collisions must be taken into account (by the KARL simulations), which are not reflected in the ACRONYM simulations. On the other hand, ions collide infrequently in the rear wall region, which is why they can also be simulated by ACRONYM. In summary, the intricate relationship between a non-collisional and partly collisional is

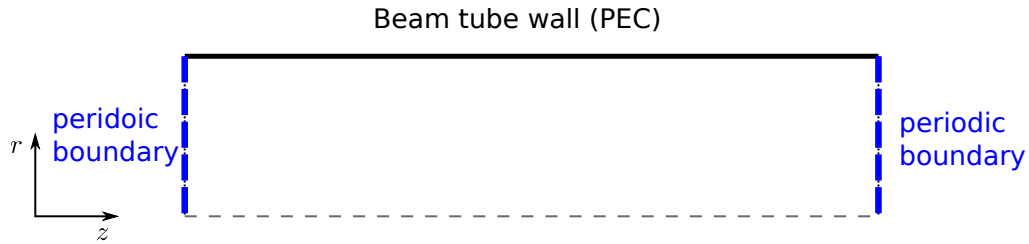


Figure 6.11.: Simulation setup for the central section. The geometry is approximated as a cylinder with two open ends. The boundary conditions of these ends were chosen to a periodic boundary. Particles are injected initially in the volume only.

currently under investigation in the two-part simulation approach with ACRONYM and KARL. Furthermore, it can be of scientific interest to study the dynamic of electrons detached from ions, in which case computational resources can be saved through the use of the ion background current.

6.3. Central Section

In the context of this thesis, a central section is called a section of the beam tube, which is located in the center of the source. It is used to investigate the evolution of the plasma without the influence of the longitudinal boundary of the rear wall. The simulation domain consists of a cylindrical tube with two open ends, where periodic boundary conditions are applied, see also figure 6.11. Hence, it is assumed that the plasma inside the simulation domain has the same properties as the plasma outside, see also section 5.2.2. Naturally, this is only the case for small conjoined parts of the source tube because of the massive neutral gas gradient. Nevertheless, it will be used in the following as a first approximation, due to the simplicity of the boundary algorithm, and due to the assumption of a collisionless plasma (in the ACRONYM simulations). The use of the periodic boundary condition also means that the injection of particles from the bulk of the plasma can be omitted. This way, less attention has to be paid to the boundary condition itself and the focus can be directed towards the temporal evolution of the particles.

Background Current

The current of ions and electrons is a vital parameter for the simulation. This could already be shown in the validation simulations, see section 5.6.1, but also in the simulations of the rear wall section, see section 6.2.3. However, the simulations did also show, that a current value below $j_{bg} \approx 0.73 \text{ nA/cm}^2$ has no significant influence on the potential in the rear wall region. The ion current in the center of the source is lower than the current at the rear wall, see also figure 4.10. Hence, at first it was investigated how and if a background current influences the electric field in the central section.

For that reason, two simulations were performed, one simulation with a background current and one simulation without background current. The current value was set to a quarter of the maximal value at the rear wall ($j_{bg} \approx 0.16 \text{ nA/cm}^2$), to address the reduction of the current in the central section. The electrons were initialized with the spectrum calculated from KARL in the center of the source. The maximal electron density was set to $n_e \approx 5.7 \text{ cm}^{-3}$. The spectrum was dissected into three parts, similar to table 6.1, but with $n_{th} \approx 5.7 \times 10^5 \text{ cm}^{-3}$, $n_{tr} \approx 4.2 \text{ cm}^{-3}$, and $n_\beta \approx 0.34 \text{ cm}^{-3}$. For simplicity, the bulk velocity of the electrons was set to zero.

The potential and electric field of both simulations after two plasma time scales can be found in figure 6.12. It can be seen that the potential and electric field of both simulations

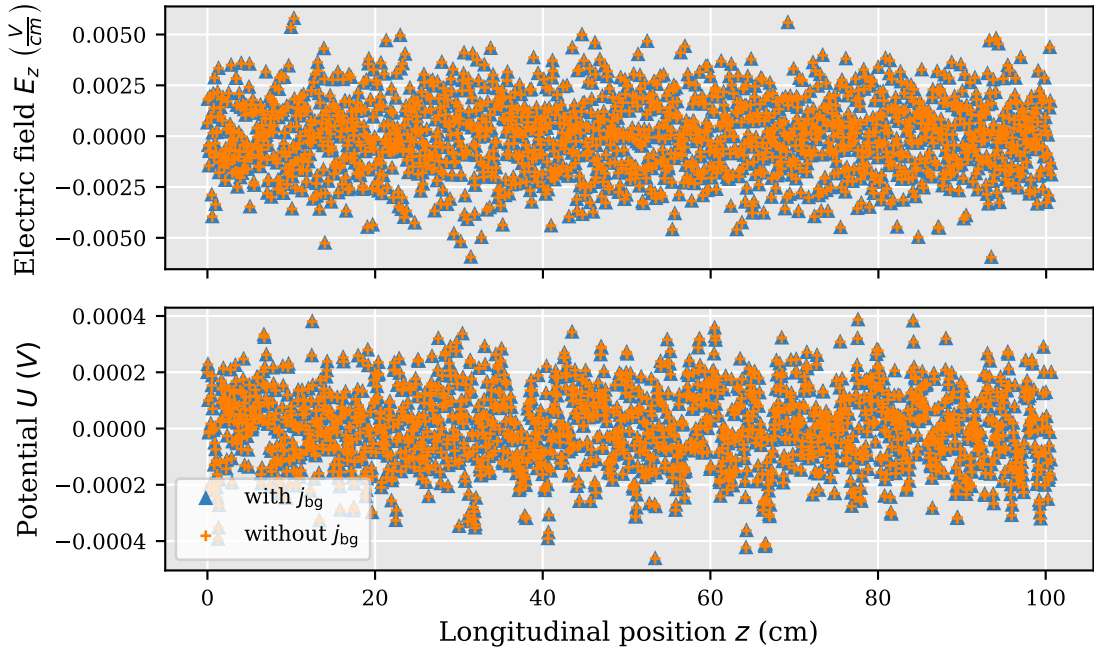


Figure 6.12.: Potential and electric field for simulations of the central section with and without background ion current. The background current of the ions is set to $j_{bg} \approx 0.16 \text{ nA/cm}^2$ for the simulation with background current. The electron density was set to $n_e \approx 5.7 \times 10^5 \text{ cm}^{-3}$ and the full spectrum of the KARL simulations used. The magnetic background field was set to $B = 2.5 \text{ T}$.

fluctuates around zero. The fluctuations of the electric field are larger than in simulation of the plasma in front of the rear wall, see section 6.2.1 for example. The field values are even larger than the field values directly in front of the rear wall. However, the potential shows values significantly below the thermal energy of the particles, and values below the potential at the rear wall boundary. Thus, no large scale fluctuations of the electric field are observed in the data.

It can also be seen that the electric field in the simulation with and without background current shows no significant differences. It must be therefore be concluded that the background current does not play a vital role in the development of the electric field at short time scales. Thus, the results of the simulations of the central section follow the same trend as before, that a small background current can be neglected.

Spatial and Temporal Electric Field Distribution

The one dimensional data of electric field and potential seems to fluctuate randomly. This assumption is contradicted qualitatively by a look at the two-dimensional data. In figure 6.13 and figure 6.14, the electric field and potential of the simulation with background current is shown in radial and longitudinal direction. It can be observed that there is a spatial substructure to the potential and the electric field. The size of the substructure features are in longitudinal, as well as in radial direction, on the order of a few millimeters. A more precise assessment of the substructures can be provided by the evaluation of the electric field in relation to the wavenumber k and the frequency ω , also called spectral analysis. This evaluation also opens the possibility to investigate plasma waves and plasma instabilities in the source.

The spectral analysis of the field was performed similar to Kilian [41]. It can be summarized in two steps: first, the electric field data is recorded at different timesteps, second, the field

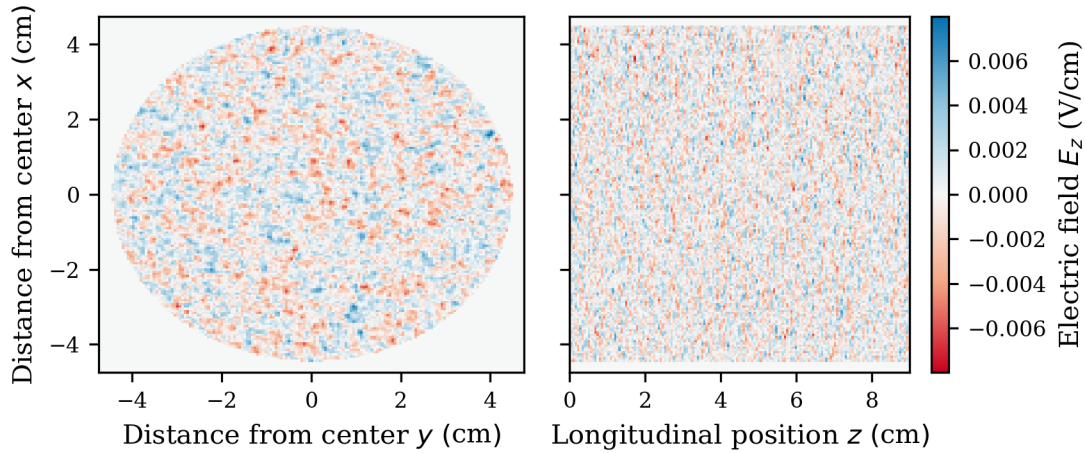


Figure 6.13.: Central longitudinal and radial cut of the longitudinal electric field. The simulation was performed with ion background current and full electron spectrum. The magnetic background field was set to $B = 2.5$ T. Left: cut through the cylinder at the center of the segment. Right: section of the simulated field, cut along the y -axis in the center of the cylinder. Only a fraction of the simulation domain is shown to preserve the aspect ratio.

data is Fourier transformed to gain a representation in dependence of the wavenumber and frequency. In the context of this thesis, the electric field was collected at multiple timesteps along a specified axis. Contrary to Kilian, the values were not collected as a mean of the field values in perpendicular direction, but used directly from a parallel line to the specified axis. This procedure was chosen, because of the additional cylindrical structure of the simulation domain. Nevertheless, tests could show that this approach produces similar results to Kilian. Similar to Kilian, the field values of each output timestep were stacked to a two-dimensional array. A Fourier analysis was performed in two dimensions, which converted the electric field component in one direction $E_i(z, t)$ towards the spectral field component $\tilde{E}_i(k_z, \omega)$. A Hanning window was applied to reduce spectral leakage. The Fourier transformation can produce imaginary results. Thus, only the absolute value of the Fourier transform was used in the results below.

The spectral analysis was applied to a simulation of the central section. The simulation was carried out with the same setup as in the previous paragraph for 12 plasma time scales, but the ions and their current were represented directly through macro particles. This change was motivated through the simulation results of section 6.2.5. They showed, that the movement of the ions is important in the description of the plasma and becomes relevant for larger time scales. The use of ion macro particles did not change the observed structure of figures 6.13 and 6.14, but ensures more precise simulation results on longer time scales. This is especially important for the spectral analysis of the field at low frequencies.

The spectral analysis was applied to three time windows, motivated in the following and discussed thereafter.

- 3 to 4 plasma time scales (figure 6.15): The total energy of the electric fields has reached a constant value over time.
- 11 to 12 plasma time scales (figure 6.16): The simulations of the rear wall sections showed that the electric field changes its shape after a longer time scale, see section 6.2.5.
- 3 to 12 plasma time scales (figure 6.17): The lowest frequency of the analysis is given by the length of the window. Thus, the analysis is stretched over the whole available

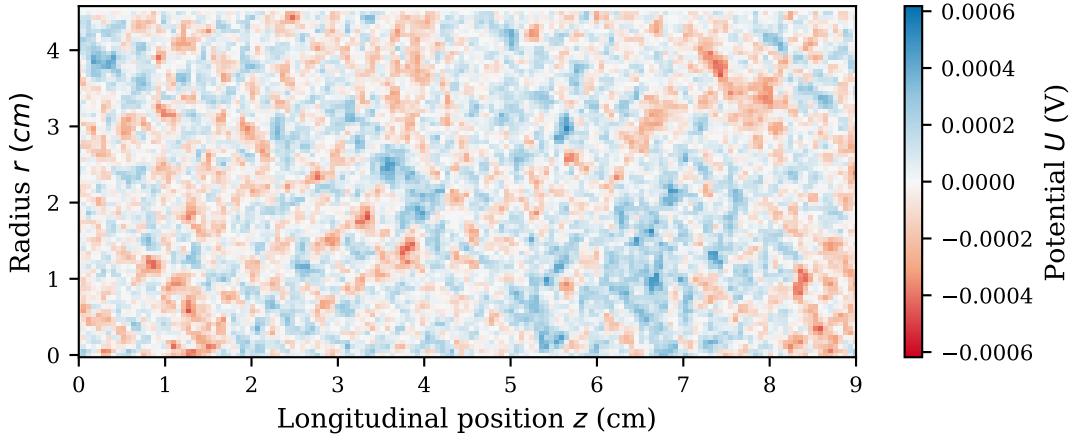


Figure 6.14.: Central longitudinal cut of the potential. The simulation was performed with ion background current and full electron spectrum. The magnetic background field was set to $B = 2.5$ T. Only a fraction of the simulation domain is shown to preserve the aspect ratio.

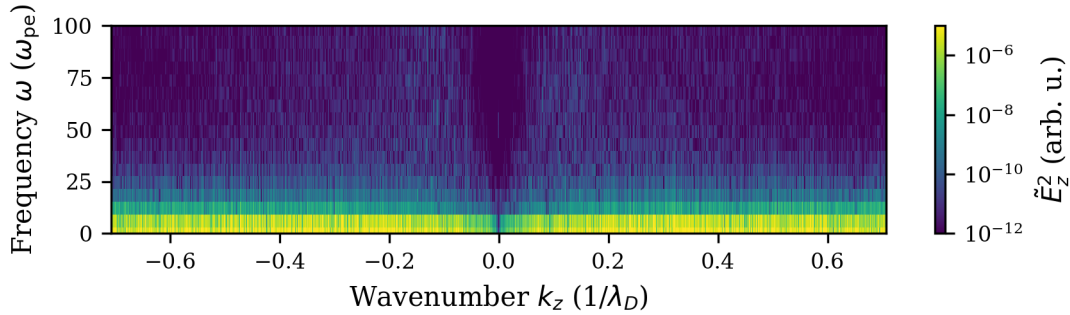


Figure 6.15.: Spectral analysis of longitudinal electric field at small times. The simulation was performed with ion particles as background and a full electron spectrum at a density of $n_e \approx 5.7 \times 10^5 \text{ cm}^{-3}$. The analysis was performed for the timesteps between 3 and 4 plasma time scales, with a selection on the temporal step size of $\Delta t \approx 6.8 \times 10^{-10}$ s.

time window, excluding the stabilization window.

The results of the spectral analysis for timesteps between 3 and 4 plasma time scales, see figure 6.15, show that most of the energy of the electric field is contained in oscillations with frequencies at or below the plasma frequency. No plasma mode structure with high frequency is discernible. In other words, the longitudinal electric field does not show a distinct dispersion relation for a plasma mode. This does not mean, that there are no plasma modes, but that this simulation could not resolve the modes because of the limited resolution.

The region of small wavenumbers was found to be void of significant amounts of energy. The window of low energy is larger for higher frequencies than for lower frequencies. This means, that there are no large-scale fluctuations observed with frequencies well above the plasma frequency. Most of the energy of the electric field resides in the region of low frequencies, with structure sizes below approximately 10 Debye length. This observation is underlined by the 2D representation of the electric field in figure 6.13, where also small structures of a few Debye lengths are discernible. Larger structures are not visible in the snapshot of the electric field. The origin of the fluctuations is unknown, but analyzed further in the third window between 3 and 12 plasma time scales, see below. However, long-term changes to the energy distribution will be discussed first.

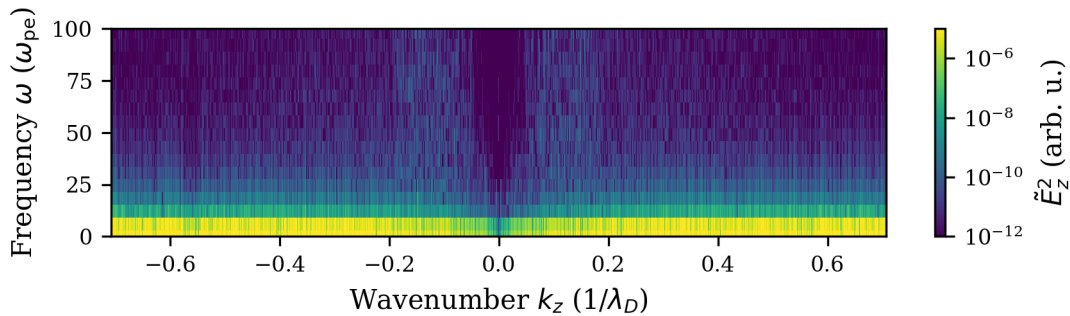


Figure 6.16.: Spectral analysis of longitudinal field at large times. The simulation was performed with ion particles as background and a full electron spectrum at a density of $n_e \approx 5.7 \times 10^5 \text{ cm}^{-3}$. The analysis was performed for the timesteps between 11 and 12 plasma time scales, with a selection on the temporal step size of $\Delta t \approx 6.8 \times 10^{-10} \text{ s}$.

No significant change of the electric field distribution could be found by a direct comparison of the electric field values of the first two windows (3 to 4 and 11 to 12 plasma time scales). Therefore, the spectral analysis method was used to investigate the differences more closely. The corresponding data of timesteps between 11 and 12 plasma time scales can be found in figure 6.16. By comparison to figure 6.15, it can be seen that the spectral shape did not change significantly after a longer time. Again, most of the energy of the electric field resided in the flow frequency band over a wide range of wavenumbers. Also, a region of low energy density was found at low wavenumbers. Thus, the description from the simulation state at 3 to 4 plasma time scales can also be applied here.

Nevertheless, it seems that an additional feature emerges in the data between the wavenumbers of $0.05 < |k_z| < 0.2$ (in units of the inverse Debye length). It manifests through an increase in the energy values over a wide range of frequencies. The origin of this additional feature is not understood yet. It is noteworthy, that this feature extends block wise over a wide range of frequencies. It is therefore unlikely that this feature is linked to one specific plasma mode. At this point, it can only be concluded that there are additional effects, which only manifests after 12 plasma time scales. However, most of the energy still resides at low frequencies, which allows for a spectral analysis at low frequencies, presented in the following.

The results of the spectral analysis between 3 and 12 plasma time scales can be found in figure 6.17. It can be seen that, even in the prolonged time window, the frequency resolution below the plasma frequency is very low, which is governed by the Nyquist-Shannon sampling theorem. Thus, conclusions on the mode structure are tenuous at best. Longer simulations would be necessary for a better resolution, but were not performed because of the constraints on the computational resources.

Nevertheless, a comparison to theoretical modes will be tried here to provide an insight in the capabilities of the method. For simplicity, the modes are calculated from a fluid approach even though it was shown in section 3.3.6 that a fluid approach is not fully applicable to the source plasma. In longitudinal propagation direction, it is expected that two plasma sound wave exist: electron sound waves and ion sound waves. They are both caused by small variations of the electron and ion density in longitudinal direction with modification by the pressure term [78]. The dispersion relation for the electron sound wave, assuming thermalized electrons only, calculates to

$$\omega_{se} = \sqrt{\omega_{pe}^2 + \left(\frac{3k_b T_e}{m_e} k\right)^2}, \quad (6.7)$$

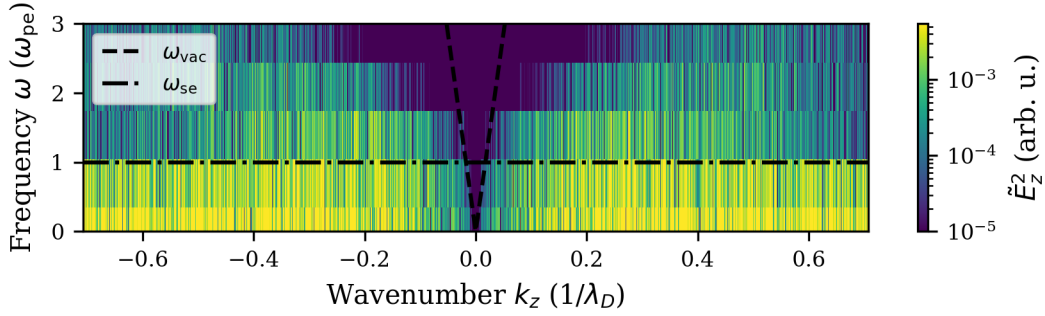


Figure 6.17.: Spectral analysis of longitudinal field at low frequencies. The simulation was performed with ion particles as background and a full electron spectrum at a density of $n_e \approx 5.7 \times 10^5 \text{ cm}^{-3}$. The analysis was performed for the timesteps between 3 and 12 plasma time scales, with a selection on the temporal step size of $\Delta t \approx 6.8 \times 10^{-10} \text{ s}$. Dispersion relation for longitudinal electron sound waves (ω_{se}) and transversal vacuum oscillation (ω_{vac}) for comparison.

with the electron temperature T_e and electron mass m_e [78]. The electron temperature $T_e = 80 \text{ k}$ is so low that the mode frequency is nearly indistinguishable from the electron plasma frequency itself ($\omega_{se} \approx \omega_{pe}$). The dispersion relation is displayed in figure 6.17 for comparison with the data. It can be seen, that some fluctuations of the plasma lie in the near vicinity of the theoretical dispersion relation. In contrast to that, there is no energy visible at wavenumbers close to zero, which should be the case for electron sound waves, see equation 6.7. This indicates that electron sound waves are not excited in the plasma. However, more precise data is necessary to verify or deny this claim.

The maximum frequency for the ion sound wave is the ion plasma frequency [78]. It is approximately a factor 100 lower than the electron plasma frequency. Thus, the dispersion relation of the ion sound waves almost coincides with the wavenumber axis of figure 6.17. Nevertheless, the data suggests, that most of the energy is resides at very low frequencies. Hence, ion sound waves can be the cause of this energy deposition. If the ion sound wave should be resolved by future simulations, then the time window should be at least a factor 1000 bigger than the current simulation. With the current simulation setup, this target can not be reached, and new simulation methods must be found.

It is noteworthy, that the region of low energy coincides with the cone spanned by the dispersion relation of a transversal electromagnetic vacuum mode (ω_{vac}), even though the spectral analysis is performed for longitudinal fields. The dispersion relation for vacuum mode acts as the maximum slope on the dispersion relation for ion sound waves (at any temperature) [78], and the exclusion might therefore be found in the data. However, the exclusion reaches well above the ion plasma frequency. At this point, it can be only be speculated about the origin of this feature, which is not tried here.

In total, it can be concluded that the electric field shows small-scale features with sizes of a few Debye lengths. The features are visible in radial, as well as in longitudinal direction. The field strength of the electric field in the features is comparable to the field strength at the rear wall boundary. However, the potential shows smaller variations than at the rear wall boundary. The spectral analysis of the electric field revealed that the fluctuations have frequencies near or below the plasma frequency. No specific plasma mode could be found in the data, but also no large-scale fluctuations were discernible. The spectral analysis after larger time scales showed a similar behavior than at lower time scales. However, the data also hinted at an increase of the energy at small wavenumbers over a wide range of frequencies. The spectral analysis over a longer time window revealed that most of the fluctuations have frequencies below the plasma frequency. A comparison to electron and

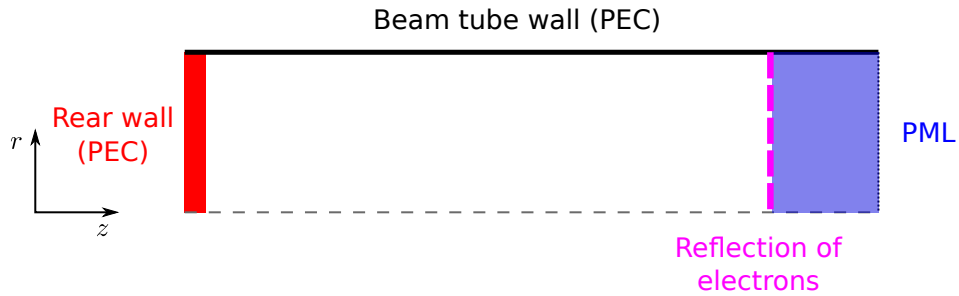


Figure 6.18.: Simulation setup for the complete source section. The geometry is approximated as a cylinder with a closed and an open end. Electrons are reflected, before they cross over to the PML region and absorbed at the rear wall or the beam tube walls.

ion sound waves was tried, but ultimately revealed that the frequency resolution is too low for a meaningful investigation. Because most of the energy resides in the lowest frequency bin, it was hypothesized that there might be a connection to ion sound waves.

6.4. Complete Source Section

The goal of the plasma simulations is the evaluation of the potential throughout the whole source tube. However, it is not feasible to simulate the complete source, especially not for parameter studies and large time scales, see section 6.1. Therefore, in the previous sections, simulations were presented which covered only a fraction of the source tube length (rear wall section and central section). Up to this point, it is unclear how to combine both sections to a coherent source model. This shortcoming was addressed by a simulation of the whole source tube, which will be described in the following.

Simulation Setup

The geometry of the source was approximated by a cylindrical tube with the dimensions of the KATRIN source ($H = 16$ m, $R = 4.5$ cm). The source tube is closed off at one side by the rear wall, which was incorporated in the simulation as a PEC boundary condition. The tube is open at the other side, which was represented by a PML boundary layer, see also figure 6.18. Electrons are assumed to be reflected by the potential of the spectrometers and the potential of the dipole electrodes. Thus, they are reflected in the simulation before they cross over to the PML region and no injection of electrons at the PML boundary was necessary. No decay injection of beta electrons and thermal electrons was used for the simulation because it was aimed for a good comparability with the simulations of the smaller sections.

The initial electron distribution was adopted directly from the KARL simulation, see section 4.3. Three different regions were distinguished in the simulation, a thermal region, a transitional region and a beta region. Electrons of each region were initialized with their own macro factor. The number of particles of each cell are adjusted to the position dependent density of the corresponding region. In the center, the number of particle per cell of the thermal region was set to 20, and for the transitional and beta region to 1. The bulk velocity of the electrons in the transitional and beta region was set to zero. The current of the ions was incorporated through a static background current. This method is justified, because the simulation could only resolve small time scales, due to computational constrains. The position dependent ion current of the KARL simulations was directly used in the simulation.

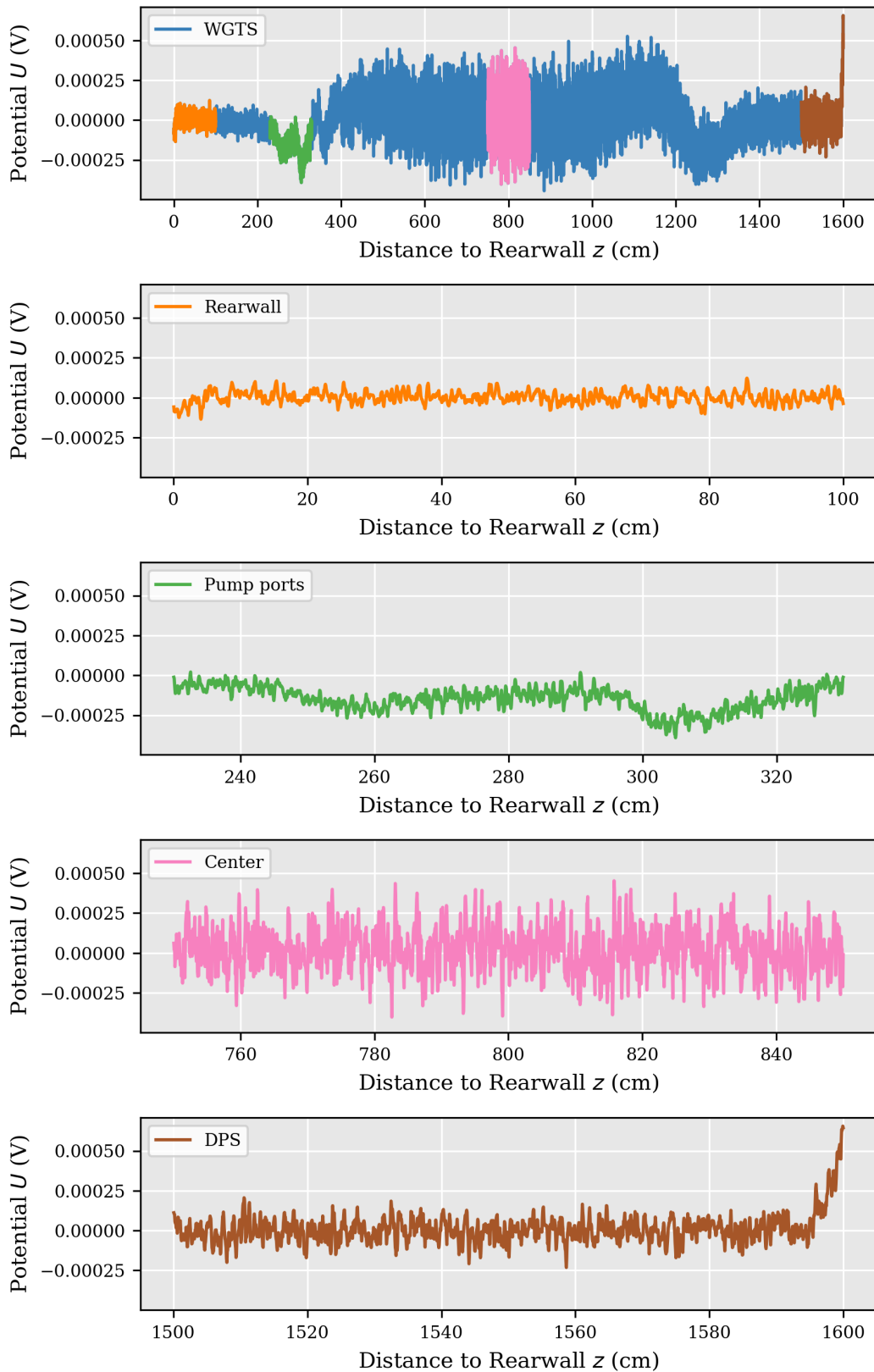


Figure 6.19.: Longitudinal potential distribution for the complete source section. The potential was evaluated after four plasma time scales at the center of the source tube. Top: full view of the potential distribution. Below top: Closeup of the potential distribution marked by colorscale.

Results

The simulation was performed for four plasma time scales. The potential along the central axis of the cylinder can be found in figure 6.19. It can be seen that the potential shows special features, which are dependent on the longitudinal position in the source. Thus, in the following the description of the potential will be separated into four parts covering a section in front of the rear wall, a section in the center of the source, a section in front of the DPS, and a section in the near vicinity of the pump fort.

In all regions, the potential fluctuates on a small scale. The height of the fluctuation is dependent on the position in the source. It ranges from approximately 0.2 meV in the low density regions to approximately 1 meV in the high density region in the center. The spatial size of the fluctuations does not exceed a few Debye lengths. This observation coincides with the observation from the simulation of the central section and the rear wall section. Therefore, it can be assumed that the origin of these fluctuations is the same. In the previous analysis, it was assumed that the fluctuations can be identified by thermal fluctuations of the plasma, although no conclusive explanation could be found so far. It is noteworthy, that the height of the fluctuations scales similarly as the electron density. They are higher in regions with higher electron density than with lower density. However, also the number of particles per cell are lower in the regions with lower density.

In the region close to the rear wall, the potential fluctuates around zero, and drops to lower values at the last few centimeters before the rear wall. This drop is not as distinct as in the simulations of the rear wall section, see section 6.2. Additionally, there is no double structure of a positive and negative potential wall visible. It can be hypothesized, that this behavior is of no physical origin but rather a result of the low particle resolution in the rear wall region. The number of particles in the rear wall region is at least a factor of 100 smaller than in the central region, due to the large density difference between the two regions. In the center, the number of thermal particles was set to 20. Thus, only in every 5th cell, there is a simulated thermal electron, and in only every 100th cell there is an electron of the transitional region. Therefore, fewer interactions of simulated particles with the boundary occur during the simulation time, which could produce a boundary layer.

In total, it can be concluded that the boundary layer at the rear wall was not resolved in the simulation of the complete source section due to the large density gradient. This behavior was already anticipated in section 5.4.1.1 where a position dependent number of particles per cell was favored over a position dependent macro factor. Thus, future simulations of the complete source sections might use a position dependent macro factor to avoid the shortcomings of the other method. However, future simulations with KARL might also reveal that the density gradient is less pronounced due to quasineutrality and the current method can be employed. Until now, the boundary layer is best described by targeted simulation of the rear wall region and not in the simulation of the complete source.

In the center of the source, the potential is similar to the potential of the simulation of the central section, see section 6.3. The fluctuation height as well as the fluctuation size is comparable in both simulations. This observation is supported by comparing the electric field of a central slice, displayed in figure 6.20, and the electric field of the central section, see figure 6.13. It can be seen that the radial distribution of the fluctuations, as well as the height of the fluctuations, coincide. In total, it can be assumed that the simulations of the central section can be used as a good approximation of the central section of the KATRIN source. Thus, the assumption of the periodic boundary condition is valid here.

At the DPS side of the source, a new feature emerges: a positive potential wall at the reflecting surface. Here, the potential rises from the background fluctuations around zero towards values above 0.5 meV over a few centimeters. This potential reflects ions back

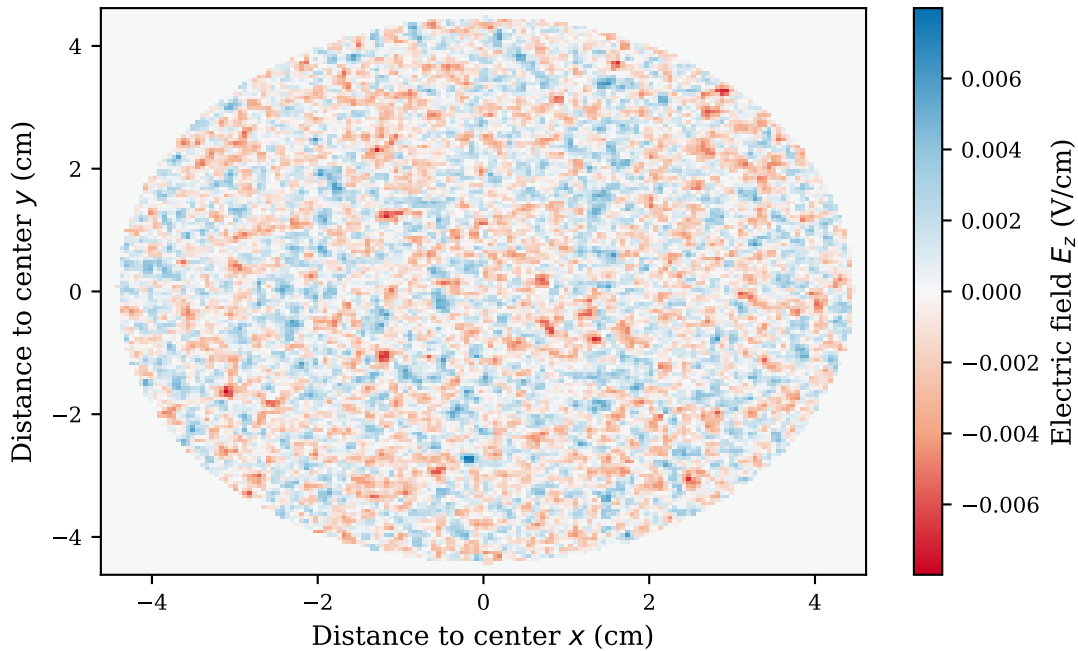


Figure 6.20.: Central radial cut of the longitudinal electric field. The electric field was evaluated after four plasma time scales. The cut was performed in the center of the source (8 m distance to the rear wall).

towards the source, while electrons are accelerated towards the DPS. However, electrons do not accumulate in this region, due to the reflection of the electrons at the DPS dipole potential. The origin of the potential wall can be explained by the background current of ions, which leave the source towards the DPS. Because electrons are not allowed to leave the source in this direction, a repulsive potential builds up to reduce the outgoing ion flux. In the simulation, the height of the potential wall increased over time. It can therefore be assumed that it is still growing, and the final structure could not be determined in this simulation. Dedicated simulations are necessary, to investigate the behavior of electrons and ions in this section. In addition, it needs to be examined how the shape of the DPS dipole electrode potential and the corresponding reflection behavior influences the shape of the plasma potential.

Additional features in the longitudinal potential are visible between 2 m and 5 m, and between 11 m and 14 m distance to the rear wall. They manifest in fluctuations of the potential on a larger scale. The fluctuations show a lower wavelength at the rear end than at the front end of the source. Furthermore, the amplitude of the fluctuations is larger at the front than at the rear end. The origin of these fluctuations is not yet understood. They arise both in the two regions, where the electron density increases significantly. Therefore, it can be assumed that the origin of these features are either linked to the increase of the density or to the reduced number of particles per cell. However, they also arise between the central section and the section in front of the DPS, where the density only drops by a maximum factor of 10. It is therefore more likely that the large scale fluctuations are a product of the reduced density than of the reduced number of particles. Furthermore, it seems that the wavelength of the fluctuations is linked to the relative density difference. In total, further studies are necessary to investigate the behavior of the plasma at large density gradients. Nevertheless, there is a large density difference between electrons and ions in the KARL simulations. These differences produce electric fields, which will reinforce quasineutrality and might reduce the gradient of the electron density. Thus, fewer effects of large density gradients might govern the potential distribution of the source.

In total, the simulation of the complete source section can be summarized by five different observations: First, the potential in front of the rear wall showed significantly different values than in the simulation of the rear wall section. However, it can be assumed that this is no physical effect, but due to the low number of particles per cell. Thus, targeted simulations are better used in this region. Second, the potential and electric field in the center are in good agreement to the simulation of the central section. Thus, the plasma in the center can be approximated by these types of simulations. Third, large scale fluctuations were found in regions with a high electron density gradient. The origin of these fluctuations are not known, and more simulations are necessary here. Fourth, the reflection of electrons at the DPS side of the source in conjunction with an outgoing ion flux produces an additional potential wall. This wall will reflect ions, which should further reduce the outgoing ion flux.

6.5. Conclusion

In this chapter, the ACRONYM code was used to simulate the plasma inside the KATRIN source. The initial conditions were set corresponding to the results of the KARL simulations in the field free case. The simulation of the complete source is demanding on computational resources. Therefore, it was decided to simulate sections of the source first: a rear wall section and a central section.

In the simulations of the rear wall section, it was investigated how the different parameters of the KARL simulation influence the boundary layer in front of the rear wall. These parameters include the shape and composition of the spectrum, the absolute density, background ion current and the shape of the current.

It could be shown that there is significant influence of the spectral composition on the boundary layer. The greatest impact on the potential had the electrons from the transitional region of the spectrum. This result is contradictory to the assumption of Kuckert [50] that the spectrum can be approximated by a thermal spectrum only. For the future, it is therefore of great importance to gain more precise estimations of the spectrum from the KARL simulations. In the same simulations, it was found that electrons can be reflected by the potential in front of the rear wall. This reflection was not limited to thermal electrons only, but extended also the electrons of the transitional region. This result is contrary to the assumption that all electrons are directly absorbed by the rear wall. The stream of electrons, traveling in opposite direction, might incite additional plasma instabilities in the source (two stream instability). An estimate on the development of instabilities could not be found and is up for future investigations.

The simulated density of electrons in front of the rear wall is significantly lower than the density of ions. Assuming quasineutrality of the plasma, it is most likely that the density of the electrons is higher in reality, and that the density of ions is lower than the estimate from the KARL simulations. It was therefore tested, how the absolute value of the electron density influences the result of the ACRONYM simulation. The ratio of the density of the thermal and the transitional region were kept constant. The simulation showed that there is a significant difference of the boundary layer between the different densities. Due to the unknown scaling between the thermal and transitional region, no direct scaling of the boundary could be found.

The boundary potential increased above the thermal energy of the electrons ($E_{\text{th}} \approx 7 \text{ meV}$) in the simulation with increased density ($n_e = 1 \times 10^6 \text{ cm}^{-3}$) to values above 20 meV. This is noteworthy, because the boundary potential in the test simulations was below the thermal energy, but was expected to be higher. Therefore, the estimated boundary potential can be thought of as a lower limit, but more elaborate test simulations are ongoing for a quantification of the reduction and effect of surface charges. Additionally, more precise

estimations will be available in the future from KARL simulations with electric background field, pinpointing the initial density.

An important input for the ACRONYM simulations is the current of the ions. The absolute value of the current is still under investigation. Hence, it was tested how the value of the background current influences the boundary layer. It could be shown that there is only a small difference between the simulation with no background current and a simulation with a current value gained by the KARL simulation. However, there is a significant difference of the potential, when increasing the current by a factor of 10. In this case, the shape of the boundary layer changed, and produced a layer, which would reflect ions instead of electrons.

The KARL simulations predict that the background current is dependent on the radius. It was therefore investigated how the radial shape of the current influences the boundary layer. It could be shown that there is no significant difference between a simulation with a constant current and a simulation with a radially linear decreasing current. Nevertheless, the simulation also showed that the height of the boundary layer is dependent on the radius. It is therefore important to use a radial dependent potential in future KARL simulations. A reduction of the simulation domain to a 1D longitudinal simulation would therefore not describe the properties of the plasma correctly.

In some ACRONYM simulations, it is assumed that the contribution of the ions to the plasma potential can be reduced to their current. This ion current is influenced on larger time scales by the potential of the boundary layer. Therefore, it was tested how the solution changes in a simulation with ion particles on large time scales. At first, it was observed that the simplification to the ion current produces similar results as a simulation with ion particles on short time scales. However, on large time scales, it could be seen that the shape of the boundary layer changed. The negative potential wall of the boundary extended well into the simulated cylinder section. The extent increased with increasing time. No static solution could be found.

The boundary potential at large time scales coincided with the thermal energy of the electrons ($E_{\text{th}} \approx 7 \text{ meV}$). As mentioned before, through comparison with test simulations, the simulated potential can be thought of as a lower limit on the true potential. Furthermore, the true electron density might be higher than implemented, see section 4.4.1, which should increase the potential difference further, see section 6.2.2.

Additional features with sizes of approximately 10 cm emerged in the potential at large time scales. They were not localized directly in front of the rear wall, but extended into the bulk of the plasma. The previous model by Kuckert [50] did not reveal such features, but they are an additional source of uncertainty on the potential variation that go beyond the rear wall boundary potential and overall shift of the potential through the rear wall potential. Thus, they can be of interest for the neutrino mass analysis. However, more elaborate simulations are necessary to investigate the features in more detail.

Simulations were also performed for a central section of the source. Periodic boundary conditions were set up to study the plasma independently of the influence of longitudinal boundaries (rear wall). The potential variations were below the fluctuations of the simulations of the rear wall section. Furthermore, no radial potential difference could be found in the data. Thus, the larger potential variations and radial potential structure are directly connected to the longitudinal boundary, and the boundary has to be included in future simulations for a full picture of the potential.

However, the simple simulation geometry allowed for an investigation of the spatial and temporal structure of the electric field. The simulation showed that the electric field has structures in radial and longitudinal direction of the size of a few Debye lengths. The

structure size is smaller than the radial resolution of the KATRIN detector and can therefore not be measured by the experiment.

A spectral analysis of the longitudinal field revealed that most of the energy of the electric field is distributed in fluctuations with frequencies below or on the order of the plasma frequency. No specific plasma mode could be identified in the data. It could also be shown that large scale fluctuations are improbable, especially for higher frequencies. The resolution at low frequencies was too low to identify any plasma modes. Longer simulations would be necessary, but with the current setup longer simulations can not be realized. Thus, new or improved algorithms must be developed.

Furthermore, the spectral analysis showed that there might be additional features emerging after longer time scales at wavenumbers between 0.05 and 0.2 inverse Debye lengths. The origin of these features is unknown, and is under investigation. This observation might hint at additional plasma instabilities, but could not be confirmed so far.

Simulations of the complete 16 m long source section were performed for small time scales. It could be seen that there are small scale fluctuations of the potential. They already showed in the simulation of the central section, as well as in the simulation of the rear wall section. The electric field fluctuations in the center were found to be in agreement with the simulations of the central section, which justifies the investigation of the central part of the source through a segmentation of the simulation domain. The potential near the rear wall was found to be smaller than in the simulation of the rear wall section. This difference was attributed to the reduced particle resolution in this region. In the future, simulations of the rear wall section with reduced and increased particle resolution, in addition with investigations of the particle density, can provide insight on this hypothesis, and explore the inherent phase space resolution of PIC simulations. However, the overall potential variation of this simulation was significantly below the thermal energy of the electrons, contrary to expectations from the one dimensional Debye layer, and also the simulations by Kuckert. Thus, the current simulation can only provide an insight into additional features of the potential, but not on the absolute scale, and more targeted simulations are necessary.

The simulations of the complete KATRIN source revealed also two additional features to the potential. First, there is a positive potential wall directly in front of the DPS section. This feature was attributed to the outgoing ion current. This current could not be mimicked by the electron movement because of the reflection of electrons. The height of the wall was found to be increasing over time. Thus, dedicated simulations are necessary in the future to investigate the behavior of the plasma in this region. Second, there were larger scale fluctuations found in the regions with large electron density gradient. The origin of these fluctuations could not be found, but it is hypothesized that they originate from the large electron density gradient. Additional simulations might provide an insight onto this behavior. Future simulations with KARL and Poisson solver might also provide electron densities, which do not show such large density differences. Thus, these features might only be a relic of the current simulation. Nevertheless, it could be observed that large scale fluctuations can occur in the potential of the plasma, which are not directly connected to the rear wall boundary but stem from the special properties of the source plasma itself.

Chapter 7

Conclusion and Outlook

The KATRIN experiment aims to measure the electron neutrino mass with a sensitivity down to 0.2 eV [37]. This challenging goal can only be reached through a precise examination of all systematic effects of the experiment. One of these effects is caused by the plasma in the high luminous windowless gaseous tritium source. Previous studies [50, 59] derived a model of the plasma, through the assumption of a diffusive plasma with a total thermalization of all charged particles in the source. Current measurements [24, 54] showed, that these models cannot fully explain the measured data, especially the current towards the beam tube walls, and the relationship between the plasma potential and the rear wall potential. Thus, this work focused on the development of a new model of the plasma.

At first, the plasma was classified by its characteristic length and time scales. It was found that the plasma is bound, strongly magnetized, partly collisional, and partly ionized. The plasma has a low but finite temperature, a net current and multiple species of charged particles, and it shows a thermal and a non-thermal component of the electron spectrum. From the collisionality of the charged particles, it is apparent that the diffusion ansatz of the previous model is not viable. Especially, electrons can not be considered collisional in the source, which was later confirmed by the KARL simulations. Furthermore, ions can only be considered collisional in the center of the source, while at the sides they act non-collisional (also confirmed by the KARL simulations). However, the longitudinal boundary (rear wall) of the plasma, which is assumed to be greatly effecting the plasma, is located in the non-collisional regime. Thus, a segmentation of the source into a collisional and non-collisional section is not viable.

A full simulation of all processes of charged particles in the source was deemed unfeasible, because of the large difference of time scales of electron and ion motion in conjunction with collisions. Thus, a two-part simulation approach was proposed and developed, where the atom physics (collisions with neutral gas) is separated from the plasma physics. Two different simulation tools were used: the newly developed KARL code and a modified version of the ACRONYM code.

KARL uses a Monte-Carlo scheme in which all charged particles are traced individually from their point of origin through their interactions until they are absorbed or recombine. The desired simulation results (position dependent densities, spectra, and currents) were produced by collecting the time spend of each particle in predefined sections of the source.

It was found that the electron spectrum in the source shows a trisection (thermal, beta, transitional), with variable weighting depending on the position in the source. This is a significant improvement of the previous study by Nastoyashchii et al. [59], where only a mean electron spectrum for the whole source was derived. Therefore, the collisionality of

electrons and ions were previously determined as collisional, but is in fact highly dependent on the position in the source.

A comparison of the simulated thermal part of the spectrum with a Maxwell-Boltzmann distribution showed that recombinations are only a secondary effect in the source. The same was observed in the absolute number of recombinations in comparison to absorption at the rear wall and DPS dipole electrodes. Thus, they can be ignored in the future, which will save computational resources. This statement must be revised if the charged particle number is significantly increased, and therefore the recombination probability is increased as well.

The investigation of the particle currents with KARL showed that there is a radial current towards the beam tube walls, which is caused by the movement of the guiding center through collisions. This current was already predicted by measurement, but was observed for the first time in simulations. Previously, it was assumed that the radial current originates from electric fields and instabilities in the source. However, no self-contained theory could be derived how these instabilities emerge. Thus, KARL simulations provide valuable insights on the charged particle motion in the source.

Additionally, the longitudinal current of charged particles could be resolved for each particle species separately, showing the expected longitudinal shape: electrons solely move towards the rear wall, while ions move to both sides of the source. With more precise estimations of the electric fields, these currents might be compared in the future to measurement data at the rear wall and at the DPS dipole electrodes for an in-situ monitoring of the plasma conditions.

Significant differences in the density of electrons and ions were observed in KARL simulations, especially in front of the rear wall and DPS. However, quasineutrality can be assumed in plasma. Thus, a Poisson solver tool was applied to the data, and the resulting electric field was used as input for subsequent simulation. The density differences were large enough to produce potential differences on the order of 10 V, which is not observed by measurement. Therefore, the potential was scaled down by a constant factor. It was discovered that the density differences are reduced in the subsequent simulation. This reduction motivates the proposal to include an internal Poisson solver in KARL in the future. This way, more accurate estimations on the density, spectrum, and currents can be expected.

Despite the success of the KARL simulations, there are improvements that can be made to get more accurate and extensive results in the future:

- Throughout the simulations, a homogeneous magnetic field was assumed. However, it is apparent that the magnetic field in the pump ports and in front of the rear wall is lower than in the central part of the source. Longitudinal gradients can create magnetic mirror effects, when the charged particles collide in regions with low magnetic fields. Thus, influences on the longitudinal density profile can be expected.
- Currently, the particle motion is described through the drift approximation. More precise results can be obtained by the Boris push algorithm [65] at the cost of computational effort. A comparison of both methods is promising, especially in the context of magnetic field gradients.
- The simulation domain was restricted so far to the 16 m of the source tube, and electrons and ions were assumed to be reflected or absorbed at the crossing towards the DPS. However, future simulations might also include the DPS section for a direct connection to the measured dipole current. Additionally, this would allow for an investigation of the imprint of the dipole field on the density distribution in the source.

- At present, electrons are absorbed, when hitting the rear wall. However, high energy electrons can be reflected by the gold plated surface, depending on the energy and impact angle [23]. Thus, these electrons move back into the source and increase the charged particle density through ionization. Additionally, they impact the spectrum in the source, for which reason they might be included in future versions of KARL. However, the inclusion increases the calculation effort, because of the statistical nature of the reflection. Thus, a thorough assessment must be employed. On the same note, electrons can be emitted by the rear wall through the use of high-intensity UV light, which impacts the plasma. This emission can be treated similarly, covering an additional experimental feature of the KATRIN source.
- So far, ions are treated as thermalized particles, which can be described by their density and temperature alone, because of their frequent collisions with the neutral gas. However, ions can gain additional energy through core recoil and non-elastic collisions. An inclusion of these effects is expected to only slightly influence the electron motion. However, it might provide insights on the measured ion current in dependence of the DPS dipole electrode potential, and conversely on the plasma in the source.
- The implemented interactions in the source represent a selection of the most relevant processes in the source, available through cross sections in literature. However, more precise measurement data might be available in the future, resulting in a higher precision of the simulation.
- The spectrum of the electrons is evaluated by the energy of the particles. However, a subdivision of the spectrum in longitudinal and radial direction can be beneficial for subsequent plasma simulations to initialize the electron distribution more accurately. This inclusion will not influence the KARL algorithm itself, because the charged particle distributions do not interact with each other (barring recombinations, which can be neglected). Therefore, only an additional output of the simulation will be created, keeping calculation effort to a minimum.

The results of KARL were used as a starting point for the plasma simulations with ACRONYM. However, additional features were added first to the PIC algorithm to include the conditions of the KATRIN source, like cylindrical conducting boundaries, injection of arbitrary electron spectra, and the use of a predefined ion background current. The new features were validated in dedicated test simulations. Differences towards the expectations were only found in the simulation of plasma in a conducting cylinder. The simulation showed lower potential values than expected from a one dimensional Debye sheath, especially at curved boundaries. More targeted simulations are ongoing to distinguish between a true physical effect or a relic of the used boundary algorithm.

Two parameters stand out for the investigation of the reduced boundary field: the particle density, and the number of particles per cell. The particle density in front of the rear wall is so low, that the macro factor is close to unity, which means that each macro particle almost represents a real electron. This means that the observed effect can be caused by the inherent granularity of the phase space partition. Simulations with various particle densities, and number of particles per cell can provide more insight into this hypothesis. However, until completion of the simulations, the absolute potential values of the ACRONYM simulations can only be taken as a lower limit on the true potential.

For the application of ACRONYM on the KATRIN plasma, the source was first segmented into two sections: a rear wall section, and a central section. This way, dedicated parameter studies could be performed, while preserving computational resources for the subsequent simulations of the complete source.

The focus of the parameter studies in the rear wall section was placed on the shape of the spectrum, the value of the electron density, and the shape and value of the ion current. This way, the most influential parameters, resulting from the KARL simulations, can be singled out, and the plasma model can be adapted accordingly.

It was observed that the non-thermal part of the electron spectrum influences the result significantly. Especially, the transitional region of the spectrum showed a big impact on the solution. It should therefore not be neglected in the description of the plasma, contradicting the initial assumption of Kuckert [50].

Also, the absolute value of the density and ion current impacted the solution heavily. Thus, precise estimations of the initial values from KARL are of utmost importance. Simulations with a radially dependent, and a radially non-dependent longitudinal ion background current showed that the radial shape of the ion current can be neglected in first order approximation. Nevertheless, a radial dependency of the potential was observed, enforcing the need of a two or three dimensional description of the plasma.

Simulations with ions of reduced mass showed that the contribution of the ions can be approximated by a static ion background at small time scales. However, the simulations also revealed that the movement of the ions is relevant at larger time scales. In these simulations, the shape of the potential changed significantly and also revealed a fluctuating substructure. More simulations are necessary here, to investigate the influence of the ion motion on the solution. A connection to the KARL simulations is apparent.

The results of the simulations of the rear wall section can be compared to simulations by Schulze [76], where a one dimensional Vlasov approach was used to evaluate the potential directly in front of the rear wall. The spectrum was approximated as a Maxwell-Boltzmann distribution with a power-law, representing the transitional region of the spectrum. A plasma potential of approximately 47 mV was found after 130 plasma timescales, which is approximately 2.5 times higher than predicted by the PIC simulations at similar conditions. The potential differences can be partly explained by differences of the initial electron spectrum, and the drift velocity. But also the different phase space resolution can be a contributing factor. The test simulations of ACRONYM also showed lower values than expected. Thus, additional simulations, comparing the ACRONYM simulations with the Vlasov simulations directly, can provide insight on the accuracy of the boundary algorithm. However, special precautions must be taken to account for the difference in dimensionality of both simulation tools.

In the ACRONYM simulations, the longitudinal phase space of the electrons revealed that there are two streams of electrons flowing in opposite direction. Thus, not all electrons moving towards the rear wall are absorbed there directly, which contradicts the assumption of the Monte Carlo simulations by Nastoyashchii et al. [59]. Thus, electrons reside much longer in the cavity than expected, changing the electron spectrum. In the future, KARL simulations with background electric fields can be used to quantify this observation. Despite the low electron gyro radius, a contribution of the electrons towards the radial current is conceivable, because of the increased time spend in the source.

Additionally, the two electron streams indicate the possibility of additional plasma instabilities (two-stream instability), which are up for future investigations. The one dimensional simulations of Schulze [76] indicate that a two-stream instability is starting to form after approximately 75 plasma time scales, solidifying the hypothesis. However, more simulations are necessary to investigate this behavior. Apart from the one dimensional Vlasov simulation, also ACRONYM simulations can be used to explore if the stability is also persistent in a multidimensional simulation domain. However, the three dimensional simulations are currently limited by the computational effort, which is necessary to explore above 45 time

scales in the rear wall region. A potential solution might be obtained through a reduction to a two dimensional approach with periodic boundaries in the third direction.

Simulations of the central section were performed with periodic boundaries in longitudinal direction to study the plasma without the influence of the rear wall. The simulations showed that the potential and electric field shows a granular substructure. The extent of the fluctuations was found to be below the spatial resolution of the KATRIN detector, and are therefore only accessible through simulation.

Spectral analysis of the longitudinal field revealed no indication of the development of a specific longitudinal plasma mode well above the plasma frequency. Most of the energy of fluctuations was found below the plasma frequency, and the occurrence of ion acoustic was speculated. However, future simulations with a better resolution below the plasma frequency demands longer simulation times, which are currently not achievable, because of the long wall clock times. Thus, the simulation strategy must be adapted. Again, a potential solution might be the reduction of the simulation domain towards two dimensions. However, information on the azimuthal structure will be lost, but so far, no special azimuthal structure was found.

The spectral analysis at time scales above ten plasma time scale hinted at the development of an instability, which ties right to the observations from Schulze, and to the simulations of the rear wall section. More simulations are necessary to deny or confirm this conjecture.

Lastly, a simulation of the complete source section with ACRONYM was performed. It could be seen that the simulation of the central section of the source is similar to the result of the complete source in the central region, indicating that a separate simulation of source segments provides valuable insights on the overall source plasma.

In the rear wall region, the potential had different values, than in the standalone simulation of this region. This behavior was attributed to the reduced particle resolution in this region, supporting the hypothesis from the test simulations. However, it is still undetermined if this is a physical effect or caused by the used algorithm.

The potential in front of the DPS showed a positive potential wall, which increased over time. This feature was not observed by other simulations so far, but is of great importance, because it reflects ions back into the source, which are otherwise absorbed in the DPS. Thus, the impact of this feature on the overall solution is up for future investigation, together with the impact of a position dependent dipole potential.

In the regions of high electron density gradient, the potential indicated large-scale fluctuations. The origin of these features is not yet understood. It can be assumed that they are connected to the density gradient, because they occur at the same position. However, KARL simulations with electric background fields show a reduced electron density gradient. Thus, high electron density gradients might not be realized in the experiment, and therefore, large scale fluctuations might not occur. Nevertheless, dedicated simulations are necessary for conformation, because if they are realized in reality, they would introduce a so far undescribed fluctuation of the potential.

All in all, the simulations with ACRONYM provided valuable insights into the source plasma of KATRIN, particularly in the assessment of relevant source parameters (electron spectrum, electron density, ion current). However, it became apparent that the model needs to be revised to cover larger time scales, especially for the evaluation of the ion motion. As mentioned before, a two dimensional approach might be a viable option, which also reduces the complexity of the curved PEC boundary condition towards a planar boundary. This way, also mirror charges can be employed in the algorithm, which enhances the accuracy of the simulation.

Other possible improvement to the algorithm can be summarized by the following list.

- Similar to the KARL simulation, a homogeneous background magnetic field was assumed in the source. However, there is a magnetic field gradient present in the pump ports and in front of the rear wall. This gradient partly confines the plasma, which introduces new density and potential variations in longitudinal direction.
- In the current version of ACRONYM, electrons are immediately reflected back into the simulation domain, when crossing over to the DPS. In reality, they are reflected by the negative potential of the dipole electrodes, with potentials between -5 V to -175 V [46]. On the one hand, the immediate reflections seem to be a good approximation for thermal electrons. On the other hand, electrons of the transitional might perform complex interactions with the dipole potential, because of their similar energy.
- The velocity of electrons and ions is initialized isotropically distributed with an additional drift velocity. A subdivision of the spectrum in the KARL simulations into a radial and longitudinal spectrum, might also be reflected in the ACRONYM simulation, reducing the carryover error towards the plasma simulation.
- The potential difference between the rear wall and the beam tube wall was set to zero in the simulation. This specific potential difference is most likely not realized in the experiment, because of unknown workfunction differences. Because of the implementation of background electric fields, ACRONYM is currently equipped to start these studies.
- Small scale workfunction differences of the rear wall, and the beam tube wall are neglected so far. Measurements show that small scale differences exist at the surfaces [77]. Thus, the influence of these differences can also be investigated with the current setup.
- The radial ion current, derived from the KARL simulations, was neglected in the background current, but can easily be activated in future simulations. However, special treatment is necessary, when using ions as macro particles, because the radial motion is created through scatterings, which are not simulated by ACRONYM.
- Macro particles are directly absorbed, when crossing the PEC boundary. This first order approximation neglects the current of the particles in their last timestep. Thus, a more intricate deletion must be found to compensate for the missing current.

Appendix

A. Analytical Calculation of the Rear Wall Potential

The potential $U(r, \theta, z)$ in a tube with an open end can be calculated by solving Poisson's equation

$$\Delta U(r, \theta, z) = 0, \quad (\text{A.1})$$

with the following boundary conditions: the rear wall potential is set to U_0 , the beam tube is kept at ground potential $U_T = 0$ and the potential far away U_∞ is not influenced by the rear wall, so it is set to zero.

A solution can be obtained by using the separation ansatz $U(r, z) = P(r) Q(\theta) Z(z)$. Thus, equation A.1 can be written as

$$PQZ \left(\frac{1}{P}(P'' + \frac{1}{r}P') + \frac{1}{r^2} \frac{Q''}{Q} + \frac{Z''}{Z} \right) = 0, \quad (\text{A.2})$$

using the notation that the primed variables are first derivatives of the variable to their arguments. Given the cylindrical geometry, the z and θ component can be expressed by choosing

$$\frac{Z''}{Z} = k^2 \quad (\text{A.3})$$

$$-\frac{Q''}{Q} = n^2, \quad (\text{A.4})$$

with n being integer and k real values. So Z and Q can be written as

$$Z(z) = \exp(kz) \quad (\text{A.5})$$

$$Q(\theta) = \exp(inz). \quad (\text{A.6})$$

Using these two solutions with the definition of $x := kr$ equation A.2 can be transformed to Bessel's differential equation

$$\frac{\partial^2 P(x)}{\partial x^2} + \frac{1}{x} \frac{\partial P(x)}{\partial x} + \left(1 - \frac{n^2}{x^2} \right) P(x) = 0, \quad (\text{A.7})$$

which is solved by Bessel functions of the first kind J_n . Thus, a general solution of the Poisson equation is found. The specific solution is calculated using the boundary conditions from above. They can be written in this context as

$$U(r, \theta, z = L) = 0 \quad (\text{A.8})$$

$$U(r = R, \theta, z) = 0 \quad (\text{A.9})$$

$$U(r, \theta, z = 0) = U_0 \cdot \Theta(R - r) \quad (\text{A.10})$$

where L and R are the length and radius of the cylinder and Θ the Heaviside function. From equation A.8 it follows that

$$Z(z) = \sinh k(L - z). \quad (\text{A.11})$$

From equation A.9 it follows that

$$k = \frac{a_{nm}}{R} \quad (\text{A.12})$$

with $J_n(a_{nm}) = 0$. The solution of Poisson's equation can now be written as

$$U(r, \theta, z) = \sum_{n=0}^{\infty} \sum_{m=1}^{\infty} J_n(kr) \sinh k(L - z) (c_{nm} \sin n\theta + d_{nm} \cos n\theta). \quad (\text{A.13})$$

From equation A.10 follows that the potential is not dependent on the angle θ . Thus, all coefficients $c_{nm} = 0$ and only $d_{0m} \neq 0$. The coefficient d_{0m} will be determined using the orthogonality of the Bessel function and the boundary condition of A.10 from the following equation

$$\int_0^R J_0\left(k_{0m} \frac{r}{R}\right) \cdot U(r, \theta, z = 0) \cdot r dr = \int_0^R J_0\left(k_{0m} \frac{r}{R}\right) \cdot U_0 \cdot \Theta(R - r) \cdot r dr. \quad (\text{A.14})$$

It follows that

$$d_{0m} = \frac{2U_0}{k_{0m} J_1(k_{0m}) \sinh k_{0m} \frac{L}{R}}. \quad (\text{A.15})$$

So the specific solution of the Poisson's equation can be written as

$$U(r, \theta, z) = 2U_0 \sum_{m=1}^{\infty} \frac{\sinh\left(k_{0m} \frac{L-z}{R}\right)}{\sinh\left(k_{0m} \frac{L}{R}\right)} \frac{J_0\left(k_{0m} \frac{r}{R}\right)}{k_{0m} J_1(k_{0m})} \quad (\text{A.16})$$

B. Conversion of Energy into Different Inertial Frames

Consider two particles p_1 and p_2 in the laboratory frame with the masses m_1 and m_2 and the kinetic energy E_1 and E_2 . The total energy E_{total} for each particle is calculated by

$$E_{\text{total},i}^2 = m_i^2 c^4 + E_i^2, \quad (\text{B.1})$$

where i is the particle index and c the speed of light. The four energy vector of one particle can then be written as

$$p_i^\mu = \left(\frac{E_{\text{total},i}}{c}, \mathbf{p}_i \right), \quad (\text{B.2})$$

where \mathbf{p}_i is the momentum of the particle i . Thus, the invariant mass s of the total system is calculated by

$$s = (E_{\text{total},1} + E_{\text{total},2})^2 - (\mathbf{p}_1 + \mathbf{p}_2)^2 \cdot c^2. \quad (\text{B.3})$$

The kinetic energy of the center of mass frame E_{cm} then calculates to

$$E_{\text{cm}} = \sqrt{s} - m_1 c^2 - m_2 c^2. \quad (\text{B.4})$$

In the target frame, the second particle is defined to be at rest, so the momentum is zero. In this case, the invariant mass reads as

$$s = m_1^2 c^4 + m_2^2 c^4 + 2m_2 c^2 E_a, \quad (\text{B.5})$$

where E_a is the total energy of the first particle in the target frame. The kinetic energy $E_{\text{kin},a}$ of the first particle in the rest frame of the second particles then calculates to

$$E_{\text{kin},a} = \frac{s - m_1^2 c^4 - m_2^2 c^4}{2m_2 c^2} - m_1 c^2. \quad (\text{B.6})$$

In the case that $m_1 \ll m_2$ it can be derived that

$$E_{\text{kin},a} \approx E_{\text{cm}}. \quad (\text{B.7})$$

In total, equations B.3, B.4 and B.6 can be used to convert the inertial frames.

List of Abbreviations

STS Source and Transport Section

SDS Spectrometer and Detector Section

WGTS Windowless Gaseous Tritium Source

DPS Differential Pumping Section

CPS Cryogenic Pumping Section

MS Main Spectrometer

PS Pre-Spectrometer

RS Rear Section

egun Electron Gun

BIXS Beta-Induced X-ray Spectroscopy

KATRIN KArllsruhe TRItium Neutrino

ELSEPA Dirac partial-wave calculation of elastic scattering of electrons and positrons by atoms, positive ions and molecules

PRO KATRIN Plasma Rear wall Optimization at KATRIN

ACRONYM Another Code for pushing Relativistic Objects, Now with Yee lattice and Macro particles

KARL KAtrin WGTS electron and ion spectrum monte caRLo

FBM Forward Beam Monitor

MAC-E magnetic adiabatic collimation with electrostatic retardation

PIC particle-in-cell

CFL Courant-Friedrichs-Lewy

PEC Perfect electrical conductor

PML Perfectly matched layers

Bibliography

- [1] N. Aghanim et al. “Planck 2018 results”. In: *Astronomy & Astrophysics* 641 (2020), A6. ISSN: 0004-6361. DOI: [10.1051/0004-6361/201833910](https://doi.org/10.1051/0004-6361/201833910).
- [2] B. Aharmim et al. “Combined analysis of all three phases of solar neutrino data from the Sudbury Neutrino Observatory”. In: *Physical Review C* 88 (2 2013), p. 025501. DOI: [10.1103/PhysRevC.88.025501](https://doi.org/10.1103/PhysRevC.88.025501).
- [3] M. Aker et al. “Analysis methods for the first KATRIN neutrino-mass measurement”. In: *Physical Review D* 104.1 (2021). ISSN: 2470-0029. DOI: [10.1103/physrevd.104.012005](https://doi.org/10.1103/physrevd.104.012005). URL: <http://dx.doi.org/10.1103/PhysRevD.104.012005>.
- [4] M. Aker et al. “Improved Upper Limit on the Neutrino Mass from a Direct Kinematic Method by KATRIN”. In: *Physical review letters* 123.22 (2019), p. 221802. DOI: [10.1103/PhysRevLett.123.221802](https://doi.org/10.1103/PhysRevLett.123.221802).
- [5] M. Aker et al. “Precision measurement of the electron energy-loss function in tritium and deuterium gas for the KATRIN experiment”. In: *European Physical Journal. C, Particles and Fields* 81.7 (July 2021). DOI: [10.1140/epjc/s10052-021-09325-z](https://doi.org/10.1140/epjc/s10052-021-09325-z).
- [6] M. Aker et al. “The design, construction, and commissioning of the KATRIN experiment”. In: *Journal of Instrumentation* 16.08 (2021), T08015. DOI: [10.1088/1748-0221/16/08/t08015](https://doi.org/10.1088/1748-0221/16/08/t08015). URL: <https://doi.org/10.1088/1748-0221/16/08/t08015>.
- [7] K. Altenmüller et al. “High-resolution spectroscopy of gaseous 83m Kr conversion electrons with the KATRIN experiment”. In: *Journal of Physics G: Nuclear and Particle Physics* 47.6 (2020), p. 065002. ISSN: 0954-3899. DOI: [10.1088/1361-6471/ab8480](https://doi.org/10.1088/1361-6471/ab8480).
- [8] J.F. Amsbaugh et al. “Focal-plane detector system for the KATRIN experiment”. In: *Nuclear Instruments and Methods in Physics Research Section A: Accelerators, Spectrometers, Detectors and Associated Equipment* 778 (2015), pp. 40–60. DOI: [10.1016/j.nima.2014.12.116](https://doi.org/10.1016/j.nima.2014.12.116).
- [9] M. Arenz et al. “The KATRIN superconducting magnets: overview and first performance results”. In: *Journal of Instrumentation* 13.08 (2018), T08005–T08005. DOI: [10.1088/1748-0221/13/08/T08005](https://doi.org/10.1088/1748-0221/13/08/T08005).
- [10] V. N. Aseev et al. “Energy loss of 18 keV electrons in gaseous T₂ and quench condensed D₂ films”. In: *The European Physical Journal D* 10 (1 2000), pp. 39–52. DOI: [10.1007/s100530050525](https://doi.org/10.1007/s100530050525).
- [11] V. N. Aseev et al. “Upper limit on the electron antineutrino mass from the Troitsk experiment”. In: *Physical Review D* 84 (11 2011), p. 112003. DOI: [10.1103/PhysRevD.84.112003](https://doi.org/10.1103/PhysRevD.84.112003).

-
- [12] Martin Babutzka. “Design and development for the Rearsection of the KATRIN experiment”. PhD thesis. Karlsruher Institut für Technologie (KIT), 2014. DOI: [10.5445/IR/1000045598](https://doi.org/10.5445/IR/1000045598). URL: <http://nbn-resolving.org/urn:nbn:de:swb:90-455986>.
- [13] Jean-Pierre Bérenger. “Perfectly matched layer (PML) for computational electromagnetics”. In: *Synthesis Lectures on Computational Electromagnetics* 2.1 (2007), pp. 1–117.
- [14] Ferdinand Cap. *Lehrbuch der Plasmaphysik und Magnetohydrodynamik*. Wien: Springer-Verlag, 1994. ISBN: 3211825703.
- [15] Francis F. Chen et al. *Introduction to plasma physics and controlled fusion*. Vol. 1. Springer, 1984. ISBN: 9783319793917.
- [16] R. Courant, K. Friedrichs, and H. Lewy. “Über die partiellen Differenzgleichungen der mathematischen Physik”. In: *Mathematische Annalen* 100.1 (1928), pp. 32–74. ISSN: 0025-5831. DOI: [10.1007/BF01448839](https://doi.org/10.1007/BF01448839).
- [17] Clyde L Cowan Jr et al. “Detection of the free neutrino: a confirmation”. In: *Science* 124.3212 (1956), pp. 103–104.
- [18] Richard Dendy. *Plasma physics: An introductory course*. Repr. Cambridge: Cambridge Univ. Press, 1996. ISBN: 0521433096.
- [19] Supriyo Dey and Raj Mittra. “A modified locally conformal finite-difference time-domain algorithm for modeling three-dimensional perfectly conducting objects”. In: *Microwave and Optical Technology Letters* 17.6 (1998), pp. 349–352.
- [20] T. Zh. Esirkepov. “Exact charge conservation scheme for Particle-in-Cell simulation with an arbitrary form-factor”. In: *Computer Physics Communications* 135.2 (2001), pp. 144–153. ISSN: 00104655. DOI: [10.1016/S0010-4655\(00\)00228-9](https://doi.org/10.1016/S0010-4655(00)00228-9).
- [21] M. Eugene Rudd. “User-friendly model for the energy distribution of electrons from proton or electron collisions”. In: *International Journal of Radiation Applications and Instrumentation. Part D. Nuclear Tracks and Radiation Measurements* 16.2-3 (1989), pp. 213–218. ISSN: 13590189. DOI: [10.1016/1359-0189\(89\)90052-6](https://doi.org/10.1016/1359-0189(89)90052-6).
- [22] E. Fermi. “Versuch einer Theorie der β -Strahlen.” In: *Zeitschrift für Physik* 88.3-4 (1934), pp. 161–177. DOI: [10.1007/BF01351864](https://doi.org/10.1007/BF01351864).
- [23] Ellen Förstner. “Optimization of the KATRIN rear wall for a keV-scale sterile neutrino search”. B.Sc. Thesis. 2017.
- [24] Fabian Ruben Friedel. “Ion and plasma systematics during the first KATRIN neutrino mass measurements”. PhD thesis. Karlsruher Institut für Technologie (KIT), 2020. DOI: [10.5445/IR/1000126837](https://doi.org/10.5445/IR/1000126837).
- [25] Alexander Fulst. “A Novel Quasi-Differential Method for MAC-E Filters and Determination and Control of the Electric Potentials of the KATRIN Experiment with a Stabilized Condensed Krypton Source and a UV Illumination System”. PhD thesis. Westfälische Wilhelms-Universität Münster, 2020.
- [26] Daniel Furse et al. “Kassiopeia: a modern, extensible C++ particle tracking package”. In: *New Journal of Physics* 19.5 (2017), p. 053012. DOI: [10.1088/1367-2630/19/i=5/a=053012](https://doi.org/10.1088/1367-2630/19/i=5/a=053012). URL: <http://stacks.iop.org/1367-2630/19/i=5/a=053012>.
- [27] A. Gando et al. “Search for Majorana Neutrinos Near the Inverted Mass Hierarchy Region with KamLAND-Zen”. In: *Physical review letters* 117.8 (2016), p. 082503. DOI: [10.1103/PhysRevLett.117.082503](https://doi.org/10.1103/PhysRevLett.117.082503).
- [28] L. Gastaldo et al. “The electron capture in ^{163}Ho experiment – ECHO”. In: *The European Physical Journal Special Topics* 226.8 (2017), pp. 1623–1694. ISSN: 1951-6355. DOI: [10.1140/epjst/e2017-70071-y](https://doi.org/10.1140/epjst/e2017-70071-y).

- [29] D. Gerlich. “Ion trap studies of ternary and radiative association processes”. In: *Nuclear Physics Concepts in the Study of Atomic Cluster Physics*. Ed. by Rüdiger Schmidt, Hans O. Lutz, and Reiner Dreizler. Vol. 404. Lecture Notes in Physics. Berlin, Heidelberg: Springer Berlin Heidelberg, 1992, pp. 194–200. ISBN: 978-3-540-55625-1. DOI: [10.1007/3-540-55625-7{\textunderscore}21](https://doi.org/10.1007/3-540-55625-7{\textunderscore}21).
- [30] B. Grosswendt and E. Waibel. “Transport of low energy electrons in nitrogen and air”. In: *Nuclear Instruments and Methods* 155.1-2 (1978), pp. 145–156. ISSN: 0029554X. DOI: [10.1016/0029-554X\(78\)90198-2](https://doi.org/10.1016/0029-554X(78)90198-2).
- [31] Alireza Haghghat. *Monte Carlo Methods for Particle Transport*. 1st ed. Baton Rouge: Chapman and Hall/CRC, 2014. ISBN: 9781466592537.
- [32] S.W. Harrison, L.J. Massa, and P. Solomon. “Binding energy and geometry of the hydrogen clusters H_n^+ ”. In: *Nature Physical Science* 245.141 (1973), pp. 31–32.
- [33] Florian Heizmann. “Analysis tools and methods for tritium data taking with the KATRIN experiment”. 51.03.01; LK 01. PhD thesis. Karlsruher Institut für Technologie (KIT), 2018. DOI: [10.5445/IR/1000093536](https://doi.org/10.5445/IR/1000093536). URL: <https://publikationen.bibliothek.kit.edu/1000093536>.
- [34] Rudolf Herrmann and Uwe Preppernau. *Elektronen im Kristall*. Vienna: Springer Vienna, 1979. ISBN: 978-3-7091-8521-6. DOI: [10.1007/978-3-7091-8520-9](https://doi.org/10.1007/978-3-7091-8520-9).
- [35] Ratko K. Janev, Detlev Reiter, and Ulrich Samm. *Collision processes in low-temperature hydrogen plasmas*. Jülich, 2003. URL: <http://hdl.handle.net/2128/249>.
- [36] Nicolai M. Josuttis. *The C++ standard library: a tutorial and reference*. Ann Arbor: Addison-Wesley Professional, 2012. ISBN: 978-0321623218.
- [37] KATRIN collaboration. *KATRIN Design Report*. FZKA scientific report 7090. 2005. URL: <http://bibliothek.fzk.de/zb/berichte/FZKA7090.pdf>.
- [38] Wilhelm H Kegel. *Plasmaphysik: Eine Einführung*. Springer-Verlag, 2013.
- [39] Jonas Kellerer and Felix Spanier. “Monte Carlo simulations of the electron - gas interactions in the KATRIN experiment”. In: *Journal of Instrumentation* (2021). In review. arXiv: [2112.15455](https://arxiv.org/abs/2112.15455) [astro-ph.IM]. URL: <https://arxiv.org/abs/2112.15455>.
- [40] R. Kersevan and J.-L. Pons. “Introduction to MOLFLOW+ : New graphical processing unit-based Monte Carlo code for simulating molecular flows and for calculating angular coefficients in the compute unified device architecture environment”. In: *Journal of Vacuum Science & Technology A: Vacuum, Surfaces, and Films* 27.4 (2009), pp. 1017–1023. ISSN: 0734-2101. DOI: [10.1116/1.3153280](https://doi.org/10.1116/1.3153280).
- [41] Patrick Kilian. “Teilchenbeschleunigung an kollisionsfreien Schockfronten”. PhD thesis. Würzburg: Universität Würzburg, 2015.
- [42] Patrick Kilian, Thomas Burkart, and Felix Spanier. “The Influence of the Mass Ratio on Particle Acceleration by the Filamentation Instability”. In: *High Performance Computing in Science and Engineering '11*. Ed. by Wolfgang E. Nagel, Dietmar B. Kröner, and Michael M. Resch. Berlin, Heidelberg: Springer Berlin Heidelberg, 2012, pp. 5–13. ISBN: 978-3-642-23868-0. DOI: [10.1007/978-3-642-23869-7](https://doi.org/10.1007/978-3-642-23869-7).
- [43] Kim and Rudd. “Binary-encounter-dipole model for electron-impact ionization”. In: *Physical review. A, Atomic, molecular, and optical physics* 50.5 (1994), pp. 3954–3967. ISSN: 1050-2947. DOI: [10.1103/physreva.50.3954](https://doi.org/10.1103/physreva.50.3954).
- [44] Earl J. Kirkland. “Bilinear interpolation”. In: *Advanced Computing in Electron Microscopy*. Springer, 2010, pp. 261–263.

- [45] M. Kleesiek et al. “ β -Decay Spectrum, Response Function and Statistical Model for Neutrino Mass Measurements with the KATRIN Experiment”. In: *Submitted to Eur. Phys. J. C.* (2018). In review. arXiv: [1806.00369](https://arxiv.org/abs/1806.00369) [physics.data-an]. URL: <https://arxiv.org/abs/1806.00369>.
- [46] Manuel Klein. “Tritium ions in KATRIN: blocking, removal and detection”. PhD thesis. Karlsruhe Institut für Technologie (KIT), 2018. DOI: [10.5445/IR/1000093526](https://publikationen.bibliothek.kit.edu/1000093526). URL: <https://publikationen.bibliothek.kit.edu/1000093526>.
- [47] Igor A. Kotelnikov and Alexander I. Milstein. “Electron radiative recombination with a hydrogen-like ion”. In: *Physica Scripta* 94.5 (2019), p. 055403. ISSN: 0031-8949. DOI: [10.1088/1402-4896/ab060a](https://doi.org/10.1088/1402-4896/ab060a).
- [48] C. Kraus et al. “Final results from phase II of the Mainz neutrino mass search in tritium β decay”. In: *The European Physical Journal C* 40.4 (2005), pp. 447–468. DOI: [10.1140/epjc/s2005-02139-7](https://doi.org/10.1140/epjc/s2005-02139-7).
- [49] L. Kuckert et al. “Modelling of gas dynamical properties of the KATRIN tritium source and implications for the neutrino mass measurement”. In: *Vacuum* 158 (2018), pp. 195–205. DOI: [10.1016/j.vacuum.2018.09.036](https://doi.org/10.1016/j.vacuum.2018.09.036). URL: <https://www.sciencedirect.com/science/article/pii/S0042207X18310972>.
- [50] Laura Kuckert. “The Windowless Gaseous Tritium Source of the KATRIN Experiment – Characterisation of Gas Dynamical and Plasma Properties”. PhD thesis. Karlsruhe Institut für Technologie (KIT), 2016. DOI: [10.5445/IR/1000065077](https://nbn-resolving.org/urn:nbn:de:swb:90-650776). URL: <http://nbn-resolving.org/urn:nbn:de:swb:90-650776>.
- [51] Rita G. Lerner and George Lockwood Trigg. *Encyclopedia of physics*. 2nd ed. New York: VCH, 1991. ISBN: 0895737523.
- [52] Thomas J. Loredo and Donald Q. Lamb. “Bayesian analysis of neutrinos observed from supernova SN 1987A”. In: *Physical Review D* 65.6 (2002). ISSN: 1550-7998. DOI: [10.1103/PhysRevD.65.063002](https://doi.org/10.1103/PhysRevD.65.063002).
- [53] L. L. Lucas and M. P. Unterweger. “Comprehensive Review and Critical Evaluation of the Half-Life of Tritium”. In: *Journal of research of the National Institute of Standards and Technology* 105.4 (2000), pp. 541–549. ISSN: 1044-677X. DOI: [10.6028/jres.105.043](https://doi.org/10.6028/jres.105.043).
- [54] Moritz Benedikt Machatschek. “A Phenomenological Theory of KATRIN Source Potential Systematics and its Application in Krypton-83m Calibration Measurements”. 51.03.01; LK 01. PhD thesis. Karlsruhe Institut für Technologie (KIT), 2021. 255 pp. DOI: [10.5445/IR/1000132391](https://doi.org/10.5445/IR/1000132391).
- [55] Alexander Curt Marsteller. “Characterization and Optimization of the KATRIN Tritium Source”. PhD thesis. Karlsruhe Institut für Technologie (KIT), 2020. DOI: [10.5445/IR/1000127553](https://doi.org/10.5445/IR/1000127553).
- [56] C. A. Miderski and Gregory I. Gellene. “Experimental evidence for the formation of $H < H^* H + 5 / e^-$ dissociative recombination”. In: *The Journal of Chemical Physics* 88.9 (1988), pp. 5331–5337. ISSN: 0021-9606. DOI: [10.1063/1.454592](https://doi.org/10.1063/1.454592).
- [57] A. I. Morozov. “Steady-state uniform Debye sheaths”. In: *Soviet Journal of Plasma Physics (English Translation)* 17.6 (1991), pp. 393–397.
- [58] Masayuki Nakahata. “Super-Kamiokande”. In: *Nuclear Physics B - Proceedings Supplements* 87.1-3 (2000), pp. 125–134. ISSN: 09205632. DOI: [10.1016/S0920-5632\(00\)00652-6](https://doi.org/10.1016/S0920-5632(00)00652-6).
- [59] A.F. Nastoyashchii et al. “Effects of Plasma Phenomena on Neutrino Mass Measurements Process Using a Gaseous Tritium β -Source”. In: *Fusion Science and Technology* 48.1 (2005), pp. 743–746. URL: http://www.ans.org/pubs/journals/fst/a_1028.

- [60] Chet Nieter et al. “Application of Dey–Mittra conformal boundary algorithm to 3D electromagnetic modeling”. In: *Journal of Computational Physics* 228.21 (2009), pp. 7902–7916. ISSN: 00219991.
- [61] Raphael Ostertag. “Investigation of Plasma Effects in the KATRIN Source with 83m Kr”. Master thesis. Karlsruher Institut für Technologie (KIT), 2020. URL: https://www.katrin.kit.edu/publikationen/mth_ostertag.pdf.
- [62] E. W. Otten and C. Weinheimer. “Neutrino mass limit from tritium β decay”. In: *Reports on Progress in Physics* 71.8 (2008), p. 086201. DOI: [10.1088/0034-4885/71/8/086201](https://doi.org/10.1088/0034-4885/71/8/086201).
- [63] W. Paul et al. “On the dynamics of the reaction of positive hydrogen cluster ions (H_5^+ to H_{23}^+) with para and normal hydrogen at 10 K”. In: *International Journal of Mass Spectrometry and Ion Processes* 149-150 (1995), pp. 373–387. ISSN: 01681176. DOI: [10.1016/0168-1176\(95\)04269-Q](https://doi.org/10.1016/0168-1176(95)04269-Q).
- [64] Wolfgang Pauli. “Offener Brief an die Gruppe der Radioaktiven bei der Gauvereins-Tagung zu Tübingen”. In: *Open letter to the group of radioactive people at the Gauverein meeting in Tübingen*. 1930.
- [65] G. Penn et al. “Boris push with spatial stepping”. In: *Journal of Physics G: Nuclear and Particle Physics* 29.8 (2003), p. 1719.
- [66] Oliver Penrose. “Electrostatic Instabilities of a Uniform Non-Maxwellian Plasma”. In: *Physics of Fluids* 3.2 (1960), p. 258. ISSN: 00319171. DOI: [10.1063/1.1706024](https://doi.org/10.1063/1.1706024).
- [67] Dietmar Petrascheck and Franz Schwabl. *Elektrodynamik*. Berlin, Heidelberg: Springer Berlin Heidelberg, 2019. ISBN: 978-3-662-59786-6. DOI: [10.1007/978-3-662-59787-3](https://doi.org/10.1007/978-3-662-59787-3).
- [68] J.B.C. Pettersson et al. “Dissociative recombination and excitation of D_5^+ by collisions with low-energy electrons”. In: *Molecular Physics* 113.15-16 (2015), pp. 2099–2104. ISSN: 0026-8976. DOI: [10.1080/00268976.2014.1003985](https://doi.org/10.1080/00268976.2014.1003985).
- [69] A. V. Phelps. “Collisions of H^+ , H_2^+ , H_3^+ , ArH^+ , H^- , H , and H_2 with Ar and of Ar^+ and ArH^+ with H_2 for Energies from 0.1 eV to 10 keV”. In: *Journal of Physical and Chemical Reference Data* 21.4 (1992), pp. 883–897. ISSN: 0047-2689. DOI: [10.1063/1.555917](https://doi.org/10.1063/1.555917).
- [70] Radek Plasil et al. “Stabilization of H^+-H_2 collision complexes between 11 and 28 K”. In: *Philosophical transactions. Series A, Mathematical, physical, and engineering sciences* 370.1978 (2012), pp. 5066–5073. ISSN: 1364-503X. DOI: [10.1098/rsta.2012.0098](https://doi.org/10.1098/rsta.2012.0098).
- [71] David M. Pozar. *Microwave engineering*. John Wiley & Sons, 2011.
- [72] Eugen Raspopin. “Systematic effects of the plasma and surfaces in the KATRIN tritium source title”. Master thesis. Karlsruher Institut für Technologie (KIT), 2021. URL: https://www.katrin.kit.edu/publikationen/mth_ostertag.pdf.
- [73] Christian Reiling. “A new Monte Carlo model of the detailed electron and ion distribution in the WGTS of KATRIN”. Master thesis. Karlsruher Institut für Technologie (KIT), 2019.
- [74] Francesc Salvat, Aleksander Jablonski, and Cedric J. Powell. “elsepa—Dirac partial-wave calculation of elastic scattering of electrons and positrons by atoms, positive ions and molecules”. In: *Computer Physics Communications* 165.2 (2005), pp. 157–190. ISSN: 00104655. DOI: [10.1016/j.cpc.2004.09.006](https://doi.org/10.1016/j.cpc.2004.09.006).
- [75] Cedric Schreiner, Patrick Kilian, and Felix Spanier. “Recovering the damping rates of cyclotron damped plasma waves from simulation data”. In: *Communications in Computational Physics* 21.4 (2017), pp. 947–980.

-
- [76] Anna Josephine Schulze. “Vlasov-Simulationen der fensterlosen gasförmigen Tritiumquelle des Karlsruhe Tritium Neutrino Experiments”. B.Sc. Thesis. 2021.
- [77] Kerstin Schönung. “Development of a Rear Wall for the KATRIN Rear Section and investigation of tritium compatibility of Rear Section components”. PhD thesis. Karlsruher Institut für Technologie (KIT), 2016. URL: <https://publikationen.bibliothek.kit.edu/1000056077>.
- [78] Ulrich Stroth. *Plasmaphysik*. Wiesbaden: Vieweg+Teubner, 2011. ISBN: 978-3-8348-1615-3. DOI: [10.1007/978-3-8348-8326-1](https://doi.org/10.1007/978-3-8348-8326-1).
- [79] Tatsuo Tabata and Toshizo Shirai. “Analytic cross sections for collisions of H⁺, H₂⁺, H₃⁺, H, H₂, and H⁻ with hydrogen molecules”. In: *Atomic Data and Nuclear Data Tables* 76.1 (2000), pp. 1–25.
- [80] S. Tamor. “Synchrotron radiation loss from hot plasma”. In: *Nuclear Instruments and Methods in Physics Research Section A: Accelerators, Spectrometers, Detectors and Associated Equipment* 271.1 (1988), pp. 37–40.
- [81] H. Tawara et al. “Cross Sections and Related Data for Electron Collisions with Hydrogen Molecules and Molecular Ions”. In: *Journal of Physical and Chemical Reference Data* 19.3 (1990), pp. 617–636. ISSN: 0047-2689. DOI: [10.1063/1.555856](https://doi.org/10.1063/1.555856).
- [82] S. Trasatti and R. Parsons. “Interphases in systems of conducting phases (Provisional)”. In: *Pure and Applied Chemistry* 55.8 (1983), pp. 1251–1268. ISSN: 0033-4545. DOI: [10.1351/pac198355081251](https://doi.org/10.1351/pac198355081251).
- [83] J.-L. Vay. “Simulation of beams or plasmas crossing at relativistic velocity”. In: *Physics of Plasmas* 15.5 (2008), p. 056701. ISSN: 1070-664X. DOI: [10.1063/1.2837054](https://doi.org/10.1063/1.2837054).
- [84] Nancy Wandkowsky. “Study of background and transmission properties of the KATRIN spectrometers”. PhD thesis. Karlsruher Institut für Technologie (KIT), 2013. DOI: [10.5445/IR/1000036631](https://doi.org/10.5445/IR/1000036631). URL: <http://nbn-resolving.org/urn:nbn:de:swb:90-366316>.
- [85] Kane Yee. “Numerical solution of initial boundary value problems involving maxwell’s equations in isotropic media”. In: *IEEE Transactions on antennas and propagation* 14 (1966), pp. 302–307.
- [86] Jung-Sik Yoon et al. “Cross Sections for Electron Collisions with Hydrogen Molecules”. In: *Journal of Physical and Chemical Reference Data* 37.2 (2008), pp. 913–931. ISSN: 0047-2689. DOI: [10.1063/1.2838023](https://doi.org/10.1063/1.2838023).

Acknowledgment

An dieser Stelle möchte ich allen Menschen danken, ohne die dieses Werk gar nicht möglich gewesen wäre. Es waren so viele, dass es mir nicht möglich ist alle hier aufzuzählen. Dennoch möchte ich einige raus greifen, die mir im besonderen Maß Rückenwind gegeben haben.

An vorderster Stelle geht mein Dank an Guido Drexlin, der mich durch die Irren der Promotion geführt hat. Ich habe durch seine Hilfe viel lernen dürfen und blicke mit Freude zurück an unseren Austausch auf Augenhöhe. In Zukunft werde ich sicherlich seine besonnene Herangehensweise und den Umgang mit Menschen in Erinnerung behalten.

Nicht weniger möchte ich Felix Spanier danken, der mich kräftig mit Rat und Tat unterstützt hat. Dabei geht es nicht nur um die sehr reichhaltigen fachlichen Gespräche, sondern auch um das stets offene Ohr, die vielen Stunden der Mühe meine Server zum Laufen zu bringen, und natürlich auch um meine Integrierung in die ACRONYM Community. Nicht zuletzt auch durch die illustren Weihnachtsessen.

Daran anschließen möchte ich meinen Dank an die ACRONYM Community, die mich sehr bereitwillig in ihren Reihen aufgenommen hat. Ein besonderer Dank geht an Patrick Kilian, der mir neue Wege für den Code aufgezeigt hat.

Natürlich möchte ich auch den vielen Menschen von KATRIN danken, die mich auf meinem Weg begleitet haben und meine Promotionszeit zu der gemacht haben, die sie war. Dabei möchte ich Martin, meinem Bürokollegen, danken für die vielen kleinen Momente zwischen der Arbeit. Zudem geht mein Dank auch an Fabian für die lustige Zeit auf Konferenzen und Dominik für die stets positive Einstellung.

Zudem möchte ich auch meinen Freunden Anna, Deike, Johannes, Charlie und Moritz zutiefst danken, die mir geholfen haben die sprachlichen Tücken zu überwinden. Auch möchte ich meinem Neffen Eldin danken, der trotz seines jungen Alters versucht hat mich zu unterstützen.

Nicht minder möchte ich meinen Eltern danken. Sie haben mich zu dem Menschen geformt, der ich heute bin. Auch haben sie mich in jeder Lebenslage mit voller Eifer unterstützt und mir den Raum ermöglicht mich weiterzuentwickeln. Dem anschließen möchte ich meinen Dank an meine eigene, aber auch erweiterte Familie. Ihr wart ein tragendes Netz durch die ganze Zeit hinweg.

Zuletzt möchte ich auch meine tiefe Dankbarkeit gegenüber meiner Partnerin Myrto zum Ausdruck bringen, die mich immer wieder ermutigt hat weiter zu machen, die mir immer wieder den Rücken frei gehalten hat und mich auch ertragen hat, wenn es nicht so gut lief. Aber natürlich auch in den schönen Momenten konnte ich mit ihr meine Erfolge feiern und konnte so die Zeit auch genießen.